Relationships Between Physical Properties And Maturation Of Organic-Rich Chalk In Two Basins In Israel: Laboratory And Field Measurements

Thesis submitted in partial fulfillment

of the requirements for the degree of

"DOCTOR OF PHILOSOPHY"

by

Omri Shitrit

Submitted to the Senate of Ben-Gurion University

of the Negev

March 2019

Beer-Sheva

Relationships Between Physical Properties And Maturation Of Organic-Rich Chalk In Two Basins In Israel: Laboratory And Field Measurements

Thesis submitted in partial fulfillment

of the requirements for the degree of

"DOCTOR OF PHILOSOPHY"

by

Omri Shitrit

Submitted to the Senate of Ben-Gurion University of the Negev

Approved by the advisors

Prof. Yossef H. Hatzor 

Prof. Shimon Feinstein 

Prof. Harold Vinegar 

Approved by the Dean of the Kreitman School of Advanced Graduate Studies

March 2019

Beer-Sheva

<u>This work was carried out under the supervision of:</u>

Prof. Yossef H. Hatzor

Prof. Shimon Feinstein

Prof. Harold J. Vinegar

In the Department of Geological and Environmental Sciences

Faculty of Natural Sciences

Ben-Gurion University of the Negev

I, Omri Shitrit, whose signature appears below, hereby declare that:

I have written this Thesis by myself, except for the help and guidance offered by my Thesis Advisors.

The scientific materials included in this Thesis are products of my own research, culled from the period during which I was a research student.

Date: March 24, 2019 Student's name: Omri Shitrit

Abstract

This dissertation presents a comprehensive rock physics study of an organic-rich chalk, of the Ghareb-Mishash Formations from the Shefela basin of central Israel. The study uses various laboratory measurements and rock physics theories to emphasize the effects imposed by porosity, organic content, maturity and fluid saturation. It is done by investigating the microstructure and finding an appropriate rock physics modeling (RPM) approach. Laboratory measurements are performed using core samples from the Zoharim and Aderet wells in the Shefela basin. The tested rock properties are porosity, density, acoustic velocities, elastic moduli, permeability, compressive strength and tensile strength. The effect of thermal maturation is examined by pyrolysis-induced maturation of the cores. The laboratory-based rock physics analysis is then compared with well-logs from the same wells. This study provides tools for quantitative analysis of the Ghareb-Mishash chalk, in purpose of geophysical exploration and rock engineering.

Many organic-rich rocks are shales, which are low in porosity, rich in organic matter and clay content, and exhibit a laminated structure. Unlike organic-rich shales, the Ghareb-Mishash chalk exhibits high porosity, typical chalk texture (mudstone-wackestone), and extreme organic enrichment of up to 20% of TOC (i.e. total organic carbon weight percentage in the matrix). The organic matter is dispersed in the matrix, instead of being laminated alongside the minerals as in shales. Because of this, the RPM in this study is inspired by RPM of both organic-rich shales and non-organic chalks. Burial depths of the Ghareb-Mishash sequence in the Shefela basin, both historically and currently, are considered shallow (several hundred meters), hence the undeveloped degree of maturation, compaction, and cementation. There are three dominant phases in the rock: 1) minerals, mainly calcite, 60-80% (volume percentage); 2) porosity, 25-45%; and 3) organic matter, 5-25%, mostly immature Type IIs kerogen. The fabric of the Ghareb-Mishash chalk manifests vertical transverse isotropy (VTI), i.e. rock properties are isotropic across the bedding-parallel direction. The anisotropy is exhibited in many of the physical properties of the rock (elastic moduli, acoustic velocities, permeability, strength). RPM is done with consideration of the rock components and their volumetric proportions, arrangement in the matrix, and mechanical role.

There are four significant novelties in this dissertation, which may be applicable beyond the scope of this study:

- **"Hydrostatic strain ratio", Ω:** Under hydrostatic compression, typical VTI rocks exhibit maximum and minimum contraction in the bedding-normal and bedding-parallel directions, respectively. The ratio between them is defined here as the "hydrostatic strain ratio", denoted by Ω. It quantifies elastic anisotropy. Because of its simplistic definition, it gives physical intuition regarding the anisotropic behavior of the rock. Ω depends on four of the five elastic constants of VTI materials, these are C_{11}, C_{12}, C_{13}, and C_{33}. Thus, Ω represents properties in the directions normal, diagonal and parallel to the bedding. A plot of Ω versus Thomsen's ε parameter for P-wave anisotropy (Thomsen 1986) reveals a strong connection between the two parameters. Ω proves more sensitive to anisotropy within the weak anisotropy range, when compared with Thomsen's ε and γ parameters. Of all known elastic anisotropy parameters, Ω is the only anisotropy parameter that is truly applicable under static conditions. All these features show that Ω can be useful in rock physics studies of VTI rocks.
- **"HDC-TIES" method:** Usually, triaxial compression tests of VTI rocks utilize multiple specimens or testing equipment that is designed specifically for a certain class of anisotropy. The proposed method is developed for analysis of triaxial compression test results, conducted on a single vertically-oriented specimen. Static elastic parameters are determined accurately and informatively using the newly developed method of Hydrostatic-Deviatoric Combination for Transversely Isotropic Elastic Stiffnesses (HDC-TIES). The HDC-TIES method considers standard triaxial compression equipment and the most common sample orientation, so that bedding-normal and bedding-parallel strains are aligned with axial and radial stresses (respectively). In HDC-TIES, the elastic constants are derived by combining the vertical Young's modulus and Poisson's ratio (E_v and ν_v) from the deviatoric compression stage, and bulk modulus and hydrostatic strain ratio (K and Ω) from the hydrostatic stage. Using the experimentally-derived values of E_v, ν_v, K and Ω, one can compute the stiffness constants C_{33}, C_{13} and $C_{11} + C_{12}$, and determine ranges of C_{11}, C_{12} and C_{66}. The HDC-TIES method is advantageous because: 1) where rock material is limited, a single test may be quite informative; 2) at the absence of VTI-adequate testing equipment; 3) heterogeneity between samples is less problematic; 4) it provides a good estimation of C_{13} which is of special interest in geophysical studies; and 5) it may be applied to existing triaxial compression test data, thus enables a repeated analysis and derivation of VTI elastic constants.

- **"HS kerogen" model:** The Hashin-Shtrikman (HS) bounds, commonly used for determining the minimum and maximum elastic moduli of granular rocks (Hashin and Shtrikman 1963; Mavko, Mukerji and Dvorkin 2009), are modified here to simulate a kerogen-supported matrix. It describes a calcite-kerogen-porosity mixture in which the kerogen is distributed effectively between the mineral grains to form a connected network that dictates the elastic behavior of the rock.
- **Petrophysical model of organic-rich rocks:** Mass and volume determination of phases in previous rock physics studies of organic-rich rocks is found to be flawed. Organic content has been directly associated with kerogen without consideration to bitumen content. Inaccurate inclusion of porosity in the model lead to mistaken bulk volume calculations, and consequently erroneous density and volume determination. A corrected approach is elaborated in this study with two major modifications: 1) TOC results are converted to organic matter volumetric content instead of kerogen content; bitumen extraction data are used to determine bitumen and kerogen contents in the organic matter; and 2) porosity is included correctly and clearly in the model, by carefully distinguishing between bulk volume and matrix volume.

The new methods proposed here are implemented in the rock physics analysis of the Ghareb-Mishash chalk. The experimental part of this study includes: 1) comprehensive characterization of the cores from the Shefela basin in their native immature state; 2) investigation of the effect of pyrolysis-induced maturation on the petrophysical and acoustic properties; and 3) interpretation of geophysical well-logs from the Shefela basin.

The immature rock properties are studied most extensively, using laboratory measurements on core samples from the Zoharim well (~ 280 m of available cores). The measurements include porosity, density, permeability, acoustic velocities (dynamic moduli), triaxial compression experiments for static moduli (via "HDC-TIES" method) and compressive strength, and Brazilian tests for tensile strength. The influence of organic content on each of these properties is evaluated based on TOC data. It is found that there is no effect of organic content on the porosity of the rock, hence the organic matter is treated as a matrix component. The porosity and organic content are the two independent variables that dominate the physical properties of the rock. Matrix density is tightly connected to the organic content, and the petrophysical model assists in deriving the average minerals density and organic matter density throughout

the Zoharim section (2.74 g/cc and 1.43 g/cc, respectively). The organic matter density is considered relatively high, mostly due to the high sulfur content within the Type IIs kerogen and due to negligible bitumen concentration.

The vertical dynamic moduli, obtained by bedding-normal P and S wave velocities measurements, are well-described using the "HS kerogen" model. Microstructure observations using backscatter scanning electron microscopy (BSEM) confirm that realization. By referencing the dynamic moduli to the Hashin-Shtrikman bounds, the 'w' parameter from Marion's bounding average method (BAM, Marion 1990) is calculated to quantify the normalized location between the bounds; w equals 1 at the upper bound and 0 at the lower bound. The Ghareb-Mishash chalk exhibits a "soft" arrangement of the components, where $w \sim 0.2$. Using the BAM model, it is possible to estimate the changes in moduli upon fluid fluid substitution. Both dynamic and static moduli decrease significantly with increasing porosity and kerogen content. The effect of porosity on them is two times stronger than the effect of kerogen. At dry state, the dynamic moduli are significantly higher than the static moduli. The dynamic/static moduli ratio decreases from ~4 to ~2 with increasing kerogen content. Unlike the elastic moduli, compressive strength and tensile strength depend solely on porosity without a clear impact by the organic content.

Anisotropy is indicated in the static and dynamic elastic moduli, permeability and tensile strength measurements. It originates from bedding-parallel alignment of fossil fragments, as well as improved pore connectivity in the bedding-parallel direction. Surprisingly, anisotropy appears to be independent of organic content, but mostly depends on porosity. Despite this peculiar observation, the relationships among the elastic anisotropy parameters in the Ghareb-Mishash chalk, namely Ω, ε and γ, are similar to those of other organic-rich rocks.

In order to study the effect of thermal maturation on the physical properties of the rock, the immature core material was pyrolyzed to simulate maturation to four different maturity levels: early-mature, mature 1, mature 2, and over-mature. Upon pyrolysis, porosity grows at the expense of organic content due to the lack of confining pressure in the pyrolysis cell. The bitumen content increases continuously until the mature 2 level, and then decreases at the exhaustion of the organic maturation (over-maturity). Using the upgraded petrophysical model, porosity and solids density measurements are corrected by considering bitumen as a pore fluid

and not as a matrix component. During pyrolysis the kerogen density increases from ~1.4 g/cc at immature, to ~1.5 g/cc at early-mature and mature 1, subsequently to ~1.7 g/cc at mature 2, and finally to extremely dense at over-maturity (>1.8 g/cc). This succession is reflected also in the acoustic measurements where S-wave velocities indicate kerogen stiffening, and might be unique to pyrolyzed Type IIs kerogens. P-wave velocities, on the other hand, decrease continuously with maturation due to the severe porosity enhancement and loss of solid organic matter. P-wave and S-wave moduli in the bedding-normal and bedding-parallel directions are described by an exponential regression versus porosity and organic content (combined), independently of the simulated maturity level. Elastic anisotropy of the pyrolyzed samples increases with porosity, while no dependence on the organic content is seen.

RPM of the Ghareb-Mishash chalk at different maturity levels is done using two models: 1) "HS+BAM": combination of HS bounds with the BAM model, calibrated to the acoustic velocities of the pyrolyzed material; and 2) "HS kerogen": modeling of a kerogen-supported granular matrix. Analysis of these RPMs is done using two types of rock physics templates (RPT): Vp/Vs versus ρ_bVp (conventional layout) and Vp/Vs versus ρ_sVs (matrix-focused layout, proposed here). The analysis shows the "HS+BAM" model displays trends unrealistic for naturally-matured rocks and thus may be good only for fluid substitution in this case. Although the "HS kerogen" model is not representative of the pyrolyzed material, it is found much more realistic and predictive of naturally-matured organic-rich chalks. The RPTs show the strongest influence is imposed by porosity, and changes in organic content are seen but less prominently. Because brine-saturated rock is modeled, maturity-effects on the rock matrix seem indistinct. However, maturation is usually associated with variable fluid saturation due to generation of oil, gas and other fluids, and that causes the Vp/Vs ratio to drop dramatically.

The observations from the laboratory study are compared with well logs from the Zoharim and Aderet wells. To add organic content to the data, TOC measurements on samples from continuous coring (spacing of 1 m) are integrated into the log data. A combination between the TOC data and the density log (CCDL) enables calculation of porosity and organic content throughout the logged section. Based on them, the "HS kerogen" model is applied. The "HS kerogen" model is found predictive of the acoustic velocities and elastic moduli in both Zoharim and Aderet wells. Overpredictions within the upper part of the Ghareb Formation

reveal a gas zone. Within this interval in the Zoharim and Aderet wells, gas saturations are estimated to 10-15% by combining the “HS kerogen” model with models that relate fluid compressibility with gas saturations. In addition, relationships for TOC determination from logs are proposed based on the neutron, density and gamma-ray logs. Organic content appears to dominate the separation between the neutron porosity and CCDL porosity, hence the main source for excess hydrogen in the rock is the organic matter. The workflow presented here are generally applicable for evaluation of porous organic-rich rocks, using both basic and advanced logging suites.

Keywords

Rock physics, petrophysics, rock mechanics, organic-rich rocks, source rocks, Ghareb-Mishash chalk, porosity, kerogen, static and dynamic moduli, P and S wave velocities, anisotropy, transverse isotropy, fluid substitution, pyrolysis, thermal maturation.

Preface

This Ph.D. dissertation is based on research carried out at the Geological and Environmental Sciences Department, Ben-Gurion University of the Negev (BGU). The research advisors were Prof. Yossef H. Hatzor, Prof. Shimon Feinstein and Prof. Harold J. Vinegar. The project was partially funded by Israel Energy Initiatives (IEI Ltd.) which also provided the core material and the well logs. The focus on the Shefela basin enabled significant progress in the study of the Ghareb-Mishash Formations, and development of novel methodologies, mainly in regard to rock anisotropy. During this study, three journal papers were published. In addition, two conference papers and three extended abstracts were published. The publications are listed below:

Journal papers

- Shitrit, O., Hatzor, Y. H., Feinstein, S., Palchik, V., & Vinegar, H. J. 2019: "Static and dynamic elastic moduli of organic-rich chalk" *Geophysical Prospecting*. DOI: 10.1111/1365-2478.12757
- Shitrit O., Hatzor Y.H., Feinstein S., Vinegar H.J., 2017: "Acoustic and Petrophysical Evolution of Organic‐Rich Chalk Following Maturation Induced by Unconfined Pyrolysis" *Rock Mechanics and Rock Engineering* Vol. 50. pp. 3273-3291. DOI: 10.1007/s00603-017-1325-9
- Shitrit O., Hatzor Y.H., Feinstein S., Palchik V., Vinegar H.J., 2016: "Effect of kerogen on rock physics of immature organic-rich chalks" *Marine and Petroleum Geology* Vol. 73. pp. 392-404 (IF 2.888; 43/188, Q1) DOI: 10.1016/j.marpetgeo.2016.03.023

Conference proceedings

- Shitrit O., Hatzor Y.H., Feinstein S., Palchik V., Vinegar H.J., 2018: "A New Method to Quantify Elastic Anisotropy of a Transversely Isotropic Medium", Paper ID We A11 16 in: *Proceedings of 80th EAGE Conference and Exhibition 2018*, June 11 – 14, Copenhagen, Denmark. DOI: 10.3997/2214-4609.201801027
- Shitrit O., Hatzor Y.H., Feinstein S., Vinegar H.J., 2018: "Rock Physics Modeling of Organic-rich Chalk: the Roles of Porosity, Organic Content and Maturation", Paper ID Tu P2 06 in: *Proceedings of 80th EAGE Conference and Exhibition 2018*, June 11 – 14, Copenhagen, Denmark. DOI: 10.3997/2214-4609.201800868
- Shitrit O., Hatzor Y.H., Feinstein S., Vinegar H.J.: "Elasticity Of Organic-rich Chalk: Insights from Measurements and Models" In: International Workshop on Rock Physics, 2017, Trondheim, Norway.
- Shitrit O., Hatzor Y.H., Feinstein S., Vinegar H.J., 2016: "Influence of Laboratory-Induced Maturation on Rock-Physics of Organic-Rich Chalks", Paper No. 72 in: *Proceedings of the*

50th U.S. Rock Mechanics Symposium, June 26 – 29, Houston, Texas. **Selected as one of the best papers in the conference.**

- Shitrit O., Rosenberg Y.O., Hatzor Y.H., Reznik I, Nguyen S., Feinstein S., Vinegar H.J., 2015: "Constitutive Model For Mechanical Properties Of Highly Porous Organic-Rich Chalks From Central Israel", Paper No. 818 in: Shale Rock Mechanics Symposium, *Proceedings of the 13th ISRM Congress*, May 10 – 13, Montreal, Canada.

Acknowledgements

There are very few people on this planet as fortunate as I am, to have such a professional, supportive and friendly working environment. The distinguished contributors are mentioned here, those who I could not have managed without.

My research advisors Prof. Yossi Hatzor, Prof. Shimon Feinstein and Prof. Harold Vinegar gave me the independence to branch in any direction I thought was worthy, and their professional and sophisticated opinions always guided me in the right direction. Yossi is thanked for accepting me as a graduate student in the first place, pushing me forward, teaching me some lessons in conciseness, sending me to conferences quite frequently, endorsing me, and showing me right and wrong (sometimes in the hard way). Shimon is thanked for exposing me to petroleum geology, and for countless hours in his office, thorough discussions on the integration of geochemistry and geophysics, black coffee and moral stories. Harold is thanked for teaching me literally everything about the oil and gas industry, dedicating a whole lot of time and thought to make sure my research is on the right track, directing me to rock physics and encouraging original thinking, hosting me at his Houston house, and for enabling the research platform by his double affiliation (at the time) in BGU and IEI Ltd.. Every student can consider himself extremely lucky to get tenth of what I got from my advisors.

This research was funded by Israel Energy Initiatives, Ltd. (IEI) through BGU contract No. 87244811. IEI is thanked for the supply of core material and fruitful collaboration throughout the study. Dr. Yoav Rosenberg is thanked for his firm, creative and systematic design of the testing scheme, and the ideal inclusion of my part in it. His insights and professional knowledge were helpful, and the cooperation was fruitful. Dr. Itay Reznik and Dr. Scott Nguyen are thanked for their part in the design of the research scheme, and their scientific insights improved the quality of this study. Dr. Yuval Bartov is thanked for providing the cores and well logs. Edna Danon is thanked for conducting the geochemical measurements and for her willingness to help in every need, no matter the effort. Leonardo Freitas is thanked for operation of the pyrolysis experiments and for being so kind, skilled and available to fix every malfunction in the laboratory instruments.

I thank Israel Ministry of Infrastructures, Energy and Water Resources for a fellowship awarded to graduate students performing research in petroleum geosciences through grant No. 214-01-031. Their scholarship was incredibly helpful throughout my studies.

Ph.D. candidacy internal committee members, Prof. Noam Weissbrod and Prof. Rami Weinberger, are thanked for their comments and suggestions. Prof. Sam Friedman (external committee member) is thanked for the review of the Ph.D. research proposal.

Dr. Vyacheslav Palchik is thanked for sharing his experience in rock mechanics and laboratory testing, and for conducting the triaxial compression tests with me.

My "roommate" Yair Gordin is thanked for joining me to the journey of studying rock physics of organic-rich rocks. We spent a lot of time brainstorming, revising, correcting, measuring, calculating, and then again. Our work together can define symbiosis.

Ilya Kutuzov is thanked for sharing his insights from his research regarding the geochemical properties of the rock samples I was investigating and their evolution through pyrolysis.

Roxana Golan from the Microscopy Unit, Ilse Katz Institute for Nanoscale Science and Technology, Ben-Gurion University of the Negev, is thanked for her support in SEM scanning.

The department of geological and environmental sciences, as a whole, is thanked for being my home for nine years. Special thanks are reserved to Mrs. Rivka Eini, Mrs. Zahala Sharabi, and Mrs. Racheli Shimon for their handling of the administrative issues. David "Diro" Koseshvilli is thanked for his constant will and availability to prepare the samples I tested.

I thank my friends and lab partners Dan Tzuker, Nir Badt, Ravit Zelig, Tal Zaslavsky, Maayan Shviro, Guy Tzur, Matan Elad, Doron Morad, Yuval Keisar, Almog Baram, Yuval Peleg, Aviran Feldheim, Nachum Kazaz, Dr. Ben-Gou He, and Dr. Juan Pablo Ibanez, for partnering my lunch and coffee breaks.

I thank my supportive family, Reuven, Ronit, Guy, Ofer, Hagar, Pnina, Michal, Yossi, Omer and Tamir. You were always there when I needed, you made me believe in myself.

My greatest love, Inbal, I thank you for supporting me in every possible way, for making me believe I can always reach higher altitudes, for making me better. Most of all, thank you for gifting me with our breath-taking daughter, Tamar.

Table of contents

List of figures

List of abbreviations

- BAM: Bounding Average Method
- BGU: Ben-Gurion University of the Negev
- BSEM: Backscatter Scanning Electron Microscopy
- CCDL: Continuous Coring-Density Log
- DSMR: Dynamic/Static Moduli Ratio
- EDS: Energy Dispersive Spectroscopy
- HDC-TIES: Hydrostatic-Deviatoric Combination for Transversely Isotropic Elastic Stiffnesses
- HS: Hashin-Shtrikman
- IF: Iso-frame
- MFL: Matrix-Focused Layout
- RPM: Rock Physics Modeling/Model
- RPT: Rock Physics Template
- SEM: Scanning Electron Microscopy
- TOC: Total Organic Carbon
- VTI: Vertical Transverse Isotropy

List of symbols

$\%R_o$: vitrinite reflectance

$\%R_{o,eq.}$: vitrinite reflectance equivalent value, estimated using the "Easy %Ro" method.

a_1, a_2: curve fitting coefficients of the ρ_s vs. TOC plot.

B_c: bitumen volume fraction of the organic matter

BIT: mass fraction of bitumen of the dry rock

b_1, b_2: curve fitting coefficients of the Ω vs. ε fitted plot.

C_{ij}: constants of the 6X6 elastic stiffness matrix

C_{pr}: carbon percentage in the organic matter

E: Young modulus

E_v: Young modulus, bedding-normal direction

e: Brie's exponent for gas saturation

f_{bit}: bitumen volume fraction of the bulk

f_k: kerogen volume fraction of the bulk

f_m: minerals volume fraction of the bulk

f_o: organic-matter volume fraction of the bulk

GR: gamma-ray log value

K: bulk modulus

$K_{HS}^{+/-/k}$: bulk modulus predictions by Hashin-Shtrikman upper bound (+), lower bound (-), and kerogen-supported model (k).

K_{bit}: incompressibility of the bitumen

K_{dry}: incompressibility of the dry rock

K_f: incompressibility of the fluid phase

K_g: incompressibility of gas

K_k: incompressibility of the kerogen

K_{om}: incompressibility of the organic matter

K_s: incompressibility of the solid phase

K_{sat}: incompressibility (bulk modulus) of the brine-saturated rock

K_w: incompressibility of water (brine)

k_{N2}: Permeability to nitrogen gas

k_L: Klinkenberg-corrected gas permeability, assumed liquid permeability

k_g: gas permeability

k_∞: gas permeability at infinite pressure

M: oedometer, P-wave modulus

$M_{HS}^{+/-/k}$: oedometer modulus predictions by Hashin-Shtrikman upper bound (+), lower bound (-), and kerogen-supported model (k).

M_v: P-wave modulus, bedding-normal direction

M_h: P-wave modulus, bedding-parallel direction

m: Archie's cementation exponent

n: Archie's saturation exponent

p: hydrostatic confining pressure

R_t: bulk resistivity

R_w: formation water resistivity

S_g: gas saturation

S_w: water (brine) saturation

T_{max}: maturity indicator, obtained from Rockeval analysis

TOC: organic carbon mass percentage of the dry rock

TOM: organic matter mass percentage of the dry rock

v_p: P-wave velocity

v_{p0}: v_p in the bedding-normal direction

v_{p90}: v_p in the bedding-parallel direction

v_{p45}: v_p in the bedding-diagonal direction

v_s: S-wave velocity

v_{s0}: v_s in the bedding-normal direction

v_{sH90}: v_s in the fast bedding-parallel direction

w: BAM normalized stiffness factor computed for C_{ij} between upper and lower HS bounds on μ and M.

β: Biot coefficient

$\Gamma_{23}(\varepsilon_4), \Gamma_{13}(\varepsilon_5)$: shear strains over a plane that includes bedding-normal and bedding-parallel directions

$\Gamma_{12}\ (\varepsilon_6)$: shear strain over the bedding plane

γ: Thomsen's S-wave anisotropy

$\Delta\sigma_a$: axial stress minus radial stress

δ: Thomsen's parameter for angular dependence of wave propagation in VTI rocks

ε: Thomsen's P-wave anisotropy parameter

$\varepsilon_1, \varepsilon_2$: normal strains over the bedding plane

ε_3: normal strain in the bedding-normal direction

ε_a: axial strain

ε_r: radial strain

ε_v: volumetric strain

κ: kerogen influence scaling factor

μ: shear, S-wave modulus

$\mu_{HS}^{+/-/k}$: shear modulus predictions by Hashin-Shtrikman upper bound (+), lower bound (-), and kerogen-supported model (k).

μ_{bit}: shear modulus of the bitumen

μ_h: S-wave modulus, bedding-normal direction

μ_k: shear modulus of the kerogen

μ_{om}: shear modulus of the organic matter

μ_v: S-wave modulus, bedding-normal direction

ν: Poisson's ratio

ν_v: Poisson's ratio, bedding-normal direction

ρ_b: bulk density

ρ_{bit}: bitumen density

ρ_{dry}: dry bulk density

ρ_f: fluid density

ρ_k: kerogen density

ρ_m: minerals density

ρ_s: solids (matrix) density

ρ_o: organic-matter density

$\rho_{s,meas.}$: solids density, measured on core plugs

$\rho_{s,t}$: solids density, corrected for bitumen in the core plugs

σ_1, σ_2: normal stresses over the bedding plane

σ_3: normal stress in the bedding-normal direction

σ_a: axial stress

σ_r: radial stress

$\tau_{12}\ (\sigma_6)$: shear stress over the bedding plane

$\tau_{23}\ (\sigma_4), \tau_{13}(\sigma_5)$: shear stresses over a plane that includes bedding-normal and bedding-parallel directions

ϕ: porosity

ϕ_D: porosity, estimated from the density log

ϕ_N: porosity, estimated from the neutron log

ϕ_{kf}: kerogen-factored porosity

$\phi_{meas.}$: porosity, measured on core plugs

ϕ_t: porosity, corrected for bitumen in the rock

1 Introduction

This dissertation emphasizes rock physics of the Ghareb-Mishash organic-rich chalk unit in the Shefela basin, central Israel. The study combines models and theories with laboratory and field measurements (typically geophysical well-logs). By that, a deep understanding of the physical behavior of the rock is accomplished, in both scientific and applicative aspects. The complexity of this rock unit is expressed in several fashions. First, the organic content is highly variable and impacts the stiffness of the rock. Second, the variability of porosity and complexity of the porous network introduce a strong influence on the physical properties of the rock. Third, the bedded nature of this rock results in anisotropy of many of the rock properties. Finally, it is uncommon to encounter rocks with high porosity together with high organic content, so that this rock physics study is probably the first to investigate that combination. Rock physics modeling (RPM) of such a unique rock requires a deep review of existing models, while leaving room for modifications.

The introduction chapter includes background on organic-rich rocks, chalks, rock physics studies, geological settings, and a general description of the methodologies. In Chapter 2 the first phase of the research is presented, in which a broad petrophysical, mechanical and acoustic evaluation of the rock in its immature native state was made. A special attention is dedicated to the effects of porosity and organic matter on these properties. This Chapter also presents the main RPM approaches employed here, including the developments proposed at the course of the Ph.D. studies. Chapter 3 focuses on the effect of thermal maturity induced by pyrolysis on the petrophysical and acoustic properties of the rock. In Chapter 4, the inferences of the laboratory and theoretical studies are applied on two depth sections using well-logs, to examine the RPM applicability and identify features throughout the depth sections.

1.1 Organic-rich rocks

Organic-rich rocks are referred to as petroleum source rocks if the organic matter in them has the potential to generate oil and gas. These hydrocarbon fluids are formed during a maturity process driven by elevated temperatures and pressures at depth. During the maturation process, the organic material decomposes to release volatile hydrocarbons, which may expel, migrate and accumulate in a conventional reservoir rock. In this case, the source rock contains residual organic material phases, such as kerogen, bitumen and pyrobitumen. If expulsion and migration are prevented, the

source rock becomes a self-sourcing reservoir, and hydraulic fracturing techniques may be used for production. In some cases, even immature source rocks can become potential reservoirs through induced thermal maturation by *in-situ* heating. Self-sourcing reservoirs and immature source rocks are considered as unconventional reservoirs, which have become more economical throughout the past decade (Vernik 2016). The interest in organic-rich rock has been continuously increasing, owing to their multiple role of organic-rich rocks in the oil and gas industry, and to the technological advances that make these resources economical (e.g. horizontal wells, hydraulic fracturing). To allow for remote detection and evaluation of organic-rich rocks rock physics studies are performed more routinely.

The organic phases in source rocks typically include kerogen (solid) and bitumen (quasi-liquid). Kerogen is the most abundant organic phase in thermally immature source rocks, and thus imposes a significant influence on the physical properties of the rock. The organic material is distributed in a fine-grained matrix of various lithologies (Figure 1), such as clay-rich shales (e.g. Bakken, Kimmeridge), marls (Eagle Ford), porcelanites (Monterey) and chalks (Niobrara, Ghareb-Mishash) (Baskin and Peters 1992; Sone and Zoback 2013a; Avseth and Carcione 2015; Bisnovat *et al.* 2015; Bridges 2016). In most of the case studies, organic-rich shales with high clay content were investigated. These rocks typically exhibit a laminated microstructure and low porosity (Vernik and Liu 1997; Zhao *et al.* 2017). However, the rock investigated here is a high-porosity organic-rich chalk, in contradiction with the wide conception that source rocks are low-porosity organic-rich shales. The inherent shape of the fossils and the prevalence of fossil fragments in a granular calcite matrix cause chalks to have different texture and higher porosity than laminated shales. Clearly, kerogen distribution in the matrix exhibits different patterns and porosity cannot be overlooked or misinterpreted in this case. In this study, great attention is dedicated to the suitability of RPM approaches to the Ghareb-Mishash chalk. This is done by examination of RPMs of both organic-rich shales and non-organic chalks. In the next two sections, physical behavior of these two rock types is overviewed. In this section, the general features of organic-rich rocks are described briefly.

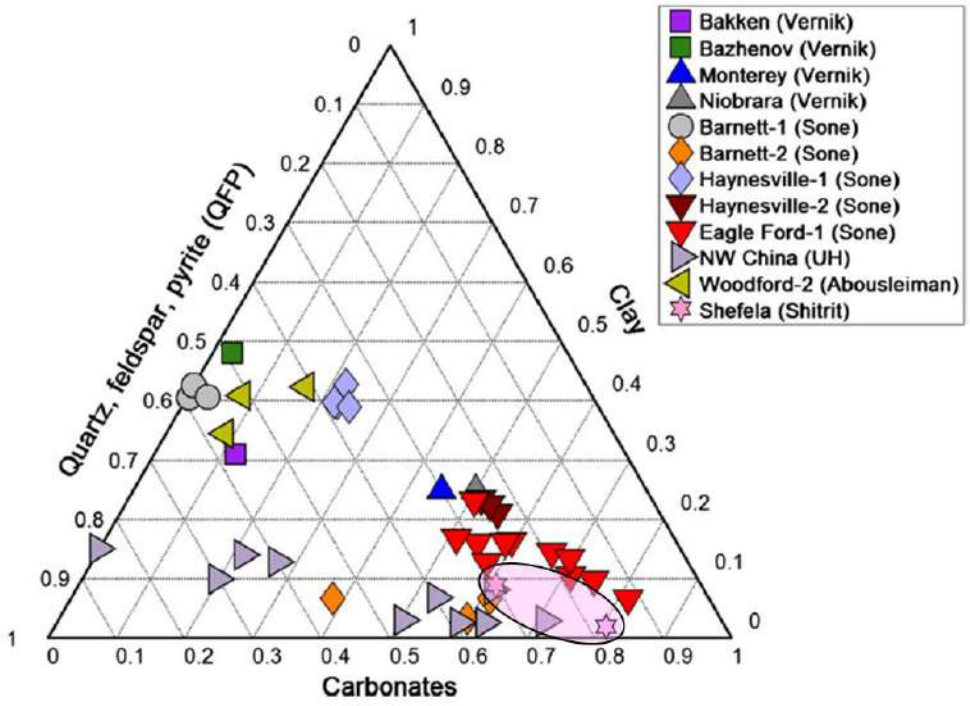

Figure 1: Mineralogy of organic-rich rocks , modified from Zhao et al. (2017): the mineralogy of the Ghareb-Mishash chalk (Shefela) ranges within the ellipse, but mostly around the lower hexagram. The Ghareb-Mishash mineralogy is reported in Table 1. Note that despite it does not show on this diagram, the QFP axis includes also the apatite content.

Organic-rich rocks are generally evaluated based on the organic matter content, chemical composition, and thermal maturity. The amount of organic matter in the rock is a measure of the potential for oil and gas generation, given the organic material composition is of a productive type (i.e. high hydrogen to carbon ratio, H/C). Organic matter amounts are typically measured by the total organic carbon (TOC), that is the weight percentage of organic carbon in the rock matrix. TOC is commonly measured in the laboratory using LECO elemental analyzer device, or by pyrolysis and combustion in a Rock Eval system. The effect of organic matter content on physical properties of organic-rich rocks is routinely examined. It may influence the acoustic velocities, elastic properties (static and dynamic), density, porosity and strength. For example, density and bedding-normal acoustic velocities have been observed to decrease with increasing organic content at almost every case study (Vernik 2016). Compressive strength, tensile strength and static Young's modulus typically manifest a decrease upon organic-enrichment (Eseme *et al.* 2007; Sone and Zoback 2013b). Porosity is also effected by organic content, as kerogen-hosted pores contribute to bulk porosity and bitumen may plug flow channels in the matrix (e.g. Katz and

Arango 2018). Quantification of the effect of organic content on the physical properties of the rock is one of the main scopes of this study. The organic material investigated here is mostly made of Type IIs kerogen, and the sulfur richness introduces unique effects which will be discussed throughout this thesis.

The organic matter properties also vary with the degree of thermal maturation. The H/C ratio in the kerogen typically reduces upon maturation, as hydrocarbons are gradually released from the kerogen, while the residual kerogen includes longer hydrocarbon chains. There are several different methods to estimate the level of maturity. The most common method measures the reflectance of incident light from a polished surface of vitrinite maceral ($\%R_o$) in petrographic analysis of rocks that contain organic matter. The vitrinite reflectance increases from ~0.2 $\%R_o$ (immature), through the windows of oil and gas generation, and as the values reach ~2 $\%R_o$ the HC potential is exploited (Tissot and Welte 1984, Vernik 2016). Maturity can also be determined from Rock-Eval measurements, in which rock powder is gradually pyrolyzed and then combusted. Rock-Eval measurements yield several parameters (Tissot and Welte 1984): 1) Transformation Index (TI), the mass ratio of free hydrocarbons over TOC; 2) Hydrogen Index (HI), the mass ratio of remaining hydrocarbon potential of the kerogen over TOC; 3) Production index (PI), calculated by $\frac{TI}{TI+HI}$; and 4) Oxygen Index (OI), which is mass ratio of oxygen in the organic material, over TOC. In order to estimate the origin of the organic material and determine the kerogen type, a plot of HI vs. OI is typically used (Van Krevelen diagram, Tissot and Welte 1984). The Rock-Eval parameter most useful for maturity quantification is T_{max}, that is the temperature at which HC generation has peaked. The T_{max} parameter increases with maturity level, as HC generation starts at ~ 420-435 °C and over-maturity level (i.e. dry gas generation) is associated with T_{max} of 465-485 °C and higher. This study utilizes maturity parameters reported by Kutuzov (2017), which include T_{max} measurements, calculated $\%R_o$ using the "Easy $\%R_o$" method (Sweeney and Burnham 1990), and HI evolution from the immature reference value (HI_0).

Rock physics studies of differentially matured rocks need to take into account the maturity-associated variations, as these are tightly related to changes occurring in the organic matter. Organic matter decomposition creates new pores which may be filled with bitumen, oil and gas, that soften the organic phase (Modica and Lapierre 2012; Eliyahu *et al.* 2015; Zargari *et al.* 2016). On the other hand, the density and stiffness of the residual kerogen increase with maturation

(Alfred and Vernik 2012; Zargari *et al.* 2013; Emmanuel *et al.* 2016). This highlights the importance of quantification of bitumen and kerogen contents within the organic matter. Solid residues like graphite, pyrite and coke (pyrobitumen) may as well form during maturation (Modica and Lapierre 2012; Bernard *et al.* 2012; Zhao *et al.* 2016). The changes that occur following maturation are of high interest to exploration of oil and gas reservoirs. To study maturation-associated changes, pyrolysis is used to simulate maturation (Zargari *et al.* 2013; Bisnovat 2013; Allan, Vanorio and Dahl 2014; Gayer 2015). Pyrolysis is used in this study to simulate four different maturity levels, as explained in Chapter 3.

1.2 Rock physics of organic-rich shales

Organic-rich shales typically exhibit strong velocity anisotropy, low velocity in the bedding-normal direction, and relatively low density and porosity (Figure 2) (Vernik and Nur 1992; Vernik and Milovac 2011). As one would expect, the elastic properties of organic-rich shales depend strongly on organic matter and clay content (e.g. Sone and Zoback 2013a; Zhao *et al.* 2016; Vernik 2016). Organic-rich shales usually display a laminated microstructure as clay minerals and kerogen particles are aligned with the bedding direction (Figure 3), thus increasing the mechanical anisotropy (Vernik and Landis 1996; Carcione 2000; Dewhurst *et al.* 2011; Sone and Zoback 2013a). Therefore, organic-rich shales are treated as vertically transversely isotropic (VTI) materials where the plane of isotropy is assumed to be horizontal. Mechanical and acoustic testing is done in three directions at least, typically 0°, 45° and 90° to the symmetry axis (the bedding-normal direction). Transversely isotropic materials can be described by five elastic constants: $C_{11}, C_{33}, C_{55}, C_{66}$, and C_{13}:

$$C_{11} = \rho_b v_{p90}^2 \, , C_{33} = \rho_b v_{p0}^2 \, , C_{55} = \rho_b v_{s0}^2 \, , C_{66} = \rho_b v_{sH90}^2 \, ,$$
$$C_{13} = \sqrt{\left(2\rho_b v_{p45}^2 - C_{11} - C_{55}\right)\left(2\rho_b v_{p45}^2 - C_{33} - C_{55}\right)} - C_{55} \, , \quad (1)$$

where ρ_b is bulk density, v_{p0}, v_{p45} and v_{p90} are the P wave velocities in the bedding-normal, bedding-diagonal and bedding-parallel directions (respectively), and v_{s0} and v_{sH90} are the S wave velocities in the bedding-normal and the fast bedding-parallel directions (respectively). Graphic description of wave propagation directions is given in Figure 4. The complete elastic stiffness matrix of such materials relates stresses and strains as follows:

$$\begin{bmatrix}\sigma_1\\ \sigma_2\\ \sigma_3\\ \tau_{23}\\ \tau_{13}\\ \tau_{12}\end{bmatrix} = \begin{bmatrix}C_{11} & C_{12} & C_{13} & 0 & 0 & 0\\ C_{12} & C_{11} & C_{13} & 0 & 0 & 0\\ C_{13} & C_{13} & C_{33} & 0 & 0 & 0\\ 0 & 0 & 0 & C_{55} & 0 & 0\\ 0 & 0 & 0 & 0 & C_{55} & 0\\ 0 & 0 & 0 & 0 & 0 & C_{66}\end{bmatrix} \cdot \begin{bmatrix}\varepsilon_1\\ \varepsilon_2\\ \varepsilon_3\\ \Gamma_{23}\\ \Gamma_{13}\\ \Gamma_{12}\end{bmatrix}, \quad (2)$$

where $C_{12} = C_{11} - 2C_{66}$, σ and ε are normal stresses and normal strains (respectively), and τ and Γ are shear stresses and shear strains (respectively). The degree of elastic anisotropy is conventionally quantified using Thomsen's parameters: ε for vertical versus horizontal P-wave anisotropy; γ for vertical versus horizontal S-wave anisotropy; and δ for angular dependence of wave propagation in weakly anisotropic rocks ($\varepsilon < 0.2$, Thomsen 1986). Description of the anisotropy parameters and their background will be elaborated in Section 2.8.1.

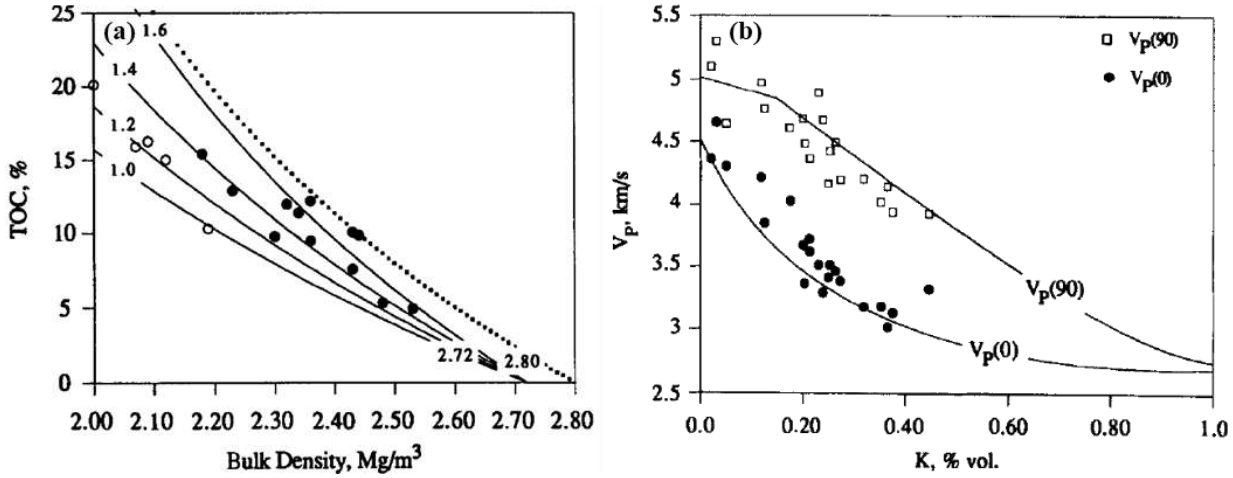

Figure 2: Influence of organic matter on physical properties of organic-rich rocks, from Vernik and Nur (1992): a) the influence of TOC on the bulk density of a low porosity shales. The numbers on the curves at the upper left corner represent assumed kerogen density, where open circles are low-maturity shales and filled circles are matured shales. b) The influence of kerogen content on the P-wave velocities in the bedding-normal and bedding-parallel directions.

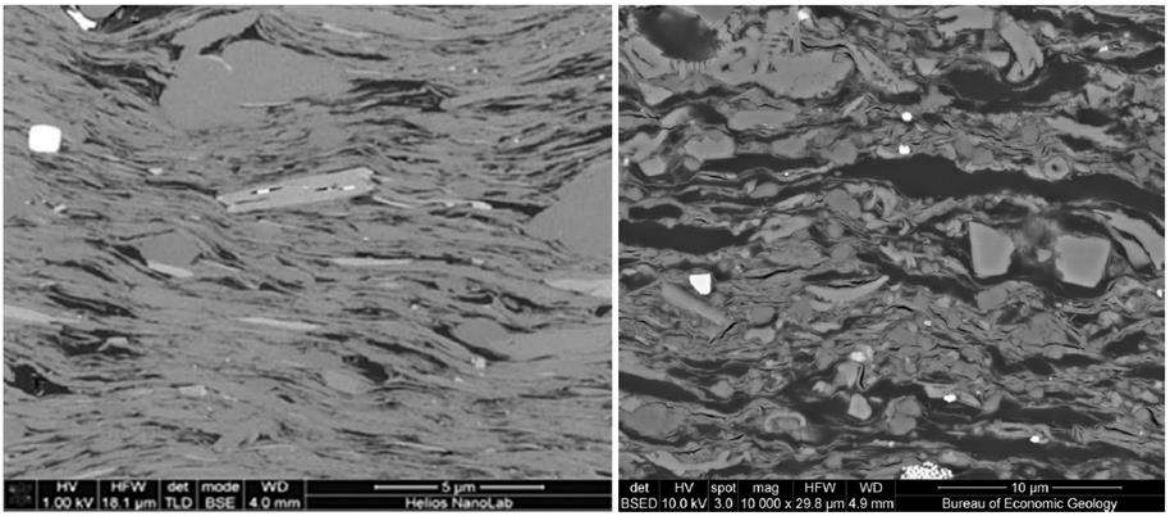

Figure 3: BSEM images of organic-rich shales, from Vernik (2016): the low porosity kerogen-shale laminated fabric is clearly observed.

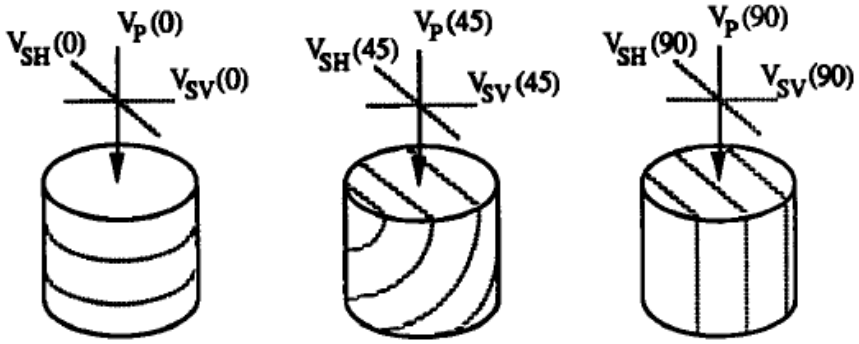

Figure 4: Wave propagation in transversely isotropic rocks is described with respect to the bedding direction (Vernik and Nur 1992). Note that Vsh(0)=Vsv(0)=Vsv(90) in transversely isotropic rocks. Note that the core sample on the left describes the bedding-normal velocities, which are most commonly measured in vertical wells in VTI rocks.

Numerous rock physics studies have been performed on organic-rich rocks, specifically on organic-rich shales (e.g. Vernik and Nur 1992; Vanorio, Mukerji and Mavko 2008; Carcione, Helle and Avseth 2011; Suarez-Rivera and Fjær 2013; Sone and Zoback 2013a; Sayers 2013a; Avseth and Carcione 2015; Zhao *et al.* 2016). The elastic properties of organic-rich shales were studied with great attention to organic content, clay content, microcracks, and porosity. In clay-rich rocks, a specific attention has been dedicated to clay properties, such as mineral transformations, clay dehydration, clay-bound water, and impacts on rock fabric (Carcione and Avseth 2015; Qin, Han and Yan 2016; Villamor Lora, Ghazanfari and Asanza Izquierdo 2016). A typical shale model

assumes layered microstructure with low porosity (often negligible), so that Backus averaging method is routinely employed (Vernik and Nur 1992; Carcione *et al.* 2011; Sayers, Fisher and Walsh 2015; Zhao *et al.* 2016; del Monte *et al.* 2018). Other rock physics models include the empirical Krief-Gassmann methods (Carcione *et al.* 2011); inclusion models like Mori-Tanaka, Dilute Scheme and Self-Consistent Approximations (Sayers *et al.* 2015; Goodarzi, Rouainia and Aplin 2016; Zhao *et al.* 2016); and theoretical bounds like Voigt-Reuss and Hashin-Shtrikman models (Sone and Zoback 2013a; Yang and Mavko 2018). A broad review of organic-rich shale models is given in Section 2.8.4, where the RPM approach selection is explained. In this section a quick review of model predictability is presented.

The Bakken shale is a case in point of rock physics of transversely isotropic source rocks (Vernik and Nur 1992; Carcione *et al.* 2011; Sayers 2013b; Sayers and Dasgupta 2014). The shale fabric is conceptualized as lenticular grains of illite rather than continuous sheets, thus a modified-Backus averaging method has been used. The anisotropy is found to depend on microcracks and low aspect-ratio pores; without incorporating them in the RPM the Backus method leads to underestimated anisotropy (Sayers and Dasgupta 2014). Carcione et al. (2011) applied modified-Backus and Krief-Gassmann methods while considering kerogen as pore infill, but they pointed that if kerogen is treated as part of the solid skeleton it is optional to model the matrix using Hashin-Shtrikman bounds (Hashin and Shtrikman 1963). Note that despite Gassmann's theory is frequently used for predicting elastic moduli, most rocks and particularly organic-rich rocks do not obey to the basic assumptions of that theory (Vernik and Milovac 2011; Thomsen 2017). Other organic-rich formations have been commonly modelled using the Backus method, perhaps too exclusively. For example, the Tanezzuft formation from Tunisia was modelled using that method and misfit values were attributed to variability in kerogen stiffness (del Monte *et al.* 2018). The Green River formation was found by Burnham (2018) to follow the Reuss (harmonic) average of the phases, which models a laminar medium more simplistically. In an examination of various organic-rich rocks by Sone and Zoback (2013a) it was found that the carbonate-rich Eagle Ford shale plots around the lower Hashin-Shtrikman bound, i.e. the rock is supported by the soft clay plus kerogen mixture (porosity was neglected in their analysis). The match of the data to the Backus, Reuss and lower Hashin-Shtrikman models implies that shale properties are dominated by the kerogen properties due to their laminated distribution in the matrix.

1.3 Rock physics of chalks

As mentioned above, the Ghareb-Mishash chalk in the Shefela basin is a unique case of an extremely organic-rich unit hosted in a chalk matrix. In this section a quick overview of chalk properties will be given. Chalks consist of mixtures of skeletal components, dominated by coccoliths and pelagic foraminifera, where the predominant mineral is calcite (Pollastro and Scholle 1986). Calcite is elastically isotropic, but it occurs in various morphologies, from flat fragments to perfectly equant grains, and the grain pack might exhibit anisotropy. At initial sedimentation at the sea floor, the carbonate particles form a high porosity ooze (~70%). Upon burial the ooze turns into chalk due to compaction. Subsequent burial causes more compaction, cementation and pressure dissolution, which contribute to porosity reduction and increased stiffness (Figure 5, Fabricius 2003). At this diagenetic level chalks may be defined as limestones, owing to the increase in induration (Fabricius 2014). Either way, the Ghareb-Mishash chalk examined here satisfies both mechanical and sedimentological definitions. The inherent shape of the fossils and the prevalence of fossil fragments in a granular calcite matrix cause chalks to have different textures and higher porosity than a typical laminated shale. The organic matter distribution in the chalk matrix is different from shales, and thus might induce different mechanical effects. The studied organic-rich chalk is believed to combine some of the characteristics of both organic-rich shales and non-organic chalks.

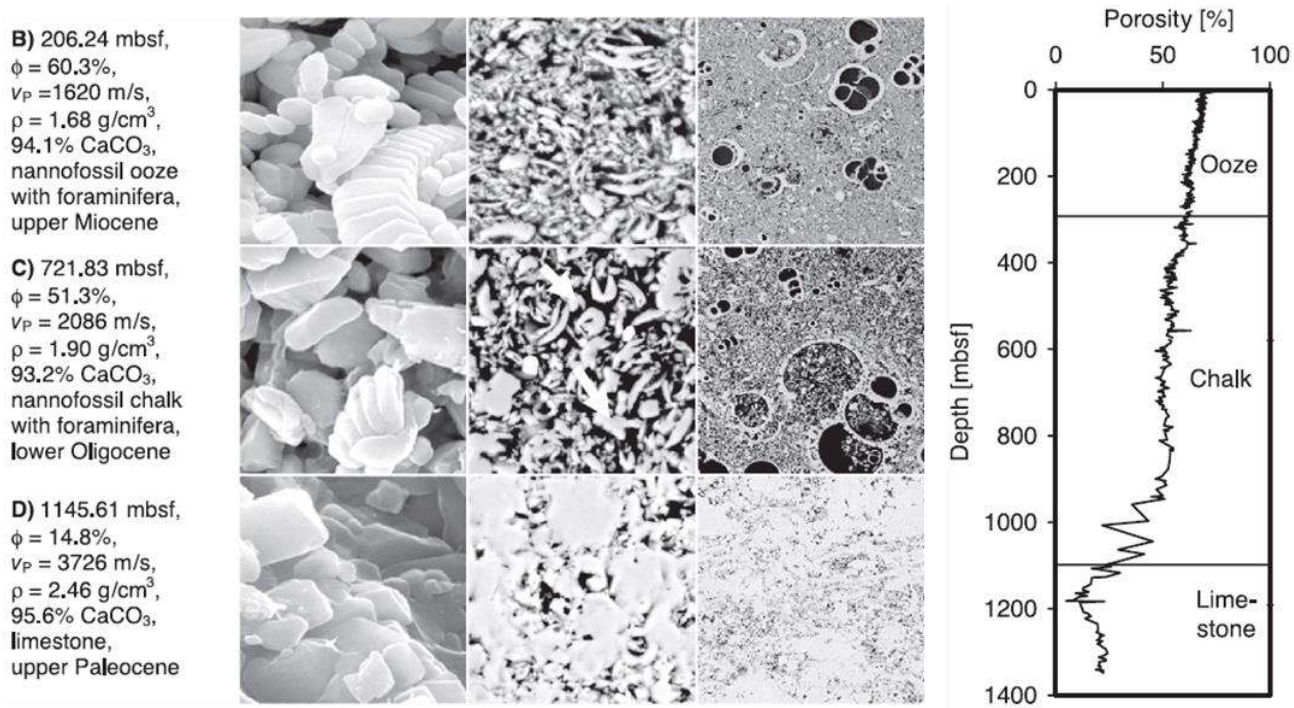

Figure 5: Textural variation of carbonate sediment in the ODP 807 site in the Pacific Ocean, from Fabricius 2003. BSEM images demonstrate the evolution from the loose pack of ooze, through the soft rock state (chalk), and ultimately to the competent rock state (limestone). Porosity-depth profile of this site is presented on the right side, to demonstrate the gradual change in carbonate texture with burial depth (in meter below sea floor).

The differences in microstructural features cause chalks to display different anisotropic behavior than shales. Chalks may exhibit elastic anisotropy (Talesnick, Hatzor and Tsesarsky 2001; Korsnes *et al.* 2008) but may as well be isotropic (Røgen *et al.* 2005; Fabricius *et al.* 2007; Olsen 2007; Palchik 2013). Korsnes et al. (2008) studied the Stevns Klint and Liege outcrop chalks, and reported isotropic permeability (1-4 mD) and tensile strength (0.5-0.58 MPa), but anisotropy in compressive strength of 20-50%. Stevns Klint chalk exhibits greater stiffness parallel to bedding but the opposite is observed for the Liege chalk. Talesnick, Hatzor, & Tsesarsky (2001) found that compressive strength of the Marasha chalk in the bedding-parallel direction is ~1.5 times greater than in the bedding-normal direction, regardless of the water content in the range of 0-50%. Even chalks that contain organic matter may manifest isotropy. For example, Niobrara chalk and marl samples which are low in porosity (~4%) and TOC of up to 5% (Type II kerogen), exhibit elastic isotropy to slight anisotropy (Bridges 2016).

Chalks typically contain a large amount of pores, so that chalk physics depends strongly on pore-scale mechanisms. In the Denver basin, the porosity of the Niobrara chalk decreases consistently with depth, from 45% at 300 meters depth to ~5% at 2,100 meters depth (Lockridge and Pollastro 1988). High porosity in chalks can be found even at great depths, as in the Tor and Ekofisk chalks from the North Sea (Japsen *et al.* 2004), where porosity of 45% at 3 km depth is caused by ~15 MPa overpressure. At the high porosity range (35-42%), the Ekofisk chalk has a bulk modulus of about 3-8 GPa and shear modulus of 3.5-6 GPa (Røgen *et al.* 2005). Olsen (2007) described in detail the poroelasticity of North Sea chalk. He found that the "Iso-frame" model (IF) and the Marion's bounding average method (BAM) are more accurate than Berryman's self-consistent model when both dry and water-saturated chalks are modelled. Both the IF and the BAM models were calculated with respect to the upper and lower Hashin-Shtrikman bounds (Hashin and Shtrikman 1963; Mavko, Mukerji and Dvorkin 2009). These observations are taken into consideration in the modeling of the organic-rich chalk examined in this study.

1.4 Static and dynamic elastic moduli

Loading conditions are generally divided into quasi-static (referred to as "static") and dynamic. In static conditions, strain rates are typically $10^{-5} - 10^{-6} s^{-1}$, and strain amplitudes are at the order of $10^{-2} - 10^{-4}$ (Fjær *et al.* 2008; Fjær, Stroisz and Holt 2013). In dynamic conditions, strain rates may range between $1\ s^{-1}$ at ultrasonic frequencies to $10^{-4} s^{-1}$ at seismic frequencies, and strain amplitudes are at the order of 10^{-7}. In an ideally homogeneous, linearly elastic material (e.g. metals, glass) the static and dynamic moduli are equal (Simmons and Brace 1965; King 1969; Ledbetter 1993). However, in most rock types static and dynamic moduli are unequal, and the difference between them has been extensively studied in the past (e.g. Zisman 1933; Simmons and Brace 1965; Jizba, Mavko and Nur 1990; Tutuncu and Sharma 1992; Gommesen and Fabricius 2001; Sone and Zoback 2013; Brotons *et al.* 2016). This discrepancy is due to variation in mechanical properties between the rock components that cause different local stress concentrations, and thus different strain magnitudes (Fjær *et al.* 2013). The dynamic/static moduli ratio (DSMR) decreases towards unity as stiffness and compactness increase (Brotons *et al.* 2016). This is mainly attributed to porosity and its various features (e.g. size, shape, distribution, association with cracks), that induce greater impact on rock deformability in static conditions. Cracks in particular increase the DSMR, by affecting the static moduli more than the dynamic moduli (King 1969; Ong *et al.* 2016; Meléndez-Martínez and Schmitt 2016). The DSMR may

approach unity upon closure of discontinuities and tightening of solid-solid contacts (e.g. Cheng and Johnston 1981; Jizba *et al.* 1990). The issue of stress dependence of the DSMR is therefore complex, as discontinuities may be either formed or closed upon changes in stress conditions. Other possible sources for difference between static and dynamic moduli are mineralogy, specifically clay content, (Tutuncu and Sharma 1992), and cement over-growth (Al-Tahini, Sondergeld and Rai 2004). The DSMR may also be influenced by dispersion in liquid-saturated rocks, but in dry rocks the effect of dispersion is insignificant (Hofmann 2006; Olsen 2007). This suggests that in dry rocks the difference between static and dynamic moduli is controlled by the differences in strain amplitudes (Fjær *et al.* 2008). The results in this study are examined with respect to the above-mentioned mechanisms. In addition, a relationship between the static and dynamic moduli of the Ghareb-Mishash chalk is established and compared with relationships that describe other rock types.

1.5 The Shefela basin

The rock formations investigated in this study are the Late Cretaceous Ghareb and Mishash formations (Mt. Scopus Group). In places where the siliceous member is missing this unit is termed as Ein-Zeitim formation (Flexer 1968). These formations, occasionally referred to as the "oil shale" unit, are spread in tens of basins in Israel (Minster 2009). Various definitions have been used for this unit, such as oil-shale (Shirav and Ginzburg 1984; Minster 2009; Burg and Gersman 2016), bituminous shale (Flexer 1968; Gvirtzman *et al.* 1989) and bituminous rocks (Gardosh and Tennenbaum 2014). This unit can be subdivided based on proximity to the ancient coastline, which influences the lithology and the burial history of the rock unit in a basin (Meilijson *et al.* 2014). The lithology of these formations in the Shefela basin is mostly chalk, with occurrences of marls, cherts, porcelanites and phosphorites. Because the bitumen amounts are quite low and the lithology is chalk, the rock unit is referred to as "organic-rich chalk" throughout the study.

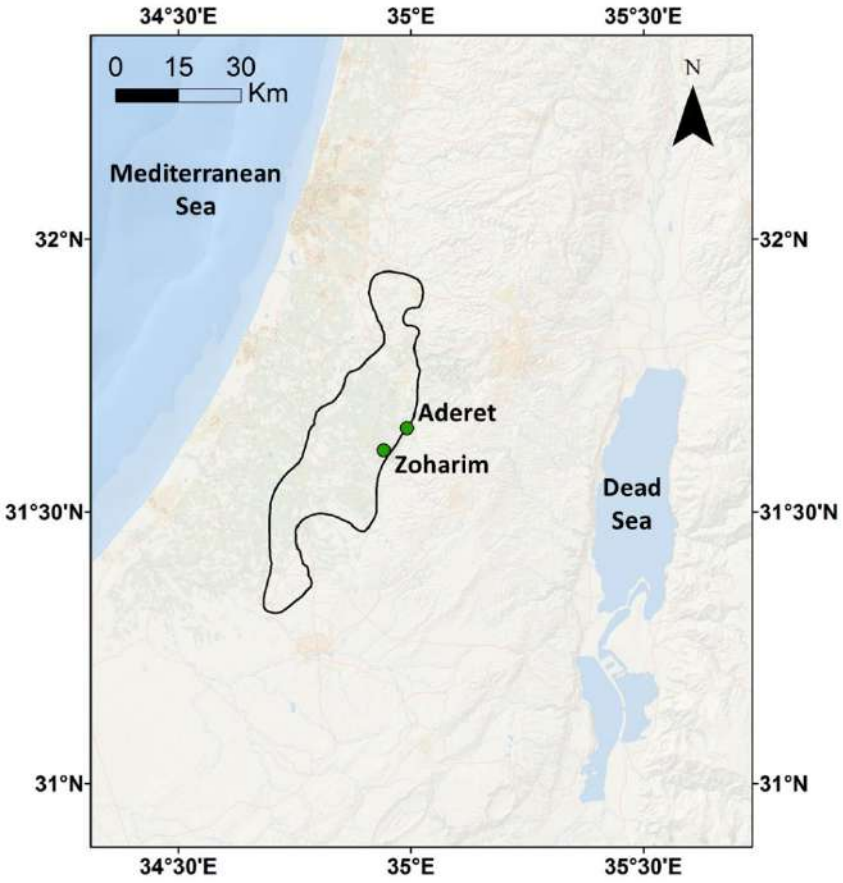

Figure 6: Map of the Shefela basin where organic-rich sequences are thicker than 150 m, delineated by Minster (2009). The thicker sequences are found in the eastern part of the basin, where the Zoharim and Aderet wells are located.

The Mount Scopus Group was deposited during the Late Cretaceous (Campanian- Maastrichtian) above the mid-Cretaceous unconformity (top Judea Group), in the terrains of the passive margins of the northern Arabian Plate and the southern margins of the Tethys ocean (Gvirtzman *et al.* 1989). High productivity upwelling systems caused oxygen depletion on the sea floor, hence anoxic-dysoxic conditions prevailed at the primary sedimentation (Eshet, Almogi-Labin and Bein 1994). The approximated duration of the high productivity system is about ~19 million years (Meilijson *et al.* 2014). Excellent preservation of the organic matter was caused by absence of oxygen, high sedimentation rates and favorable diagenesis conditions. In addition to favorable organic matter preservation conditions, the Mount Scopus Group was deposited during the formation of anticlines and synclines of the "Syrian Arc" folding system (Krenkel 1924). As a consequence, most of the Late Cretaceous organic-rich deposits in the Levant are found in synclinal structures. The Shefela deposit (Figure 6) is situated in a NE-SW elongated syncline (~90

km long and ~35 km wide), including organic-rich sections with thickness of 150-550 meters (Gvirtzman, Moshkovitz and Reiss 1985). This sequence in the Shefela basin is found at shallow depths (several hundreds of meters), and was never exposed to significantly high temperatures. Consequently, the organic-rich chalk in the Shefela basin is immature, with average T_{max} of 412°C and vitrinite reflectance of R_o~0.32% (Meilijson *et al.* 2015). The organic matter mainly consists of a kerogen Type IIs according to H/C versus O/C path in a Van-Krevelen diagram and high sulfur concentration (Spiro 1980). Currently the *in situ* maximum horizontal stress is acting in ESE-WNW direction (Gersman, Bartov and Rozenthal 2012).

1.6 Experimental methods

This research is based on numerous laboratory measurements, in order to establish a deep understanding of the physical behavior of the Ghareb-Mishash chalk. Presented in this section, a quick overview of the laboratory devices and testing methods of petrophysical, acoustic and mechanical properties, all of which are located in the Deichmann Rock Mechanics Laboratory, at Ben-Gurion University of the Negev (BGU). For convenience, the term "core plugs" is used throughout the thesis to describe cylindrical core samples, 2.54 cm long and 2.54 cm in diameter (1 inch/1 inch). Note that the methodology of the pyrolysis experiments (artificial maturation) is presented in Chapter 3.

1.6.1 Porosity, density and permeability (Coreval30)

Porosity, solids density, and Klinkenberg-corrected gas permeability were measured using Coreval30 device manufactured by Vinci Technologies. The measurements were performed using dry core plugs. Prior to the measurements, the plugs were dried in an oven for 24 hours at 105°C. Weight, length and diameter were measured to estimate bulk volume and density.

Porosity is defined as the ratio between pore volume V_p and bulk volume V_b: $\phi = V_p/V_b$. The method utilized in this research measured the pore volume (0.05 cc precision) using nitrogen gas. The tests were performed at a confining pressure of 400 psi (2.8 MPa) around an elastomer sleeve, and at room temperature. Pore volume measurement was performed based on "Boyle's law single-cell method", according to the API recommended practice for core analysis (American Petroleum Institute (API) 1998). According to Boyle's law:

$$P_1V_1 = P_2V_2 \ , \tag{3}$$

where *P* and *V* refer to gas pressure and volume, respectively. Initially, nitrogen gas was injected into the pore space of the plug and the gas pressure was elevated to P_1 (maximum 250 psi). The gas pressure dissipated within the pore space (V_p) and the calibrated dead volume of the manifold (V_d). At the same time, the unvented reference cell (V_t) and the valve volume (V_v) were filled with air at atmospheric pressure (P_a). Once pressure stabilization was achieved, the nitrogen pressure was vented to the reference cell and the nitrogen- air mixture pressure decreased to P_2. The real gas law is:

$$PV = ZnRT \ , \tag{4}$$

where *Z* is the gas deviation factor, *n* is the amount of gas moles, *R* is the universal gas constant and *T* is absolute gas temperature. The number of moles remained constant during the test, thus:

$$n_{total} = \frac{P_2(V_t+V_v+V_d+V_p)}{Z_{N_2,2}RT} = \frac{P_a(V_t)}{Z_aRT} + \frac{P_1(V_d+V_p)}{Z_{N_2,1}RT} \ , \tag{5}$$

where $Z_{N_2,1}$ and $Z_{N_2,2}$ describe the gas deviation factors of nitrogen when subjected to P_1 and P_2, respectively, and Z_a is the gas deviation factor of air. Eventually, pore volume was calculated by:

$$V_p = \frac{\left(1-\left(\frac{P_aZ_{N_2,2}}{P_2Z_a}\right)\right)V_t+V_v}{\left(\frac{P_1Z_{N_2,2}}{P_2Z_{N_2,1}}\right)-1} - V_d \ . \tag{6}$$

Once pore volume and bulk volume were obtained, the porosity and solids density, ρ_s, were determined ($\rho_s = \frac{\rho_{dry}}{1-\phi}$).

Permeability is a property that describes the ability of a porous medium to transmit fluids. Henry Darcy (1856) recognized that the flow rate of fluids through porous systems depends on the permeability of the material. The one-dimensional Darcy's flow law is given by:

$$q = k\frac{A}{\mu}\frac{dP}{dx} \ , \tag{7}$$

where q is the flow rate (fluid volume per time), A is the cross-sectional area of the porous specimen, μ is the fluid dynamic viscosity, and $\frac{dP}{dx}$ is fluid pressure gradient in the flow direction.

Permeability 'k' is conventionally reported in Darcy units (1 Darcy $= 0.986923\ 10^{-12} m^2$). The permeability coefficient is a characteristic of the rock, and it does not depend on liquid type. Practically, it is preferred to flow inertial gas through the specimen rather than liquid in order to perform simpler and shorter measurements and cause less disturbance of the samples. Unlike permeability to liquids, the permeability to gases depends on the gas properties. Klinkenberg (1941) showed that gas molecules slip on the walls of the pores during fluid flow at some finite velocity. The slippage is dictated namely by the mean free path ($\bar{\lambda}$) of the gas molecules and the pore radius, as inter-molecular rejection forces push the gas molecules over the solid surface. The Klinkenberg-corrected gas permeability is:

$$k_g = k_\infty \left(1 + \frac{4c\bar{\lambda}}{\bar{r}}\right), \tag{8}$$

where k_g is gas permeability and k_∞ is permeability of the gas at infinite pressure (~liquid permeability, k_l), c is a factor of proportionality, $\bar{\lambda}$ is the mean free path of the gas molecules and $\bar{r}$ is the mean pore throat radius. The mean free path is inversely proportional to the mean fluid pressure, so that the relation can also be written as:

$$k_g = k_\infty \left(1 + \frac{b}{p_m}\right), \tag{9}$$

where b is the gas slippage factor (in pressure units), and p_m is the mean fluid pressure within the porous network. The slippage factor is high in low permeability samples by being inversely proportional to $\bar{r}$. Permeability measurements were performed using the "pressure-falloff, axial gas flow" technique, according to API recommended practice (section 6.4.1.1 in American Petroleum Institute (API) 1998).

First, nitrogen is injected into the core plug to reach the initial upstream pressure while the sample is unvented. After thermal and pressure equilibrium is established, the outlet valve is vented to atmospheric level while gas pressure is continuously recorded at the upstream. Jones (1972), proposed an expression for axial flow at any position (x) and time (t):

$$q_{[x,t]} = \frac{-V_t\left(1+\delta f_{[c,g]}\right)}{P_{[x,t]}+P_a}\frac{\partial P_{0[t]}}{\partial t}, \tag{10}$$

where V_t is the tank volume, δ and $f_{[c,g]}$ are correction factors accounting for mass flow variation within the plug, $P_{[x,t]}$ is the pressure at any time and location and P_a is atmospheric pressure. The upstream pressure decrease rate is given by the term $\frac{\partial P_{0[t]}}{\partial t}$. Calculations lead to:

$$y_{c,P_{gn}} = i + mP_{g,n} \ . \tag{11}$$

The right-hand term of Equation (11) is a straight line with slope *m* and intercept *i*:

$$m = \frac{k_\infty A}{29.39 \mu L} \ , \qquad i = 2m(P_a + b) \ . \tag{12}$$

The left-hand term of Equation (11) is the "corrected instantaneous flow rate function". The linearity of the representation of $y_{c,P_{gn}}$ implies that the gas flow through the specimen obeys Darcy's law. The whole calculation progress is automatically programmed in the Coreval30 system.

1.6.2 Acoustic velocities (AVS 350)

Ultrasonic velocities of the core plugs were measured using the Acoustic Velocity System (AVS350) manufactured by Vinci Technologies (Figure 7). Electric signals at constant pulse repetitions were converted to ultrasonic waves, which converted back to electric current using 500 kHz piezoelectric transducers, located at both sides of the core plug (Figure 7). P-waves were generated by axis-parallel transducers, and S-waves by two transducers (S1 and S2) arrayed over the transverse plane and perpendicular to each other. The configuration of the transducers within the end caps is shown in Figure 7: P transducers are at positioned in the external part of the end caps, S2 are in the internal parts, and S1 are in between P and S2. The S1 and S2 transducers can be rotated over the transverse plane, as seen by the sketches in Figure 7,

, so that five different waveforms are available: 1) P transmitted and received; 2) S1 to S1, shortest S-wave travel; 3) S2 to S2, longest S-wave travel; and 4) and 5) S1/S2 to S2/S1, mid-distance S-wave travel. This configuration allows also examination of shear wave anisotropy, if the wave propagates in the bedding-parallel direction. Transit times through the core plugs and end caps are picked in an oscilloscope, thus wave velocities are calculated by:

$$v = \frac{L}{t_{corrected}}, \tag{13}$$

where L is the length of the plug and $t_{corrected}$ is the end cap corrected travel time, determined based on first-arrivals picking. The time correction is the picked arrival time minus the travel time in the stainless steel end-caps ($t_{corrected} = t_{total} - t_{endcap}$). The t_{endcap} was determined for each of the five waveforms, by conducting several calibration sets using stainless steel and copper standards, which have predetermined acoustic velocities: $V_{p,Cu} = 4.66\ km/s, V_{s,Cu} = 2.23\ km/s$; $V_{p,Steel} = 5.79\ km/s, V_{s,Steel} = 3.235\ km/s$. P- and S- wave picking was associated with velocity error of maximum 3.5% in dry conditions, while in water-saturated conditions P- wave error reduced to 0.5% (S-wave error remained the same).

Velocity measurements were performed while applying axial, radial and pore pressures with individual controls. This allows to replicate *in-situ* stresses. For example, where a core plug with its axis normal to the bedding is measured, axial, radial and pore pressures are applied according to the assumed vertical stress, horizontal stress and pore pressures in the field, respectively.

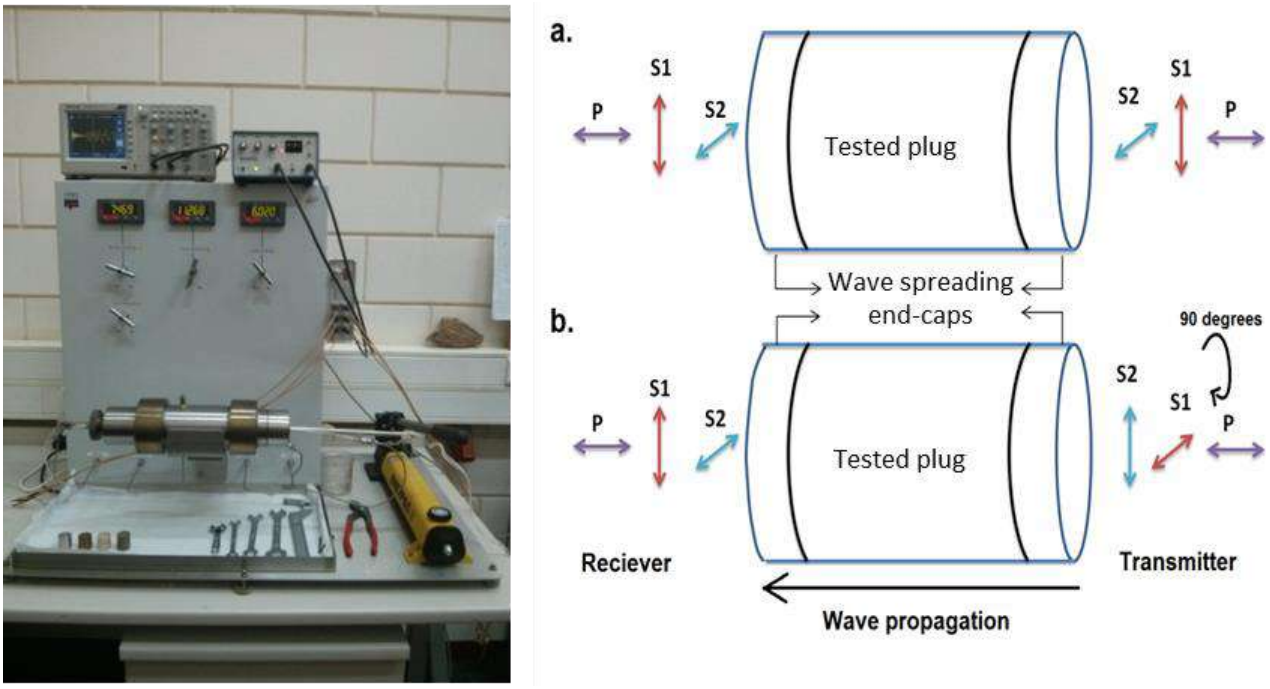

Figure 7: The AVS350 system for P- and S-wave velocities measurements. The stress waves are induced by piezoelectric transducers, oriented in such way to induce compression and shear distortions in the plug. The waves pass through the tested plug and two stain-less steel end caps (one on each side). The stress waves are translated back to an electric current, and arrival times of the waves are picked in the oscilloscope. To identify shear waves in the oscilloscope, the S-wave transducers S1 and S2 are rotated for polarization (transition from (a) to (b) in the sketch).

1.6.3 Static elastic moduli and compressive strength (triaxial compression system)

Compression experiments were performed using a hydraulic, servo-controlled triaxial testing system manufactured by TerraTek Inc., model FX-S-33090. The stiff load frame was operated using a closed-loop servo control with maximum axial force of 1.4 MN, stiffness of $5x10^9$ N/m, and confining pressure capacity of 70 MPa. The linearities of the load cell, strain transducers, and confining pressure are 0.5%, 1%, and 0.25% full scale, respectively. Axial stress, confining pressure, axial strain and the two orthogonal radial strains were continuously recorded during the tests. Triaxial tests were performed under a constant axial strain rate of $1 \cdot 10^{-5} s^{-1}$. The confining pressure was controlled by a manual valve. Tests were carried out on NX size samples, i.e. right circular cylinders with nominal diameter of 54 mm and length/diameter ratio of approximately two, with specimen ends flattened to less than ± 0.01 mm (International Society for Rock Mechanics 2007). All compression tests were performed with the bedding plane direction normal to the axis of the solid cylinders, thus defining the samples as vertically-oriented (Figure 8). No

horizontally-oriented samples were available as the core diameter of ~ 3 inches (~75 mm) was too short for the experimental setup. After the specimens were drilled and polished, they were kept at room conditions for at least 24 hours before the tests. The specimens were not dried in an oven because of their tendency to crack during heating.

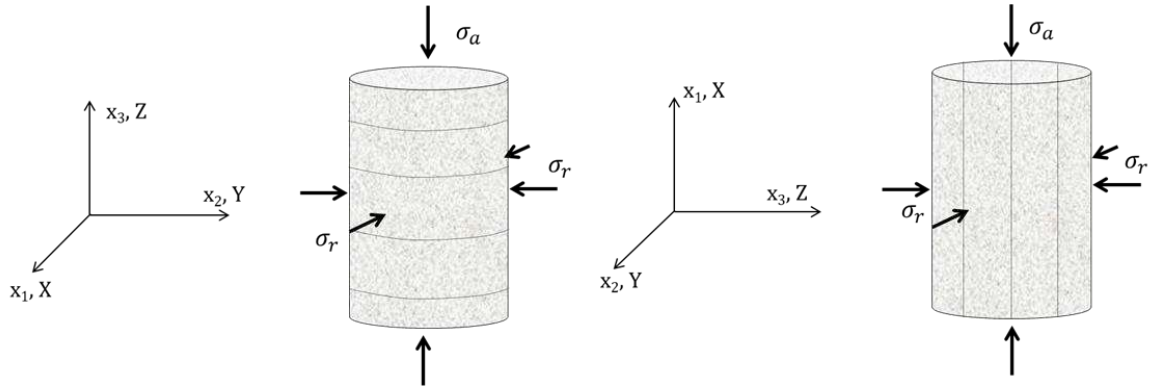

Figure 8: Sketch of two types of specimens commonly used for mechanical testing of VTI rocks: vertically-oriented sample (left) and horizontally-oriented samples (right). In this study, only vertically-oriented samples were tested.

Triaxial compression experiments were performed to obtain the static elastic constants and the compressive strength of the rock. Each triaxial experiment started with a hydrostatic (non-deviatoric) compression stage until the desired confining pressure value was reached. Confining pressure values were chosen to be similar to the minimum horizontal stress in the Zoharim section, estimated from hydraulic jacking tests (Golder Associates 2011). Continuous recording of the strains throughout the hydrostatic stage allowed to obtain the static bulk modulus. In the subsequent deviatoric compression stage, the axial stress was elevated while confining pressure was maintained at the final value from the hydrostatic stage. The methodology of elastic moduli derivation is detailed in Section 2.2.4.

1.6.4 Tensile strength (Brazilian apparatus)

Indirect (Brazilian) tensile strength tests were performed using a manual, hydraulic, mini-load frame (SBEL model PLT-75). Cylindrical specimens were used, 54 mm diameter and 27 mm thickness, maintaining t/D ratio of 0.5, according to ASTM and ISRM standards. The specimens were kept at room conditions before the tests. In Brazilian tests the load is applied on a projection width with angle α, which is considered to be very small, and the stress distribution is calculated

accordingly (Hondros 1959, Fairhurst 1964). The normal stress in the horizontal sidewards direction ($\sigma_{\theta y}$) at the center of the disc is:

$$\sigma_{\theta y} \sim \frac{P}{\pi R \alpha t}[2\alpha - \alpha] = \frac{P}{\pi R t} = \frac{2P}{\pi D t}\ , \tag{14}$$

where *P* is the force applied by the piston in the vertical direction, and *R, t* and *D*, are the radius, thickness, and diameter of the disc (respectively). At tensile failure, the piston force reaches maximum force and the tensile strength is calculated. The calculated stress is considered as the index property "Brazilian tensile strength". Tensile strength is usually anisotropic in bedded specimens, where tension in the bedding-normal direction fractures the specimen more easily than tension that acts in the bedding-parallel direction. Samples were drilled both parallel and perpendicular to the bedding direction, to estimate the strength anisotropy. Tensile strengths were measured both in the bedding-normal direction (tension applied normal to bedding direction) and the bedding-parallel direction (tension applied parallel to bedding direction).

1.7 Thesis outline

This Ph.D. thesis is basically composed of three parts: 1) comprehensive characterization and analysis of the Ghareb-Mishash chalk in its native immature state; 2) examination of the effect of pyrolysis-induced maturation on rock properties; and 3) application of the RPM to field measurements from the Shefela basin. New methodologies have been developed at the course of this study. All of the novel methodologies are applied in the analysis of the immature chalk properties, hence presented at the beginning of part (1).

In the first chapter (Chapter 2), novel methods are developed, and existing methods are adjusted according to the needs of this study. These methods are specifically designed for the Ghareb-Mishash chalk, but may be applied on various VTI rocks, particularly organic-rich rocks. The novelties include the hydrostatic strain ratio (Ω), the "HDC-TIES" procedure, the "HS kerogen model", and the improvement in density and volume determination of phases in organic-rich rocks. Description of existing methods being employed in this study is given as well, including effective medium theories and fluid substitution models. Then, a broad characterization of the immature Ghareb-Mishash chalk is presented. The characterization includes laboratory measurements of petrophysical, mechanical and acoustic properties. Because the availability of native state core samples was highest, this chapter is the heart of this study. The theoretical approaches are

evaluated by their applicability to the experimental results. The core material availability at the native state allowed to perform analyses of static-dynamic moduli relationships and rock strength. Interrelationships between the experimental datasets enabled further examination of the rock properties.

In the second chapter (Chapter 3), results of artificially-matured samples are described. These results include petrophysical and acoustic measurements of post-pyrolysis core plugs. Combination of these results with geochemical data allows examination of the influence of bitumen and kerogen fractions on various properties. Evolution of rock properties is investigated using the dataset of immature rock properties as reference. Finally, rock physics templates are created in purpose of geophysical prospecting of porosity, organic-content and maturity.

In the third chapter (Chapter 4), the observations from the experimental and theoretical investigation are applied to field measurements from the Zoharim and Aderet wells in the Shefela basin. The field measurements in this study are obtained from well-logs. Another dataset being used in this chapter is continuous coring data. Although these geochemical measurements were performed in the laboratory (by IEI Ltd.), the amount of measurements is sufficiently high and their spacing within the depth section is relatively dense. Therefore, continuous coring dataset is also referred to as field measurements. Then, different datasets are combined to extract information on rock properties *in-situ*. The "HS kerogen" model applicability as a prospecting method is inspected. This model assists in the estimation of gas saturation within the upper part of the Ghareb Formation.

2 Immature rock properties

2.1 Introduction

In this chapter, measurements of petrophysical, mechanical and acoustic properties are reported. The petrophysical properties mainly include the porosity, density and permeability of the rock. Completion of the petrophysical dataset is enabled by TOC measurements conducted on the same core samples. The mechanical properties include VTI static moduli, tensile strength and compressive strength. The acoustic properties include the P-wave and S-wave velocities, mainly in the bedding-normal direction. The rock properties are cross-correlated to examine effects of rock constituents and their geometrical arrangement on bulk properties, such as elastic moduli, acoustic velocities, strength, permeability, and their anisotropic behavior. The Zoharim section is at the focus of this study. The depth section in the Zoharim well is divided into four units: 1) upper part of the Ghareb Formation (330-410 m), with the highest porosity and rich in TOC; 2) lower part of the Ghareb Formation (410-482 m), with the high porosity and very rich in TOC (15-20 %wt.); 3) upper part of the Mishash Formation (482-557 m), with lower porosity than the overlying Ghareb Formation, but TOC content is about the same as in the upper part of the Ghareb; and 4) lower part of the Mishash (557-610 m), which is significantly lower in porosity and TOC.

2.2 Analytical methods

Various tests have been carried out in this study, and their analysis requires appropriate analytical approaches. Common practice methods are combined with new analytical developments. The innovational methods are presented in this section.

2.2.1 Petrophysical model of organic-rich rocks

Before interpretation of petrophysical results, it is important to construct the petrophysical model of the Ghareb-Mishash chalk. The model developed here is applicable to organic-rich rocks, summarized into a block diagram of densities and volume fractions. Two improvements of the traditional analytical methods are proposed: 1) precise consideration of the porosity; and 2) derivation of the bitumen fraction in the organic matter. The Ghareb-Mishash chalk is a high porosity mixture of organic and inorganic components. The organic phase at the immature state is primarily kerogen Type IIs, while bitumen amounts are negligible. The presented modeling improvement includes the bitumen because it becomes quite important in higher maturity levels.

In past rock physics studies of organic-rich rocks, TOC was often converted straightforwardly to kerogen content, while neglecting the effects of bitumen and missing out the effect of porosity (e.g. Vernik and Nur 1992; Sone and Zoback 2013a; Carcione and Avseth 2015):

$$f_k = \frac{TOC\left(\rho_b - \rho_f \phi\right)}{C_{pr}\rho_k(1-\phi)}, \tag{15}$$

where f_k is the volume fraction of kerogen, ρ_k, ρ_f and ρ_b are the densities of kerogen, fluid phase and the fluid-saturated rock, respectively, ϕ is the porosity, and C_{pr} is the weight percentage of carbon in the organic matter. Simple mass and volume balance analysis of these quantities shows that f_k reduces to the kerogen fraction of the solid matrix (V_k/V_s), instead of the bulk volume (V_k/V_b). Nevertheless, it has been traditionally introduced into models as bulk kerogen fraction. Moreover, this relationship suggests that the TOC is entirely associated with kerogen. This induces more inaccuracy, as the presence of bitumen within the organic phase may alter rock properties (e.g. elastic moduli, porosity, permeability and solids density). It is verified that bitumen has different elastic moduli than kerogen (Eliyahu *et al.* 2015), thus distinction between kerogen and bitumen is highly in favor. As a result, this relationship is problematic, especially in high porosity organic-rich rocks. The correct formulation is as follows (to facilitate the understanding of this argument, physical expressions of each parameter is given in squared brackets):

$$f_o = \frac{TOC\rho_{dry}}{C_{pr}\rho_o} \;\; , i.e. \left[\frac{V_o}{V_b} = \frac{\frac{m_{organic\ C}}{m_s}\cdot\frac{m_s}{V_b}}{\frac{m_{organic\ C}}{m_{organic\ material}}\cdot\frac{m_{organic\ material}}{V_{organic\ material}}}\right] \tag{16}$$

where f_o is the organic matter fraction of the bulk volume, and ρ_o is the density of the organic matter. Further derivation of bitumen and kerogen concentrations is enabled by results of bitumen extraction experiments (see next paragraph). It should be noted that bitumen in the samples is considered part of the solid phase in the porosity measurements, even though it is practically a viscous pore-filling liquid. Presented below are detailed formulations of phases and their introduction into the block diagram (Figure 9).

In this derivation, bulk volume fractions are designated by f, masses by m, and densities by ρ, and the subscripts ‘s’, ‘m’, ‘o’, ‘k’ and ‘bit’, respectively refer to the solids, minerals, organic matter, kerogen, and bitumen. By combining the dry rock density with the measured porosity, solids

density is obtained ($\rho_s = \frac{\rho_{dry}}{1-\phi}$). Assuming an average minerals density in the depth section ρ_m, average organic matter density ρ_o, and average carbon weight percentage in the organic matter C_{pr}, the relationship between ρ_s and TOC shall follow this trend:

$$\rho_s = \frac{a_1}{1 + a_2 TOC}, \tag{17}$$

where $a_1 = \rho_m$, $a_2 = \frac{\frac{\rho_m}{\rho_o} - 1}{C_{pr}}$. By fitting Equation (17) to experimental data, and assuming a reasonable value of C_{pr} (typically 70% in an immature Type II kerogen, Vernik 2016), ρ_m and ρ_o are estimated. Bitumen extraction measurements by Kutuzov (2017), performed on the same core material, enables the estimation of bitumen and kerogen fraction in the rock. Bitumen was extracted using a Soxhlet extractor and a dichloromethane/methanol (9:1 v/v) mixture for 72 hours. The results were reported as the loss of mass after bitumen extraction, divided by the initial mass. In this study, this quantity is referred to as BIT:

$$BIT = \frac{m_{bit}}{m_s}. \tag{18}$$

Consequently, the bitumen concentration in the organic matter, B_c, can be written as:

$$B_c = \frac{f_{bit}}{f_o} = \frac{BIT}{TOM} \cdot \frac{\rho_o}{\rho_{bit}}, \tag{19}$$

using the TOM as the weight percent of total organic material, before the bitumen extraction (note that $TOM = TOC/C_{pr}$). The bitumen density could not have been measured because the extracted bitumen was diluted. Therefore, reasonable bitumen density range of 1.0 -1.1 g/cc is considered in this study (Orr 1986; Baskin and Peters 1992; Hofmann 2006; Han, Liu and Batzle 2006; G. Wang *et al.* 2010). The block diagram is now completed using bitumen and kerogen fractions and kerogen density:

$$f_{bit} = B_c f_o , \tag{20}$$

$$f_k = f_o - f_{bit} , \tag{21}$$

$$\rho_k = \frac{\rho_o f_o - \rho_{bit} B_c f_o}{f_k} \,. \tag{22}$$

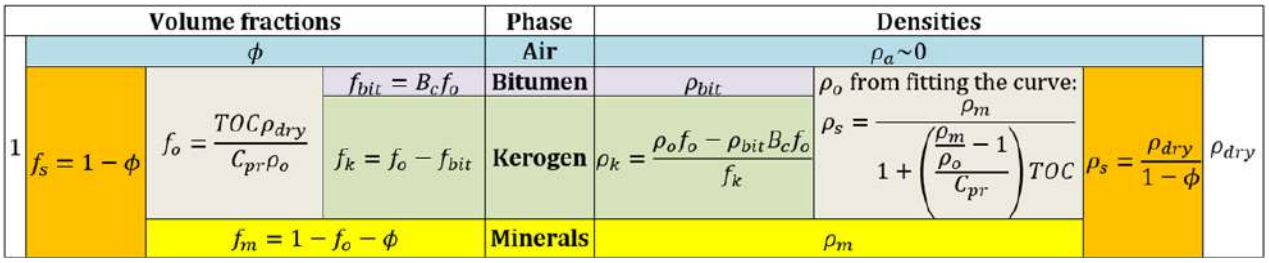

Figure 9: Block diagram of the phases in organic-rich rocks: Volume fractions are marked by 'f' and densities by 'ρ'. The subscripts 's', 'm', 'o', 'k' and 'bit', refer to solids, minerals, organic matter, kerogen, and bitumen (respectively). C_{pr} is the weight percentage of carbon in the organic matter, increasing with maturity from 70% to 85% (Vernik and Milovac, 2011)

2.2.2 Acoustic velocities, theoretical bounds and fluid substitution

Acoustic velocities are the square root of the ratio of a dynamic elastic modulus over bulk density. The dynamic moduli used for these purposes are typically the bulk modulus 'K', shear modulus 'μ', and oedometer modulus 'M'. The oedometer and shear modulus are frequently referred to as the P-wave and S-wave moduli, respectively. Dynamic moduli are evaluated from wave velocity measurements, either in the field (seismic methods, well-logs) or in the laboratory. In order to model wave velocities, rock physics theories commonly estimate the dynamic moduli and density of rocks. In this section, the estimation of the dynamic moduli is presented. Density estimation was presented in the previous section.

The dynamic moduli primarily depend on the relative concentrations of the rock constituents and on their geometrical arrangement in the matrix (Mavko *et al.* 2009). Matrix stiffness relates to mechanical interactions at the contacts between stiff and soft grains within a porous medium. Elastic moduli of multiphase materials are calculated using the Hashin-Shtrikman (HS) bounds (Hashin and Shtrikman 1963; Mavko *et al.* 2009):

$$K_{HS}^{+/-} = \left(\sum_{i=1}^{n} \frac{f_i}{K_i + \frac{4}{3}\,\mu_{max/min}} \right)^{-1} - \frac{4}{3}\mu_{max/min} \,, \tag{23}$$

$$\mu_{HS}^{+/-} = \left(\sum_{i=1}^{n} \frac{f_i}{\mu_i + \zeta_{max/min}} \right)^{-1} - \zeta_{max/min} \ , \tag{24}$$

where '+' and '-' denote upper and lower bounds, f_i is the volume fraction of each phase, and *max* and *min* refer to the theoretical moduli of the stiffest and softest phases, respectively. The ζ of each phase is calculated by (Mavko *et al.* 2009):

$$\zeta = \frac{\mu}{6}\left(\frac{9K + 8\mu}{K + 2\mu}\right) . \tag{25}$$

The upper bound represents the moduli of a homogeneous granular package where the stiff phase forms a perfectly continuous network, while the softer phases are embedded in them. The average modulus of the mineralogical constituents in this case is denoted by subscript *max*. The lower bound represents the moduli of a matrix supported by the softest phase, i.e. fluid-suspended matrix, thus dominated by the elastic moduli of the pore fluid, denoted by subscript *min*. In order to compare the measured P-wave moduli with the models, the oedometer modulus is calculated by:

$$M = K + \frac{4}{3}\mu \ . \tag{26}$$

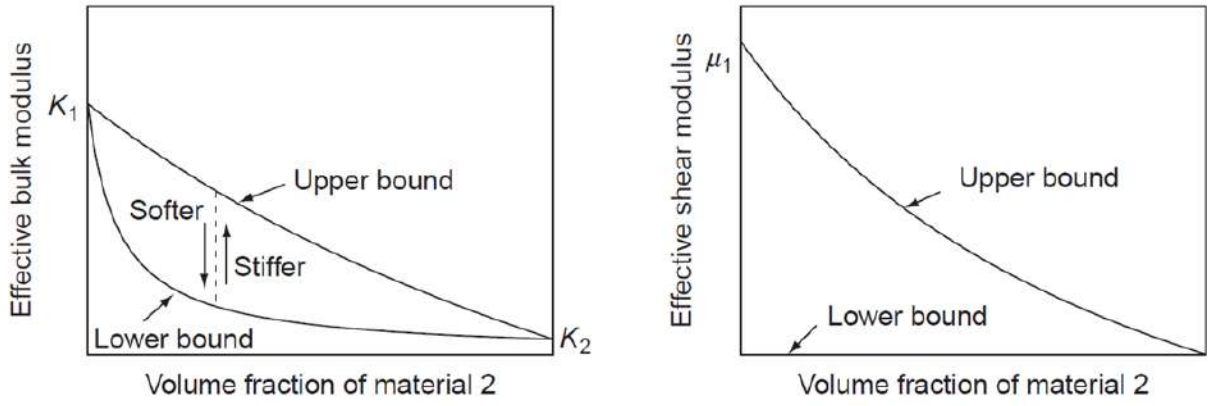

Figure 10: Schematic of the Hashin-Shtrikman bounds of bulk modulus (a) and shear modulus (b), of a two-phase material (Mavko *et al.* 2009). Phase 2 is considered softer than phase 1. Where there are more than two phases, the bounds lose their continuous form.

The true moduli of rocks normally fall somewhere between the upper and lower HS bounds. This is simply demonstrated in the schematic Figure 10. Some models use the relative location of a measured modulus between the bounds as a parameter for rock physics modeling and fluid substitution. In this study, Marion's bounding average method (BAM) is used (Marion 1990).

Marion's BAM model argues that the vertical position of the experimental value between the theoretical HS bounds is a measure of the matrix stiffness. This characteristic is defined by the normalized stiffness factor 'w':

$$w = \frac{A - A^{-}}{A^{+} - A^{-}} \,, \tag{27}$$

where w is the BAM normalized stiffness factor, and A represents any of the computed elastic moduli. The 'w' of each modulus is a characteristic of the geometrical arrangement of the phases and should not change upon fluid substitution. This way, elastic moduli at any fluid composition can be estimated. It should be noted that although the BAM fluid substitution model makes a lot of sense, it was invented based on a heuristic approach rather than on a physical approach (Olsen *et al.* 2008b). The alternative is the "Iso-frame" model (Fabricius 2003), which divides the matrix components into two groups: particles in suspension and particles in the solid frame. It is represented by the "Iso-frame" parameter 'IF' which ranges between 0 and 1, corresponding to the lower and upper HS bounds, respectively. However, the "Iso-frame" model involves more assumptions than the BAM model. In order to minimize the amount of assumptions in this study, the BAM model is chosen. This issue is elaborated in the discussion on rock physics modeling approaches (Section 2.8.1).

Another fluid substitution model, that is the most common, is the Biot-Gassmann's method (Biot 1941; Gassmann 1951). This method is typically applicable when using seismic frequencies, where the induced pore pressure is equilibrated throughout the pore space (i.e. there is sufficient time for the pore fluid to flow and eliminate wave-induced pore-pressure gradients). The bulk modulus of fluid-saturated and dry rocks are given by:

$$K_{sat} = K_s(1 - \beta) + \frac{\beta^2 K_s K_f}{K_f(\beta - \phi\,) + K_s\phi} \,, \tag{28}$$

$$K_{dry} = K_s(1 - \beta)\,, \tag{29}$$

where subscripts *sat*, *dry* and *s* refer to the bulk modulus of saturated rock, dry rock and solid phase, respectively. This method involves an approximation of the effective bulk modulus of the

solid phase, 'K_s'. The most common approximation of K_s is the Voigt-Reuss-Hill (VRH) average of the solid phases (Mavko *et al.* 2009):

$$K_{VRH} = \frac{\left(\sum_{i=1}^{n} \frac{f_i}{K_i(1-\phi)}\right)^{-1} + \sum_{i=1}^{n} \frac{f_i}{1-\phi} K_i}{2}, \tag{30}$$

The Biot's coefficient β is a dimensionless coefficient ranging from 0 to 1. β is also known as the effective stress coefficient (Mavko *et al.* 2009; Zoback 2010):

$$\sigma = S - \beta P_p \,, \tag{31}$$

where σ is the effective stress, S is the total stress, and P_p is the pore fluid pressure. The shear modulus of rocks is assumed to remain constant upon fluid substitution, hence μ_{sat} equals μ_{dry}.

2.2.3 The "HS kerogen" model

As explained above, the geometrical arrangement of rock constituents results in a modulus that plots somewhere between the upper and lower HS bounds. In this study, another approach is proposed, on the basics of Hashin-Shtrikman bounds. Assuming the rock is primarily divided into three phases: minerals, organic matter and pores, there are three HS curves that simulate a matrix supported by each of these phases. Just as "HS+" and "HS-" simulate mineral-supported matrix and fluid-supported matrix (respectively), a similar concept can be used to approximate moduli of a kerogen-supported matrix. Hashin-Shtrikman approximation of such matrix is defined here as "HS kerogen". A sketch of this concept is given in Figure 11. This is done by introducing the shear modulus of kerogen in Equation (23) and the ζ of kerogen in Equation (24):

$$K_{HS}^{k} = \left(\sum_{i=1}^{n} \frac{f_i}{K_i + \frac{4}{3}\,\mu_k}\right)^{-1} - \frac{4}{3}\mu_k \,, \tag{32a}$$

$$\mu_{HS}^{k} = \left(\sum_{i=1}^{n} \frac{f_i}{\mu_i + \zeta_k}\right)^{-1} - \zeta_k \,. \tag{32b}$$

The model is defined as "kerogen-supported", because the kerogen particles are supporting the rock. Consequently, assignment of theoretical elastic moduli of the organic material should be as

accurate as possible. Many studies used moduli of kerogen based on extrapolation of results to a 100% kerogen, using various rock physics models (e.g. Vernik and Landis 1996). Others used the measurements of porous kerogen composites, and estimated intrinsic kerogen moduli using Biot-Gassmann's model (Yan and Han 2013). Here the moduli of immature kerogen are assigned based on atomic force microscopy (AFM) measurements by Emmanuel *et al*. (2016) on immature Type II kerogen. They found the reduced Young's modulus (E_r) to be 7.1 GPa. In order to use these measurements for estimation of the bulk and shear moduli of kerogen, E_r needs to be converted to E assuming a reasonable Poisson's ratio of kerogen. Each combination of E and ν are directly associated with a pair of K and μ in isotropic materials, such as kerogen:

$$K = \frac{E}{3(1-2\nu)}\ , \tag{33}$$

$$\mu = \frac{E}{2(1+\nu)}\,. \tag{34}$$

A Poisson's ratio of 0.35 was assumed, following checks within the reasonable range (0.05-0.45, Ahmadov, Vanorio and Mavko 2009), and while comparing to values reported for Type II kerogens (e.g. Carcione *et al.* 2011; Yan and Han 2013). This results in Young's modulus of 6.4 GPa, that leads to bulk modulus of 7.1 GPa and shear modulus of 2.4 GPa. The organic material in the immature state is approximately 94% kerogen and 6 % bitumen (based on bitumen extraction measurements). Reported bitumen velocities (Han *et al.* 2006) are converted to elastic properties assuming density of ~1.05 g/cc. These velocities match approximately the bitumen modulus found in Zargari *et al.* (2013) using nanoindentation. The elastic moduli of the immature organic material (OM) is calculated using a Voigt-type of averaging:

$$K_{om} = B_c K_{bit} + (1-B_c)K_k\ , \tag{35}$$

$$\mu_{om} = B_c \mu_{bit} + (1-B_c)\mu_k\ . \tag{36}$$

The resultant bulk and shear moduli of the organic material are estimated to be 6.9 GPa and 2.3 GPa, respectively. Note that where the bitumen distribution in the organic matter is more significant, as in mature source rocks, another averaging method is used (see Section 3.5). Theoretical elastic moduli used for the calculations are summarized in Table 1.

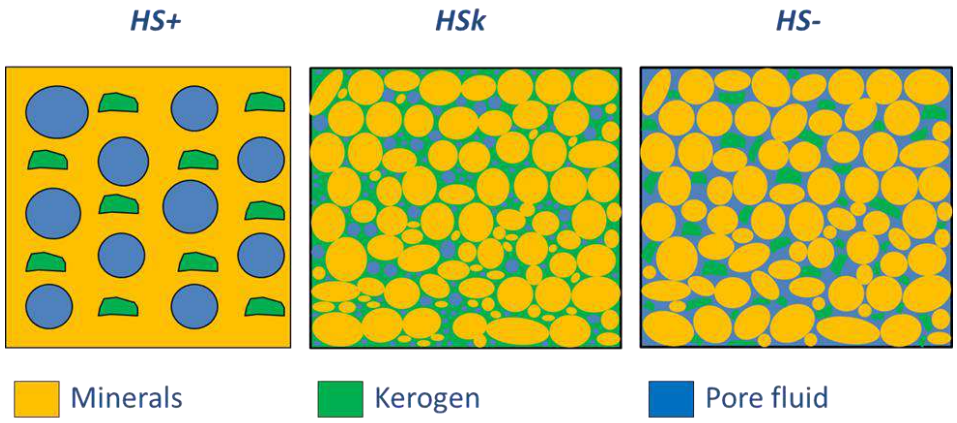

Figure 11: HS conception of load-supporting phases in the rock: upper bound ('HS+', minerals-supported matrix), lower bound ('HS-', fluid-suspension), and the "HS kerogen" model ('HSk', kerogen-supported matrix).

Table 1: Elastic moduli of rock components: Minerals moduli are taken from Mavko *et al.* (2009), and clay minerals specifically from Wang *et al.* (2001). Ranges of volume percentage of each mineral in the Ghareb-Mishash chalk are taken from X-ray diffraction data provided by IEI Ltd. and Gordin *et al.* (in prep.). Elastic properties of immature kerogen are based on Emmanuel *et al.* (2016), assuming a Poisson's ratio of 0.35. The elastic properties of bitumen are taken from Han *et al.* (2006).

Mineral	%v	K [GPa]	μ [GPa]
Kaolinite	<1	44.2	22.1
Illite	<1	60.4	25.4
Smectite	0-5	9.3	6.9
Calcite	60-80	71	30
Dolomite	<1	80	48
Quartz	3-10	37	45
K-spar	<1	37.5	15
Plag	<1	75.6	25.6
Pyrite	<1	147	132
Apatite	0-20	85	46
Minerals average		**66**	**32**
Kerogen		7.1	2.4
Bitumen		3.5	0.7
Organic matter average		**6.9**	**2.3**
Air		0.0001	0
Brine		2.32	0

2.2.4 The "hydrostatic strain ratio": a new anisotropy parameter for VTI rocks

Analyzing the elastic behavior of transversely isotropic rocks can be done by tests on a single core sample using special experimental methods. For example, static moduli can be measured using hollow cylinders testing methodology (Talesnick *et al.* 2001) or using six strain gauges installed at a specific configuration (Togashi, Kikumoto and Tani 2017). Dynamic moduli can be measured using piezoelectric transducers glued at multiple directions (e.g. Sarout *et al.* 2007). However, because standard configuration of laboratory devices were primarily designed for isotropic materials, static and dynamic moduli of VTI rocks usually require multiple measurements. For full characterization of VTI materials specimens are usually drilled in three directions, usually the bedding-normal, bedding-parallel and bedding-diagonal directions. In some cases, in wells for example, core material is limited and specimens can be drilled only parallel to the borehole axis. Normally these are vertical wells drilled into horizontal rock beds, hence the cores are referred to as vertically-oriented. Common compression systems for static measurements are suited for solid cylinders with strain recorded only in the axial and radial directions. There is a considerable amount of uniaxial and triaxial compression test data obtained on vertically-oriented VTI specimens in regular compression testing equipment (Figure 8). To overcome this obstacle, a new method is developed here for analyzing test results in a manner that maximizes the information available from a single compression test of a vertically-oriented VTI specimen. Note that this development is applicable for basins that are developed in horizontally layered rock formations.

Transversely isotropic rocks are typically characterized using five independent elastic stiffness constants: $C_{11}, C_{12}, C_{13}, C_{33}$ and C_{55}. Alternatively, elasticity can be described using engineering constants, for example the Young's modulus, Poisson's ratio and shear modulus in the vertical and horizontal directions, for example the $E_v, \nu_v, E_h, \nu_h,$ and μ_v (Lo, Coyner and Toksöz 1986; Higgins *et al.* 2008; Togashi *et al.* 2017). A typical deviatoric compression stage, either in uniaxial or triaxial tests, yields two elastic moduli, for instance the Young's modulus and Poisson's ratio. Young's modulus is calculated from the slope of the linear segment of the stress difference - axial strain curve ($\Delta\sigma_a$ versus ε_a), within the elastic range. Poisson's ratio is determined as the ratio between radial and axial strains ($-\varepsilon_r/\varepsilon_a$) within the same range (note that compression and contraction are here considered positive). These techniques are typically employed on VTI rocks

with no consideration of the role of the confining pressure in a triaxial test. The analysis presented below accounts for the theoretical role of confining pressure on the slopes from which static moduli are derived.

There are two stages in a standard triaxial test: the hydrostatic compression stage and the subsequent deviatoric compression stage. The stress-strain relationships of a VTI rock are expressed using Hooke's law (Mavko *et al.* 2009):

$$\begin{bmatrix}\sigma_1\\ \sigma_2\\ \sigma_3\\ \sigma_4\\ \sigma_5\\ \sigma_6\end{bmatrix} = \begin{bmatrix} C_{11} & C_{12} & C_{13} & 0 & 0 & 0\\ C_{12} & C_{11} & C_{13} & 0 & 0 & 0\\ C_{13} & C_{13} & C_{33} & 0 & 0 & 0\\ 0 & 0 & 0 & C_{55} & 0 & 0\\ 0 & 0 & 0 & 0 & C_{55} & 0\\ 0 & 0 & 0 & 0 & 0 & C_{66}\end{bmatrix}\begin{bmatrix}\varepsilon_1\\ \varepsilon_2\\ \varepsilon_3\\ \varepsilon_4\\ \varepsilon_5\\ \varepsilon_6\end{bmatrix}, \tag{37}$$

where subscripts 1, 2, and 3 denote normal stresses and strains, and subscript 4, 5, and 6 denote shear stresses and strains (an alternative form of Equation (2)). These subscripts are the Voigt-notated directions of stiffness constants in anisotropic elastic materials (Fjær *et al.* 2008; Mavko *et al.* 2009), and should not be confused with maximum and minimum principal stresses. In VTI rocks, subscripts 1 and 2 represent the directions within the transverse plane, and subscript 3 represents the bedding-normal direction (Figure 8). Directions 4, 5 and 6 represent shear components over the 2-3, 1-3 and 1-2 planes, respectively. In a vertically-oriented specimen direction 3 coincides with the axial direction and directions 1 and 2 with the radial directions. Note that the radial strains in directions 1 and 2 must be equal; otherwise the material has a lower class of symmetry and transverse isotropy cannot be assumed. Furthermore, in order to perform the analysis, it is assumed that the axis of the sample is perfectly aligned with the bedding-normal direction and that the faces of the sample are parallel (i.e. perfect cylinder). This theoretical section is based on the analysis of two special cases of a vertically-oriented VTI sample: hydrostatic compression and triaxial compression. Typically, the boundary conditions of triaxial compression consider a stress state in which uniform lateral stresses are confining the specimen (i.e. $\sigma_r = \sigma_1 = \sigma_2$), and the axial piston induces the maximum stress ($\sigma_a = \sigma_3$, see Figure 8). In hydrostatic tests the boundary conditions are $\sigma_1 = \sigma_2 = \sigma_3 = p$. By introducing the boundary conditions of both hydrostatic and triaxial compression into Equation (37), the shear stresses are zero ($\sigma_4 = \sigma_5 = \sigma_6 = 0$). Therefore, by inverting the matrix in Equation (37), introducing the stresses applied on a

vertically-oriented VTI sample in a typical triaxial test, and focusing on the non-zero terms, the strains are:

$$\begin{bmatrix}\varepsilon_r\\ \varepsilon_r\\ \varepsilon_a\end{bmatrix}=\frac{1}{C_{33}(C_{11}+C_{12})-2{C_{13}}^2}\begin{bmatrix}\frac{C_{11}C_{33}-{C_{13}}^2}{C_{11}-C_{12}} & \frac{{C_{13}}^2-C_{12}C_{33}}{C_{11}-C_{12}} & -C_{13}\\ \frac{{C_{13}}^2-C_{12}C_{33}}{C_{11}-C_{12}} & \frac{C_{11}C_{33}-{C_{13}}^2}{C_{11}-C_{12}} & -C_{13}\\ -C_{13} & -C_{13} & C_{11}+C_{12}\end{bmatrix}\begin{bmatrix}\sigma_r\\ \sigma_r\\ \sigma_a\end{bmatrix}, \tag{38}$$

where the radial strain ε_r aligns with the confining pressure σ_r, and the axial strain ε_a aligns with the axial stress σ_a that is applied by the piston. The resultant strains in triaxial stress conditions are:

$$\varepsilon_a=\frac{\sigma_a(C_{11}+C_{12})-2\sigma_r C_{13}}{C_{33}(C_{11}+C_{12})-2{C_{13}}^2}, \tag{39}$$

$$\varepsilon_r=\frac{\sigma_r C_{33}-\sigma_a C_{13}}{C_{33}(C_{11}+C_{12})-2{C_{13}}^2}\ . \tag{40}$$

As seen, four of the five unknown stiffness constants of a VTI material are mobilized: C_{13}, C_{33}, C_{11} and C_{12}. The stress-strain relations elaborated here are used to obtain these parameters. First to be derived are the Young's modulus, Poisson's ratio and bulk modulus, for vertically-oriented VTI samples. Defined at uniaxial stress conditions ($\sigma_r=0$), the vertical Young's modulus and vertical Poisson's ratio are:

$$E_v=\frac{\sigma_a}{\varepsilon_a}\ , \tag{41a}$$

$$\nu_v=-\frac{\varepsilon_r}{\varepsilon_a}\ . \tag{41b}$$

Thus:

$$E_v=C_{33}-\frac{2{C_{13}}^2}{C_{11}+C_{12}}\ , \tag{42}$$

$$\nu_v=\frac{C_{13}}{C_{11}+C_{12}}. \tag{43}$$

Note that the definition of the vertical Poisson's ratio, ν_v, is referred to as ν_{31} in many studies (e.g. Sone and Zoback 2013a; Yan, Han and Yao 2016). A deviatoric compression stage provides two independent stress-strain relationships (Figure 12): stress difference versus axial strain ($\Delta\sigma_a$versus ε_a) and stress difference versus radial strain ($\Delta\sigma_a$versus ε_r). The $\Delta\sigma_a$versus ε_a relationship can be now written as:

$$\frac{\Delta\sigma_a}{\varepsilon_a} = \frac{(\sigma_a - \sigma_r)\left(C_{33}(C_{11} + C_{12}) - 2{C_{13}}^2\right)}{\sigma_a(C_{11} + C_{12}) - 2\sigma_r C_{13}}. \tag{44}$$

Rearranged to a linear equation:

$$\Delta\sigma_a = \varepsilon_a\left(C_{33} - \frac{2{C_{13}}^2}{C_{11} + C_{12}}\right) + \sigma_r\left(\frac{2C_{13}}{C_{11} + C_{12}} - 1\right) = E_v\varepsilon_a + \sigma_r(2\nu_v - 1)\,. \tag{45}$$

Similarly, the $\Delta\sigma_a$versus ε_r curve can be written as:

$$\Delta\sigma_a = -\frac{E_v}{\nu_v}\varepsilon_r + \sigma_r\left(\frac{C_{33}}{C_{13}} - 1\right)\,. \tag{46}$$

Equations (45) and (46) can be used to describe the linear segment of the stress-strain curves, as demonstrated in Figure 12. Equations (45) and (46) prove that the confining pressure, theoretically, does not influence the slopes of the stress-strain curves, but only the intercepts with the vertical axis. In this analysis, only the slopes of these linear relationships are used for deriving the elastic moduli, as the value of intersection with the vertical axis is sensitive to deviations induced by the experimental procedure. The Poisson's ratio is derived using Equation (46) in order to conform with its basic definition, as shown in Equation (43). Note that the $-\varepsilon_r/\varepsilon_a$ ratio in triaxial tests is stress dependent as indicated by Equations (39) and (40), thus deviates from the basic definition of Poisson's ratio. It should be remarked that this stress dependency exists also in isotropic rocks, and in fact all Poisson's ratios from triaxial tests should be derived as done here.

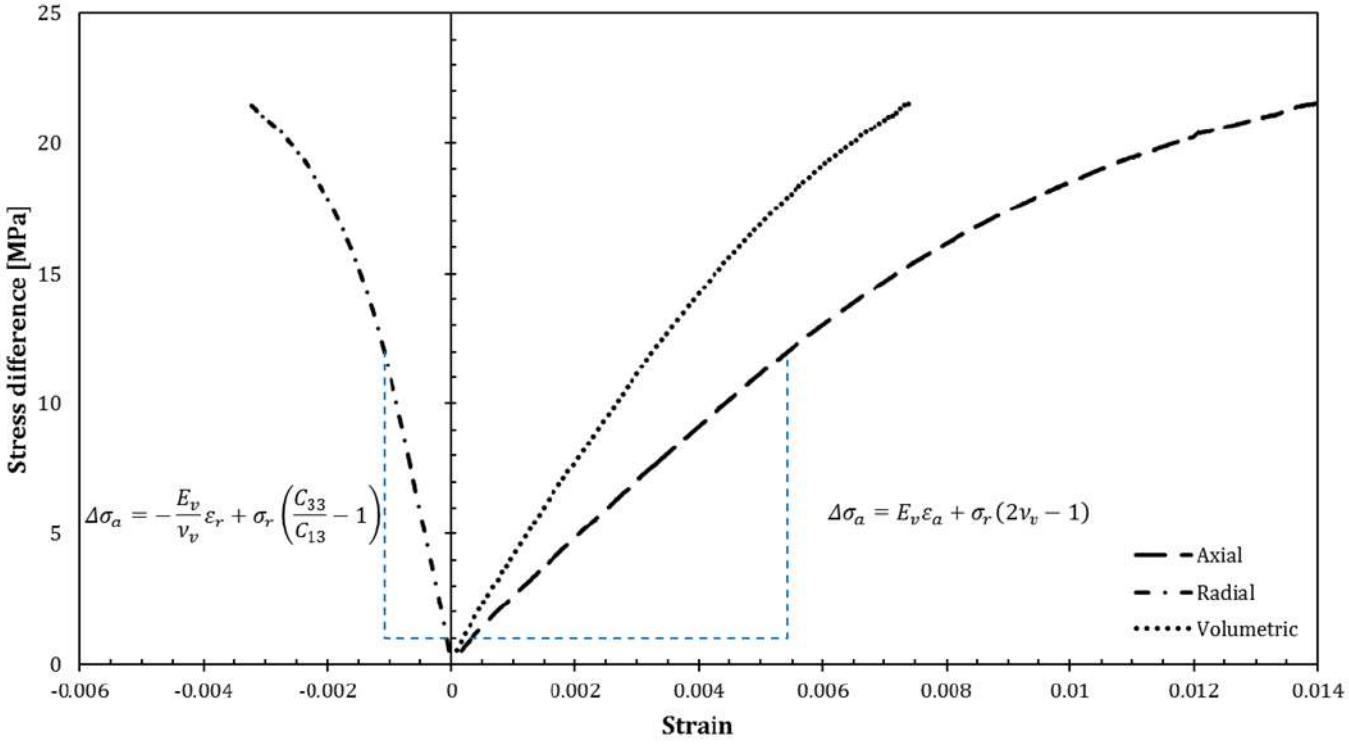

Figure 12: Stress-strain curves in a deviatoric compression stage of a triaxial experiment using a vertically-oriented VTI sample. Mathematical expressions are presented for the linear parts of the axial and radial strain curves. This example originates from 431.5 m depth in the Zoharim well.

Triaxial tests normally start with a hydrostatic compression stage ($\sigma_r = \sigma_a = p$). The bulk modulus is defined as the slope of the linear segment of the confining pressure versus volumetric strain curve (p versus ε_v, Figure 13):

$$K = \frac{p}{\varepsilon_v} = \frac{p}{\varepsilon_a + 2\varepsilon_r} \ , \tag{47}$$

and by combining Equations (39), (40) and (47):

$$K = \frac{C_{33}(C_{11} + C_{12}) - 2{C_{13}}^2}{C_{11} + C_{12} - 4C_{13} + 2C_{33}} \ . \tag{48}$$

Equations (42), (43) and (48) were first presented by King (1964), and their derivations are given here to explain the elaboration of relationships between the measured engineering moduli and Voigt-notated stiffness constants in VTI rocks.

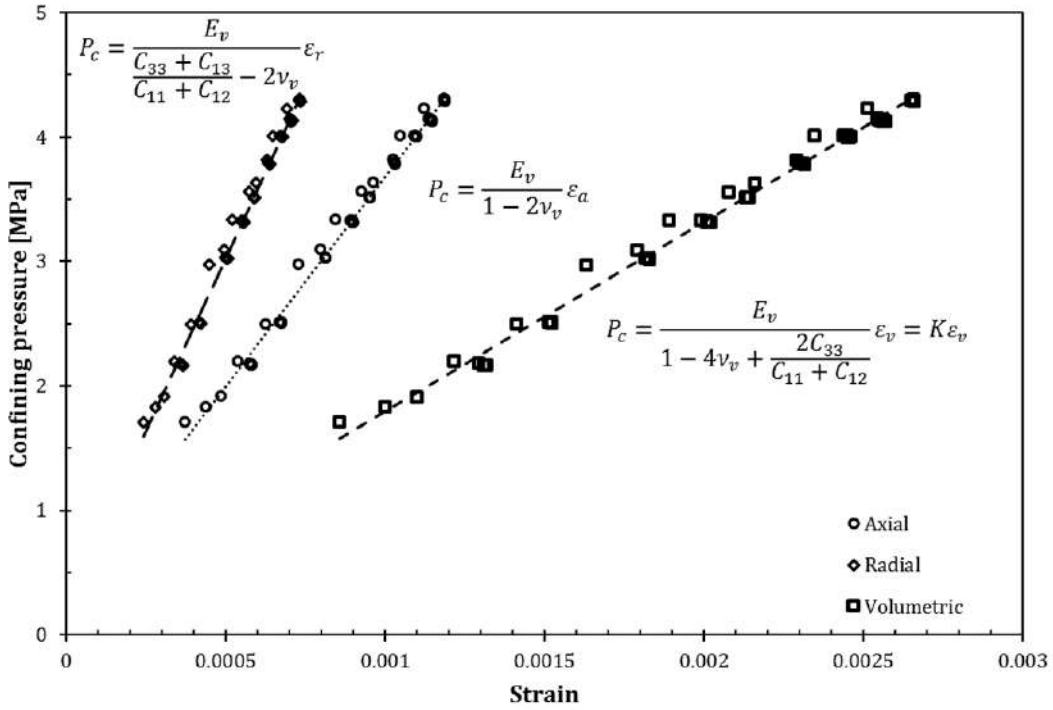

Figure 13: Stress-strain curves in a hydrostatic (non-deviatoric) compression stage using a vertically-oriented VTI sample. Mathematical expressions are presented for the linear parts of the axial, radial and volumetric strain curves. The shown example originates from 431.5 m depth in the Zoharim well.

Using Equations (42), (43) and (48), the parameters E_v, ν_v and K from a single triaxial test can be used to compute C_{33}, C_{13} and $C_{11}+C_{12}$ as follows:

$$C_{13} = \frac{2KE_v}{\frac{E_v - K}{\nu_v} + 4K(1-\nu_v)}, \tag{49}$$

$$C_{33} = E_v + 2\nu_v C_{13}\,, \tag{50}$$

$$C_{11} + C_{12} = \frac{C_{13}}{\nu_v}\,. \tag{51}$$

In a triaxial test each compression stage provides two independent curves: p versus ε_v and ε_r versus ε_a from the hydrostatic stage, and $\Delta\sigma_a$ versus ε_r and $\Delta\sigma_a$ versus ε_a from the deviatoric stage. Consequently, there are four equations that can be used to solve the four unknown stiffness constants activated in these compression tests: C_{11}, C_{12}, C_{13} and C_{33}. Unfortunately, C_{11} and C_{12} cannot be separated in this system of equations, and only their sum can be computed when

vertically-oriented specimens are tested. However, the fourth equation can be used to confirm that both the hydrostatic stage and the deviatoric stage are within the same elastic range of the rock. This check is the validation that the elastic moduli derived from the compression tests are truly representative of the material. It is done by means of the ratio between radial strain and axial strain during the hydrostatic stage (Figure 14), defined here as the "hydrostatic strain ratio", Ω:

$$\Omega = \left(\frac{\varepsilon_r}{\varepsilon_a}\right)_{hydrostatic} = \frac{\frac{pC_{33} - pC_{13}}{C_{33}(C_{11} + C_{12}) - 2C_{13}^{\ 2}}}{\frac{p(C_{11} + C_{12}) - 2pC_{13}}{C_{33}(C_{11} + C_{12}) - 2C_{13}^{\ 2}}} = \frac{C_{33} - C_{13}}{C_{11} + C_{12} - 2C_{13}} \ . \qquad (52)$$

Hence:

$$C_{11} + C_{12} = \frac{C_{33} - C_{13}}{\Omega} + 2C_{13} \ . \qquad (53)$$

Equations (51) and (53) must lead to the same result to ensure that the constants are derived correctly. From Equation (52) it is seen that the hydrostatic strain ratio must be positive, and for isotropic rocks should equal one (Figure 14). In typical VTI rocks Ω should be lower than one, and Ω can be used to scale anisotropy. Equation (52) can be modified to:

$$\Omega = \frac{C_{33} + C_{13} - 2C_{13}}{C_{11} + C_{12} - 2C_{13}} . \qquad (54)$$

It is inferred therefore that in a typical VTI source rock $C_{33} + C_{13} \leq C_{11} + C_{12}$.

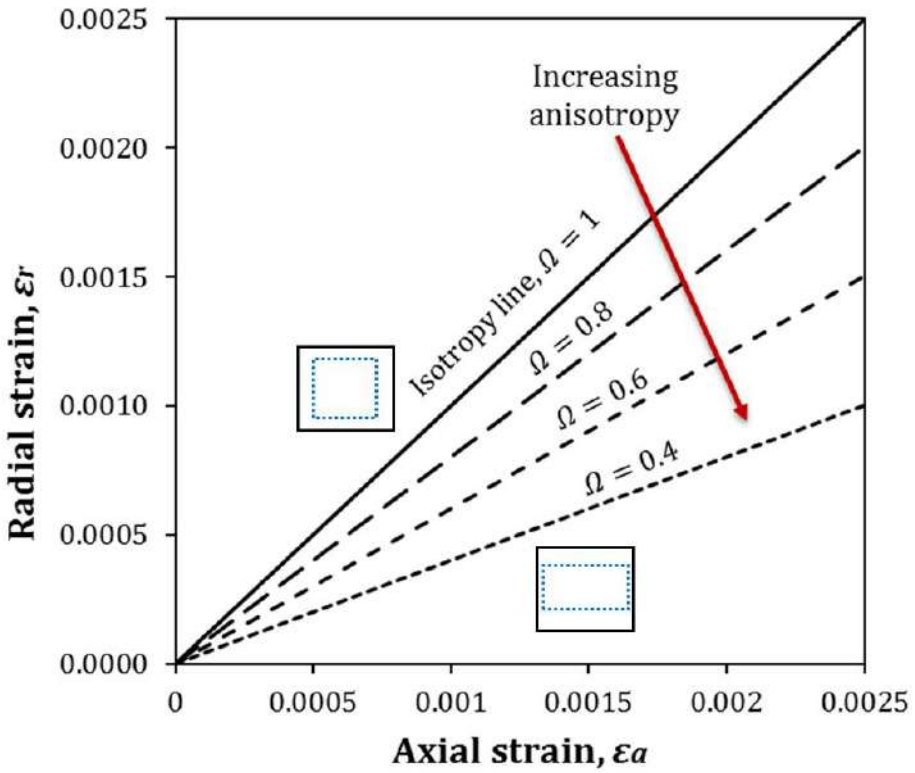

Figure 14: Graphical description of the "hydrostatic strain ratio": schematic radial strain - axial strain curves with a slope of 'Ω', that is the hydrostatic strain ratio. The value of Ω decreases from one (isotropic rock, squared profile turns into a smaller square) with increasing anisotropy of a typical VTI rock (squared profile turns into a flattened rectangle).

Although C_{11} and C_{12} cannot be isolated, some constraints for their minimum and maximum values may be defined. Just as the values of $C_{11} + C_{12}$ and C_{33} were derived from Equations (50) and (51), difference between them can be calculated as well:

$$C_{11} + C_{12} - C_{33} = \Delta C_{11-33} + C_{12} \ , \tag{55}$$

where ΔC_{11-33} equals the difference between C_{11} and C_{33}. In a typical VTI material negative Thomsen's ε values are very uncommon (e.g. Vernik and Liu 1997; Zhao *et al.* 2017), thus $\Delta C_{11-33} \geq 0$. In addition, C_{12} must be positive. Those two physical constraints, together with the experimentally derived $C_{11} + C_{12}$ and C_{33}, enable definition of the minimum and maximum possible values of C_{11}, C_{12}, and consequently C_{66} (refer to Equations (1) and (2), and their explanations). The value of C_{11} cannot exceed $C_{11} + C_{12}$ or go below C_{33}; the value of C_{12} cannot go below zero; minimum C_{11} (i.e. C_{33}) would enforce maximum C_{12}, thus can be expressed by $C_{11} + C_{12} - C_{33}$. Given below, a summary of the constrained the ranges of C_{11} and C_{12}:

$$C_{12,max} = C_{11} + C_{12} - C_{33}\,, \tag{56a}$$

$$C_{12,min} = 0\,, \tag{56b}$$

$$C_{11,max} = C_{11} + C_{12}\,, \tag{57a}$$

$$C_{11,min} = C_{33}\,. \tag{57b}$$

Moreover, since $C_{66} = \frac{C_{11}-C_{12}}{2}$, then:

$$C_{66,max} = \frac{C_{11,max} - C_{12,min}}{2}\,, \tag{58a}$$

$$C_{66,min} = \max\left\{\frac{C_{11,min} - C_{12,max}}{2}, 0\right\}. \tag{58b}$$

The set of theoretical solutions described in this section is summarized in the procedure shown in Figure 15. It shows the workflow of hydrostatic-deviatoric combination for transversely isotropic elastic stiffnesses (HDC-TIES). The HDC-TIES method is designed for results from a single triaxial compression experiment, conducted on a vertically-oriented sample. Note that the HDC-TIES procedure may be used not only where core material is limited, but also where data require repeated analysis due to misinterpretation or where multiple core samples yield inconsistent results.

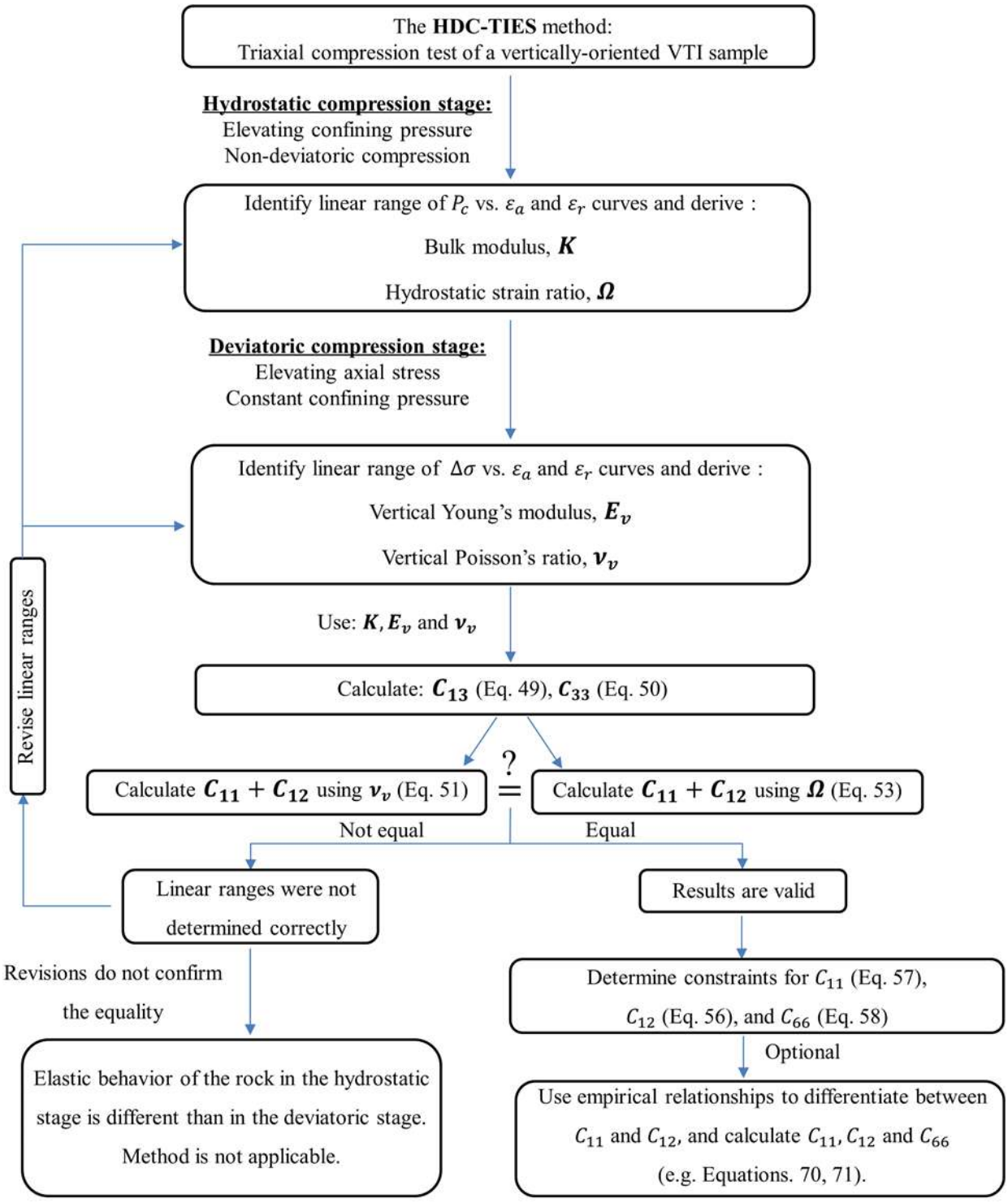

Figure 15: The HDC-TIES method: a flow diagram showing the application of the method, using results from a single triaxial compression experiment, performed on vertically-oriented VTI sample.

2.3 Petrophysical properties

In this section, results of porosity, solids density and permeability measurements are reported, together with the corresponding organic contents. The petrophysical results were obtained from Coreval30 measurements on oven-dry core plugs, and TOC data were collected for each plug separately using LECO SC632. By considering the bitumen as a pore-filling liquid, the true porosity (ϕ_t) is the sum of the measured porosity and the bitumen fraction ($\phi_t = \phi_{meas.} + f_{bit}$). However, the porosities and solids densities measured on the immature core material are representative of the true porosity and solids density, as the bitumen fraction is only 6% of the organic material (not exceeding 1% of bulk volume).

Core porosity measurements in the Zoharim section show that porosity decreases with depth, due to the effects of compaction and cementation. Porosity decreases consistently from ~45% at the top of the Ghareb-Mishash complex to ~23% at the bottom (Figure 16). The rate of porosity reduction with depth exhibits two different trends: 3%ϕ /100 m in the Ghareb Formation, and 10%ϕ/100 m in the Mishash Formation (note that here the percentage is the amount of porosity loss and not a relative percentile decrease). Similar rates of porosity decrease with depth are observed in the Aderet well (data from Bisnovat *et al.* 2015), which is 7 km from the Zoharim well (Figure 6), where the rates are -2%ϕ /100 m in the Ghareb Formation and -7%ϕ /100 m in the Mishash Formation. The top of the Aderet sequence is shallower than Zoharim's by ~ 65 meters, and the Ghareb-Mishash interface by ~ 25 meters. The rate of porosity decrease of the Ghareb Formation is very similar to the rate observed in the organic-lean Niobrara chalk (Lockridge and Pollastro 1988). From Figure 17 it is clear that the porosity and TOC are not correlated, thus the porosity is independent of the organic content. This means that kerogen is matrix component and not a pore infill material. It is further concluded that kerogen content has only a minor influence on the rate of compaction. Note that porosity decrease curves (i.e. compaction curves) are usually assumed to follow an exponential trend. Such a compaction curve will be proposed in Section 4.2.5, by adding data from well-logs and from other basins.

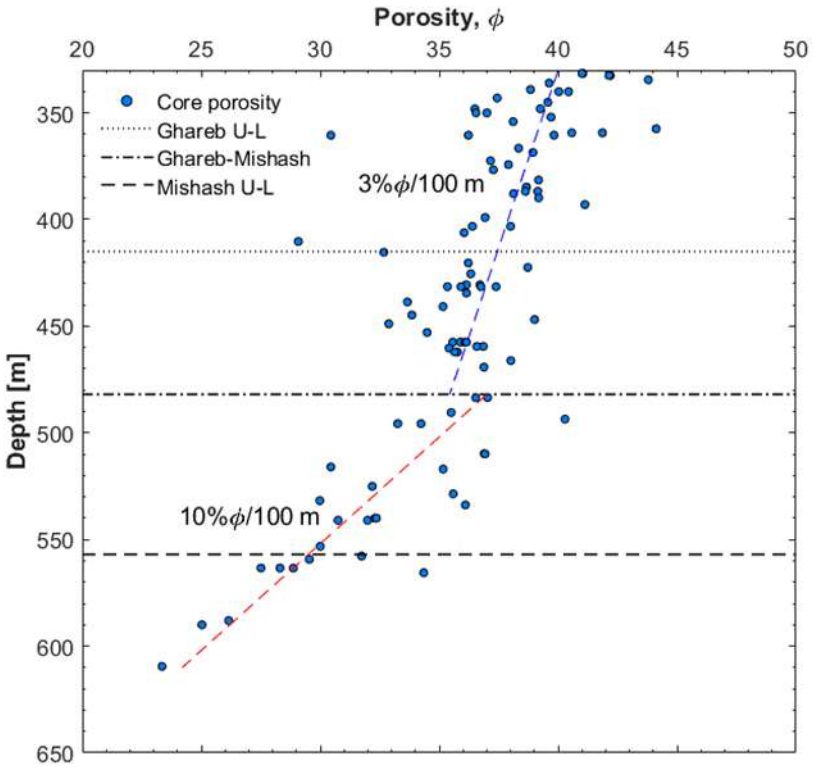

Figure 16: Depth profile of porosity in the Zoharim section. Linear curves mark the decrease rate of porosity with depth. Transitions between the four sub-units are shown, where the letters 'U' and 'L' denote upper and lower parts of each formation.

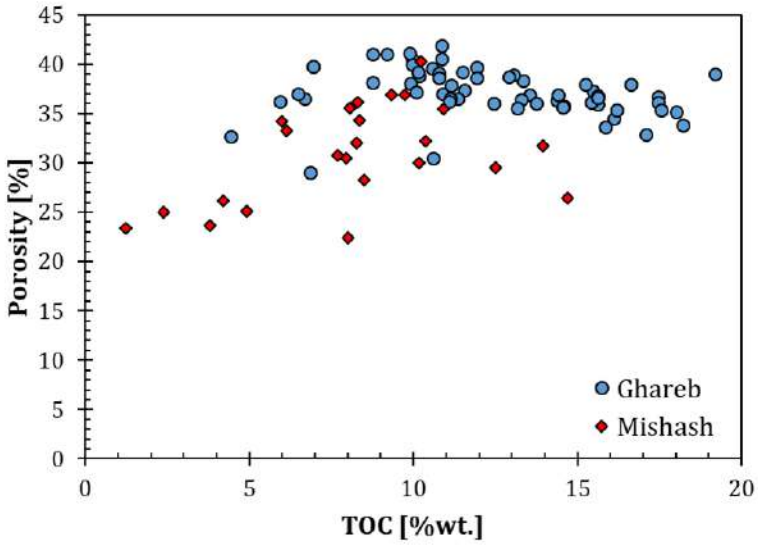

Figure 17: Cross-plot of porosity versus TOC. No dependence between the two variables is observed, neither in the Ghareb nor in the Mishash formations.

Solids density depends almost exclusively on the changes in TOC as predicted by Equation (17) (Figure 18). By plotting the solids density versus TOC, the best-fit coefficients a_1 and a_2 are estimated using root mean squared (RMS) analysis. The results of this analysis show that minerals density averages about 2.74 g/cc, which is approximately the density of calcite. The kerogen density is found to be 1.43 g/cc, which is a little higher than other Type II kerogens, presumably due to high sulfur concentration. Analysis of Aderet cores using data measured in this study and by Bisnovat (2013), yields similar kerogen density of 1.37 g/cc. The error on ρ_o is at the order of 0.06 g/cc, due to 5% uncertainty in C_{pr}. Including the accuracy of the TOC measurements (~1% relative standard deviation), the resultant error on f_o is estimated to be 5.5%. As mentioned above, this analysis forms the basis for the next steps in the study because the volumetric fraction of organic matter is essential. In addition, these results may be used for porosity determination from datasets that include TOC and density logs. For example, when TOC is measured using cuttings or continuous coring, and well-logs include the density tool, a combination between them enables the porosity calculation:

$$\phi = (\rho_s - \rho_b)/(\rho_s - \rho_f)\,. \tag{59}$$

Examples for this combination are provided in Chapter 4.

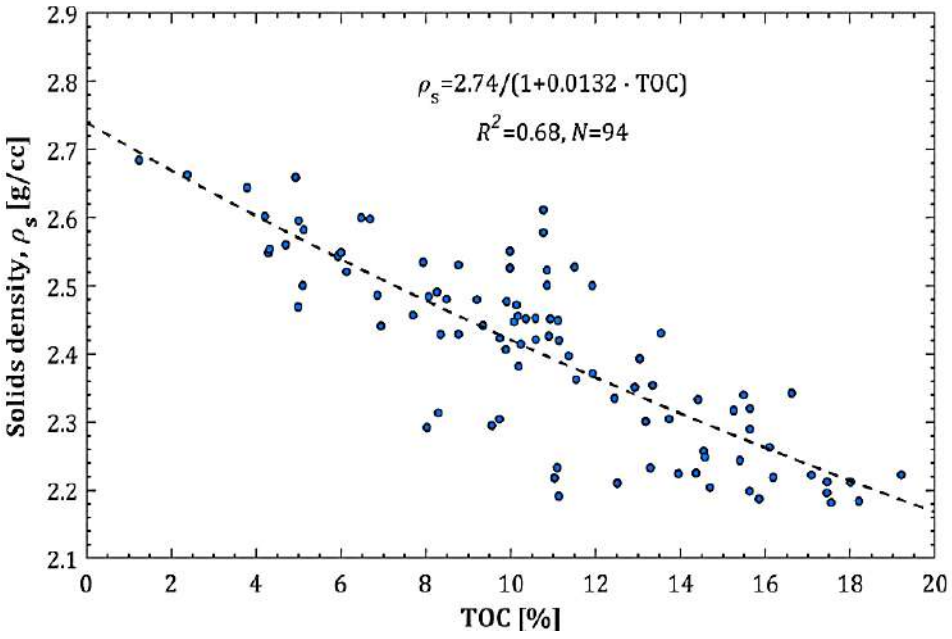

Figure 18: Solids density plotted versus TOC. The trendline is fitted based on the relationship in Equation (17).

The Klinkenberg-corrected gas permeability (K_l) measurements reflect the tight, anisotropic nature of the Ghareb-Mishash chalk. The permeability of the rock is within the micro to milli Darcy range. In Figure 19a it is suspected that the permeability increases with organic content, according an apparent positive trend. No clear relationship with porosity is observed (Figure 19b). By fitting a power-law regression, the correlation seems more significant when plotting K_l versus the organic content. As expected, bedding-normal permeability is lower than the bedding-parallel permeability. The permeability anisotropy is enhanced with increasing porosity, while organic-content does not induce a distinct pattern (Figure 20). The Klinkenberg gas slippage factor (b) decreases with both organic-content and porosity (Figure 21). Equations (8) and (9) show that b is inversely related to mean pore radius, thus high b indicates small pore size.

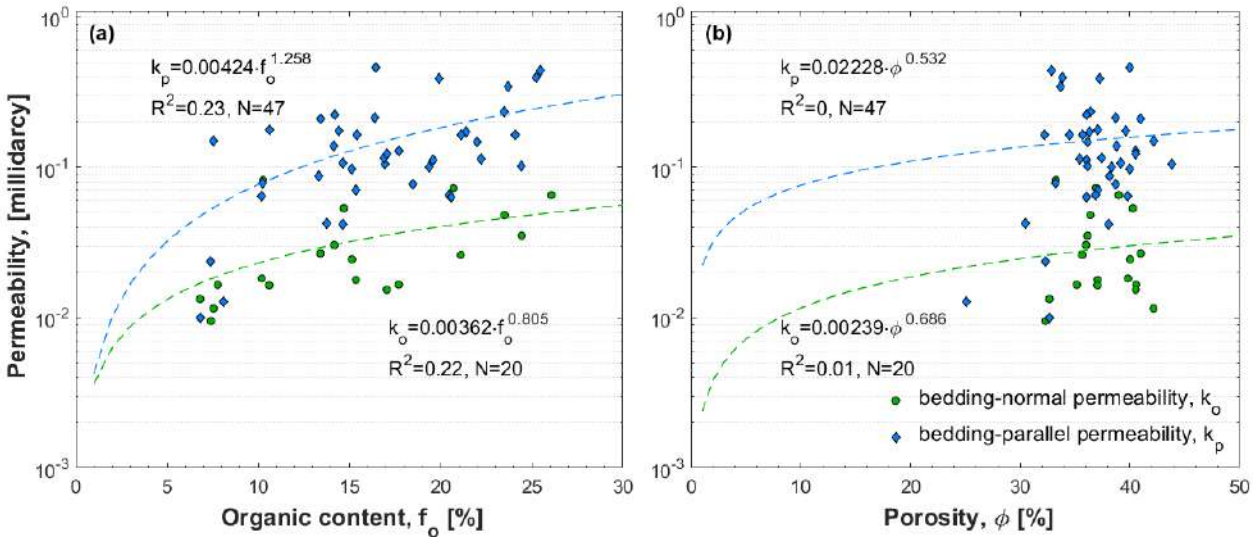

Figure 19: Klinkenberg-corrected permeability of the Ghareb-Mishash chalk, plotted vs. organic content (a) and porosity (b). Power-law trendlines, correlation coefficient (R^2) and number of observations (N) are shown for bedding-normal (circles) and bedding-parallel (diamonds) permeability as a function of organic content and porosity. The permeability, in both directions, appears to correlate with the organic content but unrelated to porosity.

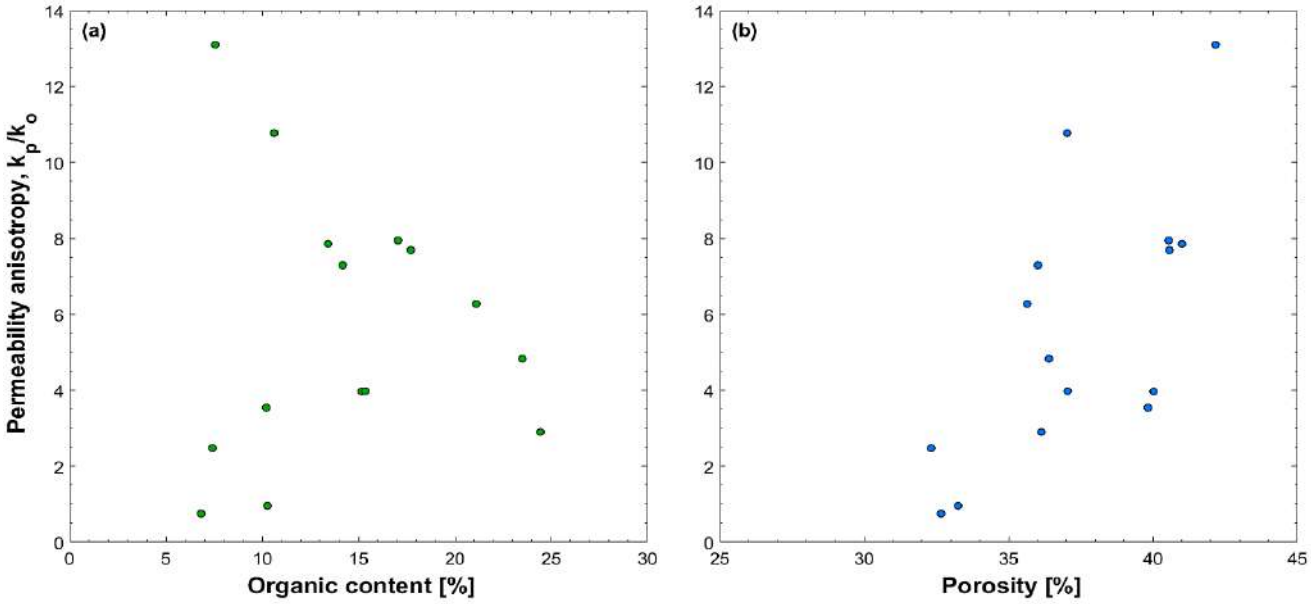

Figure 20: Permeability anisotropy, represented by the ratio of horizontal/vertical permeability (k_p/k_o), plotted versus organic content (left) and porosity (right).

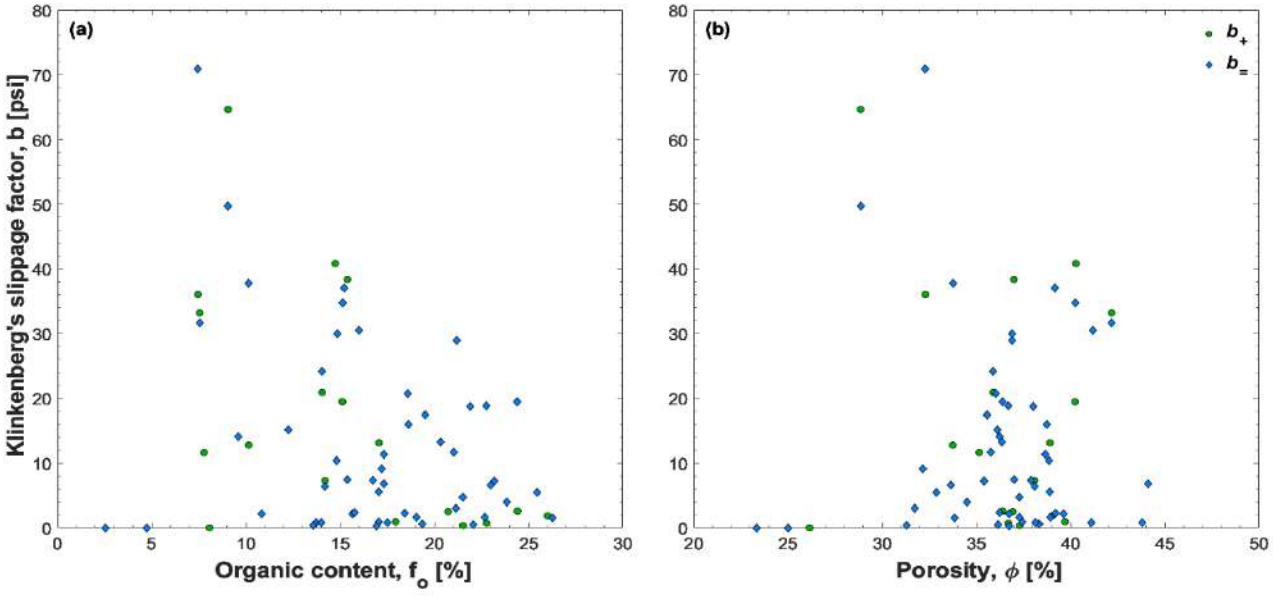

Figure 21: Klinkenberg's gas slippage factor, '*b*', plotted versus organic content (left) and porosity (right). Wherever permeability was measured in the bedding-normal direction, the '*b*' factor is marked by subscript '+', and those measured in the bedding-parallel direction are marked by subscript '='. Note that '*b*' is inversely related to the mean pore size.

To interpret these results, the trends are summarized: increase in porosity is related to increase in permeability, mean pore size and anisotropy; increase in organic-content is also related with increased pore size and permeability. The first conclusion is that permeability increases with pore

size, and this makes perfect sense. The fact that increased organic-content is related with increased pore size may be explained by two mechanisms: 1) organic matter distribution between the grains causes larger inter-particle pores; and 2) organic-hosted porosity is relatively large and effective. The first mechanism seems more reasonable because the organic material is mostly dispersed in the fine-grained matrix, and there are very few accumulations of it (micrographs are presented in Section 2.7). Additionally, although organic-hosted pores are known to exist, their size is rather small and organic-hosted porosity is partially isolated (Löhr *et al.* 2015). Thus, organic-hosted pores do not contribute much to fluid flow. Note that increased pore size does not necessarily mean increased porosity, as no clear relationship is observed between either porosity and organic-content (Figure 17), or between Klinkeberg's b factor and porosity (Figure 21). In contrast to previous presumptions, the permeability anisotropy is enhanced by porosity and is not related to the organic-content. This highlights the difference between organic-rich chalks and shales. The kerogen is integrated within the matrix rather than laminated, and only few organic accumulations exhibit some bedding-parallel elongation. On the other hand, the pore connectivity seems to improve at high porosities, hence the positive correlation between permeability and organic content. This means that the density of flow barriers is lower in the bedding-parallel direction. These interpretations are based on the analysis of the petrophysical measurements, but they align with other observations that will be presented later in this thesis (e.g. electron microscopy, rock stiffness, elastic anisotropy).

2.4 Acoustic velocities and dynamic moduli

2.4.1 Acoustic velocities

The acoustic velocities measurements of the immature material were performed using different kinds of core plugs: 1) vertically-oriented plugs to measure the bedding-normal velocities, V_{p0} and V_{s0}, using brine-saturated core plugs (Table 2); 2) vertically-oriented and horizontally-oriented plugs, to measure the bedding-normal and bedding-parallel velocities, V_{p0}, V_{s0}, V_{p90} and V_{sH90}, using dry core plugs (Table 3). It should be noted that full characterization of acoustic anisotropy was not within the scope of this study. Acoustic anisotropy is characterized by Gordin *et al.* (in prep.), and some of their results will be included in this thesis. In this section, the acoustic velocities are examined versus depth, porosity and TOC. The incorporation of dynamic moduli and rock physics theories will be described in Section 2.4.2.

The ultrasonic P- and S- wave velocities of the brine-saturated chalk show a mild increase with depth within the Ghareb and upper Mishash Formations (Figure 22, Table 2). The acoustic velocities are somewhat lower than those reported for other high porosity chalks (Japsen *et al.* 2004; Olsen 2007; Maldonado, Batzle and Sonnenberg 2011). This is possibly due to the compliant nature of kerogen compared to calcite, as well as the shallow depth of burial. The acoustic velocities in the lower Mishash interval are much higher due to sharp decrease in porosity and TOC. The bedding-normal dry rock velocities are slightly lower than the bedding-normal saturated rock velocities (Figure 22, Table 2 and Table 3). As expected, the bedding-parallel velocities are significantly higher than the bedding-normal velocities (Table 3, dry rock velocities). The issue of acoustic anisotropy will be further addressed in Chapter 3, where the effect of thermal maturation is investigated.

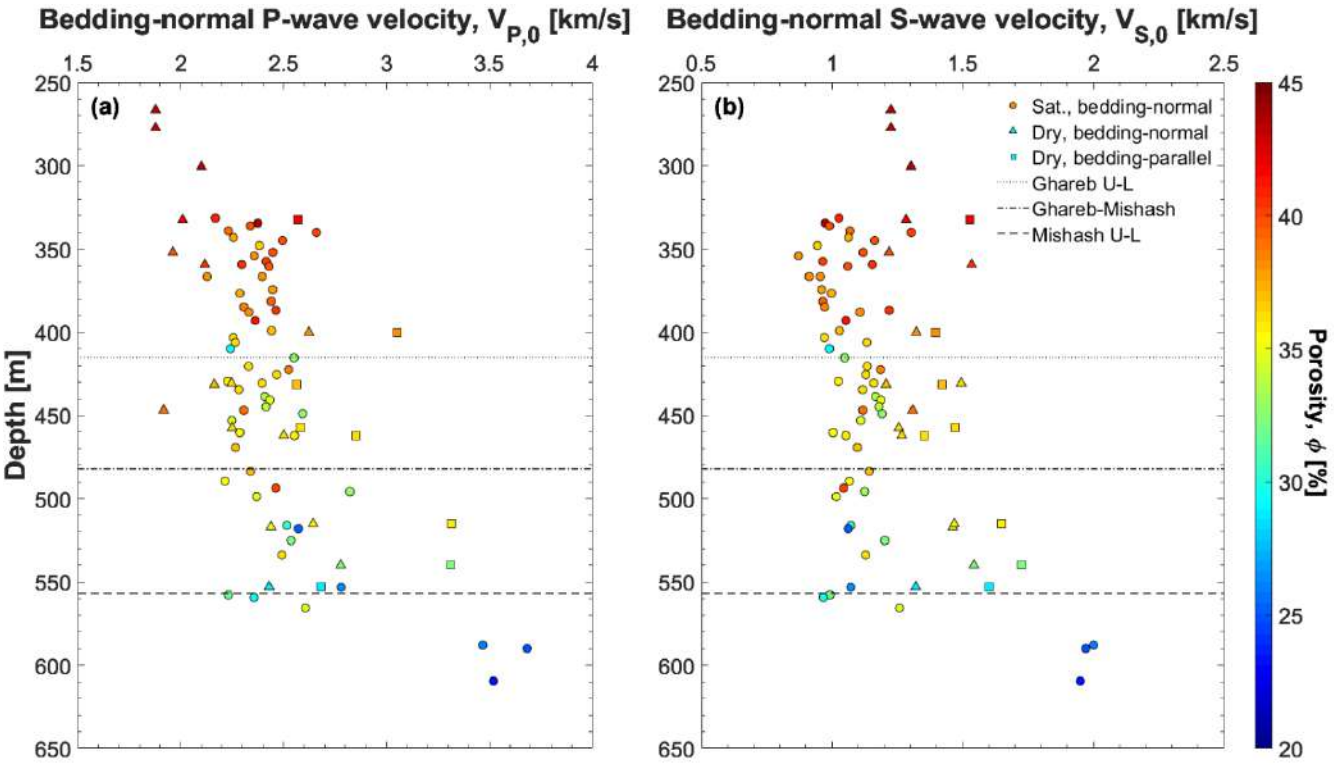

Figure 22: Depth profiles of P-wave velocities (a) and S-wave velocities (b), measured using the AVS. The presented data include bedding-normal velocities of brine-saturated core plugs (circles) and dry core plugs (triangles), and bedding-parallel velocities of dry core plugs (squares). Data points are color-coded to porosity. Transitions between the four sub-units are shown, where the letters 'U' and 'L' denote upper and lower parts of each formation.

Seven experiments were made to examine velocity change of dry rock versus saturated rock, to evaluate the applicability of fluid substitution models. Water saturations, i.e. volumetric percentage of water in the pores, were computed by the bulk density referenced to the dry bulk density ρ_{dry} and water-saturated bulk density ρ_{sat} ($= \rho_{dry} + \phi\rho_w$). Note that full water saturation was confirmed by stability of the pore pressure during the measurements in the AVS350. Figure 23 presents an example of the change in acoustic velocities versus water saturation. This example manifests a small increase of 0.15 km/s (~7%) in P-wave velocity and a strong decrease of 0.33 km/s (~22%) in S-wave velocity with increasing brine saturation. The diverging nature of Vp and Vs with increasing water saturation is expressed by an increase of the Vp/Vs ratio, from 1.5 in dry conditions to 2.1 at saturated conditions. This observation is typical to granular rocks. In dry conditions more friction is mobilized across grain contacts and the pores are filled with a low Vp phase (air). In water-saturated conditions the water reduces the friction between the grains and the pore fluid (water) has higher P-wave velocity. Comparisons of six other pairs of dry and water-saturated rock velocities exhibit the same trend. The results of these comparisons will be presented in the next section on fluid substitution.

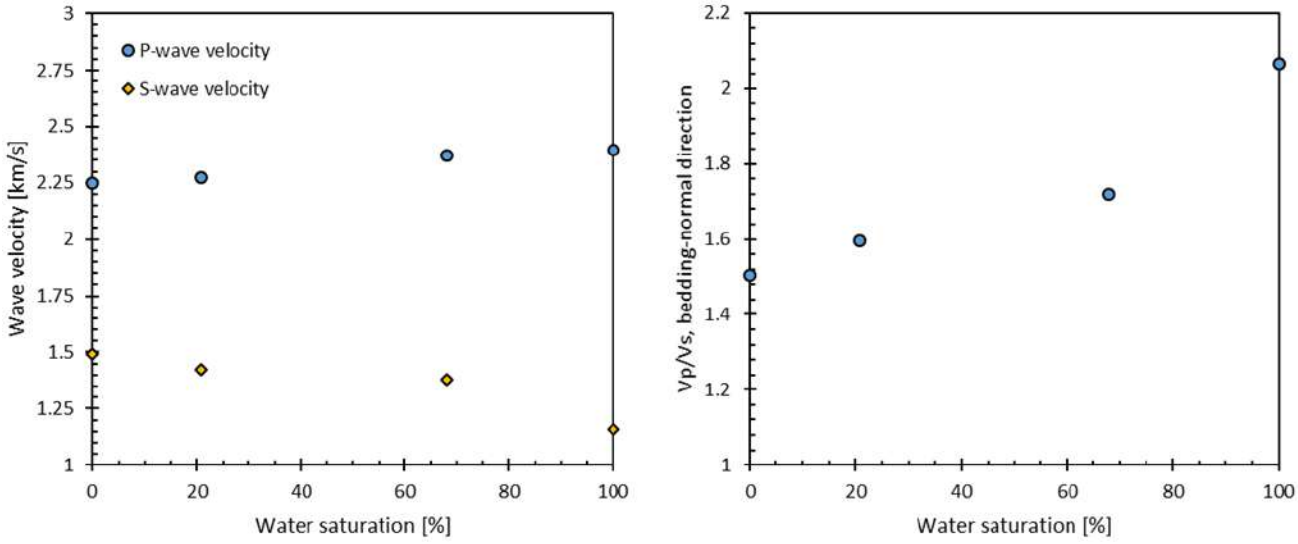

Figure 23: The effect of water saturation on the bedding-normal velocities (left) and Vp/Vs ratio (right) of a sample from the Zoharim well, at 431 m depth.

Table 2: Acoustic P-wave and S-wave velocities measured on brine-saturated plugs in the bedding-normal direction. The error on Vp is 0.5%, and on Vs is 3.5%.

Depth [m]	Porosity [%]	TOC [%wt.]	Dry rock density [g/cc]	Vp [km/s]	Vs [km/s]	Pc [MPa]	Pp [MPa]
331.5	41.0	9.2	1.46	2.17	1.03	6.8	2.9
334.5	43.8	10.34	1.64	2.38	0.97	6.9	2.9
336.1	39.6	9.74	1.48	2.34	0.99	6.9	2.9
339.1	38.8	9.7	1.46	2.23	1.07	7	2.9
340.1	40.0	9.98	1.52	2.66	1.30	7.0	2.9
343.1	37.4	11.45	1.48	2.26	1.06	7.1	2.9
345	39.6	8.58	1.57	2.50	1.16	7.1	3
348	36.5	11.5	1.57	2.38	0.94	7.2	3
352	39.7	11.92	1.50	2.45	1.12	7.2	3.1
354.1	38.1	9.59	1.53	2.36	0.87	7.3	3.1
357.5	40.0	10.03	1.64	2.42	0.97	7.4	3.1
359.4	40.6	10.85	1.63	2.30	1.15	7.4	3.1
360.5	39.8	6.94	1.47	2.43	1.06	7.4	3.1
366.6	38.3	13.4	1.45	2.40	0.96	7.5	3.2
366.6	38.3	13.4	1.45	2.13	0.91	7.5	3.2
374.5	37.9	10.72	1.50	2.45	0.96	7.6	3.3
376.7	37.3	13.57	1.47	2.29	1.00	7.7	3.3
381.5	39.2	9.7	1.51	2.44	0.97	7.6	3.3
384.8	38.7	11.3	1.45	2.31	0.97	7.8	3.4
386.8	40.5	10.77	1.58	2.46	1.22	7.9	3.4
387.9	38.1	8.51	1.57	2.33	1.11	7.9	3.4
393	41.1	10.87	1.42	2.36	1.05	8	3.4
399.1	36.9	13.54	1.53	2.44	1.03	8.1	3.5
403.2	36.4	16.62	1.42	2.26	0.97	8.2	3.6
406.2	36.0	13.17	1.49	2.27	1.13	8.2	3.6
410	29.1	8.29	1.76	2.24	0.99	8.2	3.6
415.4	32.7	4.43	1.54	2.55	1.05	8.4	3.7
420.5	36.2	15.67	1.43	2.33	1.13	8.4	3.7
422.5	38.7	12.83	1.44	2.53	1.19	8.5	3.7
425.5	36.3	15.14	1.42	2.47	1.13	8.5	3.8

Depth [m]	Porosity [%]	TOC [%wt.]	Dry rock density [g/cc]	Vp [km/s]	Vs [km/s]	Pc [MPa]	Pp [MPa]
429.5	36.0	18.02	1.42	2.23	1.02	8.6	3.8
430.6	36.1	17.45	1.40	2.40	1.16	8.6	3.8
434.5	36.1	15.42	1.43	2.28	1.12	8.7	3.9
438.7	33.7	16.34	1.45	2.41	1.17	8.8	3.9
440.8	35.2	16.53	1.44	2.43	1.19	8.8	3.9
444.8	33.9	17.55	1.44	2.42	1.18	8.9	4
446.9	39.0	19.2	1.36	2.31	1.12	8.9	4
448.9	32.9	17.08	1.49	2.59	1.19	8.9	4
453	34.5	16.24	1.49	2.25	1.11	9	4
460.3	35.4	15.5	1.44	2.29	1.00	9.1	4.1
462.1	35.7	14.54	1.45	2.55	1.05	9.2	4.1
469.2	36.9	13.91	1.47	2.27	1.10	9.3	4.2
483.5	37.0	6.48	1.64	2.34	1.14	9.5	4.3
489.5	35.5	10.93	1.58	2.22	1.07	9.7	4.4
493.6	40.3	10.24	1.44	2.46	1.04	9.7	4.4
495.7	33.3	6.13	1.68	2.82	1.12	9.8	4.5
498.7	35.0	8.17	1.56	2.37	1.02	9.8	4.5
516	30.4	7.86	1.76	2.52	1.07	10.2	4.7
518	25.1	4.08	1.99	2.57	1.06	10.2	4.7
525.1	32.2	9.29	1.66	2.54	1.20	10.3	4.8
533.8	36.1	13.92	1.48	2.49	1.13	10.5	4.8
553.2	26.5	13.49	1.63	2.78	1.07	10.9	4.9
557.8	31.7	13.86	1.52	2.23	0.99	11	5
559.3	29.5	13.68	1.56	2.36	0.97	11	5.1
565.6	34.4	7.51	1.59	2.61	1.26	11.1	5.1
588	26.1	4.2	1.92	3.47	2.00	11.6	5.4
590	25.0	2.38	2.00	3.68	1.97	11.6	5.4
609.5	23.4	1.38	2.06	3.52	1.95	12.1	5.6

Table 3: Acoustic P-wave and S-wave velocities measured on dry plugs in the bedding-normal (0) and bedding-parallel directions (90). The error on Vp and Vs is 3.5%.

Depth [m]	Porosity [%]	TOC [%]	Dry density [g/cc]	Confining pressure [MPa]	V_P 0 [km/s]	Vs 0 [km/s]	V_P 90 [km/s]	V_{SH} 90 [km/s]
332.5	42.17	5.16	1.50	6.9	2.01	1.28	2.57	1.53
431.5	37.05	11.08	1.39	8.6	2.16	1.21	2.56	1.42
457.5	36.02	9.65	1.47	9.0	2.25	1.26	2.58	1.47
540	32.33	4.30	1.73	10.6	2.78	1.54	3.31	1.72
517	35.17	4.69	1.66	10.2	2.44	1.46	-	-
553	28.78	11.65	1.67	10.0	2.43	1.32	2.68	1.60

2.4.2 Dynamic moduli and fluid substitution

As noted earlier, the acoustic velocities depend on the dynamic moduli and bulk density of rocks. The majority of the acoustic measurements in this part of the study give the dynamic vertical oedometer modulus 'M_v' (C_{33}) and vertical shear modulus 'μ_v' (C_{55}), in brine-saturated conditions. Analysis of these results is performed in this section.

The petrophysical properties of the rock, namely the porosity and organic content, have a significant impact on the dynamic moduli. These effects are modelled using rock physics theories. The RPM utilized here is based on the Hashin-Shtrikman variational approach (HS, Hashin and Shtrikman 1963), which is applicable to granular materials. Graphical representation of the measurements and the bounds is complex, as there are three dominant phases: minerals, pore fluid, and organic matter. The rock constituents are very different from one another in their elastic stiffness and density. As a result, the HS bounds demonstrated in Figure 10 are no longer smooth and continuous when plotted versus a single property (e.g. porosity, organic content). For example, the HS bounds may exhibit a smooth and continuous shape where organic content is set to a constant value and then the only variable is porosity (Figure 24a, c). However, since both kerogen and porosity affect the elastic moduli it is logical to sum them into a single parameter as follows:

$$\phi_{kf} = \phi + \kappa \cdot f_k \ , \tag{60}$$

where ϕ_{kf} is the kerogen-factored porosity, and κ is the dimensionless kerogen influence scaling factor that scales the effect of kerogen. This sort of summation was defined by Prasad *et al*. (2011)

as "porosity-modified kerogen content", as they examined six different types of organic-rich rocks. Here, this parameter is referred to as "kerogen-factored porosity", because kerogen effects are scaled to those of porosity and not vice-versa. Prasad *et al*. (2011) suggested an influence factor of $\kappa = 0.4$, i.e. the sum of porosity and 40% of the kerogen content. In this analysis, values of 'κ' within the range of $0 < \kappa < 1$ are tested in order to find the most representative 'κ' for the Ghareb-Mishash chalk.

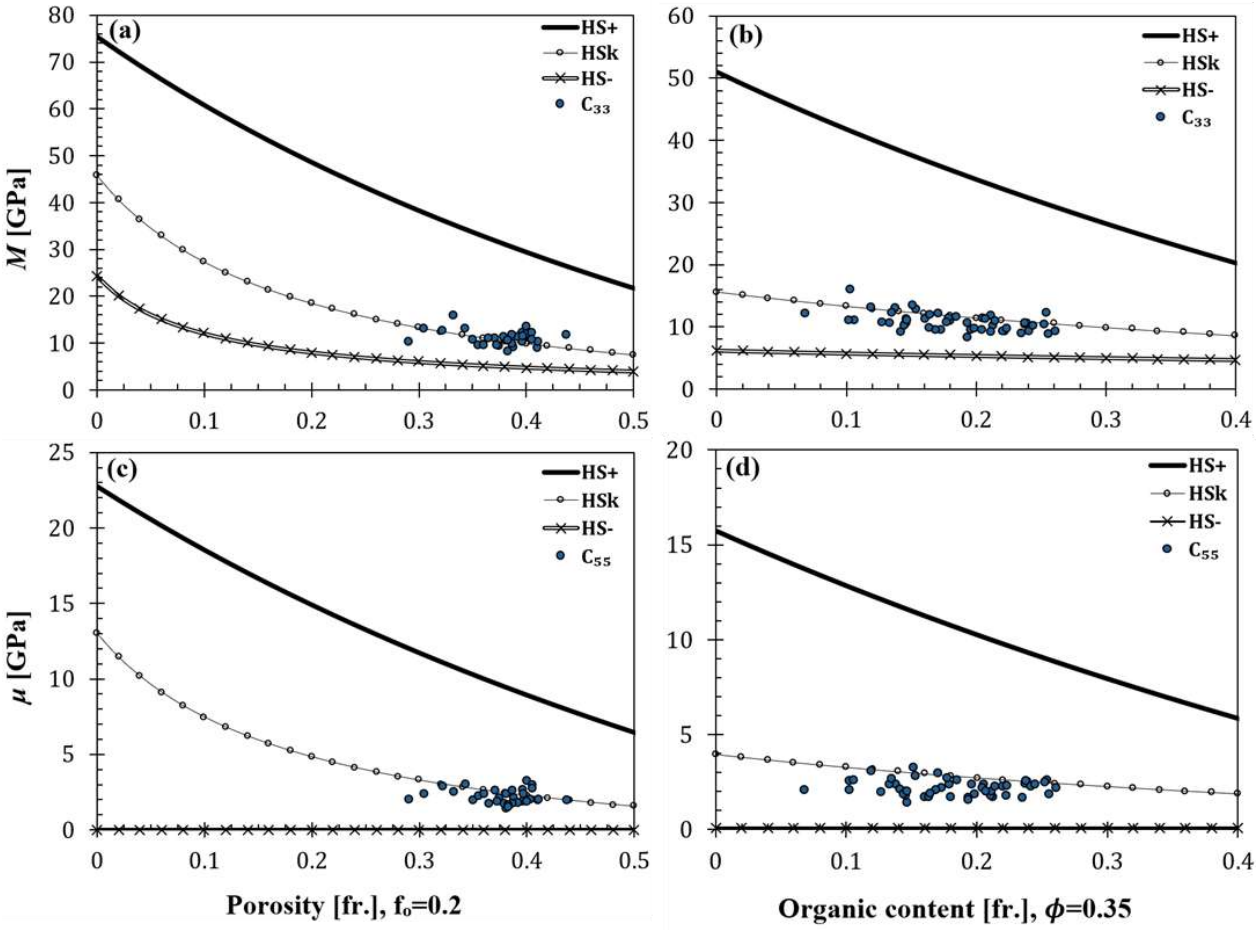

Figure 24: Hashin-Shtrikman models of three extreme scenarios 'HS+', 'HS-', and 'HSk'. Oedometer and shear moduli are in the upper and lower panels (respectively), versus the change in porosity at constant organic content (left) and versus the change in organic content at constant porosity (right). The plotted results are the vertical moduli within organic content range of 10-20% (a, c) and porosity range of 30-40% (b, d).

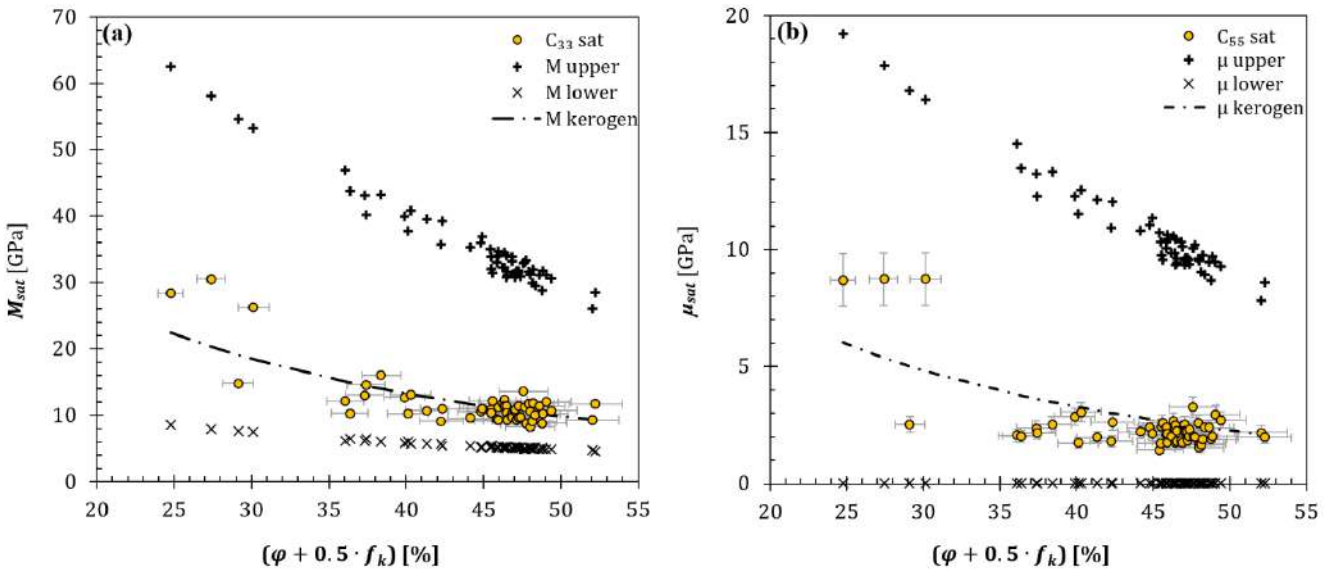

Figure 25: Dynamic elastic moduli in brine-saturated conditions of the Ghareb-Mishash chalk: oedometer modulus (a) and shear modulus (b) plotted versus the kerogen-factored porosity. The upper bound, lower bound and "HS kerogen" curve are the Hashin-Shtrikman models that represent matrix supported by minerals, fluid and kerogen, respectively. These values were calculated for each measured core plug individually. The circles represent measured values of C_{33} and C_{55}.

The vertical dynamic moduli of brine-saturated rock, C_{33} and C_{55}, are given in Figure 25, including the HS bounds and the "HS kerogen" model. Because the data appear to follow the "HS kerogen" model, the kerogen influence factor 'κ' is adjusted to give it a curve-like appearance. The "HS kerogen" obtains a form of a continuous curve using κ =0.5, thus the results in this section are presented versus $\phi_{kf} = \phi + 0.5 \cdot f_k$. The kerogen influence factor represents two important features of the kerogen: 1) kerogen-hosted porosity that might be undetected in the porosity measurements; and 2) kerogen is softer than the minerals by an order of magnitude. The concordance of the experimental data with the "HS kerogen" model suggests that the bedding-normal velocities are explained well by conceptualizing a kerogen-supported matrix. To study this further, results of dry rock velocities normal and parallel to the bedding direction are examined as well. The dry rock data are obtained in two ways: 1) direct measurements on dry core plugs, and 2) estimations of dry rock moduli using brine-saturated data and fluid substitution models.

First, in order to perform fluid substitution correctly, its validity should be verified. To do that, 7 core plugs were measured in dry and saturated conditions. The models used here are the Biot-Gassmann model and Marion's BAM model (Figure 26). As seen, both models yield the same

results for shear modulus, but the oedometer modulus is depicted much better using the BAM model, while Biot-Gassmann's results in significant overestimation of the dry C_{33}. Therefore, fluid substitution in this research is performed using Marion's BAM model. To apply BAM, the relative locations of each measured Vp or Vs between the upper and lower HS bounds is calculated; these are the BAM normalized stiffness factors w_{C33} and w_{C55}. Subsequently, the HS bounds are calculated considering dry rock, and the 'w' values from the previous step are used to estimate the dry rock moduli. Figure 27 presents dry rock data collected using dry core measurements and BAM-estimated moduli using the brine-saturated rock data. As seen, the measured vertical moduli plot near the BAM-calculated values. The horizontal moduli, C_{11} and C_{66}, plot higher than the vertical moduli because typical VTI rocks are stiffer in the bedding-parallel direction.

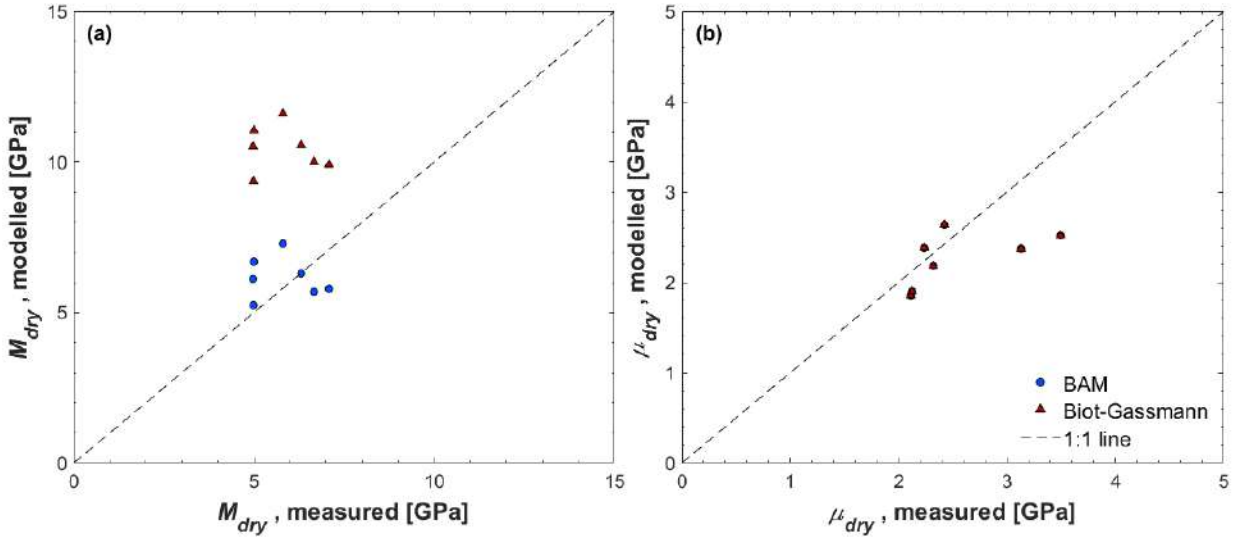

Figure 26: Examination of Marion's BAM (circles) and Biot-Gassmann's (triangles) fluid substitution models: the modelled values are plotted versus the measured oedometer (a) and shear (b) of the dry rock samples.

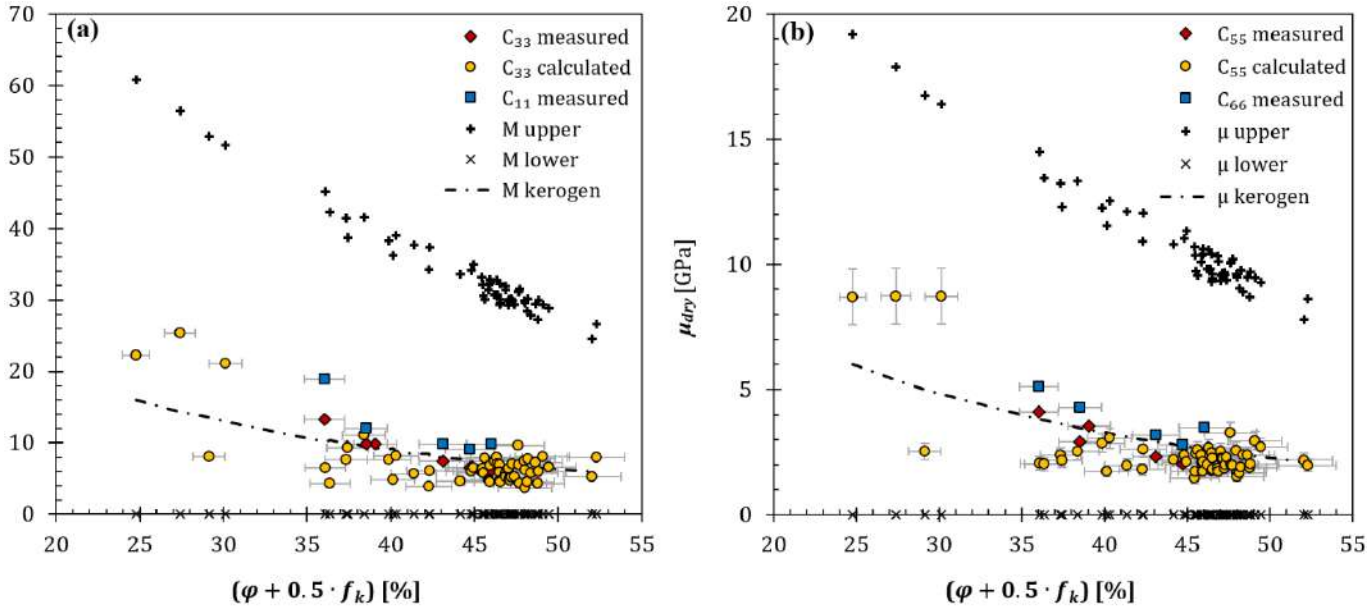

Figure 27: Dynamic elastic moduli in dry conditions of the Ghareb-Mishash chalk: oedometer modulus (a) and shear modulus (b) plotted versus the kerogen-factored porosity. The upper bound, lower bound and "HS kerogen" curve are the Hashin-Shtrikman curves that represent matrix supported by minerals, fluid and kerogen, respectively. These values were calculated for each measured core plug individually. The circles represent calculated values of C_{33} and C_{55} based on the BAM model. The measured dry rock dynamic elastic moduli are also presented: C_{33} and C_{55} from bedding-normal wave velocities (diamonds) and C_{11} and C_{66} from bedding-parallel wave velocities (squares).

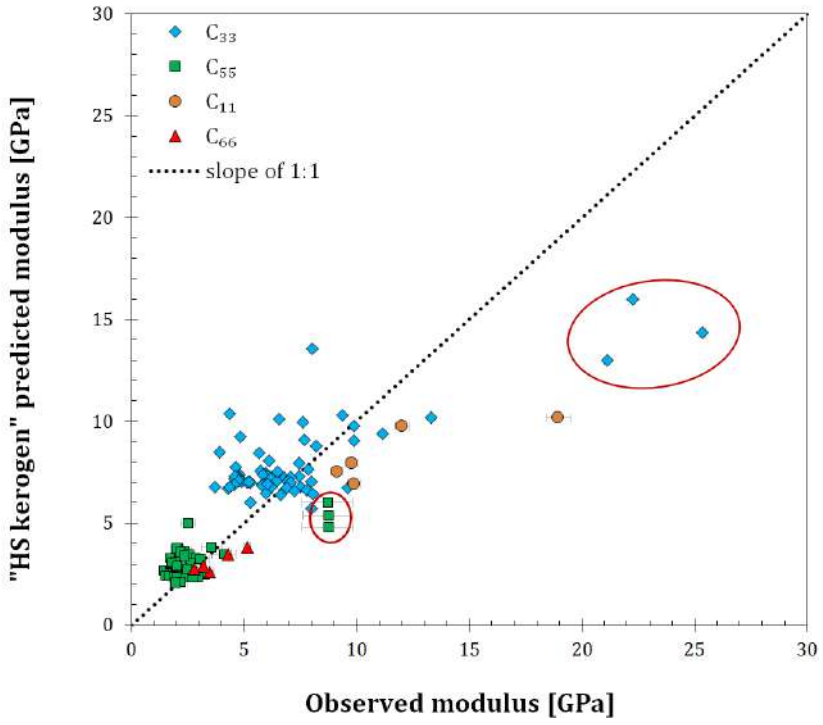

Figure 28: Insights on microstructure from dynamic measurements: The values of dynamic moduli predicted using the "HS kerogen" model plotted against the values observed from measurements and fluid substitution. Marked in red circles, are three samples from the organic-lean zone at the bottom of the depth section. This zone is more compacted and cemented, and consequently manifests higher stiffness than the "HS kerogen" predicted values. Note that the stiffer horizontal moduli C_{11} and C_{66} plot to the right of the vertical moduli C_{33} and C_{55}.

The poroelastic coefficients 'w' and 'β', derived from the BAM and Biot-Gassmann's models, reflect the matrix stiffness of the rock. They depend on the geometrical arrangement of the solid constituents, their intrinsic stiffnesses, and degree of cementation and compaction. The mean BAM stiffness factors are $w_{C33} = 0.2$ and $w_{C55} = 0.22$. Although the Biot-Gassmann model is inapplicable for fluid substitution in the Ghareb-Mishash chalk, examination of β is still worthwhile. The average Biot coefficient in the sequence is $\beta \sim 0.85$. The poroelastic coefficients derived from both models indicate that the Ghareb-Mishash chalk is an appreciably soft rock, whereas the measured values are closer to the lower HS bound (hence the w is low). The average Biot coefficient obtained here also indicates the chalk softness, being higher with respect to other rock types, that exhibit $\beta < 0.8$ (e.g. Table 4 in Detournay and Cheng 1993). The variations of these coefficients with depth reveal changes in matrix stiffness. It is typically assumed that during initial compaction porosity decreases, but β remains close to unity, as it only rearranges the grains

relative to each other (Alam *et al.* 2010). Matrix-stiffening is assumed to be caused by increased compaction, contact cementation and recrystallization. To explore these expected trends, the poroelastic coefficients of each plug are profiled versus depth in the Zoharim section. Unlike the acoustic velocities and the porosity, changes of the poroelastic coefficients with depth are not apparent within the Ghareb and upper part of the Mishash Formations (Figure 29). Although organic content is assumed to affect matrix stiffness, it is hard to distinguish its effect from the other properties. The BAM normalized stiffness factors w_{C33} and w_{C55} values correlate well with each other, and range between 0.1 and 0.3 (Figure 30a). Exceptionally high values of ~0.4 originate from the deep zone of the Mishash Formation. In Figure 30b it seems that kerogen affects the normalized stiffness factors to some extent, although the scatter is considerably large and without a clear trend. Possible reasons for this scatter are the natural heterogeneity of the rock in the Zoharim section, namely in mineralogy, geometrical arrangement of the particles, their sizes and shapes, as well as the degree of cementation and compaction. Figure 30 also includes normalized stiffness factors of the horizontal moduli of the rock, w_{C11} and w_{C66}. The horizontal moduli are stiffer than the vertical ones, hence they obtain higher 'w'. Organic content does not seem to cause any influence on them.

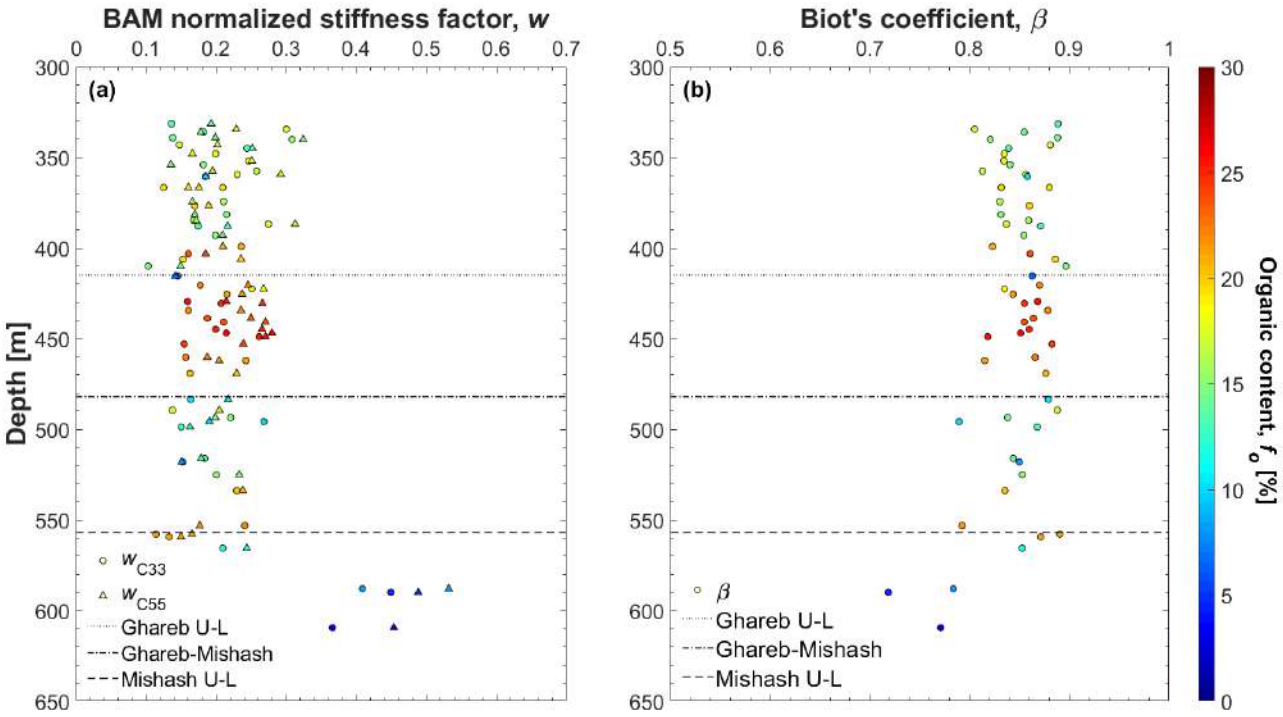

Figure 29: Depth profiles of the poroelastic coefficients of matrix stiffness, derived from the fluid substitution models: BAM normalized stiffness factor (a) and Biot's coefficient (b). The BAM normalized stiffness factors are computed separately for vertical oedometer modulus (circles) and shear modulus (triangles). Transitions between the four sub-units are shown, where the letters 'U' and 'L' denote upper and lower parts of each formation.

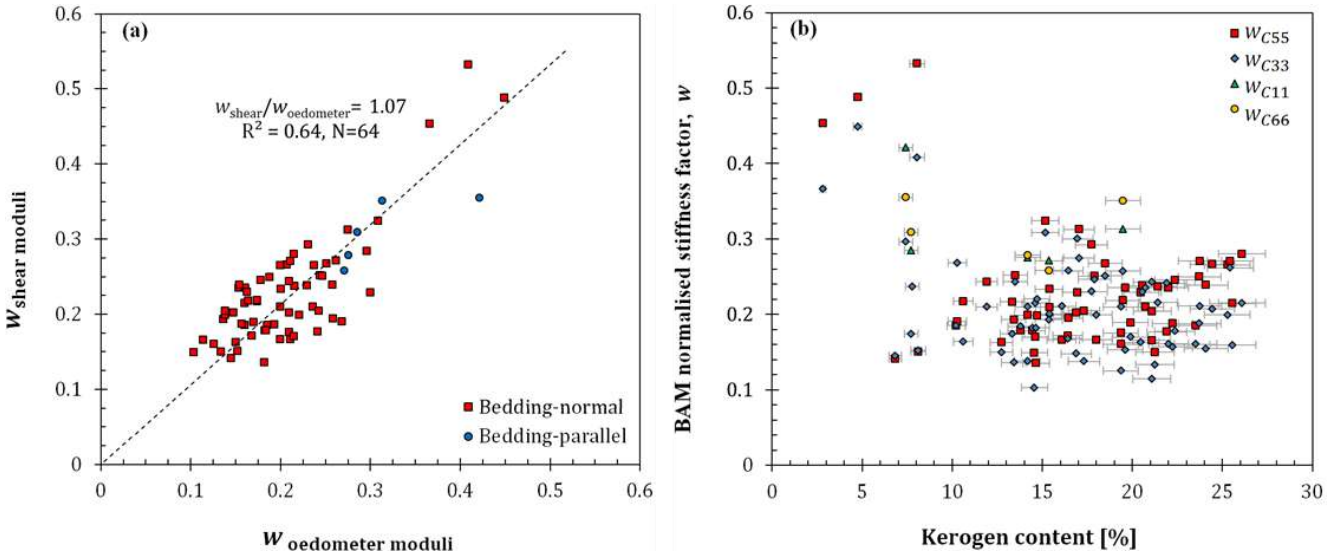

Figure 30: Normalized stiffness factors of the organic-rich chalk: a) The 'w' of the oedometer and shear moduli are comparable in both bedding-normal and bedding-parallel directions. b) Scatter plots of the normalised stiffness factors $w_{C11}, w_{C33}, w_{C55}$ and w_{C66} versus kerogen volume fraction. The 'w' of the horizontal moduli C_{11} and C_{66} plot higher than those of the vertical moduli C_{33} and C_{55}.

2.5 Static moduli (kerogen-factored porosity)

The results of hydrostatic and triaxial compression experiments are summarized in Table 4. The values derived using the HDC-TIES method, C_{13}, C_{33} and $C_{11} + C_{12}$, and the bounds of C_{11}, C_{12} and C_{66}, are given in Table 5. The results include tests on core samples from the Zoharim well, and repeated analyses of compression tests performed by Bisnovat *et al.* (2015) using samples from the Aderet well. The reported errors are the normalized root mean square (RMS) of the data points with respect to the linear curves, from which the static moduli in Table 4 are derived. In some of the triaxial tests linear segments were less detectable, and a wider range of moduli is reported (e.g. 609.5 m depth in Zoharim well). Consequently, the propagated errors in Table 5 are significantly larger. Note that the error induced by stress and strain measurements is negligibly small, and contained in the RMS error analysis. The investigation here focuses on the dependence of each of the elastic moduli on the soft phases: porosity and kerogen. Once again, the kerogen-factored porosity is calculated by inserting values of 'κ' within the range of $0 < \kappa < 1$ and fitting different types of regressions (linear, logarithmic, exponential and polynomial). The highest coefficients of determination (R^2) are gotten using an exponential regression and $\kappa \sim 0.5$, just as the dynamic moduli. Note that the results from the Zoharim and Aderet wells are similar, so there is no distinction between the two wells in this analysis.

Vertical Young's modulus and vertical Poisson's ratio are obtained from triaxial and uniaxial compression tests. Bulk modulus and hydrostatic strain ratio are obtained from triaxial and hydrostatic compression tests. The vertical Young's modulus shows a strong dependence on both porosity and kerogen content (Figure 31a-b). It is seen that when the kerogen-factored porosity is used, the scattered data points exhibit better convergence (Figure 31c). The bulk modulus reveals a similar pattern (Figure 31d-f). The vertical Poisson's ratio does not show any clear trend versus porosity or kerogen, but it is seen that at $\phi < 35\%$ the range is 0.15-0.24 and at a higher porosity it can exceed 0.3 (Figure 32a-b). The hydrostatic strain ratio, which reveals the anisotropy magnitude, should depend on the geometrical features of the solid constituents and the pores. However, it does not exhibit a clear regression on either porosity or kerogen content (Figure 32c-d). The behavior of the static vertical Poisson's ratio and the hydrostatic strain ratio is further investigated in the discussion section of this chapter.

Table 4: Summary of elastic constants derived from hydrostatic, triaxial and uniaxial tests on cores from Zoharim and Aderet wells.

Well	Depth [m]	Test	ϕ [%]	f_k [%]	ρ_{dry} [g/cc]	E_v [GPa]	ν_v	K [GPa]	Ω
Zoharim	332.5	Hydrostatic	42.17	7.7	1.50			1.60 ± 0.15	0.49 ± 0.05
Zoharim	469.2	Hydrostatic	36.88	21.2	1.47			1.37 ± 0.04	0.40 ± 0.02
Zoharim	339.1	Triaxial	38.84	14.7	1.43	1.73 ± 0.01	0.18 ± 0.00	1.16 ± 0.02	0.57 ± 0.05
Zoharim	360.5	Triaxial	38.00	14.3	1.47	1.66 ± 0.01	0.18 ± 0.00	1.27 ± 0.03	0.45 ± 0.04
Zoharim	431.5	Triaxial	35.92	24.5	1.38	2.21 ± 0.03	0.20 ± 0.01	1.52 ± 0.15	0.62 ± 0.01
Zoharim	457.5	Triaxial	35.57	21.1	1.45	2.57 ± 0.01	0.22 ± 0.02	1.63 ± 0.03	0.71 ± 0.00
Zoharim	517	Triaxial	38.70	15.0	1.84	2.34 ± 0.04	0.29 ± 0.01	1.50 ± 0.33	0.40 ± 0.08
Zoharim	540	Triaxial	35.65	11.3	1.68	3.68 ± 0.02	0.19 ± 0.01	2.11 ± 0.40	0.58 ± 0.06
Zoharim	559.3	Triaxial	29.54	21.1	1.54	2.39 ± 0.01	0.15 ± 0.00	1.87 ± 0.04	0.47 ± 0.01
Zoharim	588	Triaxial	26.15	8.1	1.92	5.36 ± 0.05	0.17 ± 0.01	3.80 ± 0.11	0.72 ± 0.01
Zoharim	609.5	Triaxial	23.35	2.6	2.03	8.68 ± 0.26	0.24 ± 0.03	4.40 ± 0.29	0.98 ± 0.08
Aderet	274.1	Hydrostatic	39.50	14.2	1.46			1.38 ± 0.09	0.57 ± 0.03
Aderet	340.2	Hydrostatic	38.00	12.7	1.55			3.20 ± 0.32	0.32 ± 0.03
Aderet	336.2	Triaxial	39.00	14.7	1.51	1.69 ± 0.05	0.16 ± 0.01	1.31 ± 0.06	0.50 ± 0.01
Aderet	336.2	Triaxial	39.00	13.7	1.49	1.78 ± 0.27	0.29 ± 0.04	1.20 ± 0.11	0.53 ± 0.01
Aderet	341.2	Triaxial	42.78	15.9	1.43	1.46 ± 0.02	0.16 ± 0.02		
Aderet	342.3	Triaxial	40.50	14.3	1.41	3.75 ± 0.56	0.37 ± 0.06		
Aderet	346.3	Triaxial	40.81	17.4	1.42	1.49 ± 0.01	0.30 ± 0.00	1.58 ± 0.02	0.64 ± 0.01
Aderet	352	Triaxial	36.00	19.6	1.45	2.00 ± 0.20	0.18 ± 0.03	1.44 ± 0.06	0.71 ± 0.01
Aderet	599.6	Triaxial	25.03	4.4	2.00	7.74 ± 0.39	0.17 ± 0.01		
Aderet	291.9	Uniaxial	40.47	19.3	1.37	1.11 ± 0.06	0.20 ± 0.01		
Aderet	341.2	Uniaxial	40.82	12.4	1.45	2.76 ± 0.14	0.32 ± 0.02		
Aderet	358.4	Uniaxial	40.63	16.3	1.40	1.63 ± 0.08	0.30 ± 0.01		
Aderet	376.5	Uniaxial	39.33	24.9	1.32	1.98 ± 0.10	0.21 ± 0.01		
Aderet	417.5	Uniaxial	38.56	25.6	1.33	1.90 ± 0.10	0.26 ± 0.01		
Aderet	449.5	Uniaxial	38.58	19.6	1.41	2.78 ± 0.14	0.25 ± 0.01		
Aderet	572.2	Uniaxial	28.82	6.9	1.86	8.36 ± 0.42	0.23 ± 0.01		

Table 5: Values of C_{13}, C_{33}, and $C_{11} + C_{12}$, and constraints on C_{11}, C_{12} and C_{66}, as derived using the HDC-TIES method. The errors are propagated from the values in Table 4.

Depth [m]	C_{13} [GPa]	C_{33} [GPa]	$C_{11}+C_{12}$ [GPa]	C_{11} [GPa]		C_{12} [GPa]	C_{66} [GPa]	
				Min.	Max.	Max.	Min.	Max.
339.1	0.58 ± 0.03	1.94 ± 0.12	3.18 ± 0.17	1.8	3.4	1.5	0.9	1.7
360.5	0.67 ± 0.05	1.9 ± 0.14	3.72 ± 0.25	1.8	4	2.2	0.9	2
431.5	0.8 ± 0.21	2.53 ± 0.72	4.06 ± 1.11	1.8	5.2	3.4	0.9	2.6
457.5	0.89 ± 0.2	2.96 ± 0.76	4.09 ± 1.03	2.2	5.1	2.9	1.1	2.6
517	1.24 ± 0.64	3.07 ± 1.64	4.2 ± 2.17	1.4	6.4	4.9	0.7	3.2
540	1.22 ± 0.53	4.15 ± 1.85	6.41 ± 2.82	2.3	9.2	6.9	1.1	4.6
559.3	0.91 ± 0.06	2.67 ± 0.19	6.03 ± 0.39	2.5	6.4	3.9	1.2	3.2
588	1.86 ± 0.29	5.99 ± 1.06	11.01 ± 1.84	4.9	12.8	7.9	2.5	6.4
609.5	2.44 ± 0.8	9.84 ± 3.81	12.4 ± 4.42	6	16.8	10.8	3	8.4
336.2	0.65 ± 0.13	1.89 ± 0.45	4.11 ± 0.85	1.4	5	3.5	0.7	2.5
336.2	0.79 ± 0.38	2.24 ± 1.48	2.74 ± 1.4	0.8	4.1	3.4	0.4	2.1
346.3	1.13 ± 0.05	2.16 ± 0.12	3.83 ± 0.19	2	4	2	1	2
352	0.74 ± 0.32	2.27 ± 1.29	4.06 ± 1.9	1	6	5	0.5	3

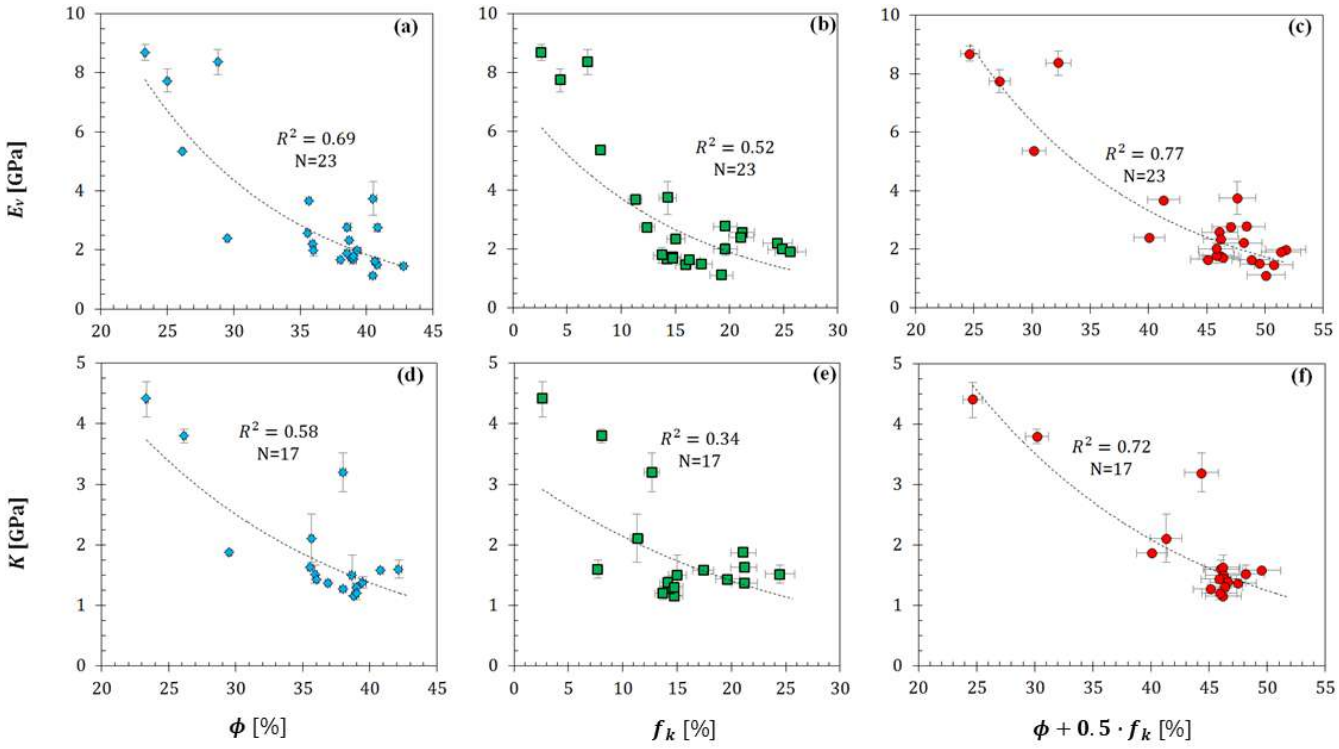

Figure 31: The effect of soft phases on static vertical Young's modulus and bulk modulus of organic-rich chalk: scatter plots of vertical Young's modulus (upper panel) and bulk modulus (lower panel), versus porosity (a, d), kerogen volume percentage (b, e), and the kerogen-factored porosity (c, f). An apparent exponential regression of the stiffness constants is best fitted to kerogen-factored porosity with κ=0.5.

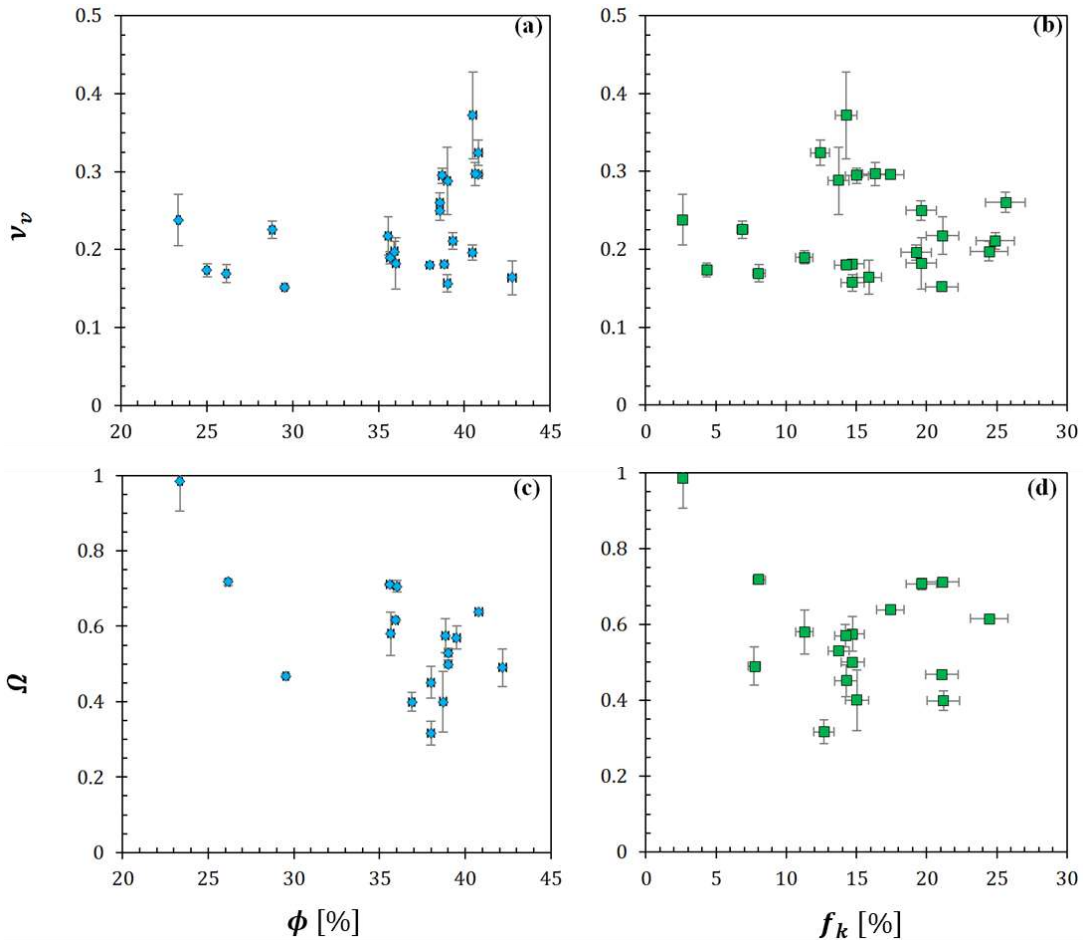

Figure 32: The effect of soft phases on static vertical Poisson's ratio and hydrostatic strain ratio of organic-rich chalk: scatter plots of vertical Poisson's ratio (upper panel) and hydrostatic strain ratio (lower panel), versus porosity (a, c) and kerogen volume percentage (b, d).

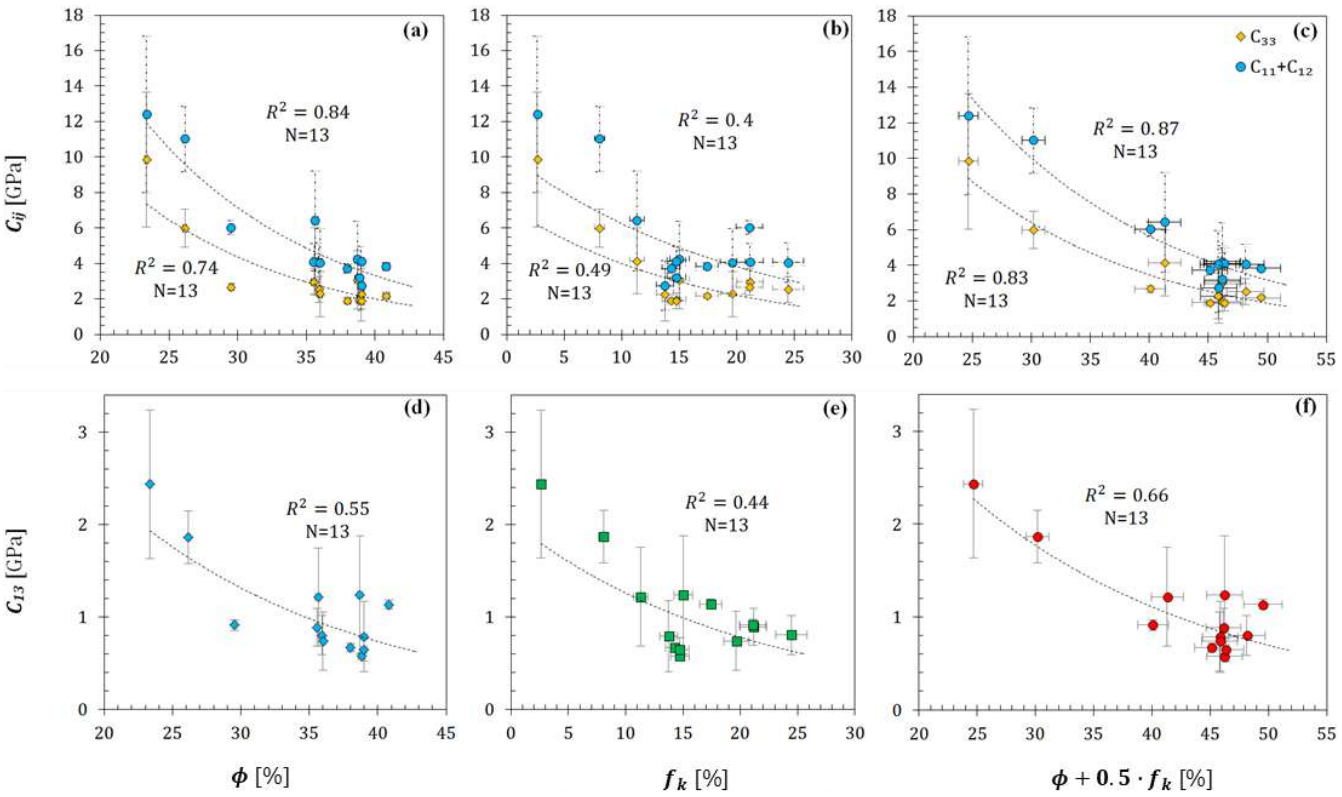

Figure 33: The effect of soft phases on static elastic stiffness constants of organic-rich chalk: scatter plots of static $C_{33}, C_{11} + C_{12}$ (upper panel) and C_{13} (lower panel), versus porosity (a, d), kerogen volume percentage (b, e), and the kerogen-factored porosity (c, f). An apparent exponential regression of the stiffness constants is best fitted to kerogen-factored porosity with κ=0.5.

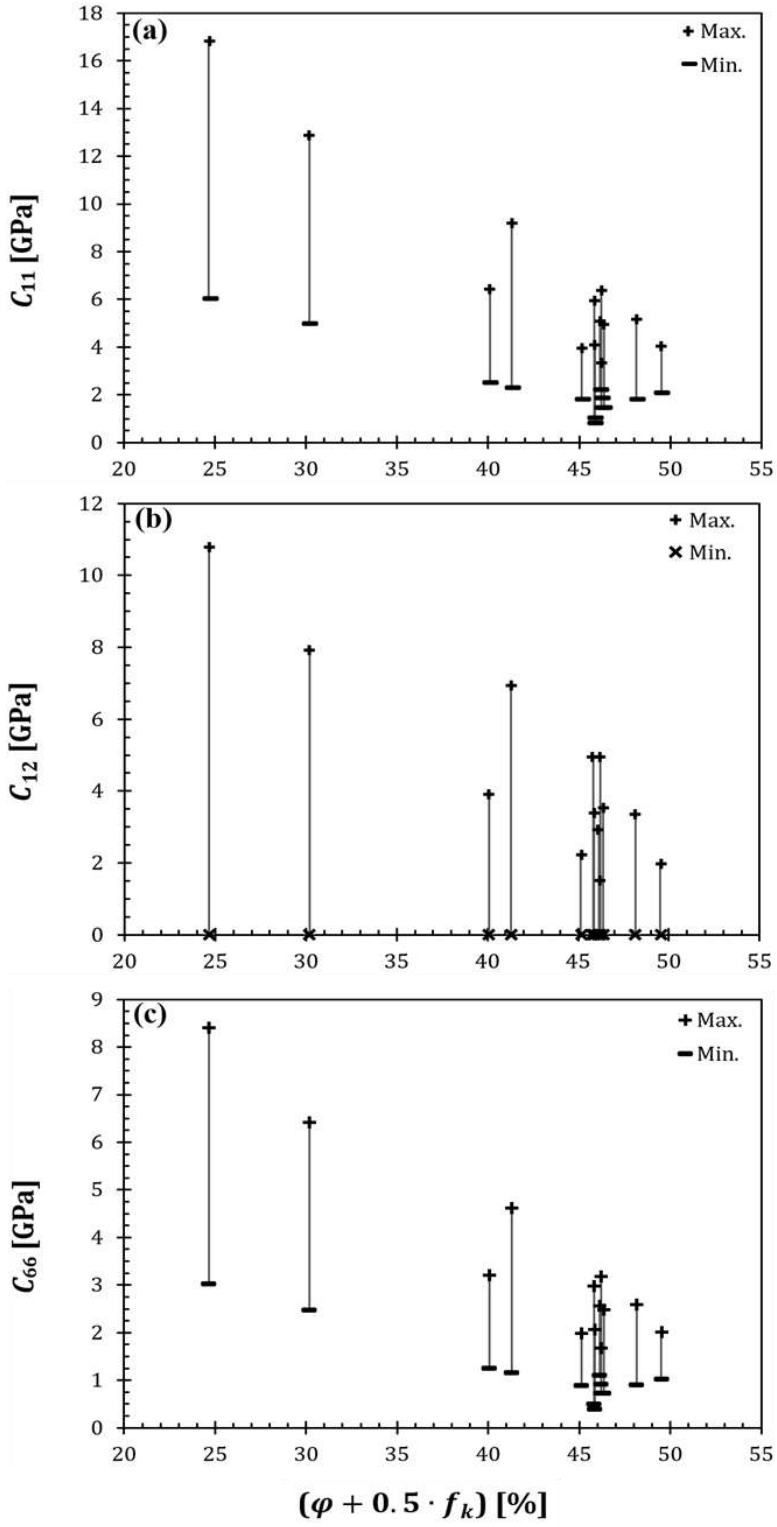

Figure 34: Constrained elastic stiffness constants: minimum and maximum possible values of C_{11} (a), C_{12} (b) and C_{66} (c) versus the kerogen-factored porosity.

The stiffness constants C_{13}, C_{33} and $C_{11}+C_{12}$ can be computed using the HDC-TIES procedure only where linear elastic response is observed in both the hydrostatic and deviatoric stages of the triaxial compression experiment. These stiffness constants depend on both porosity and kerogen, and correlate best with the kerogen-factored porosity (Figure 33). The conditions for stability of a transversely isotropic medium (positive strain energy, see Carcione 2014) cannot be fully examined here as not all stiffness constants are known, but it is confirmed that:

$$(C_{11}+C_{12})C_{33} > 2C_{13}^2 \ . \tag{61}$$

The minimum and maximum values for C_{11}, C_{12} and C_{66} are calculated according to Equations (56-58) (Table 5, Figure 34). Although only the constrained values are given in Figure 34, it is possible to estimate these parameters using empirical relationships and reasonable ratios of C_{12}/C_{11} (optional step in Figure 15).

Occasionally, the derivation of K is not as precise as done in this study. It is therefore interesting to examine the error introduced using two common approximations of bulk modulus rather than the exact expression in Equation (48). If isotropy were to be assumed then the bulk modulus would be calculated by:

$$K = \frac{E}{3(1-2\nu)} \ . \tag{62}$$

The comparison shown in Figure 35 ("isotropic medium equation" series) indicates that this approximation under-estimates the true bulk modulus by ~26%. It is very important to note that the bulk modulus is independent of direction, because pressure is applied equally from all directions. As a result, insertion E_v and ν_v into Equation (62) is wrong (examples for this type of mistakes may be found in Henriksen et al. 1999; Korsnes *et al.* 2008). The bulk modulus of an anisotropic medium is sometimes estimated using the best-isotropic approximation (Cavallini 1999; Carcione 2014):

$$K = \frac{1}{9}\left(C_{11}+C_{22}+C_{33}+2(C_{12}+C_{13}+C_{23})\right) = \frac{1}{9}\left(C_{33}+4C_{13}+2(C_{11}+C_{12})\right). \tag{63}$$

Note that the latter term in Equation (63) is the reduction of the first term in VTI materials. Indeed, the best-isotropic approximation and the true bulk modulus of the Ghareb-Mishash chalk are in good agreement (Figure 35).

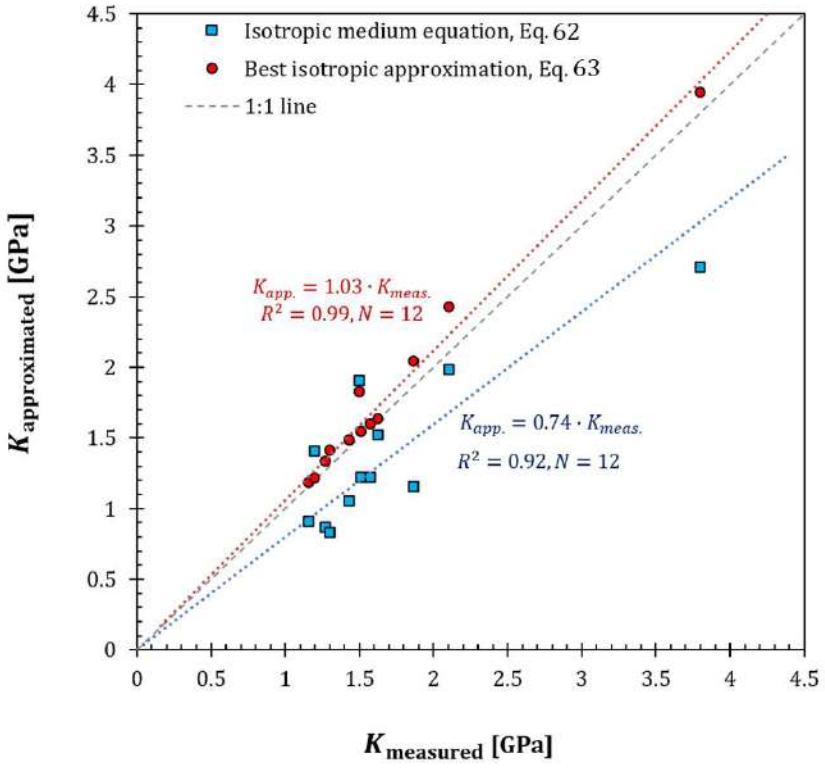

Figure 35: Comparison between the true bulk modulus versus two approximations of it, using mistakenly the isotropic medium equation (squares, Equation (62)), and the best isotropic approximation (circles, Equation (63)).

2.6 Rock strength

Tensile strengths of air-dried Zoharim cores are summarized in Table 6 and Figure 36a. A general tensile strength increase with depth is observed, but in the upper part of the Mishash Formation the strength is somewhat constant or even decreased. Mechanical anisotropy is clearly exhibited, as the chalk is more resistant to tensional stresses acting parallel to bedding ($\sigma_{t,p} = 1.8 - 5\ MPa$) rather than normal to bedding ($\sigma_{t,n} = 0.5 - 3.5\ MPa$). The average bedding-parallel/bedding-normal strength ratio is about 1.5 (force directions are demonstrated in Figure 36b).

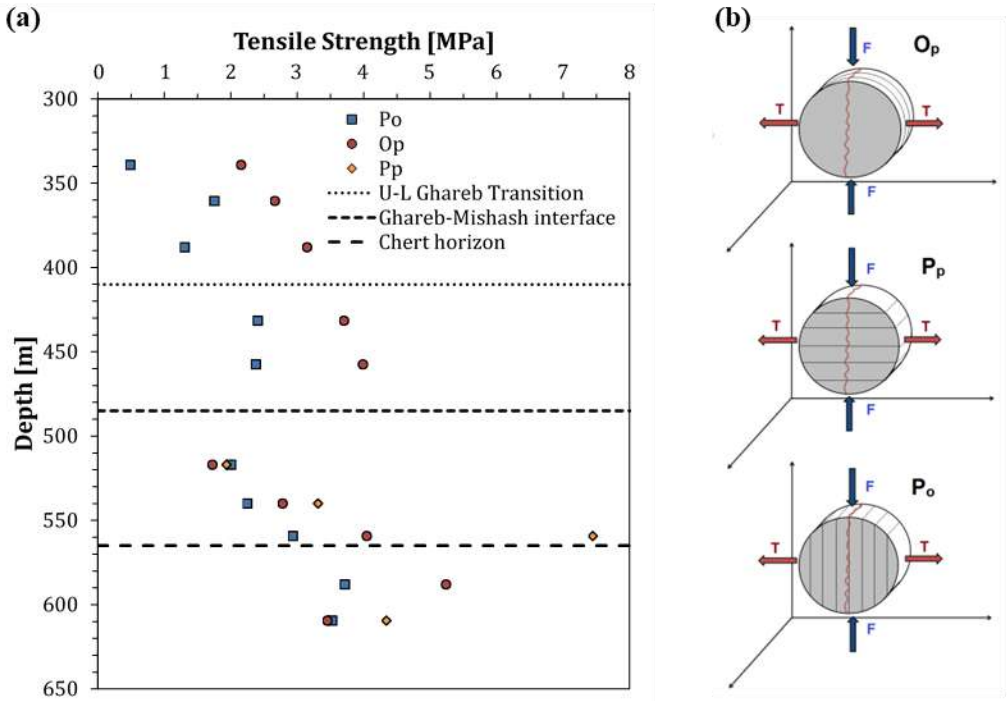

Figure 36: Tensile strength of the Ghareb-Mishash chalk: a) Tensile strength plotted vs. depth. The tested orientations are demonstrated in (b): O_p and P_p represent the horizontal strength (i.e. bedding-parallel tension), and P_o represents the vertical strength (i.e. bedding-normal tension).

Table 6: Strength results from compression and tension tests.

				Triaxial compression test			Brazilian test	
Depth [m]	Porosity [%]	TOC [%]	Dry density [g/cc]	Confining pressure [MPa]	Peak stress difference [MPa]	Young's modulus [GPa]	Vertical tensile strength [MPa]	Horizontal tensile strength [MPa]
339.1	38.84	10.31	1.43	3.65	9.78	1.72	0.48	2.16
360.5	38.00	9.74	1.47	4.55	17.8	1.63	1.75	2.66
388.9	38.65	10.2	1.52	6.37	19.7	-	1.32	3.13
431.5	35.92	17.72	1.38	4.9	29.2	2.14	2.41	3.69
457.5	35.57	14.6	1.45	6	31.23	2.57	2.37	3.99
517	38.7	8.18	1.84	5.86	17.4	2.12	2.00	1.81
540	35.65	6.74	1.68	5.6	28	3.68	2.26	3.04
559.3	29.54	13.68	1.54	6.37	42.4	2.39	2.92	5.75
588	26.15	4.21	1.92	6.77	49.66	5.36	3.72	5.24
609.5	23.35	1.3	2.03	7.54	52.8	8.28	3.53	3.89

Triaxial compression tests of air-dried cores are summarized in Table 6, and strengths are plotted against depth in Figure 37. It is evident that the strength generally increases with depth, but in the upper part of the Mishash Formation the compressive strength decreases, as observed for the tensile strength. This is most possibly a result of sampling highly porous cores from the upper part of the Mishash Formation. This inference is based on the linear regression between both compressive strength and tensile strength with porosity, as seen in Figure 38. Surprisingly, no clear dependency between strength and kerogen volume is observed (Figure 39). The average ratio between compressive strength and tensile strength in the normal direction is about 13.5. This value exceeds the ratio of 8 suggested by Griffith's criterion (Griffith, 1921), most likely due to bedding-parallel weakness planes that greatly reduce the bedding-normal tensile strength.

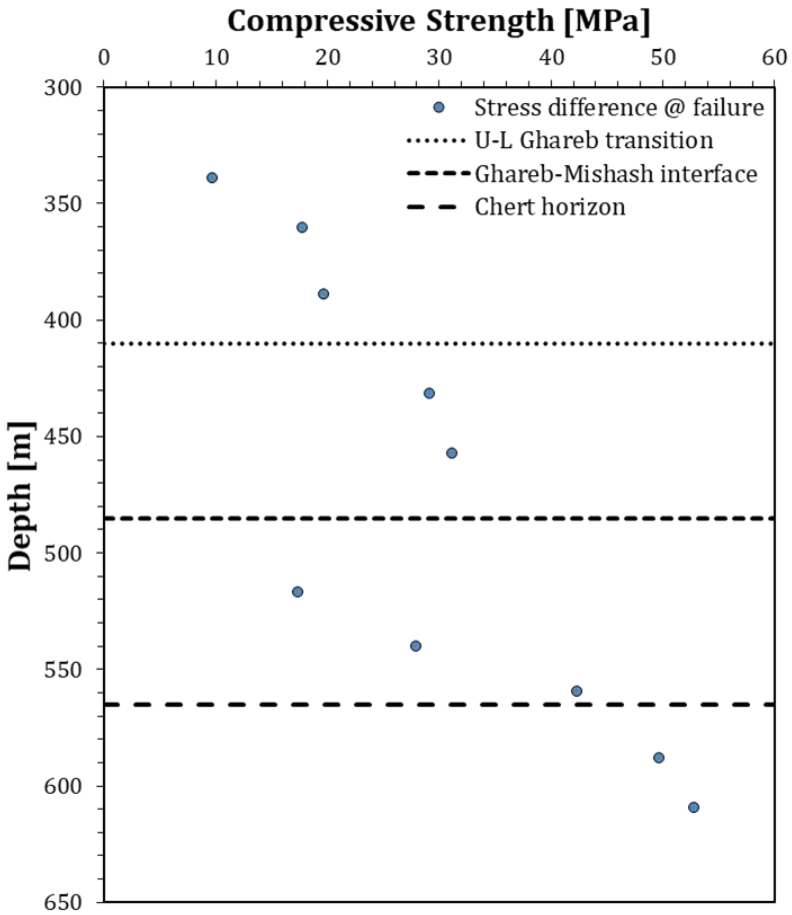

Figure 37: Peak stress difference plotted vs. depth, confining pressures are given in Table 6.

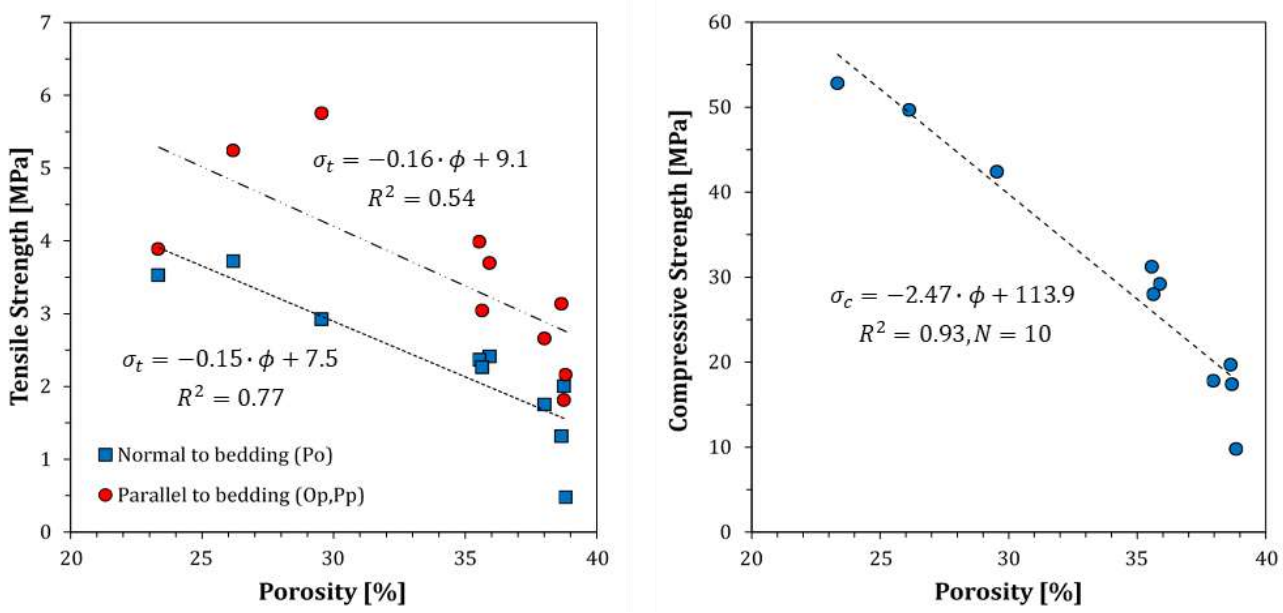

Figure 38: Strength and porosity: horizontal tensile strength (circles in (a)), vertical tensile strength (squares in (a)), and compressive strength (b) decrease linearly with porosity.

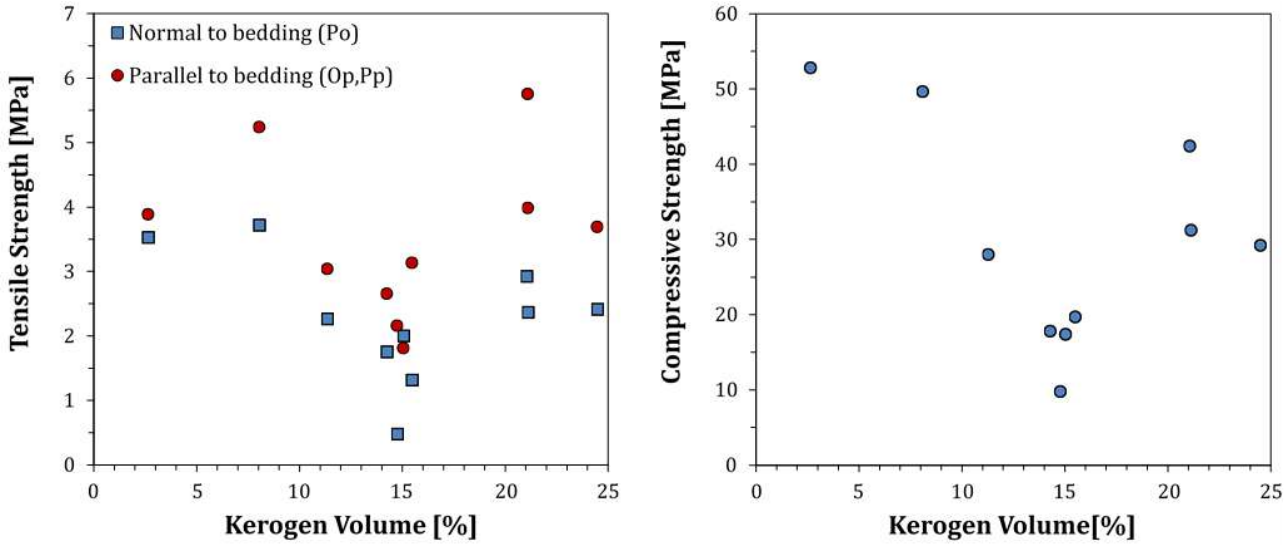

Figure 39: Strength and kerogen content: horizontal tensile strength (circles in (a)), vertical tensile strength (squares in (a)), and compressive strength (b) show very little relationship with kerogen volume.

2.7 SEM

In order to compare the experimental results and their analyses with microstructural properties, three samples were analyzed by backscatter SEM. Prior to scanning, the samples were polished mechanically using carborundum 1000 abrasive powder, to reduce surface roughness to the order of few microns. Afterwards, the surface was cleaned using compressed air and kept in a desiccator. Then the samples were taken to surface characterization in the Ilse-Kats Institute for Nanoscale Science & Technology at BGU. The samples were scanned in a high-resolution SEM (Verios XHR 460L), and also in a lower resolution environmental SEM (Quanta 200). The voltage and current of the electron beam were adjusted to obtain good quality images without damaging the organic matter. Note that where the beam is too intense, the organic material heats and therefore stiffens irreversibly. Due to the density difference between the organic material and the different minerals, in backscatter SEM (BSEM) dark material is identified as organic material. The selected samples are taken from shallow, middle, and deep parts of the Zoharim section, and they differ by porosity, organic content, anisotropy and matrix stiffness. The microstructural inferences from the measurements are compared with the BSEM micrographs.

The porosity decrease with depth is reflected in the micrographs (Figure 40), as the shallow, middle and deep samples show features of increasing compaction. Development of cementation and recrystallization are identified in the deep zone (zoomed area in Figure 40e), and contribute to porosity reduction and increased matrix stiffness. Based on the classification used by Loucks *et al.* (2012), the porosity is mostly associated with inter-particle porosity between the matrix grains. Intra-particle porosity within fossil bodies (Figure 40a) and organic matter hosted pores also contribute to the total porosity but to a smaller extent. Organic matter hosted pores are assumed to be included in the total porosity, but they are hard to detect in the micrographs. Nonetheless, they are known to exist in the kerogen, based on the findings that immature Type IIs kerogen from the Monterey Formation is inherently porous (Löhr *et al.* 2015). Moreover, the kerogen influence factor of κ=0.5 is partly linked with the effect of isolated un-measurable porosity in the kerogen. The permeability results indicate that organic material is associated with increased pore size. The micrographs in Figure 40a-d manifest the predominance of kerogen in the fine-grained matrix, and their contribution to inter-particle porosity. The inter-particle porosity is distributed in a mudstone-wackestone textured matrix, hence the kerogen is a primary factor in the physical behavior of the rock. Some calcite concentrated zones (Figure 40b-d) exhibit mudstone texture as in non-organic

chalks. Because of the dominance of the inter-particle porosity, the grain contacts in the matrix are believed to have the strongest influence on rock stiffness.

The fine-grained matrix mostly includes kerogen and microcrystalline calcite as indicated by energy dispersive spectroscopy (EDS). The abundance of kerogen and pores in the fine-grained matrix causes it to appear in darker shades in BSEM (Figure 40a, c). The difference in shades of kerogen and calcite is most visible in the organic-lean sample (Figure 40e, f), where the kerogen is dispersed in small accumulations. As assumed in the "HS kerogen" model, the matrix in most of the samples is seen to be composed of kerogen-calcite mixture (most evident in Figure 40a, c). The matrix may seem homogeneous at a scale of hundreds of microns, but at scale of tens of microns and below it appears heterogeneous. The bedding direction is visible at the scale of tens of microns and above, as inferred from the preferred orientation of elongated skeleton fragments and organic aggregates (Figure 40a, c). However, many of the elongated particles have various orientations, even vertical. In addition, many of the detrital grains and the pores are more equant rather than flat. Therefore, bedding-aligned fabric is less prominent than in a typical shale (Vernik and Nur 1992; e.g. Sone and Zoback 2013a).

Anisotropy and stiffness of organic-rich rocks is frequently associated also with microfractures, especially at increased maturity levels (Vernik 1994; Zargari *et al.* 2013). Microfractures are identified (arrows in Figure 40a, c, abundant in Figure 40d). Nevertheless, their origin is questionable as any fracture may have been formed originally in the rock, during core extraction, or by the polishing process of the surface prior to the scans. The sample in Figure 40c-d has both horizontal and vertical permeability measured, as well as the elastic anisotropy. The permeability anisotropy is k_h/k_v=7.3, i.e. intermediately anisotropic, just as the elastic anisotropy ($\Omega = 0.71$). Unlike most of the intervals in the Ghareb-Mishash sequence, the deepest zone includes none of the above-mentioned anisotropy enhancing features, hence the isotropic nature of this sample. It is deduced that the anisotropy of the Ghareb-Mishash chalk is caused by sub-horizontal preferred orientations of mineral particles and kerogen, and possibly by bedding sub-parallel microfractures as well. Permeability anisotropy is correlated with porosity because the pore connectivity in the bedding-parallel direction is improved more significantly at high porosities.

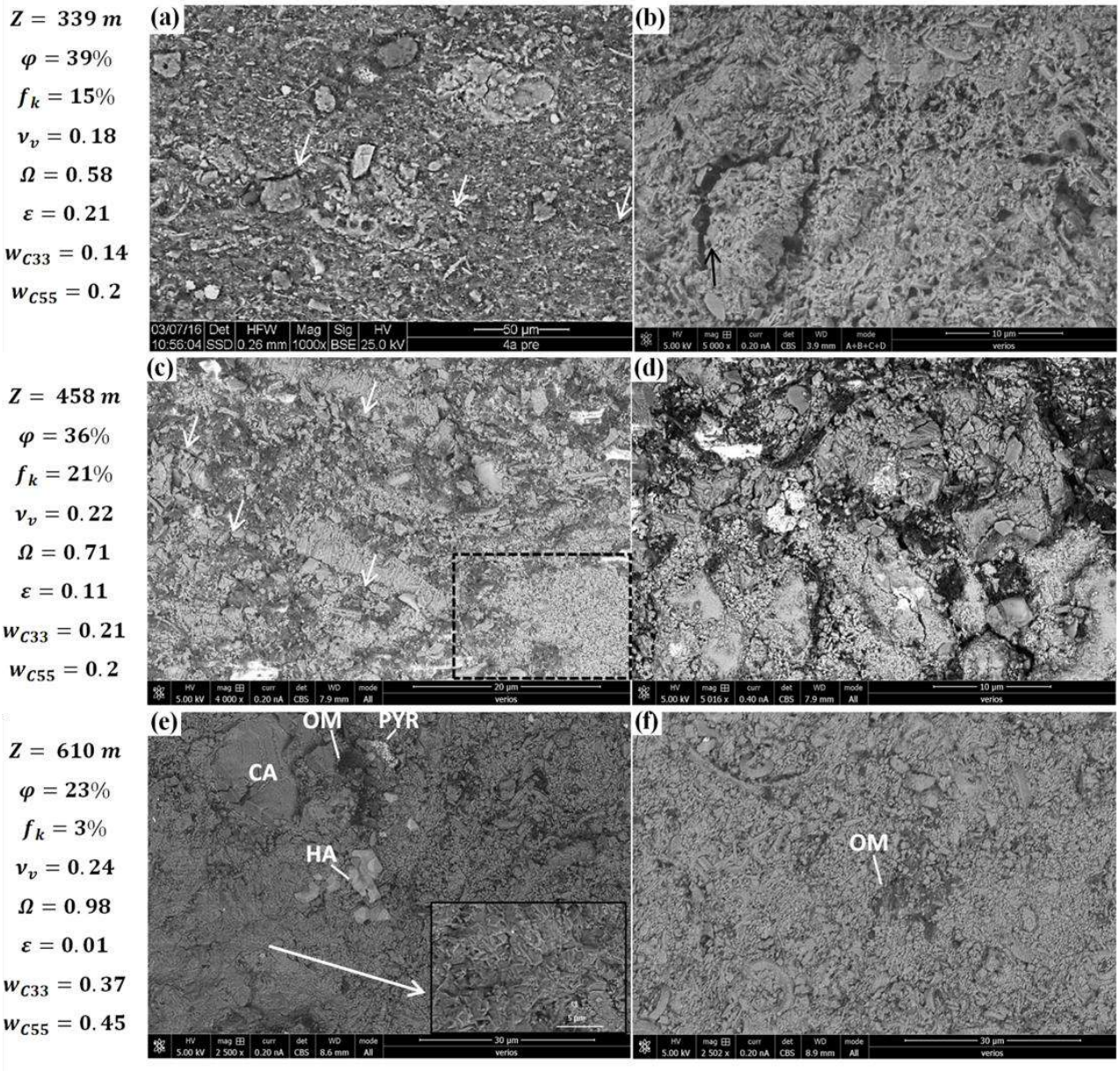

Figure 40: BSEM images of core samples from three depth intervals in the Zoharim well. The samples are taken from depths of 339 m (upper panel, a-b), 458 m (middle panel, c-d), and 610 m (lower panel, e-f). Legend: OM- organic material, CA- calcite, HA- halite, PYR- pyrite. Arrows in (a) and (c) point to bedding-parallel microfractures. Arrow in (b) points to a zone that may have been disturbed during the polishing of the surface. Rectangle in (c) delineates a zone of calcite grains, textured as typical chalk mudstone. Zoomed area in (e) reveals texture of calcite recrystallization and cementation.

2.8 Discussion

2.8.1 Hydrostatic strain ratio as an anisotropy parameter

The hydrostatic strain ratio theoretically should be a good parameter for evaluating the elastic anisotropy because it is defined by the simplest conception of 2D anisotropy: bedding-normal strain over bedding-parallel strain, under hydrostatic compression. In this section its applicability as an anisotropy parameter is examined by comparisons with Thomsen's anisotropy parameters and its behavior in VTI organic-rich rocks. First, it is desired to obtain a relationship between the Ω and the anisotropy parameters. The widely known Thomsen's anisotropy parameters ε, γ and δ are (Thomsen 1986):

$$\varepsilon = \frac{C_{11} - C_{33}}{2C_{33}} , \tag{64}$$

$$\gamma = \frac{C_{66} - C_{55}}{2C_{55}} , \tag{65}$$

$$\delta = \frac{(C_{13} + C_{55})^2 - (C_{33} - C_{55})^2}{2C_{33}(C_{33} - C_{55})} . \tag{66}$$

The Ω (defined in Equation (52)) can be expressed in terms of Thomsen's ε:

$$\Omega = \frac{C_{33} - C_{13}}{C_{33}(1 + 2\varepsilon) + C_{12} - 2C_{13}} = \frac{C_{33} - C_{13}}{C_{33} + C_{12} - 2C_{13} + 2C_{33}\varepsilon} . \tag{67}$$

This equation can be rearranged to a convenient trend line:

$$\Omega = \frac{b_1}{1 + b_2\varepsilon} , \tag{68}$$

with:

$$b_1 = \frac{C_{33} - C_{13}}{C_{33} + C_{12} - 2C_{13}} , \tag{69}$$

$$b_2 = \frac{2C_{33}}{C_{33} + C_{12} - 2C_{13}} . \tag{70}$$

The hydrostatic strain ratio theoretically equals 1 when the rock is isotropic ($\varepsilon = 0$, $b_1 \xrightarrow{C_{12}=C_{13}} 1$). Thus, the Ω versus ε curve becomes:

$$\Omega = \frac{1}{1 + b_2\varepsilon} \ . \tag{71}$$

To examine the applicability of Ω, the results from this study are combined with acoustic velocities and density measurements of other organic-rich rocks at dry conditions, reported by Vernik and Liu (1997). The organic-rich formations included in their data are low porosity samples ($\phi < 10\%$) from the Bakken shale, Bazhenov shale, North-Sea Kimmeridge shale, Woodford shale, Lockatong shale, Niobrara chalk; and high porosity samples ($\phi > 10\%$) from the Monterey Formation and Japan (undeclared geological data). Their dataset includes vertical and horizontal P-wave and S-wave velocities, which allow to calculate $C_{11}, C_{33}, C_{55}, C_{66}$, and C_{12}. Calculation of C_{13} was enabled only where Thomsen's δ was reported, hence C_{13} data are fewer. In order to increase the amount of data for comparison, a multiple variable linear regression is performed to obtain a relationship between C_{13} and $C_{11}, C_{33}, C_{55}, C_{66}$ (as in Figure 5 in Yan *et al.* 2016), which is specifically suitable for organic-rich rocks ($R^2 = 0.85$):

$$C_{13} = -0.857 - 0.019C_{11} + 0.663C_{33} - 1.526C_{55} + 0.531C_{66} \ . \tag{72}$$

The Ω is calculated using the values of C_{11}, C_{12}, C_{13} and C_{33} (Equation (52)). The C_{13} approximation in Equation (72) was used only where the Vernik data and Liu did not include Thomsen's δ. Then, Ω is compared with Thomsen's ε and γ to examine the anisotropic behavior. These relationships are expected to follow the trend in Equation (71).

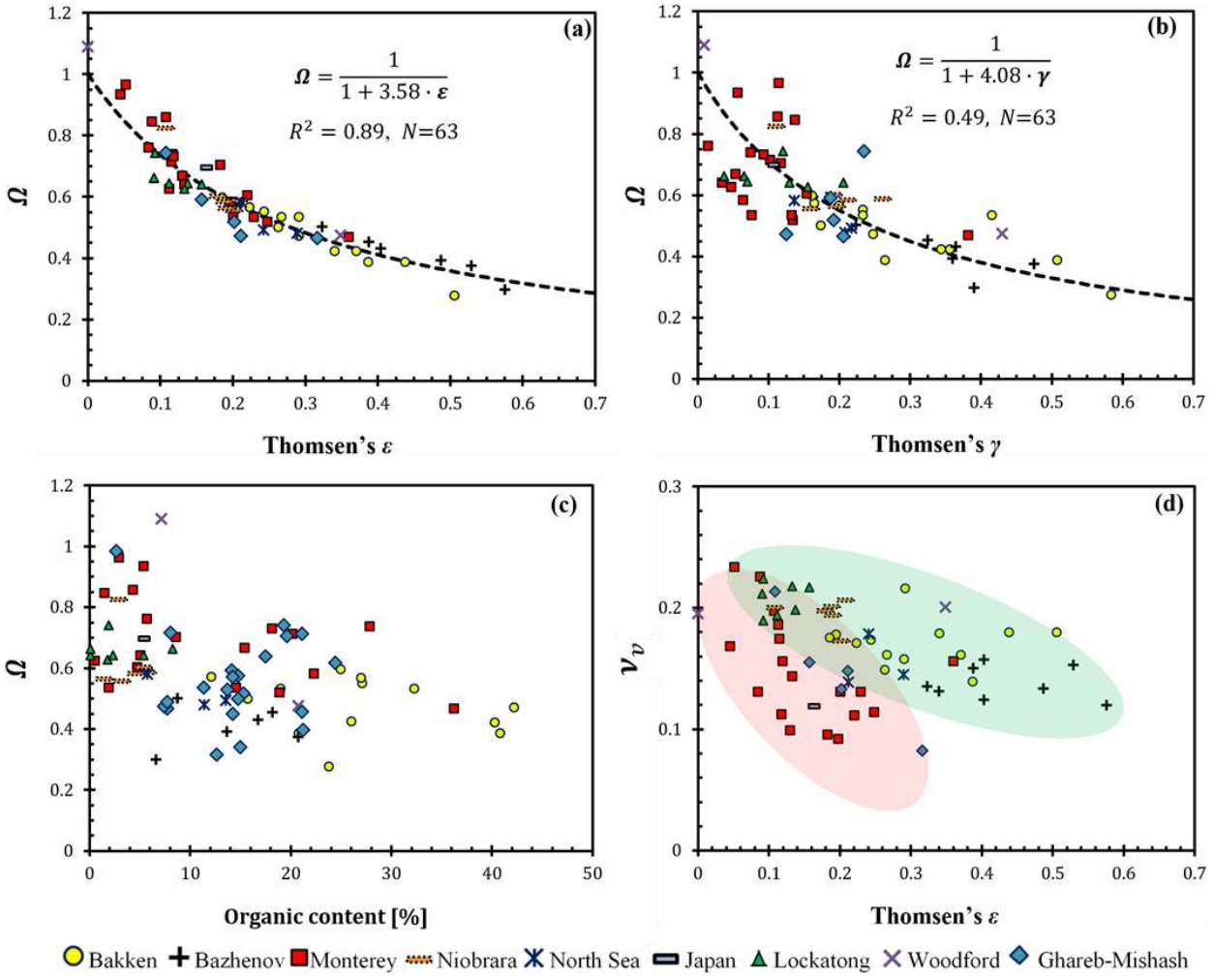

Figure 41: Anisotropy of organic-rich rocks, examined based on acoustic velocities and densities of various source rocks at dry conditions, reported by Vernik & Liu (1997). These data are shown together with results of the Ghareb-Mishash organic-rich chalk studied in this paper. Hydrostatic strain ratios are plotted versus Thomsen's ε (a) and γ (b). Trendline equation in (a) follows the expression derived in Equation (71), and the trend in (b) is assumed to follow the same pattern. c) The anisotropy of the organic-rich rocks, expressed by Ω, reveals a general decrease with increasing kerogen content. Empty diamonds represent static data of Ghareb-Mishash Formations. d) The vertical Poisson's ratio is affected by the degree of anisotropy (expressed by ε). By subdividing the organic-rich rocks to porosity groups, at $\phi > 10\%$ (Monterey, Ghareb-Mishash, Japan, in the red area) the vertical Poisson's ratio is more sensitive to anisotropy than in low porosity rocks ($\phi < 10\%$, Bakken, Bazhenov, North-Sea, Niobrara, Woodford, Lockatong, in the green area).

Figure 41a shows that Ω exhibits a very good correlation with Thomsen's ε parameter, based on the relationship in Equation (71) and with $b_2 = 3.58$ ($R^2 = 0.89$). This observation can be used to convert between the two anisotropy parameters. The b_2 fitting parameter (3.58 in Figure 41a) may be used further to separate between the static C_{11} and C_{12} and approximate them, as well as

the static C_{66} (optional step in Figure 15). Thomsen's γ parameter shows a similar correlation with Ω, although a larger scatter is indicated (Figure 41b) because none of the shear moduli appears in the definition of Ω. Figure 41a-b reveal that Ω decreases sharply in the weak anisotropy range (i.e. ε < 0.2), indicating that Ω is more sensitive to changes in the magnitude of anisotropy than ε and γ within this range. Where the anisotropy is higher, Ω is less indicative of anisotropy in comparison to ε and γ. In Figure 41c the relationship between Ω of source rocks and organic content is examined (static values of Ω of the Ghareb-Mishash Formations are included). Although the results are scattered, a trend of increased anisotropy with organic enrichment is indicated. The scatter is large because anisotropy is not exclusively related to organic content, but also depends on the features of the mineralogical particles and the pores. Figure 41d shows that the vertical Poisson's ratio is negatively correlated with elastic anisotropy. Interestingly, the decrease in the high porosity organic-rich formations is sharper than in the low porosity formations. It is concluded from Figure 41 that the Ghareb-Mishash chalk shares a common anisotropic behavior with other organic-rich rocks, especially with high-porosity rocks.

This analysis points to beneficial features of Ω as an anisotropy parameter: 1) it is easily measured in standard hydrostatic compression tests; 2) its definition as the ratio between bedding-parallel and bedding-normal contraction has a clear physical intuition; 3) it correlates well with the well-established Thomsen's anisotropy parameters, thus may be used for approximations in the absence of measured data; 4) it quantifies the magnitude of anisotropy by being strongly influenced by C_{11} and C_{33} (like ε), but it also expresses the difference between C_{12} and C_{13}; and 5) if derived from a triaxial experiment, it may be used for elastic constants derivation using the HDC-TIES method. Because the hydrostatic strain ratio is calculated using bedding-normal and bedding-parallel strains, it is already available from existing results of hydrostatic tests that can thus be revisited to enrich existing datasets. Among its advantages, it is important to recall that it assumes linear elasticity, and that the strain measurements align with the bedding-normal and bedding-parallel directions. If either of these conditions is not fulfilled, the derivation of Ω is invalid.

2.8.2 Hydrostatic strain ratio and Poisson's ratio

The static elastic horizontal-to-vertical strain ratios, ν_v at deviatoric compression and Ω at hydrostatic compression, are compared in Figure 42a. Generally, a decrease in Ω seems associated with lower ν_v is detected, although there are only 12 observations and the results are scattered. It

is inferred that increased anisotropy reduces the vertical Poisson's ratio. This is also supported by the conclusion from Figure 41d. This corresponds to the expectation for a typical VTI material, that increased anisotropy should enhance bedding-normal contraction with respect to bedding-parallel extension (i.e. lower ν_v). As seen in Figure 32a, ν_v has a wider range at high porosity. These observations imply that the sensitivity of ν_v to anisotropy is enhanced at high porosity. This may explain the improved correlation when vertical Poisson's ratio is plotted against the product of Ω and porosity (Figure 42b). This behavior is found typical to the Ghareb-Mishash chalk tested here in static conditions, and less representative of other organic-rich rocks that are much less porous and tested in dynamic conditions. The reason for this difference is lithological, as chalk matrix exhibits different geometrical arrangement and higher porosity with respect to shales. The dominance of porosity is smaller or absent in clay-rich shales which are much less porous and more strongly affected by clay and organic content (Sayers 2013a).

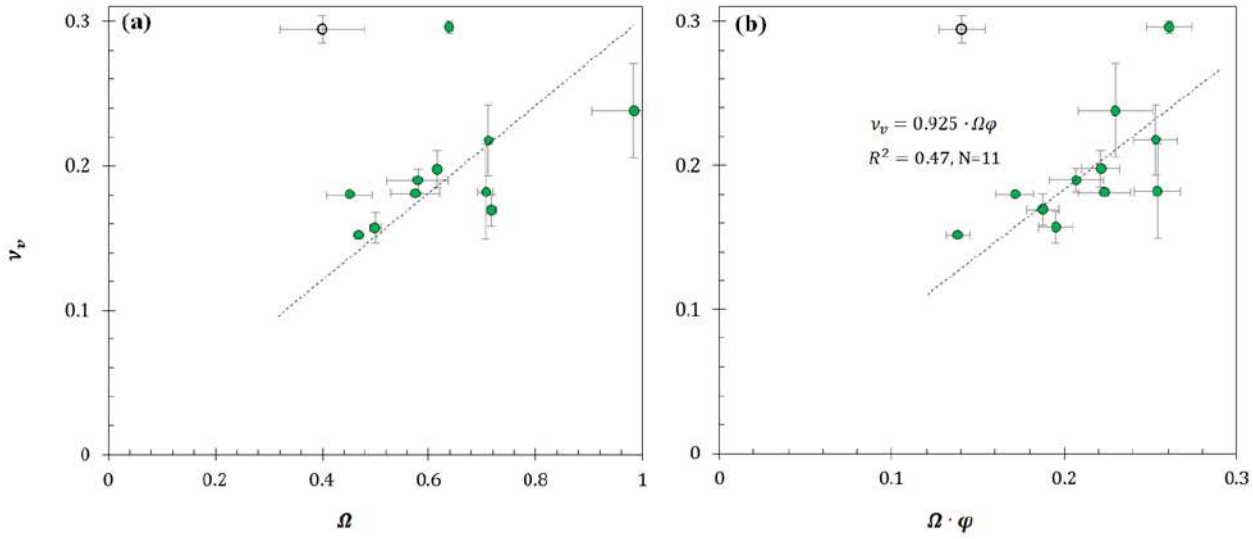

Figure 42: Hydrostatic strain ratio and vertical Poisson's ratio: a) vertical Poisson's ratio plotted versus hydrostatic strain ratio of the Ghareb-Mishash chalk from the Zoharim and Aderet wells. b) Vertical Poisson's ratio plotted versus the product of the hydrostatic strain ratio and porosity ($\Omega \cdot \phi$), showing an improved correlation with respect to (a). The empty data point in (a) and (b) originates from 517 m depth in the Zoharim section is excluded from the linear fits and thought to be anomalous in this comparison between strain ratios.

2.8.3 Comparison between static and dynamic moduli

The dissimilarity between the static and dynamic datasets limits the comparison between static and dynamic elastic moduli. In this study, elastic constants derived from static measurements are

C_{13}, C_{33} and $C_{11} + C_{12}$, while from dynamic measurements these are C_{33} and C_{55}. Derivation of C_{13} from dynamic measurements is usually prone to significant errors (Yan *et al.* 2016), while this value is derived more easily and accurately from static measurements using the HDC-TIES method. The shear moduli C_{55} and C_{66} are unavailable from the static measurements performed here. Consequently, the most significant comparison that can be made is between static and dynamic vertical oedometer moduli, C_{33} (M_v).

As expected, the dynamic C_{33} are consistently higher than their corresponding static values (Figure 43a). To allow for comparison with other static-dynamic relations it is preferred to convert C_{33} to E_v. The acoustic measurements of source rocks reported by Vernik and Liu (1997, Figure 41) indicate that C_{33} is ~1.11 times higher than E_v in dynamic conditions ($R^2 = 0.99$, Figure 43b). Although no direct measurements of dynamic E_v were obtained in this study, the correlation in Figure 43b is found extremely useful in order to approximate it. This way, measured static E_v are compared with approximated dynamic E_v (Figure 43c), in a dry organic-rich chalk:

$$C_{33,s} = 0.35 \cdot C_{33,d} + 0.1\ [GPa]\ , \tag{73}$$

$$E_{v,s} = 0.35 \cdot E_{v,d} + 0.02\ \ [GPa], \tag{74}$$

where subscripts d and s designate dynamic and static elastic moduli, respectively.

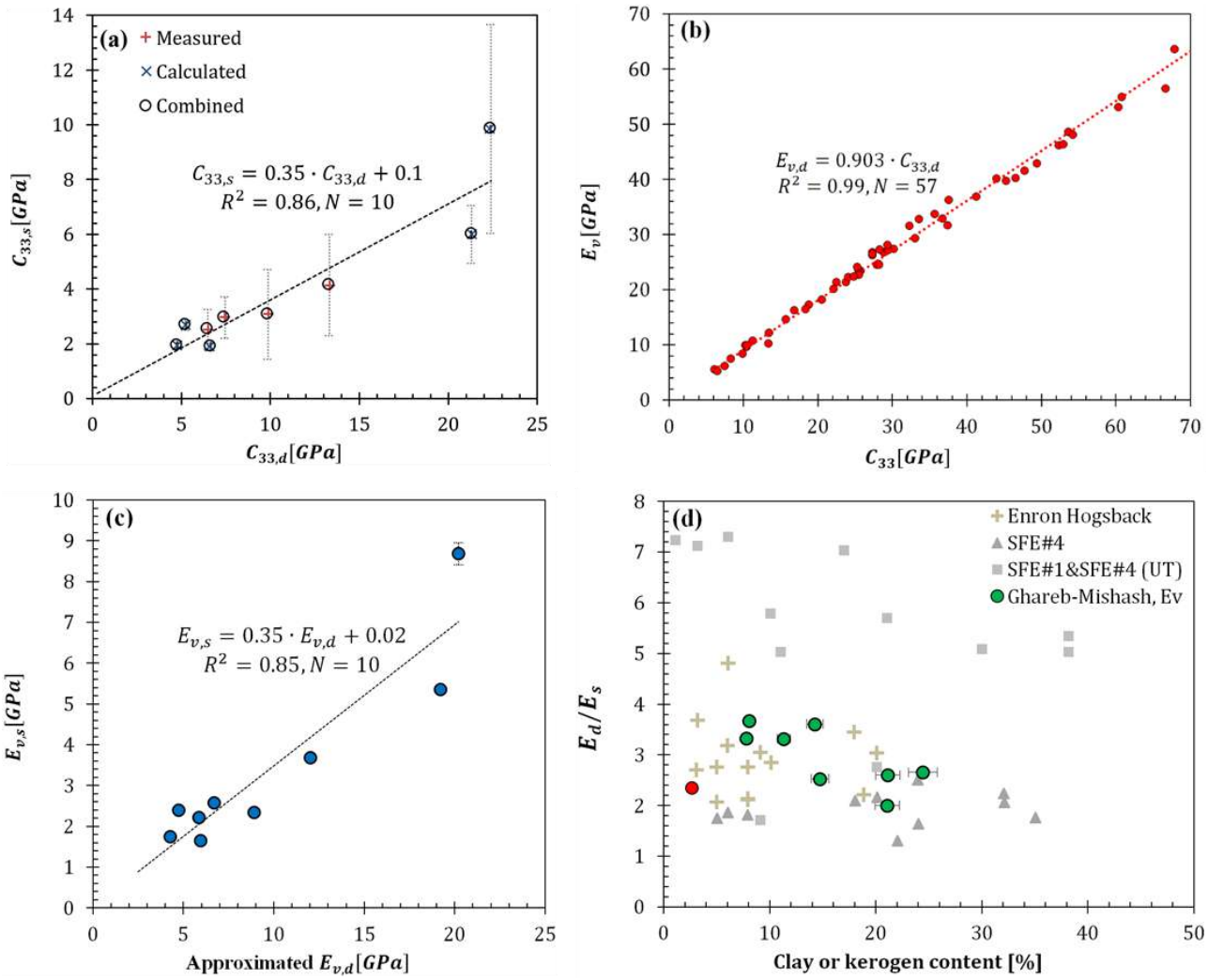

Figure 43: Relationships between dynamic and static moduli: a) Linear correlation between the static and dynamic vertical oedometer modulus of the studied organic-rich chalk in dry conditions. Dynamic values include measured C_{33} and calculated C_{33} using BAM model. b) Compilation of E_v and C_{33} data of organic-rich rocks using the results by Vernik and Liu 1997. This enables the approximation of dynamic E_v from C_{33} measurements. c) Linear correlation between the static and dynamic vertical Young's modulus of the studied organic-rich chalk, based on the static measurements and the conversion shown in (b) for dynamic E_v. d) The decrease of dynamic/static E_v ratio upon increase in kerogen content. This trend is similar to that of a tight gas sand upon increase in clay content in (Tutuncu and Sharma 1992). Data point marked in red originates from depth of 609.5 m, which is much lower in porosity and kerogen content than the other samples ($\phi = 23.4\%$, $f_k = 2.6\%$) and known to be significantly more compacted and cemented, thus interpreted as anomalous.

Static-dynamic relationships are useful in estimating static elastic moduli for engineering applications, as the dynamic values are easier to obtain (e.g. from well-logs or core data). Many relationships have been suggested for these purposes by estimating the static Young's modulus,

E_s, using the dynamic Young's modulus, E_d (Mavko *et al.* 2009; Najibi *et al.* 2015; Brotons *et al.* 2016). Soft rocks with static Young's modulus smaller than 15 GPa exhibit a linear relationship of $E_s = 0.41 \cdot E_d - 1.06$ [GPa] (Z. Wang and Nur 2000). Data by Sone and Zoback (2013a), obtained on various organic-rich shale formations, yield a relationship of $E_s = 0.97 \cdot E_d - 11.6$ [GPa] (first loading cycle). Olsen, Christensen and Fabricius (2008a) found that in dry North Sea chalk the dynamic and static elastic moduli are nearly equal (first loading cycle, measured with strain gauges). Gommesen and Fabricius (2001) formulated a different trend for North Sea reservoir chalks (Tor and Hod Formations); at brine-saturated conditions the static oedometer modulus, M_s, is related to dynamic modulus M_d : $\ln(M_s) = 1.36 \cdot \ln(M_d) - 7.6 \cdot \phi/\phi_c$, where ϕ/ϕ_c is the ratio between porosity and critical porosity.

The static-dynamic relationship of vertical Young's modulus of the Ghareb-Mishash chalk appears most similar to the relationship suggested for soft rocks (Z. Wang and Nur 2000; Mavko *et al.* 2009). It behaves very differently from organic-rich shales and North Sea chalks (e.g. Olsen *et al.* 2008; Sone and Zoback 2013a), in which dynamic and static moduli are much closer to each other. In particular, Niobrara chalk which has about 25% clay content, and lower porosity and organic content, exhibits DSMR of 1.18-1.3 (Bridges 2016). These ratios are much lower than the Ghareb-Mishash chalk, which has much higher porosity and TOC and very low clay content. This observation highlights the unique behavior of the Ghareb-Mishash chalk.

The differences between the static and dynamic elastic moduli are generally explained by several mechanisms. Microfractures and low aspect ratio pores cause non-linear deformations during static loading and irreversible strains occur, while in dynamic conditions they have a much smaller effect (Olsen 2007). Moreover, this difference may be caused by viscoelastic and micro-plastic strains in static loading rates, where strain amplitudes affect soft phases more severely (Mashinsky 2003). It was previously reported that clay content decreases the DSMR (Jizba *et al.* 1990; Tutuncu and Sharma 1992). Here, it is found that the DSMR decreases with increasing kerogen content (Figure 43d). This effect is similar to that of clay content on the DSMR of tight gas sand (Tutuncu and Sharma 1992). It is deduced that the DSMR in the Ghareb-Mishash chalk is high primarily due to high porosity, microfractures, soft pore geometry, and weak intergranular contacts, as in many other soft sedimentary rocks. Kerogen has an opposite effect by decreasing the DSMR. Yet, the source for difference between static and dynamic moduli may be a good subject for further

research, requiring more data of static and dynamic moduli, unloading-reloading cycles, varying clay contents and higher resolution SEM images. It would also be interesting to investigate the behavior of kerogens of different types, maturity levels, lithologies and degrees of mechanical compaction. Furthermore, static-dynamic moduli comparison of horizontally-oriented samples of this rock is needed for better understanding of the mechanical behavior.

2.8.4 Rock physics modeling approaches

The rock examined in this study is considered to be a source rock, due to high organic content and fine-grained texture. Rock physics modeling of organic-rich rocks has initiated during the 90's in a series of papers by Lev Vernik (Vernik and Nur 1992; Vernik 1994; Vernik and Landis 1996; Vernik and Liu 1997). Rock physics studies of organic-rich rocks have emerged during the past decade because of the advances in production technologies from unconventional reservoirs. All of these rock physics studies rely on the foundations by Vernik's studies. Organic-rocks are typically considered to be VTI, and therefore rock physics modeling conceptualize a layered microstructure of organic-matter and minerals (typically clays), combined into a VTI composite. In this sense, Vernik's and subsequent rock physics studies applied Backus averaging method (e.g. Carcione *et al.*, 2011):

$$\begin{aligned}
\overline{C_{11}} &= \langle C_{11} - C_{13}^2 C_{33}^{-1} \rangle + \langle C_{33}^{-1} \rangle^{-1} \cdot \langle \overline{C_{33}^{-1} C_{13}} \rangle^2 \,, \\
\overline{C_{33}} &= \langle C_{33}^{-1} \rangle^{-1} \,, \\
\overline{C_{13}} &= \langle C_{33}^{-1} \rangle^{-1} \cdot \langle \overline{C_{33}^{-1} C_{13}} \rangle \,, \\
\overline{C_{55}} &= \langle C_{55}^{-1} \rangle^{-1} \,, \\
\overline{C_{66}} &= \langle C_{66} \rangle \,,
\end{aligned} \tag{75}$$

where the $\langle x \rangle$ brackets denote volumetric averaging, e.g. $\langle C_{33} \rangle = \left(\sum_i \frac{f_i}{C_{33,i}} \right)^{-1}$. Still, as common as the Backus model is, the introduction of the mechanical role of porosity is doubtful because pores are concepted as inclusions or layers instead of an interconnected network. This assumption is reasonable as long as the porosity is considerably low, as in most organic-rich shales. However, the studied organic-rich chalk is very porous and forms a connected pore network. For demonstration, Figure 44 shows the Backus-predicted values of bedding-normal P- and S- wave

moduli. It is clearly seen that the Backus method fails to predict the moduli of the rock when the porosity is included. The Backus averaging method may also be used to characterize a background matrix (e.g. Zhao et al 2016), and then introduce the porosity inclusions using other models (described below). Either way, the Backus method is considered unsuitable for the studied organic-rich chalk, because of the basic assumptions of this model. From the BSEM micrographs it is observed that neither the rock nor the background matrix exhibits a layered structure, as assumed in the Backus method. The Ghareb-Mishash chalk should be described as a granular package, just as typical chalks are. The kerogen particles are dispersed among the chalk matrix particles.

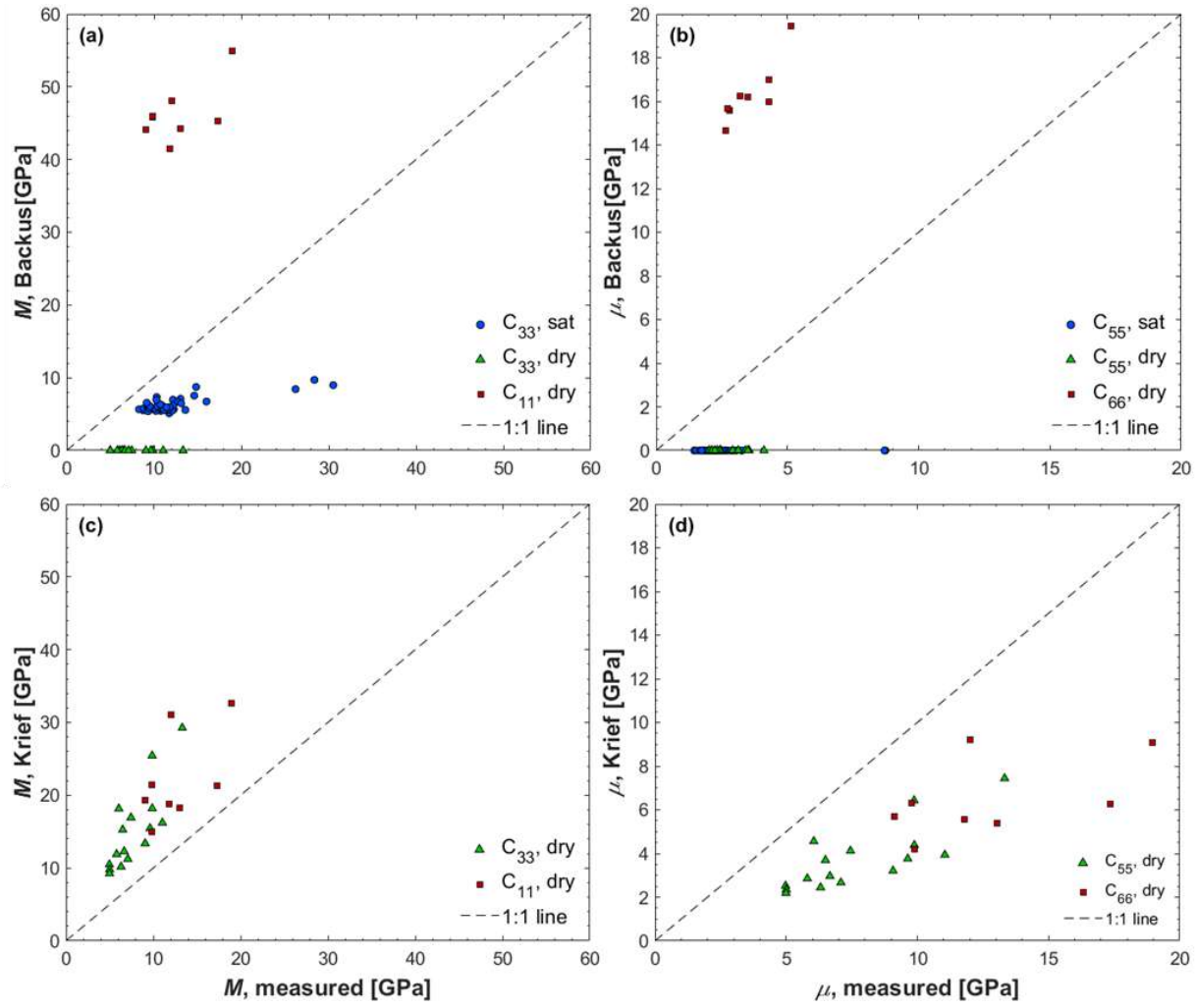

Figure 44: Inapplicability of the Backus model and Krief model: Measured vertical and horizontal oedometer modulus (left) and shear modulus (right) versus the Backus-calculated moduli (top) and Krief-calculated moduli (bottom). Krief approximations used A=2, B=1, as these exponents got the best vicinity of the data points to the 1:1 line. Neither Backus's nor Krief's models is representative of the Ghareb-Mishash chalk.

Another model that has been used for organic-rich rocks modeling was the Krief-Gassmann model (Carcione *et al.* 2011). Similar to the Backus averaging method, this model applies to laminated shales, and the kerogen is considered as pore infilling material, and not as part of the load bearing matrix. The authors state that at a porosity of 50% the rock behaves as a fluid suspension. This is clearly not the case in this study, as the porosity of the measured rock samples is almost 50%, and the moduli plot much higher than Reuss bound (softest possible pore geometry). Furthermore, even if the kerogen were to be included in the solid matrix, it still deviates from the experimental data. For example, Figure 44 shows a combination of Krief's relations with a background matrix modelled using the Backus method. The analysis shows that even the best-fit 'A' and 'B', 2 and 1 (respectively), cannot fit the model to the experimental data, hence the inapplicability of this method.

Another type of modeling is matrix homogenization methods, which introduce rock constituents based on different approaches, as explained below. Few common methods have been examined by Goodarzi *et al.* (2016; 2017), all of which have the basic form of:

$$\mathbb{C}_{hom} = \mathbb{C}_0 + \sum_{i=1}^{N} f_i(\mathbb{C}_i - \mathbb{C}_0) * \mathbb{A}_i \ , \tag{76}$$

where $\mathbb{C}$ is the stiffness matrix of the rock ('hom'), the background matrix ('0'), and each inclusion ('i'). The $\mathbb{A}_i$ of each homogenization method is different, where it includes different approaches for the introduction of inclusions into the background matrix. They all require determination of Hill's shape tensor $\mathbb{P}_i$ of each phase (combination of Green's function with $\mathbb{C}_i$), as well as the concentration of each type of inclusions. For example, the Dilute Scheme uses $\mathbb{A}_i = \left[\mathbb{I} + \mathbb{P}_{I_i}^0 * (\mathbb{C}_i - \mathbb{C}_0)\right]^{-1}$ to model the simplest case of a background matrix with inclusions that have no mechanical interaction between them. A similar method, the Mori-Tanaka method, accounts for mechanical interaction between the inclusions. These two methods can model a limestone with a calcite background matrix, and predominant vuggy porosity; high porosity is better represented by the Mori-Tanaka method and low porosity by the Dilute Scheme method. Another possibility is to use the Self-Consistent Scheme (Ortega, Ulm and Abousleiman 2007; Wetzel, Kempka and Kühn 2017), in which each inclusion is assumed to be embedded in an unknown homogenized medium. The homogenized moduli are solved iteratively, with model

inputs of volume fraction, shape tensor and stiffness matrix of each phase. Although this method may seem to have the highest potential for accurate predictions, it is somewhat unfavorable due to the high amount of input parameters. For example, calcite may occur as visible fossils, varying from equant to flat, and include intra-particle voids. It may as well occur as fine grains. Quantification and parametrization of each occurrence is very hard to perform accurately, especially when these features vary with depth. Moreover, it is undesirable to have a large amount of input variables, especially where most of them are postulated. On the other hand, it seems that a suitable matrix homogenization method has the best odds to fully characterize a VTI medium. It is noted here that further research in this direction should explore the best-fit homogenization method, combined with multiple microstructure scan (e.g. BSEM) and high-quality image processing.

Rock physics modeling of chalks has been performed traditionally using Hashin-Shtrikman bounds for stiffest and softest pore geometries. These bounds have always been considered better than the Voigt and Reuss bounds because they narrow the range of possible moduli at specific volumetric proportions of phases in the rock. The models which are usually jointed with the HS bounds are Marion's BAM and "Iso-frame". As mentioned earlier, the main disadvantage in the "Iso-frame" approach is the requirement of determination of solids effective bulk and shear moduli (K_s and μ_s, respectively). The solid phase includes both the minerals and the organic material, thus the effective solids moduli depend on the organic content. It is hard to determine the appropriate averaging method of effective solids moduli (e.g. Voigt, Reuss, VRH, Backus), because it is practically impossible to obtain a direct measurement of them. The averaging method is usually selected based on trial and error of different methods, and eventually finds the value that is best-fitted to the experimental data. In that sense, the heuristic approach by Marion is in favor, because only the relative location between the HS bounds is used, assuming it is independent of the fluid composition. This model is not restricted to any physical concept other than that, so there is no necessity in further assumptions to quantify the elastic moduli. That being noted, the "Iso-frame" model is a subject for further research which should include more pairs of measured moduli at dry and fluid-saturated conditions, to find the appropriate averaging method for solids effective moduli. If the "Iso-frame" is well-constrained, then it is preferable.

The reasons why the "HS kerogen" model was invented at the course of this study are: 1) the HS approach is suitable for a composite of multiple-phases in numerous case studies; 2) there is a necessity in a model that involves a key microstructural feature, e.g. matrix-supporting phases; 3) it is advantageous to use a model with the minimum possible assumptions; and 4) this model can be easily implemented in modules of prospecting programs designed for analysis of well-logs and seismic surveys. The main pitfall of the "HS -kerogen" model is that it solves the vertical moduli alone, and cannot indicate the anisotropy and moduli in other directions.

2.9 Conclusions

This chapter laid the foundations of rock physics analysis of an organic-rich chalk. It is the first comprehensive rock physics study conducted on a high-porosity VTI organic-rich rock. It accounts for the anisotropic nature of this rock, expressed by the elastic properties, strength, and permeability. The conclusion of this chapter may be divided into two main subjects: the proposed innovational approaches and the characterization of the physical properties of the Ghareb-Mishash chalk.

Listed below are the main novel approaches, developed and presented at the course of this study:

"HDC-TIES" approach Static elastic parameters are derived reliably using the HDC-TIES procedure, designed here for a single triaxial experiment on a vertically-oriented VTI rock sample. Using the experimentally derived values of E_v, ν_v, K and Ω, it is now possible to compute the stiffness constants C_{33}, C_{13} and $C_{11}+C_{12}$, and determine ranges of C_{11}, C_{12} and C_{66}. This procedure is believed to be useful where: 1) compression test data require repeated analyses; 2) multiple specimens from the same core yield inconsistent results; and 3) core material is limited.

"Hydrostatic strain ratio", Ω A new anisotropy parameter is defined: "hydrostatic strain ratio", denoted by Ω. It describes the anisotropic response of a VTI material during hydrostatic compression as function of the elastic constants C_{11}, C_{12}, C_{13}, and C_{33}. The Ω parameter is obtained experimentally using both static and dynamic measurements. The Ω is inversely related to Thomsen's ε and γ parameters. The obtained relationship between Ω and Thomsen's ε (i.e. $\Omega = \frac{1}{1+b_2\varepsilon}$) is fitted best with $b_2 = 3.58$. As described in the Section 2.8.1, the "hydrostatic strain ratio" is simply defined, easily measured, uniquely informative, and highly applicable. It is concluded

that wherever the elastic anisotropy of VTI rocks is investigated, it is desirable to measure or estimate Ω, along with Thomsen's anisotropy parameters.

"HS kerogen" model The "HS kerogen" model predicts well the bedding-normal dynamic moduli. This suggests that the kerogen is effectively dispersed in the matrix, thus forming a load-supporting phase in most of the samples. Backscatter SEM observations confirm that the fine-grained matrix is composed of kerogen-calcite mixture. The "HS kerogen" model is simple and useful for bedding-normal acoustic velocities, which are at the focus of this study. A broader description of the entire stiffness matrix of a high-porosity organic-rich chalk still requires further investigation. It is suggested that such investigation should combine a suitable matrix homogenization method with high quality image processing.

Mass and volume determination in organic-rich rocks A common mistake is found in the determination of mass, volume and density of phases in organic-rich rocks. This mistake was corrected by incorporating the porosity so that volumes of each solid phase are actually divided by the bulk volume. Another common mistake was indicated, where TOC was exclusively associated with kerogen, disregarding bitumen content. This mistake was corrected as well, by determining the bitumen concentration in the organic matter (B_c), using bitumen extraction experiments.

The Ghareb-Mishash chalk properties were analyzed using the developments and improvements shown above, as well as application cross-correlation of the properties and common practice methods. The main conclusions are:

1. Porosity decreases with depth in the Shefela basin due to natural compaction. The decrease rate within the Mishash Formation is higher than in the overlying Ghareb Formation because of increased cementation and calcite recrystallization.
2. There is no relationship between porosity and organic content, despite the high abundance of organic material. This leads to two important conclusions- kerogen should be considered as matrix component and not as a pore-infill material; organic content does not enhance the compaction rates.
3. The static and dynamic moduli depend primarily on the volumetric sum of porosity and 50% of the kerogen content. The use of 50% porosity-like effect of the kerogen also leads to the

smooth appearance of the "HS kerogen" curve. Second-order effects are induced by porosity-reducing mechanisms, like compaction and cementation.

4. The dynamic C_{33} and C_{55} of the dry rock are properly derived by combining the Hashin-Shtrikman bounds with Marion's BAM fluid substitution model, given the corresponding brine-saturated values.
5. Mechanical anisotropy reduces the vertical Poisson's ratio (ν_v). The sensitivity of vertical Poisson's ratio to anisotropy is increased in high porosity source rocks.
6. Permeability depends on both organic content and porosity. High organic content is associated with increased inter-particle pore size; hence the permeability increases in organic-rich samples. Permeability anisotropy is related to porosity because it improves the horizontal pore connectivity more than the vertical permeability.
7. Dynamic moduli are consistently higher than static moduli mostly due to a non-linear dissipative response of porosity, microfractures, and inter-granular contacts to static loading (higher strain amplitudes). Kerogen introduces a clay-like effect by lowering the DSMR.
8. There is no clear effect of organic content on the poroelastic stiffness coefficients 'w' and 'β'. The poroelastic coefficients mimic the soft geometrical arrangement of the particles in the matrix.
9. As in other source rocks, elastic anisotropy is related to microstructural features such as bedding-parallel alignment of minerals and kerogen particles. The relationships between the anisotropy parameters in the Ghareb-Mishash chalk are similar to those of other organic-rich rocks.
10. Mechanical strength of the Ghareb-Mishash chalk is similar, but somewhat lower, than in chalks of the same porosity but with no or negligible organic matter content. Both compressive strength and tensile strength depend on the porosity of specimen. Horizontal tensile strength is higher by a factor of ~1.5 than the vertical tensile strength, due to preliminary bedding-parallel discontinuities.

3 Thermal maturation effects on rock properties

3.1 Introduction

In this chapter the effect of thermal maturation is explored. The organic material in the Ghareb-Mishash section from the Shefela basin is at the immature end of the thermal maturation scale. Thermal maturation can be induced experimentally by pyrolysis. To examine the effect of maturity on the rock properties, four pyrolysis experiments were performed to simulate different maturity levels. Table 7 summarizes the maturity parameters of each of the five batches of core samples (ordered by increasing maturity): immature, Ex41 (early-mature), Ex43 (mature 1), Ex47 (mature 2), and Ex42 (over-mature). The properties of the immature samples are referred to as the pre-pyrolysis data, and they are the reference in the examination of pyrolysis-induced changes in rock properties. The post-pyrolysis properties measured in this study include the petrophysical properties (porosity, density, permeability), and the acoustic velocities. TOC measurements and pyrolysis experiments were performed by IEI Ltd., in the organic geochemistry laboratory at the department of Geological and Environmental Sciences at BGU. Bitumen extraction and maturity indicators are taken from Kutuzov (2017), who performed an organic geochemistry analysis on the same Ghareb-Mishash native state and post-pyrolysis core samples. After the presentation of the results, a discussion is dedicated to the observations, the RPM strategy, and the question of how representative the pyrolysis experiments are of the natural maturation process.

This chapter lays the methodology of the pyrolysis experiments and a qualitative description of the material transformation. Then the petrophysical evolution upon pyrolysis is described. Afterwards, acoustic measurements, BSEM observations and rock physics modeling are presented. Rock physics analysis is performed using the approaches described in the previous Chapter (typically “HS kerogen” and BAM). In this Chapter a greater attention is dedicated to geophysical prospecting using rock physics templates.

Table 7: Maturity parameters of the studied maturity levels: the T_{max}, HI and maximum pyrolysis temperature are measured values. The %Ro and maturity level are estimated from the measured maturity indicators.

Lab ID	T_{max} [°C]	HI [mg_{HC}/g_{TOC}]	HI/HI_0	Maximum pyrolysis temperature [°C]	%Ro		Maturity level, modified from Vernik (2016)	Classification (this study)
imm	412	652	1	0	0.32	I	Compaction, Early-Methane	Immature
ex41	421	650.5	~1	276	0.64*	II/III	Onset of bitumen generation, H_2O expulsion/Advanced oil generation	Early -mature
ex43	432	550	0.84	304	0.78*	IVa	Peak of bitumen generation	Mature 1
ex47	445	313.5	0.48	338	1.07*	IVb	Peak of oil generation	Mature 2
ex42	496	55	0.08	377	1.57*	Vi	Dry-gas	Over-mature

* Vitrinite reflectance equivalent values ($\%R_{o,eq.}$), determined using the "Easy $\%R_o$" method (Kutuzov 2017)

3.2 Pyrolysis experiments (induced maturation)

Pyrolysis experiments were performed in order to induce thermal maturation in the Ghareb-Mishash chalk samples. Unconfined pyrolysis experiments were performed in semi-open dry pyrolysis reactors (Model 4622 Parr Instruments Inc., USA). All of the experiments were performed with backpressure at atmospheric level throughout the entire process, and are therefore referred to as "unconfined". The maturation was induced in the absence of water (as in Ryan *et al.* 2010), hence the pyrolysis is defined as "anhydrous". The experiments were conducted in the organic geochemistry laboratory at BGU. A schematic of the pyrolysis experiments is given in Figure 45. The immature core samples were placed in the pyrolysis reactors, and crushed rock powder was spread in the voids between the plugs to optimize temperature equilibration in the cell. The pyrolysis reactors were equipped with three band-shaped heating elements to maintain homogeneous temperature inside the cell. After sealing the cells, the samples were flushed several

times with nitrogen gas to expel all oxygen from rock pores and dead spaces in the system. In case there is any oxygen presence during heating, a combustion of the organic material occurs instead of pyrolysis-induced maturation. Heating was conducted in two stages. First, temperature was elevated rapidly (25°C/day) up to ~200°C and kept for several hours to ensure soaking of the interstitial and rock pore water. Subsequently, the temperature was elevated at a slow rate (2°C /day), until the target temperatures were achieved. The four pyrolysis experiments were terminated at different maximum temperatures (Table 7). In Ex42, that represents the over-mature stage, heating was stopped when volatile hydrocarbon detection at the outlet declined to zero. After reaching the maximum heating temperature, the samples were cooled back to room temperature, the post-pyrolysis samples were collected and kept in a desiccator to maintain dry conditions. It should be stated here, that the pyrolysis experiments produced considerable amounts of volatile hydrocarbons, among other fluids (e.g. carbon dioxide, hydrogen sulfide, water). In this study, the focus is dedicated to the residual rock properties, but other studies were dedicated to the properties of the fluid products as well (Rosenberg *et al.* 2017; Kutuzov 2017).

Table 7 presents geochemical data of the five maturity levels investigated in this study. The measured maturity parameters are the Rock-Eval pyrolysis parameters T_{max} and hydrogen index (HI). Because the HI depends on the initial hydrocarbon total potential and on the type of the organic matter, Table 7 includes the HI/HI_0 ratio, where HI_0 represents the immature reference HI. The native state immature samples are characterized by low T_{max} of ~412°C, as determined from Rock-Eval analysis. This corresponds to vitrinite reflectance of $\%R_o$=0.32 (Kutuzov 2017). Because vitrinite is nearly absent in the rock, no direct vitrinite reflectance was measured on the pyrolyzed samples but $\%R_o$ were calculated by Kutuzov (2017) from the pyrolysis heating history using the "Easy $\%R_o$" model (Sweeney and Burnham 1990). In this study, vitrinite reflectance values that were estimated rather than measured are designated by "$\%R_{o,eq.}$". The description of each of the studied maturity levels is given in Table 7, including qualitative description by Vernik (2016), and maximum pyrolysis temperatures.

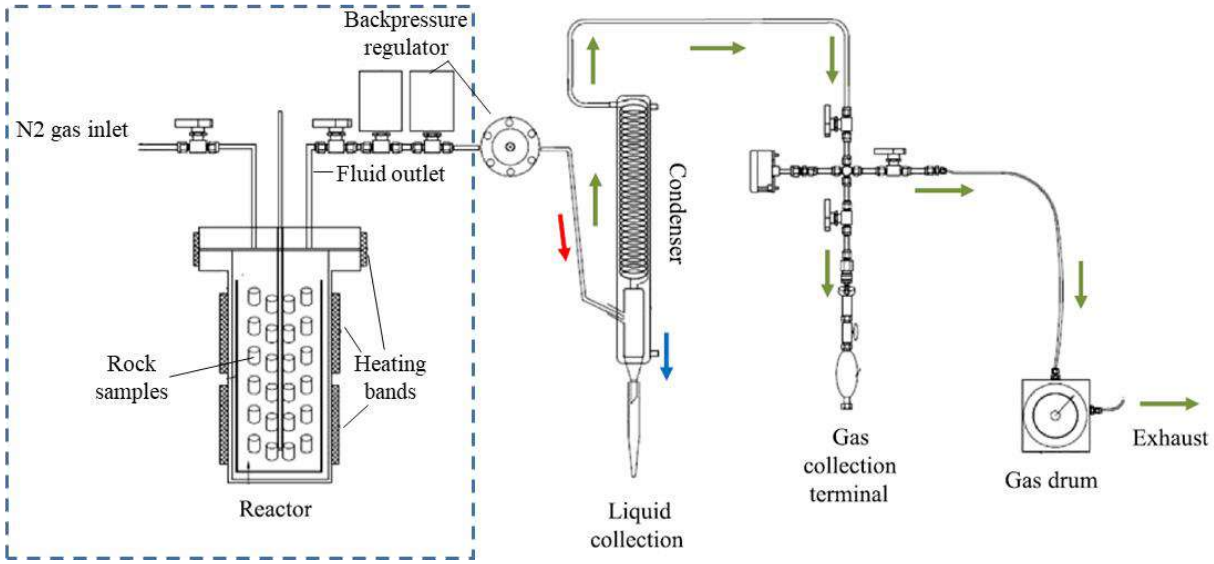

Figure 45: Scheme of the pyrolysis experiments, modified from Rosenberg et al. (2017). This study was focused on the part delineated by the dashed rectangle.

3.3 Petrophysical properties

The petrophysical properties of the rock are closely related to the geochemical parameters that indicate thermal maturity (Table 7). Before presentation of the results and their analysis, it is important to note that the post-pyrolysis material contains significant amounts of bitumen that affect the petrophysical measurements. By considering the bitumen as a pore-filling liquid, the true porosity (ϕ_t) is the sum of the measured porosity and the bitumen fraction ($\phi_t = \phi_{meas.} + f_{bit}$). Similarly, the solids density obtained from the Coreval30 measurements ($\rho_{s,meas.}$) reads the bitumen content as a solid phase, and the true solids density ($\rho_{s,t}$) is corrected using ϕ_t:

$$\rho_{s,t} = \frac{\rho_{s,meas.}(1 - \phi_{meas.}) - \rho_{bit} f_{bit}}{1 - \phi_{meas.} - f_{bit}} \ . \qquad (77)$$

For convenience, throughout this thesis ρ_s and ϕ are the solids density and porosity measured by the Coreval30. The values corrected for bitumen content are referred to as "true solids density" and "true porosity", designated by $\rho_{s,t}$ and ϕ_t.

The analysis starts by plotting the measured solids density versus TOC and fitting the trend line in Equation (17). In Figure 46, the results of the five maturity stages are presented along with the regression coefficients. The minerals density is found to be well represented using a value of 2.74 g/cc, except in the over-mature stage where pyrite precipitation took place (ρ_{pyrite}~5 g/cc), and

the minerals density was estimated to 2.77 g/cc. The minerals density remains nearly constant throughout the pyrolysis due to the stability of calcite and the low clay content of the rock samples. Using the fitting of the data to Equation (17), the values of minerals density and a_2 are used to estimate the density of the organic material, while assuming reasonable carbon weight percentage in the organic matter (C_{pr}). The evaluation of C_{pr} is based on reasoning that maturation causes hydrogen depletion and increased carbon concentration in the kerogen. However, these assumptions are associated with an uncertainty in C_{pr} of 5%. Then, the procedure described in Section 2.2.1 is performed to obtain densities of the organic material, bitumen concentration and kerogen density. The results of this analysis are presented in Table 8. Except for the very high kerogen density in the over-mature Ex42 samples, the results are in conformity with reported densities of organic material. The abnormality of Ex42 will be corroborated in the discussion of this chapter.

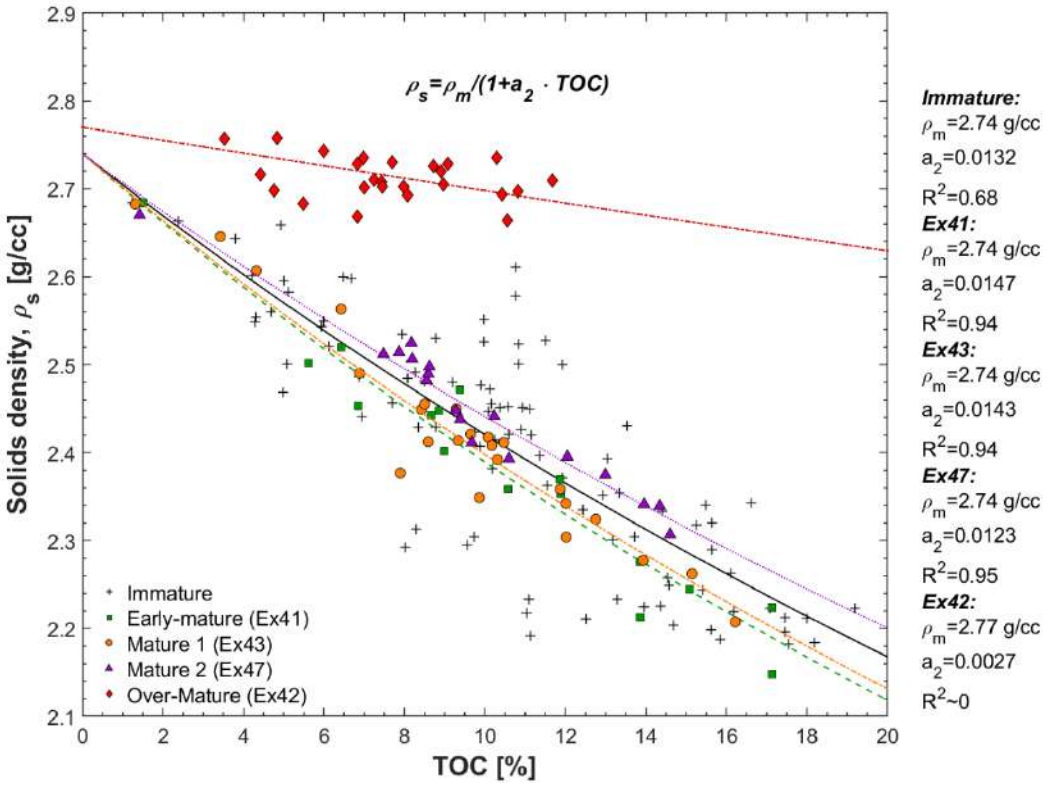

Figure 46: Solids density versus TOC at each maturity stage: measured results and the best fit trends, that follow the equation at the top of the figure. Regression coefficients are summarized in the list (right). A constant minerals density (ρ_m) was set constant at 2.74 g/cc at all maturity stages, except the over-mature stage where ρ_m=2.77 g/cc, due to pyrite precipitation.

Table 8: Geochemical parameters of the studied pyrolysis-induced maturity levels: the five maturity levels are presented: immature (imm), early-mature (Ex41), mature 1 (Ex43), mature 2 (Ex47) and over-mature (Ex42). The TOC conversion ratios were obtained by plotting post-pyrolysis TOC versus pre- pyrolysis TOC of the core plugs, and fitting a linear trendline. The average sulfur weight percentage (TS) was obtained by LECO measurements. The values of carbon percentage in the organic matter (C_{pr}) are assumed, but an error of ~5% is accounted for in further calculations. The organic matter density (ρ_o), bitumen concentration in the organic matter (B_c), and kerogen density (ρ_k) are calculated by considering the error on C_{pr}, as well as 0.02 g/cc error in mineral density and 0.0005 error in a_2.

Lab ID	TOC conversion ratio [%]	Average TS [%wt.]	C_{pr} [%]	ρ_o [g/cc]	B_c [g/cc]	ρ_k [g/cc]
imm	-	2.12	70	1.42 ± 0.12	0.06 ± 0.01	1.45 ± 0.17
ex41	3.3	1.56	70	1.35 ± 0.11	0.30 ± 0.03	1.48 ± 0.14
ex43	8.5	1.47	73	1.34 ± 0.10	0.39 ± 0.04	1.53 ± 0.14
ex47	16	1.03	78	1.40 ± 0.11	0.48 ± 0.04	1.72 ± 0.16
ex42	32	0.89	85	2.26 ± 0.81	0.29 ± 0.11	2.76 ± 1.00

The trends in Figure 47a show that the bitumen causes negligible underestimation of the porosity at the immature (~3%) and over-mature (~0%) rock samples, and a significant underestimation (~11-14%) of the true porosity at the early-mature and mature states. The estimated liquid permeability is always lower than the gas permeability (Figure 47b). The magnitude of that difference depends on the mean pore radius (Equation (8)), assuming the proportionality factor 'c' remains constant. The resulting mean pore radius of the immature rock is at the order of 500 nm, while that of the pyrolyzed samples is on the order of 200-300 nm. This decrease in mean pore size is presumed to originate from increase of bitumen content and generation of small-sized pores. Both mechanisms indicate the increase of true porosity. As kerogen reduces its volume through pyrolysis, the new bitumen originates at the same locations in the matrix. The new bitumen may as well invade the pre-existing porous network and narrow the pore throats. Hence, permeability is influenced by two opposite mechanisms: porosity enhancement that increases permeability, versus narrowing and plugging of pore throats by bitumen, that lower the permeability. Note that if bitumen is considered as a fluid, then the permeability measurements of the post-pyrolysis

samples yield the effective permeability to nitrogen and not the total permeability, as the bitumen interferes with nitrogen flow.

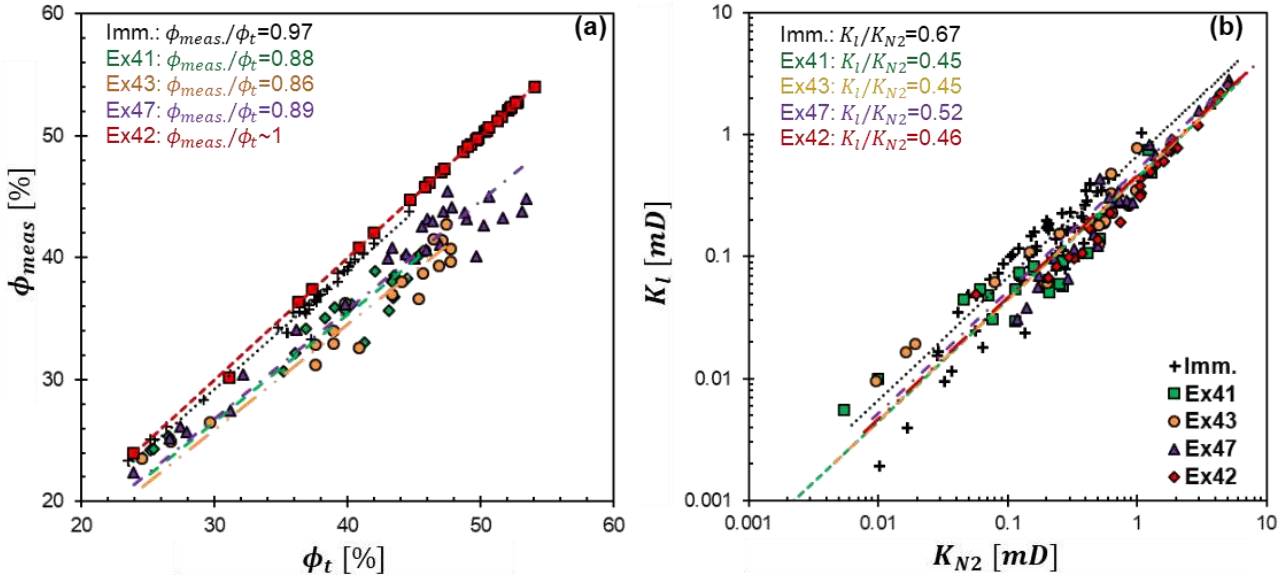

Figure 47: Experimental deviations due to bitumen content: a) The measured porosity for Ex41 (early mature), Ex43 (mature 1), and Ex47 (mature 2) ($\phi_{meas.}$) underestimates the true porosity (ϕ_t) due to bitumen content in the pores, thus corrected by: $\phi_t = \phi_{meas.} + f_{bit}$. The underestimation in Ex42 (over-mature) is negligible. Bitumen volume fractions (f_{bit}) are calculated using Equation (20) and B_c in Table 8. b). The ratio of apparent liquid permeability to gas permeability (K_L/K_{N2}) at each maturity stage reveals a decrease with mean pore size. This is caused by development of small-sized pores during pyrolysis and bitumen content that plugs the pores.

Figure 48 shows the evolution of both the measured and corrected ρ_s during induced maturation. The measured solids density values (Figure 48a) indicate insignificant change at the Ex41, Ex43 and Ex47, which is masked by bitumen contained in the samples, while the over-maturity in Ex42 is expressed by constant ρ_s of ~2.7g/cc. The corrected densities reveal a clearer trend of matrix densification with increasing maturity (Figure 48c). The change in solids density is a function of the initial organic richness of the samples, as shown in Figure 48b, d. A similar picture is revealed in Figure 49 by observing the evolution in the measured porosities. Porosity enhancement upon unconfined pyrolysis is clearly seen, with dependence on the initial organic content. The porosity enhancement of over-mature samples is identical to the values reported by Bisnovat (2013), established from three different pyrolysis experiments using plugs from the Aderet well. The observations of porosity enhancement align with the TOC conversion ratio, reported in Table 8.

The permeability also increases with pyrolysis-induced maturation (Figure 50), because of the porosity enhancement, and thus the similar patterns. The gradual change in relative volume of each phase through pyrolysis-induced maturation is schematically presented in Figure 51.

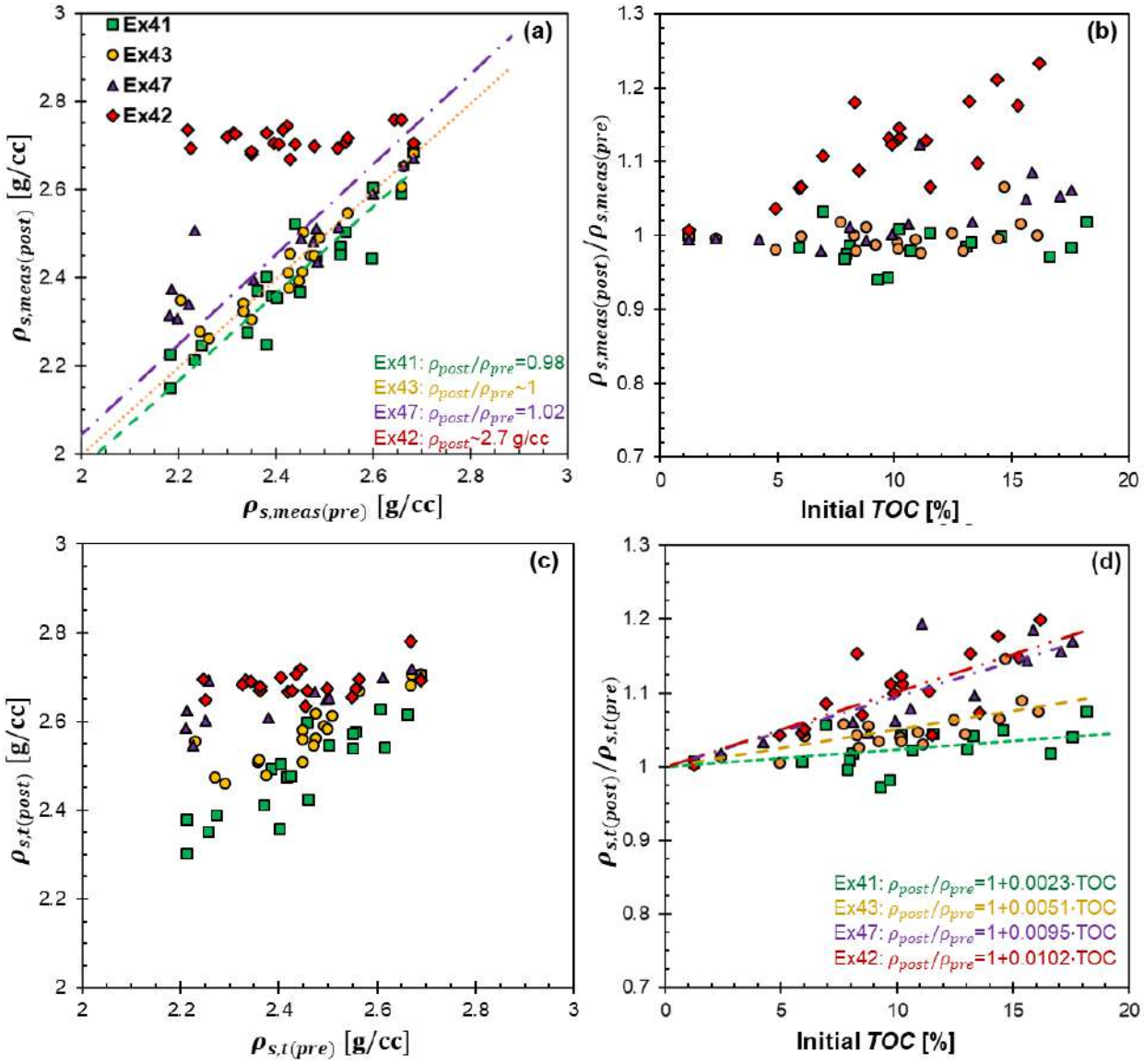

Figure 48: The changes of solids density upon pyrolysis: due to bitumen generation, the solids density from the measurements, ρ_{meas}, appears to remain nearly constant at the early-mature and mature levels (a). The initial organic-richness dominates the ratio of measured solids density after and before pyrolysis, $\rho_{s,post}/\rho_{s,pre}$ (b). Where the bitumen is excluded from the material, consistent increases in true solids density ($\rho_{s,t}$) upon maturation is observed (c), and the initial organic-richness clearly affects that increase (d).

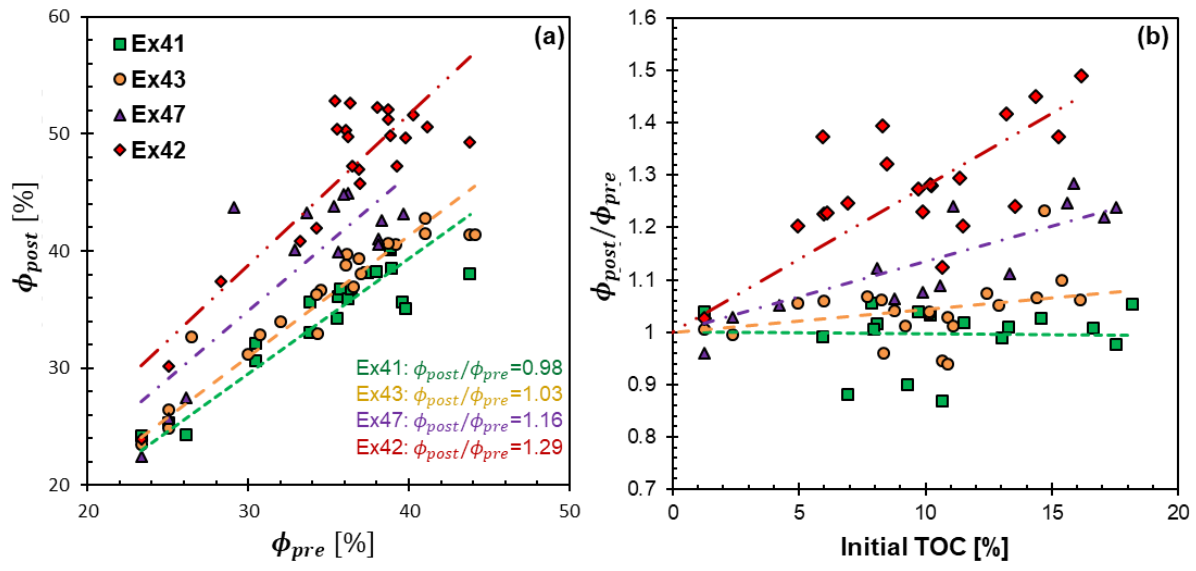

Figure 49: The changes in porosity upon pyrolysis: the four maturation groups exhibit gradual increase in porosity enhancement ratios, due to progressive conversion of solid organic matter to fluid products (a). The relative increase in porosity, represented by (ϕ_{post}/ϕ_{pre}), seems to depend no only on the maturity level but also on the initial organic content(b).

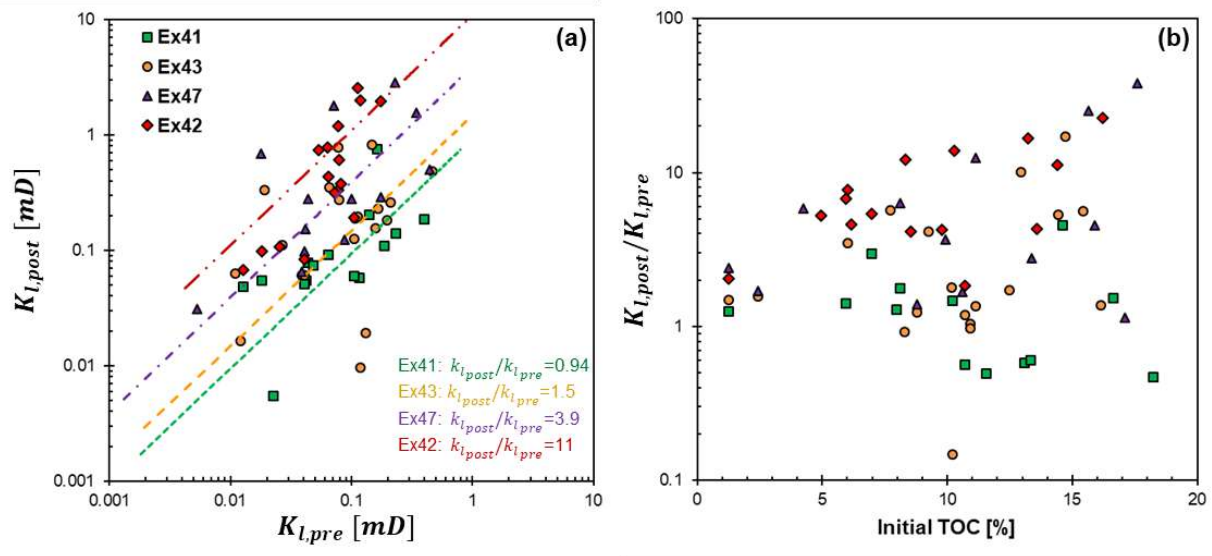

Figure 50: The changes in permeability upon pyrolysis: the four maturation groups exhibit gradual increase in liquid permeability (K_l) enhancement ratios, due to progressive porosity enhancement (a). The scatter is somewhat large due to second-order effects such as microstructural heterogeneities and bitumen content. The ratio of permeability after and before pyrolysis, $K_{l,post}/K_{l,pre}$, shows a positive correlation with the initial organic content (b).

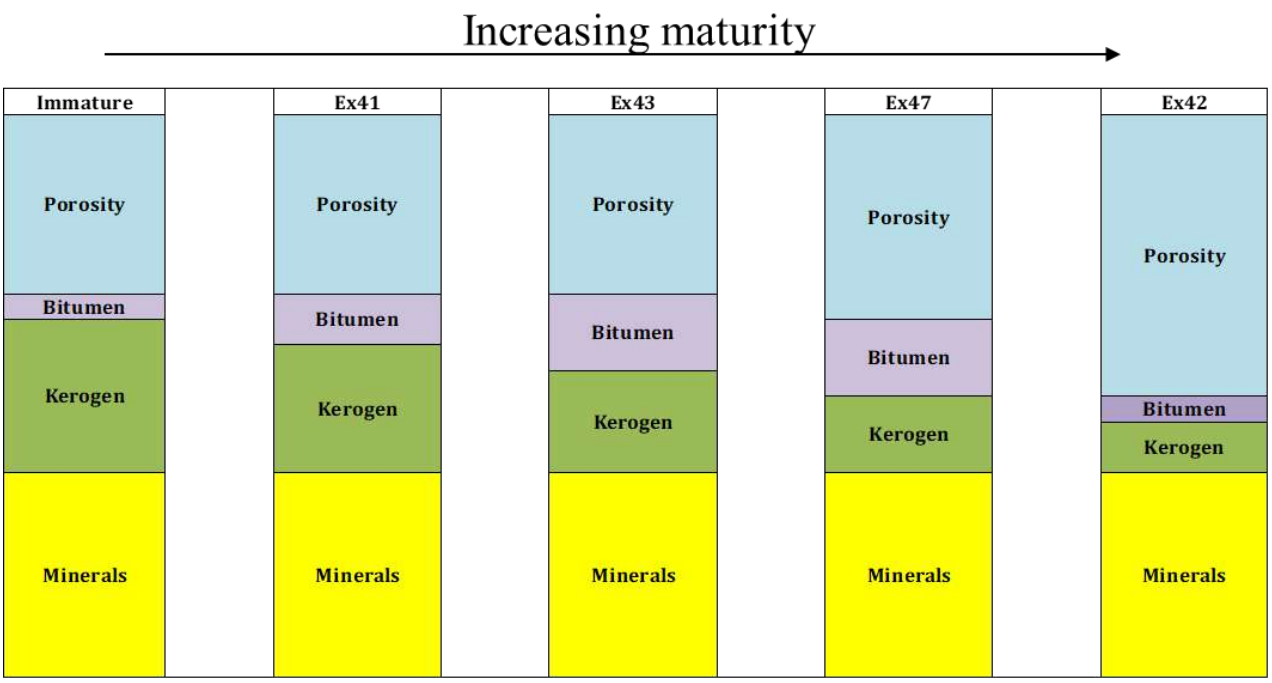

Figure 51: Scheme of the relative volume changes in the rock upon unconfined pyrolysis.

Some observations can be made by integrating these results. In the early-mature Ex41 samples, the TOC conversion is very low, i.e. most of the initial organic matter remained within the sample, but a portion of it is transformed into bitumen. This results in permeability decrease, while negligible changes in the measured porosity and solids density are seen. The apparent liquid permeability decreases where initial TOC is greater than 10% (Figure 50b). In the mature-1 Ex43 samples, the TOC loss is ~8.5% (Table 8), and there are higher amounts of bitumen in the samples. Thus, Ex43 exhibits a continuation of organic decomposition and pore development process, initiated in the early-mature Ex41. The continuation of this trends is observed in the mature-2 Ex47 samples, where TOC reduced by ~16% (Table 8) and bitumen contents are considerably high. The organic matter at this maturity level is about half kerogen and half bitumen (volumetrically). The porosity enhancement at this stage is distinct despite the high bitumen saturation. The permeability increases by a factor of ~4 (Figure 50a). The true solids density at this stage is much closer to the ultimate density (2.7 g/cc). In the over-mature Ex42 samples, the severe TOC loss (32%) and high kerogen density cause the solids density to be nearly constant at the ultimate value. At this stage, there are significant amounts of pyrobitumen, also known as petroleum coke, which are solid residues formed during the pyrolysis. Although it would be beneficial to quantify pyrobitumen content, it was unavailable at the course of this study. Because the pyrobitumen is a solid residue,

it is included in the kerogen phase. Pyrobitumen has a density of 2.0-2.2 g/cc, thus causes the density increase of the post-pyrolysis organic matter. The shrinkage of the organic phase results in porosity increase by a factor of ~1.29 and permeability enhancement by an order of magnitude. The progressive porosity enhancement through pyrolysis causes the permeability to increase exponentially (Figure 52). Note that all post-pyrolysis results are consequent to unconfined pyrolysis; the impact of the lack of backpressure will be elaborated in the Discussion section.

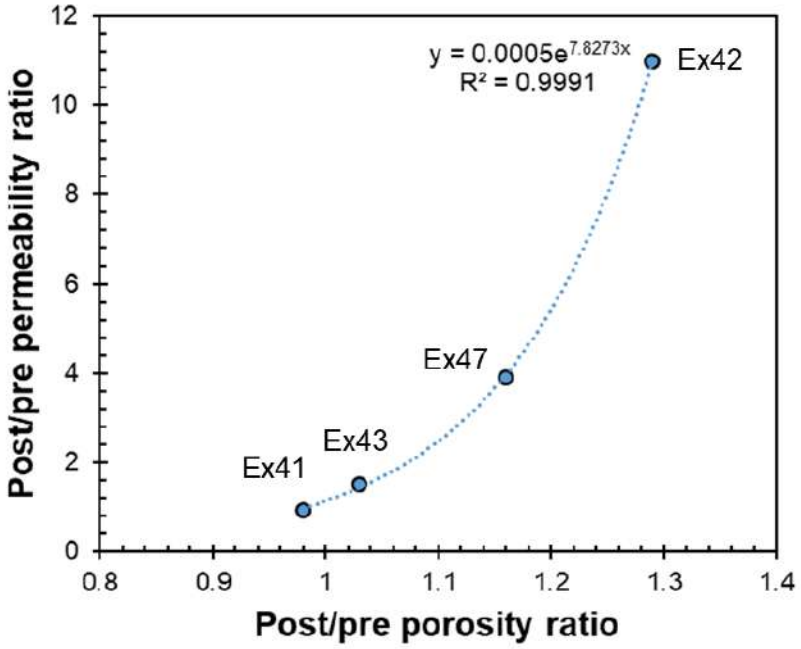

Figure 52: Permeability versus pyrolysis-induced changes in porosity: the four pyrolysis experiments show the continuous increase in permeability as function of porosity enhancement. As the post-pyrolysis to pre-pyrolysis ratio of porosity increases, the same ratio of permeability increases exponentially.

3.4 Acoustic properties

The acoustic velocities of the pyrolyzed samples simulate the effect of thermal maturity on the elastic behavior of the rock. The acoustic velocities of the immature pre-pyrolysis core plugs were presented in the previous chapter. Post-pyrolysis acoustic velocities were mostly measured in the bedding normal direction, using brine-saturated plugs. To allow for an examination of anisotropy and fluid saturation effects, some samples from each maturity level were measured also in the bedding parallel direction and using dry core plugs. In order to establish a more accurate reference

of the immature rock, results by Gordin *et al.* (in prep.) of bedding-normal and bedding-parallel velocities of dry plugs are added to the dataset here. Their data also include measurements from a naturally-matured occurrence of the Ghareb-Mishash chalk in the Southern Golan Heights basin. All of the results are summarized in Table 9.

The changes in the bedding-normal velocities V_{p0} and V_{s0} (referred here as Vp and Vs) upon pyrolysis are presented in Figure 53. Acoustic velocities were measured at the same stress levels as in the immature state. The petrophysical changes observed in the previous section result in the Vp decrease with increasing maturation, because P-waves are known to be sensitive to porosity and pore-filling fluids. The S-waves are less sensitive to changes in porosity but more to variations in the solid matrix, as they cannot travel through fluids. Consequently, the Vs increases with maturation (Figure 53), despite the significant porosity enhancement. This is due to the densification and stiffening of the solid phase. These trends of the acoustic velocities are directly connected to the elastic moduli in the bedding-normal direction: vertical oedometer modulus (C_{33}) and vertical shear modulus (C_{55}). These elastic moduli are used here to examine and calibrate effective elastic medium theories for the purpose of modeling and geo-prospecting of a source rock with high porosity.

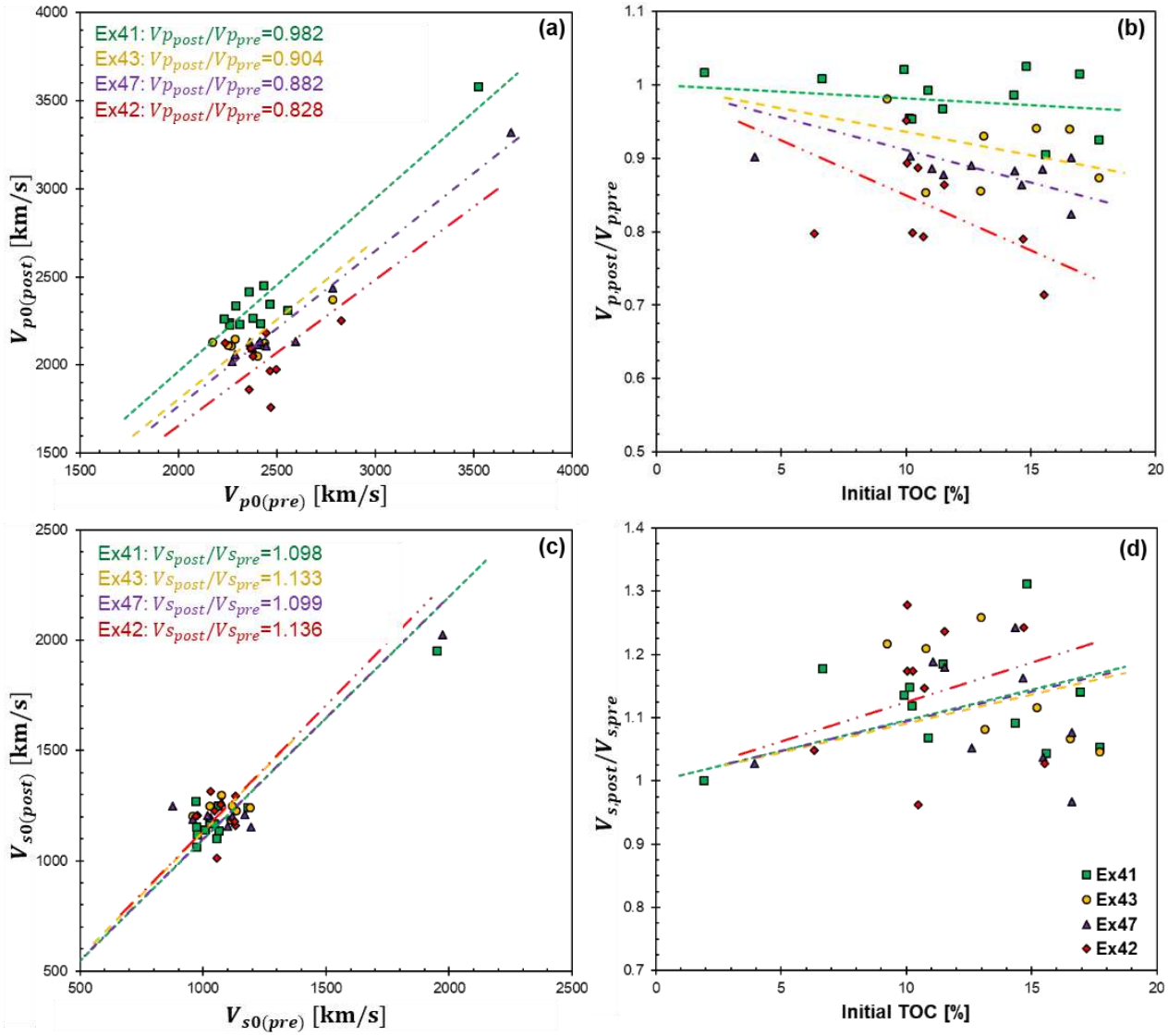

Figure 53: Changes in acoustic velocities with maturation, induced by four pyrolysis experiments: P-wave velocities generally decrease (a) due to porosity enhancement, increased bitumen content, and kerogen volume loss. S-wave velocities increase due to increased stiffness of the residual kerogen, despite the counter-acting effect of increased porosity and bitumen content (c). The changes in the acoustic velocities are dictated by the initial organic richness (b, d).

Table 9: Acoustic measurements in the bedding-normal and bedding-parallel directions, of brine-saturated and dry plugs. Data by Gordin *et. al* (in prep.) of dry rock velocities are included, to examine the applicability of the models to naturally-matured organic-rich chalk and enlarge the acoustic anisotropy dataset at the immature stage.

Batch	Depth [m]	Porosity [%]	TOC [%]	Dry density [g/cc]	Vp 0 [km/s]	Vs 0 [km/s]	Vp 90 [km/s]	Vs 90 SH [km/s]
Ex41, sat	334.5	38.02	9.81	1.46	2.27	1.12		
	337.5	39.63	9.82	1.48	2.21	1.14		
	343.1	38.14	10.51	1.47	2.24	1.14		
	345.1	35.63	8.66	1.57	2.30	1.27	2.65	1.44
	360.5	35.06	6.43	1.64	2.45	1.25		
	368.6	38.52	10.58	1.45	2.23	1.12	2.50	1.26
	384.8	38.46	11.08	1.45	2.23	1.15		
	403.2	38.26	13.86	1.40	2.23	1.06		
	429.5	40.79	16.40	1.31	2.26	1.17		
	444.8	34.33	17.13	1.44	2.23	1.24	2.53	1.29
	460.3	35.41	9.58	1.43	2.33	1.14		
	462.1	36.75	15.08	1.42	2.31	1.10		
	490.5	34.20	9.93	1.56	2.36	1.22		
	493.6	40.29	9.90	1.44	2.35	1.17		
	528.6	36.13	8.85	1.56	2.45	1.30		
	559.3	29.10	14.32	1.60	2.41	1.27		
	609.5	24.25	1.87	2.03	3.58	1.95		
Ex41, dry	345.1	35.63	8.66	1.57	1.81	1.17	2.58	1.55
Ex43, sat	331.5	42.20	8.46	1.42	2.13	1.25	2.42	1.31
	350	36.97	10.31	1.51	2.08	1.19		
	366.6	40.14	11.87	1.41	2.05	1.20		
	372.5	38.30	10.17	1.48	2.15	1.22		
	406.2	38.79	12.01	1.44	2.11	1.23	2.47	1.33
	434.5	39.00	13.93	1.38	2.15	1.25		
	440.8	37.79	16.22	1.38	2.12	1.24	2.44	1.33

Batch	Depth [m]	Porosity [%]	TOC [%]	Dry density [g/cc]	Vp 0 [km/s]	Vs 0 [km/s]	Vp 90 [km/s]	Vs 90 SH [km/s]
Ex43, sat, continued	453	37.34	15.15	1.43	2.11	1.18		
	519	22.98	3.43	2.04	2.58	1.37		
	541	33.40	6.88	1.66	2.25	1.26	2.78	1.40
	553.2	32.65	9.86	1.59	2.37	1.30	2.69	1.42
	609.5	23.49	1.31	2.05			3.67	1.99
Ex43, dry	331.5	42.20	8.46	1.42	1.88	1.20	2.43	1.38
	406.2	38.79	12.01	1.44	1.76	1.16	2.47	1.21
	440.8	37.79	16.22	1.38	1.78	1.15	2.29	1.34
	541	33.40	6.88	1.66	2.20	1.50	2.80	1.82
	553.2	32.65	9.86	1.59	2.12	1.48	2.62	1.75
Ex47, sat	354.1	41.03	8.55	1.46	2.13	1.25		
	366.6	42.82	12.05	1.37	2.12	1.19	2.47	1.28
	374.3	42.55	9.39	1.40	2.07	1.19		
	399.1	39.49	12.30	1.35	2.11	1.20		
	410.3	30.40	6.28	1.81	2.48	1.38		
	420.4	44.96	8.19	1.38	2.12	1.25		
	431.5	44.30	14.60	1.29			2.37	1.36
	434.5	44.15	13.95	1.32	2.06	1.20		
	438.7	43.23	12.99	1.35	2.13	1.21		
	448.9	40.25	13.95	1.40	2.14	1.15		
	469.2	43.81	10.60	1.34	2.02	1.15		
	498.7	42.55	9.28	1.47	2.10	1.21		
	553.2	36.17	9.67	1.54	2.44	1.26		
	588	26.80	4.80	1.91	2.99	1.67	3.54	2.11
	590	25.45	3.30	1.97	3.32	2.02	3.65	2.06
Ex47, dry	366.6	42.82	12.05	1.37	1.62	1.23	2.38	1.37
	431.5	44.30	14.60	1.29	1.58	1.11	2.19	1.26
	588	26.80	4.80	1.91	2.68	1.67	3.47	2.09
	590	25.45	3.30	1.97	3.13	1.82	3.63	2.10

Batch	Depth [m]	Porosity [%]	TOC [%]	Dry density [g/cc]	Vp 0 [km/s]	Vs 0 [km/s]	Vp 90 [km/s]	Vs 90 SH [km/s]
Ex42, sat	334.5	48.96	7.84	1.39	2.05	1.20	2.32	1.31
	339.1	49.80	6.82	1.37	2.12	1.25		
	348.1	47.23	8.97	1.42	1.89	1.22	2.43	1.25
	393	50.16	7.13	1.35	2.09	1.01	2.27	1.31
	399.1	45.79	6.83	1.45	2.18	1.31		
	425.5	52.30	10.55	1.27	1.76	1.16		
	457.5	50.43	8.66	1.35	1.95	1.20	2.22	1.27
	466.2	52.23	8.72	1.30	2.10	1.25		
	493.6	51.58	6.97	1.32	1.97	1.23		
	495.7	41.41	4.30	1.58	2.25	1.18	2.53	1.38
	509.8	47.01	6.58	1.45	1.98	1.22	2.31	1.21
	533.8	49.68	7.28	1.36	1.98	1.29	2.35	1.26
	559.3	45.44	9.99	1.42	1.86	1.20	2.39	1.33
Ex42, dry	334.5	48.96	7.84	1.39	1.60	1.09	2.08	1.31
Gordin, dry	400	38.11	10.00	1.49	2.62	1.32	3.05	1.397
	462	36.33	13.30	1.45	2.50	1.27	2.85	1.352
	515	35.79	9.70	1.58	2.64	1.47	3.31	1.646
	553	28.78	9.30	1.67	2.54	1.36	2.88	1.598
	913	28.05	9.20	1.72	2.70	1.62	3.12	1.681
	920	27.34	11.50	1.69	2.75	1.61	3.16	1.705
	1031	2.79	11.60	2.07	3.34	1.83	3.91	1.939
	1039	9.87	8.40	2.10	3.54	2.10	4.05	2.244
	1059	13.87	5.10	2.18	3.77	2.16	4.31	2.454
	1198	0.33	4.40	2.43	4.50	2.38	4.92	2.510
	1280	1.24	5.50	2.29	4.40	2.46	4.95	2.733

The oedometer and shear moduli of the Ghareb-Mishash chalk, at all maturity levels, align over a single trend when plotted against the kerogen-factored porosity, using kerogen influence factor of κ=0.5 (Figure 54, Figure 55). This observation conforms with the behavior of the static and dynamic moduli of the immature rock. The empirical exponential fits in Figure 54 and Figure 55 seem to yield good predictions of the vertical and horizontal moduli of the rock, in both dry and brine-saturated conditions. These relationships are expected to enable moduli predictions at greater burial depths. The applicability of these relationships will be tested in the discussion of this chapter.

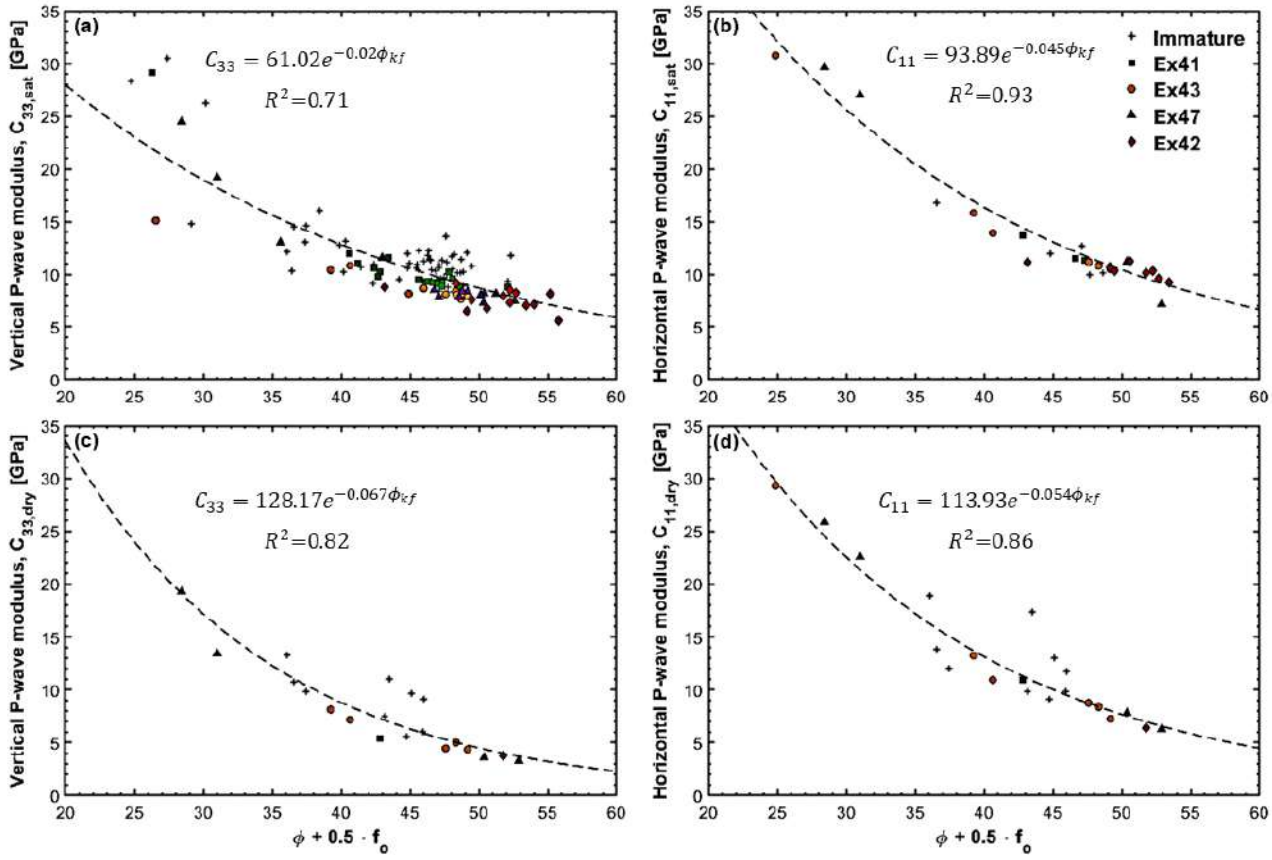

Figure 54: Oedometer (P-wave) moduli versus kerogen-factored porosity: the vertical (left) and horizontal (right) oedometer moduli in brine-saturated (upper panel) and dry conditions (lower panel) depend strongly on the kerogen-factored porosity (ϕ_{kf}), using a kerogen influence factor of κ=0.5. At all maturity levels, the moduli are best-fitted using an exponential regression.

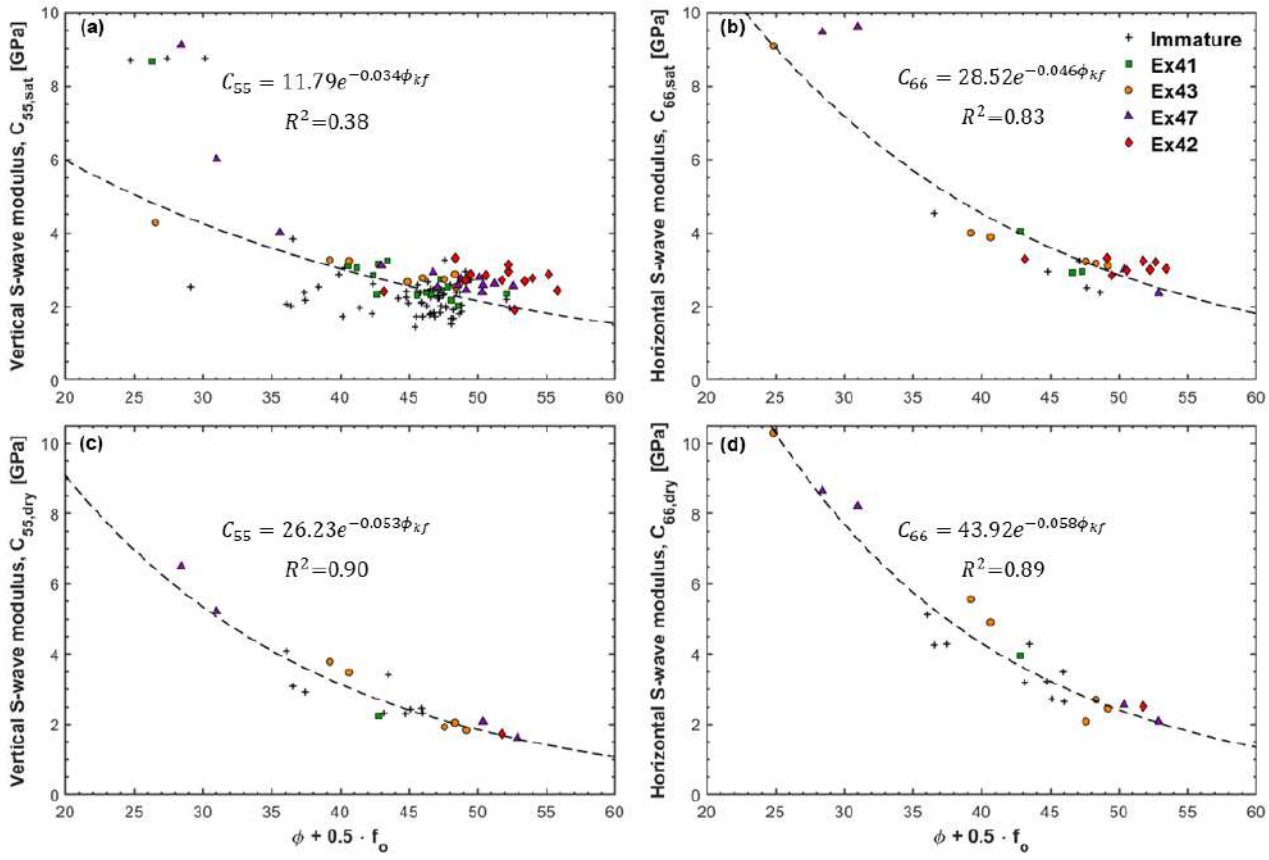

Figure 55: Shear (S-wave) moduli versus kerogen-factored porosity: the vertical (left) and horizontal (right) shear moduli in brine-saturated (upper panel) and dry conditions (lower panel) depend strongly on the kerogen-factored porosity (ϕ_{kf}), using a kerogen influence factor of κ=0.5. At all maturity levels, the moduli are best-fitted using an exponential regression.

The anisotropy of organic-rich rocks is known to be influenced by maturation. The effect of pyrolysis-induced maturation is investigated here using Thomsen's anisotropy parameters ε and γ for P-wave and S-wave anisotropy (respectively), as well as the hydrostatic strain ratio Ω. The anisotropy is examined with respect to the two primary factors: porosity and organic content. Figure 56 shows the anisotropy parameters in both dry and brine-saturated conditions are barely influenced by the organic content (including the kerogen and the bitumen). While typical organic-rich rocks increase their anisotropy with organic content, here there is no such trend. In fact, the organic content does not seem to cause any effect on the anisotropy of the pre-pyrolysis and post-pyrolysis material. Even more surprising, when the bitumen content is excluded from the solid phase, the kerogen content seems to decrease the anisotropy (Figure 57). However, where anisotropy is plotted versus porosity a positive trend is indicated, especially in the P-wave

anisotropy of the dry rock (Figure 58). The new anisotropy parameter- "hydrostatic strain ratio", is examined in Figure 59. It is calculated using Equation (52), with the measured values of C_{11}, C_{33}, C_{55} and C_{66}, and approximated values of C_{13} (Equation (72)). The Ω results also indicate that the anisotropy of the dry rock is increased with porosity, while in brine-saturated conditions Ω does not relate to either porosity or organic content (Figure 59). From the acoustic anisotropy results it is observed that: 1) the maturity level is not reflected by the anisotropy; 2) anisotropy is increased in dry conditions; 3) the brine-saturated Ghareb-Mishash chalk is weakly anisotropic (Thomsen's $\varepsilon < 0.2$). It is believed that all of these observations are due to the high porosity of the Ghareb-Mishash chalk, which gets even more porous upon pyrolysis-induced maturation. Yet, the interrelationship between Ω and ε in dry conditions (Figure 60) is described well using the empirical equation found in Figure 41b. In brine-saturated conditions the scatter is smaller, and the regression coefficient increases to $b_2 \sim 5$.

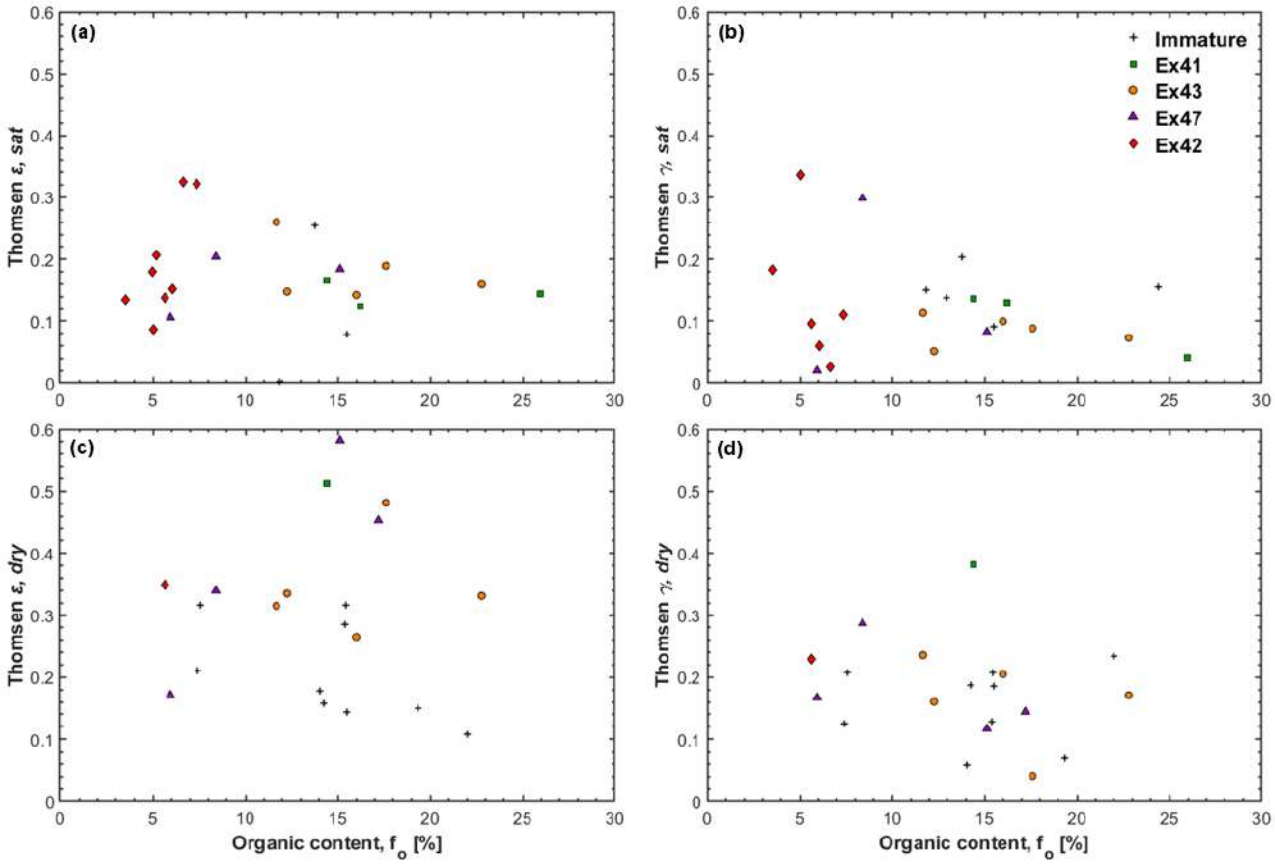

Figure 56: Thomsen anisotropy parameters and organic content: no clear dependence on organic content is seen. P-wave anisotropy (left) and S-wave anisotropy (right) at all maturity levels, in both saturated (upper panel) and dry conditions (lower panel) are presented.

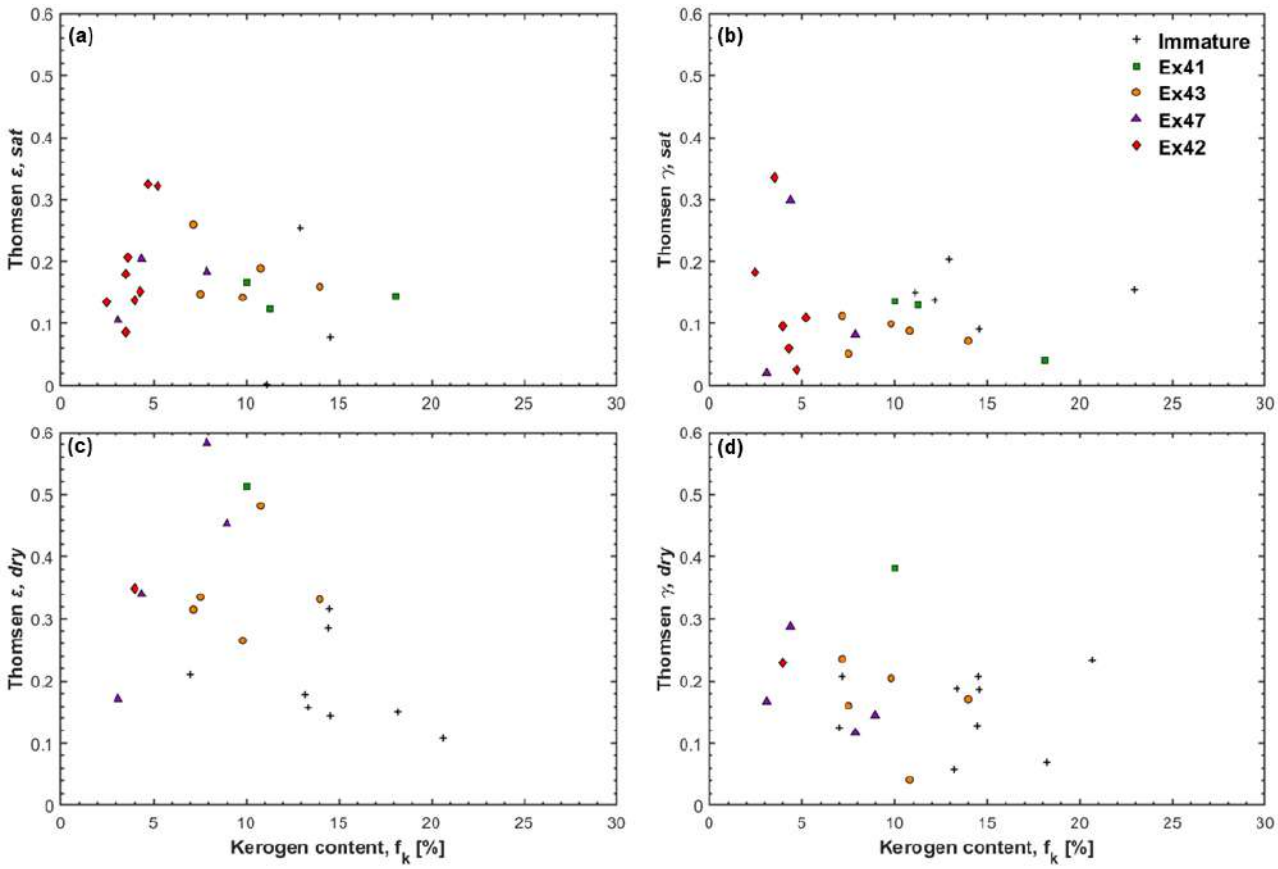

Figure 57: Thomsen anisotropy parameters and kerogen content (bitumen content is excluded): no clear dependence on kerogen content is seen. P-wave anisotropy (left) and S-wave anisotropy (right) at all maturity levels, in both saturated (upper panel) and dry conditions (lower panel) are presented.

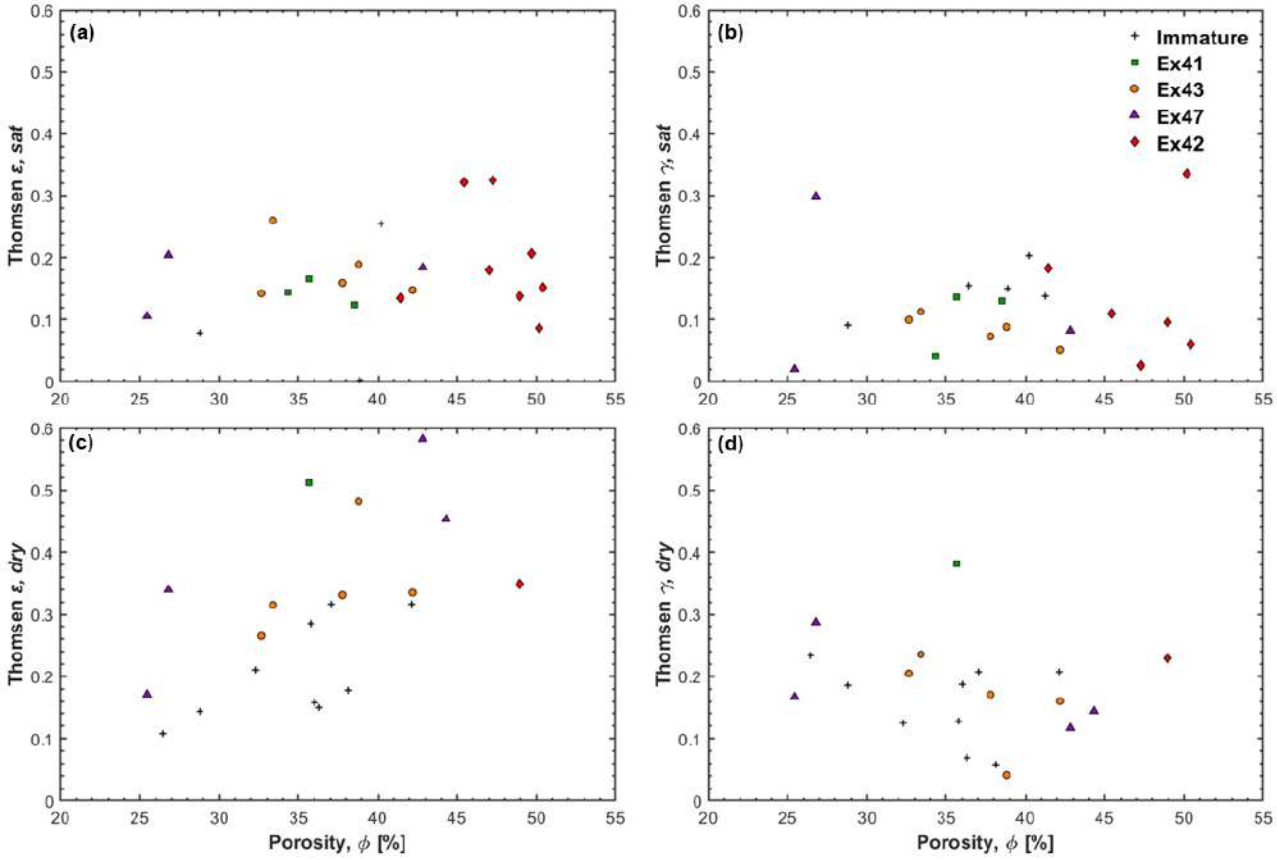

Figure 58: Thomsen anisotropy parameters versus porosity: P-wave anisotropy (left) and S-wave anisotropy (right) at all maturity levels, in both saturated (upper panel) and dry conditions (lower panel). Positive trend is indicated, most distinctly in the P-wave anisotropy of the dry rock samples (c).

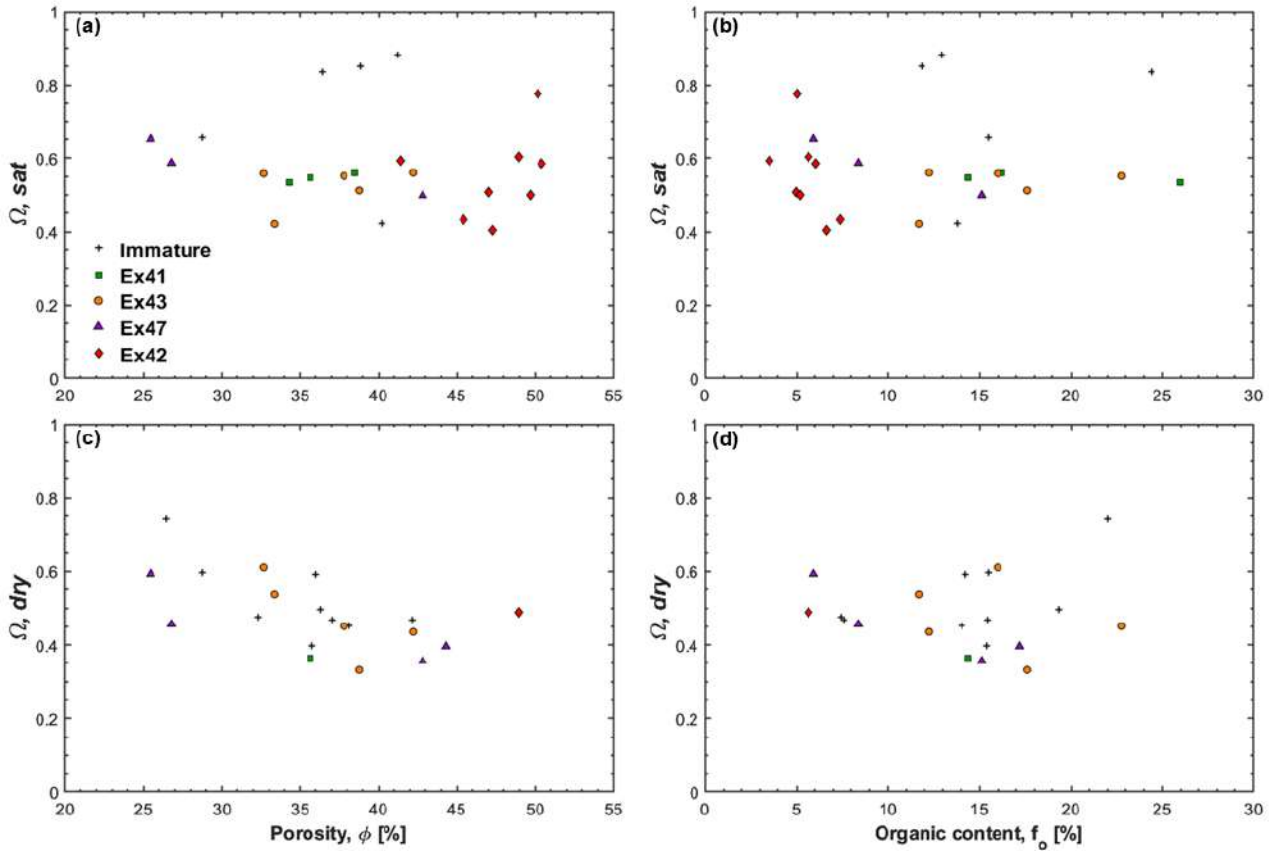

Figure 59: Hydrostatic strain ratio of native state and pyrolyzed Ghareb-Mishash chalk, in saturated (upper panel) and dry conditions (lower panel), plotted against the porosity (left) and organic content (right). The hydrostatic strain ratio was calculated using measured C_{11}, C_{33}, C_{55} and C_{66}, and approximated C_{13} from Equation (72).

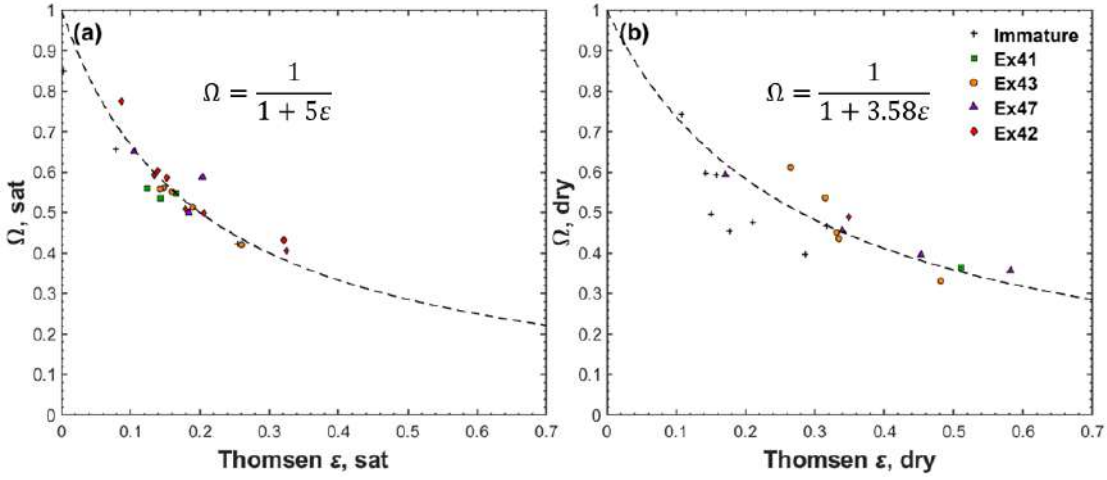

Figure 60: Ω versus Thomsen's ε: the hydrostatic strain ratio exhibits different relationships with Thomsen's ε in saturated (a) and dry conditions (b). No difference between the maturity levels is observed.

3.5 Rock physics analysis

Using the petrophysical and acoustic properties, rock physics models can be constructed in order to draw some inferences on rock properties. The analysis here is very similar to that in the previous chapter, only here the changes in the organic phase are focused. The porosity enhancement is assumed to take place within the organic material, as kerogen is partially transformed to bitumen, oil and gas. Thus, the kerogen particle structure, which initially had very little porosity, becomes more porous and the produced fluids are inside these pores. In the pyrolysis experiments, oil and gas were expelled, as well as other fluid products, while bitumen remained within the sample. The high boiling point of bitumen causes it to remain inside the sample during pyrolysis, release the volatile fraction and ultimately turn to coke in the over-mature state. The organic phase may be modelled using Kuster-Toksöz model (Kuster and Toksöz 1974; Y. Li *et al.* 2015), describing spherical inclusions of bitumen embedded in the kerogen:

$$K_{om} = \frac{K_k + \left(B_c \frac{K_{bit} - K_k}{K_k + \frac{4}{3}\mu_k} P_{kb} \right) \frac{4}{3}\mu_k}{1 - B_c \frac{K_{bit} - K_k}{K_k + \frac{4}{3}\mu_k} P_{kb}} , \tag{78}$$

$$\mu_{om} = \frac{\mu_k + \left(B_c \frac{\mu_{bit} - \mu_k}{\mu_k + \zeta_k} Q_{kb} \right) \zeta_k}{1 - B_c \frac{\mu_{bit} - \mu_k}{\mu_k + \zeta_k} Q_{kb}} , \tag{79}$$

where $P_{kb} = \frac{K_k + \frac{4}{3}\mu_k}{K_{bit} + \frac{4}{3}\mu_k}$ and $Q_{kb} = \frac{\mu_k + \zeta_k}{\mu_b + \zeta_k}$ are geometrical factors of spherical inclusions of bitumen in kerogen, and ζ_k is given by Equation (25). As before, bitumen bulk and shear moduli are taken from Han *et al.* (2006). Here, the determination of kerogen modulus is even harder since there is very little documentation of intrinsic kerogen moduli at increased maturation. Atomic force microscopy measurements of kerogen at three different maturity levels (Emmanuel *et al.* 2016) are used for modeling, by assuming Poisson's ratio of kerogen is ~ 0.35. The kerogen moduli and the Kuster-Toksöz calculated moduli are summarized in Table 10. The elastic moduli of minerals are the same as in the immature state, except that in the over-mature state pyrite precipitation slightly increases the moduli of the minerals. In this study, the analysis considers dry and brine-

saturated pores. The effect of oil and gas saturation on the results will be investigated in the discussion.

Table 10: Elastic moduli of the kerogen and of organic material at each maturity level.

Maturity level	B_c [v/v]	K, kerogen [GPa]	μ, kerogen [GPa]	K, organic material [GPa]	μ, organic material [GPa]
Immature	0.06	7.1	2.4	6.9	2.3
Early-mature	0.303	10	4	7.2	2.6
Mature 1	0.386	18	6	9.5	3.3
Mature 2	0.479	18	6	8.2	2.8
Over-mature	0.294	18	6	11.0	3.8

The results are examined with respect to the kerogen-supported rock model, to identify microstructural changes. As seen in the previous chapter, the "HS kerogen" model predicts the vertical moduli of the immature rock. Here, the vertical moduli of the rock at each maturity stage are examined (Figure 61). Note that "HS kerogen" predictions already account for kerogen stiffening upon maturation and for bitumen contents. The "HS kerogen" predicted moduli of the rock are higher than the measured ones at each of the four maturity levels. This simply implies that upon unconfined pyrolysis-induced maturation, the matrix obtains softer geometrical arrangement. The mechanics of such softening is as follows: during the pyrolysis solid kerogen releases volatile HC; the residual kerogen reduces its volume, and turns denser and stiffer; because there is a volume loss of the solid phase, and due to the absence of confining pressure, the porosity of the plugs increases; the pyrolysis cell is flushed with nitrogen and vented, so that most of the generated fluid is expelled from the pore system, and nitrogen fills in. As a result, the chalk that was initially kerogen-supported, shifts gradually towards a suspended granular framework (i.e. less supported by minerals and kerogen, more supported by the pore fluid). For this reason, post-pyrolysis data points plot closer the lower HS bound, and the softening becomes more severe as maximum pyrolysis temperature increases (i.e. higher maturity level). The evolution of the S-waves, however, reveal an interesting phenomenon: increase in kerogen stiffness and density causes stiffening, which counteracts with the porosity enhancement. The increase in S-wave moduli is clearly reflected by the increase in Vs (Figure 53), however, S-wave moduli predictions using the "HS kerogen" model result in overestimations of ~10-35%, due to the porosity enhancement. The

"HS kerogen" predictions lead to significant overestimations of the P-wave moduli (~50-85%) in Ex 43, Ex47 and Ex42; smaller overestimations of the P- and S- wave moduli are seen in Ex41 (~30% and 18%, respectively). These observations indicate that upon unconfined pyrolysis-induced maturation, the porosity enhancement causes the P-waves to travel slower, because there is a substitution of kerogen by porosity. The S-waves are less sensitive to the porosity enhancement, but the change in the solid constituents is reflected more prominently. For this reason, the difference between the "HS kerogen" predictions and the measured C_{55} is smaller. This implication is also seen by the dependence of Vp/Vs ratio of the bedding-normal velocities on porosity (Figure 62). The porosity enhancement decreases the Vp/Vs ratio, partly because of the mechanism described here. The decrease in Vp/Vs is also related to kerogen stiffening that increases the S-wave modulus, while the P-wave modulus is much less influenced by this effect.

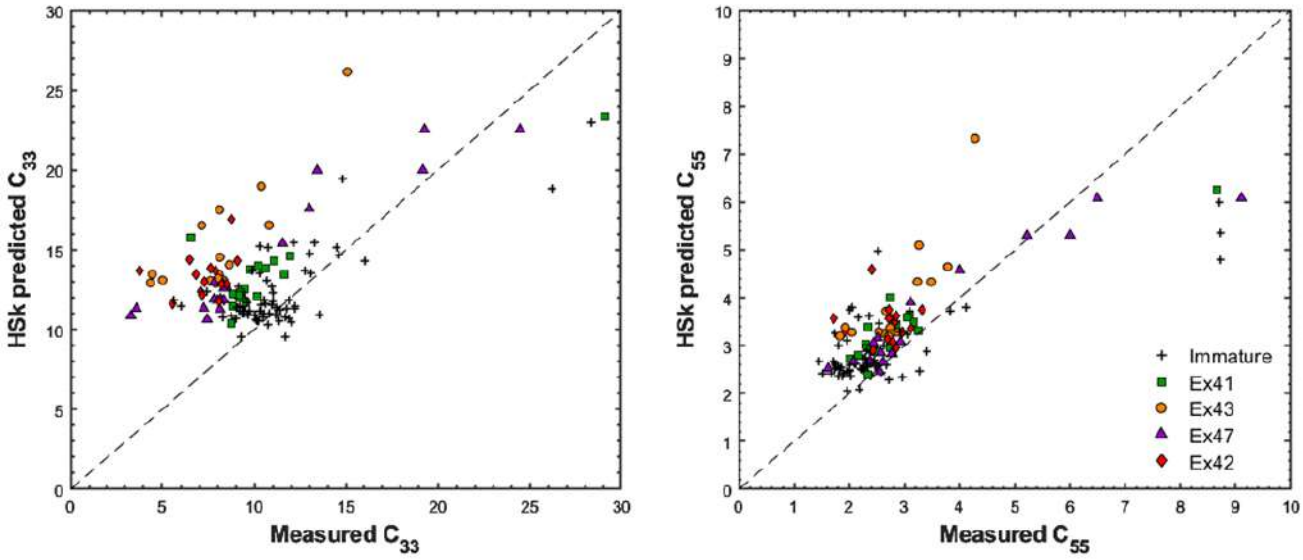

Figure 61: Source rock stiffness template of the Ghareb-Mishash chalk at different maturity levels: "HS kerogen" predicted values plotted versus the measured values of vertical P-wave modulus C_{33} (a) and S-wave modulus C_{55} (b), at each simulated maturity level. The P-wave moduli depart from a kerogen-supported matrix towards a fluid suspended matrix, with increasing pyrolysis-simulated maturity.

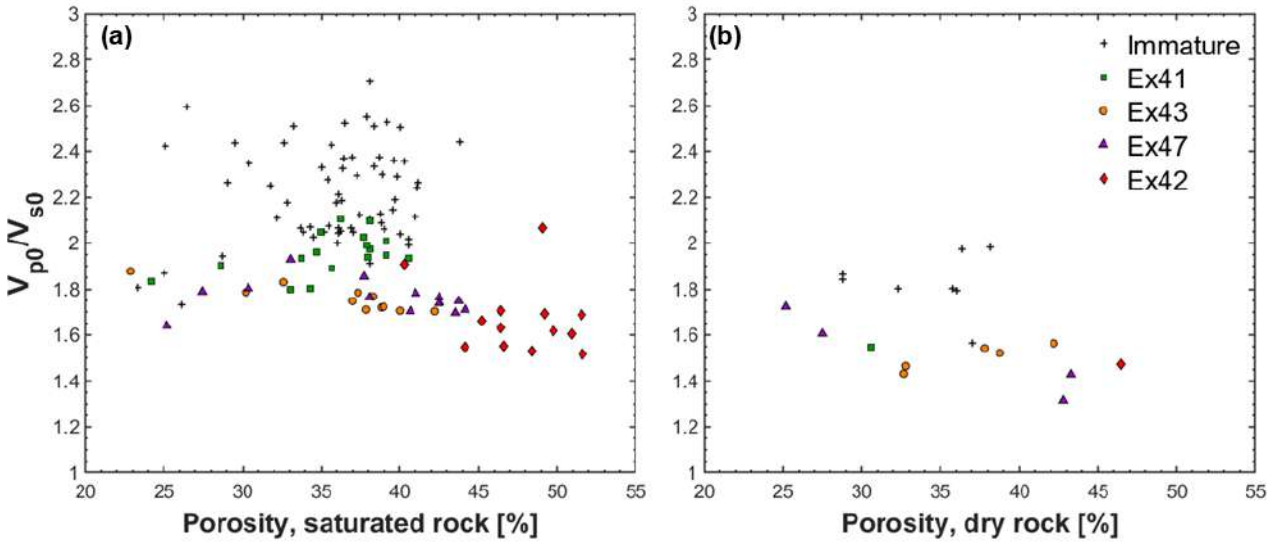

Figure 62: The Vp/Vs ratio of bedding-normal velocities of saturated (a) and dry core plugs (b) is decreased upon the porosity enhancement.

The geometrical arrangement evolution is best-described using the BAM normalized stiffness factors. Except some abnormally stiff samples from the deep organic-lean zone in the Zoharim section, most samples exhibit soft geometry in the bedding-normal direction, with $w \leq 0.3$. Figure 63 and Figure 64 show those bedding-normal (vertical) and bedding-parallel (horizontal) normalized stiffness factors versus porosity and organic content. It is seen that the w_{C33} and w_{C11} are somewhat affected by the porosity, while the organic content seems to have minor influence on them. As noted before, the S-wave moduli are less sensitive to porosity. Consequently, the w_{C55} and w_{C66} are constant at ~0.25 and ~0.3, respectively, at porosities higher than 30% and organic contents higher than 5%. The samples from the low porosity organic-lean zone are almost isotropic and much stiffer than the rest of the samples, with normalized stiffness factors of 0.4-0.55. Neither the porosity nor the organic content impose significant effect on the normalized stiffness factors of the S-wave moduli. These observations point to the key influencer in pyrolysis-induced maturation, that is the porosity enhancement. The organic matter has a limited influence because of the high porosity. These implications apply for the post-pyrolysis experiments, but they seem questionable in the case of natural maturation (see Discussion).

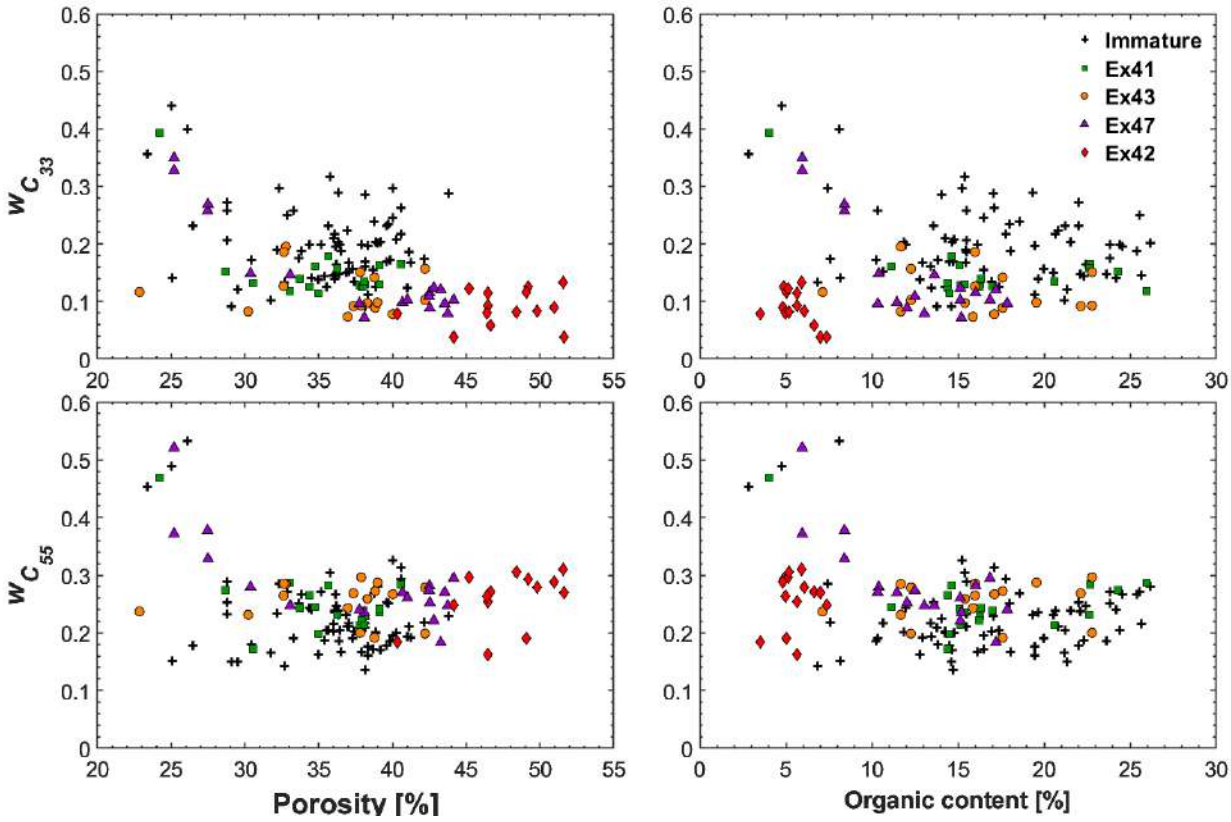

Figure 63: The BAM normalized stiffness factors ('w') of the Ghareb-Mishash chalk in the bedding-normal direction at different maturity levels: w of bedding-normal P-wave ($w_{C_{33}}$, upper panel) and S-wave moduli ($w_{C_{55}}$, lower panel), plotted versus porosity (left column) and organic content (right column). Trends are hardly seen, as results are fairly scattered

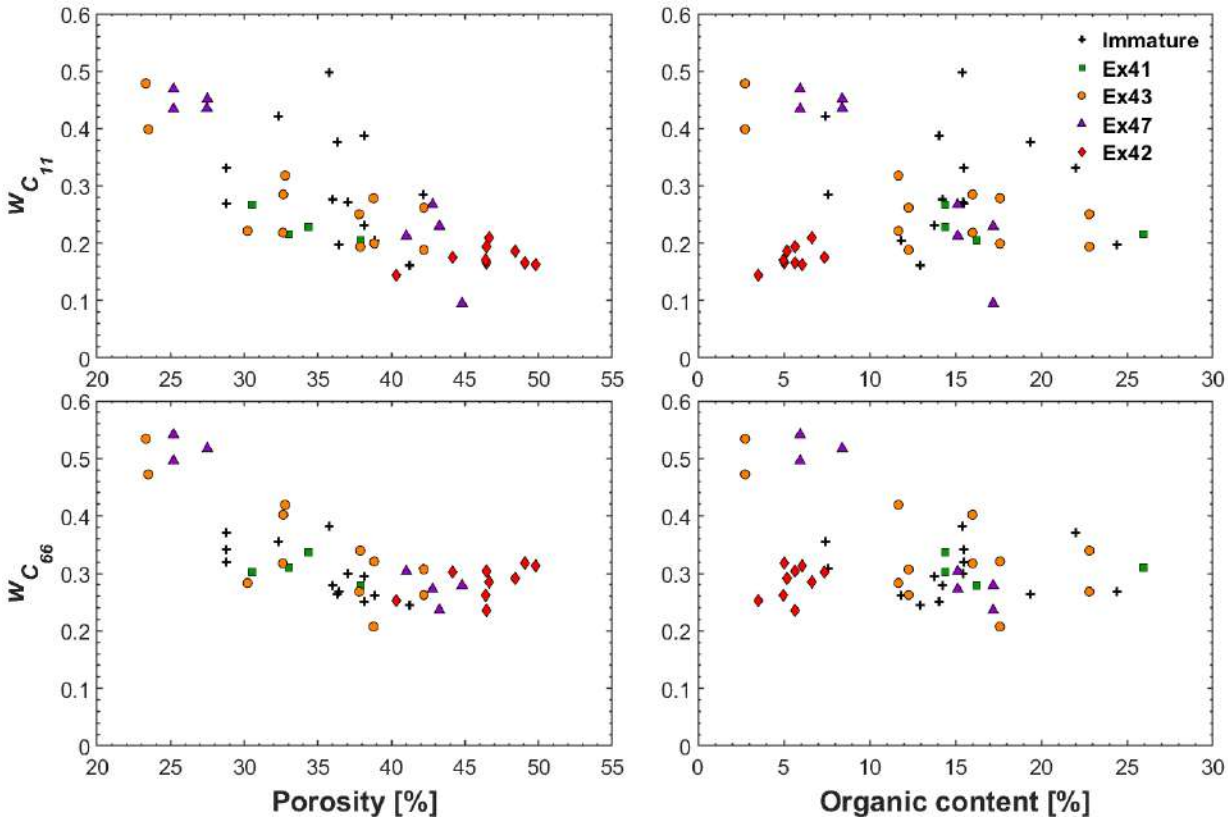

Figure 64: The BAM normalized stiffness factors ('w') of the Ghareb-Mishash chalk in the bedding-parallel direction at different maturity levels: w of bedding-parallel P-wave ($w_{C_{11}}$, upper panel) and S-wave moduli ($w_{C_{66}}$, lower panel), plotted versus porosity (left column) and organic content (right column). Trends are hardly seen, as results are fairly scattered

Two models are used here to investigate microstructural properties of the rock at each maturity stage. These models, in their essence, aim to predict the elastic moduli of the rock. One model is the "HS kerogen", which hypothesizes a kerogen-supported matrix, and the other model combines the HS bounds with Marion's BAM fluid substitution model ("HS+BAM"), which is calibrated to the results of the post-pyrolysis plugs. Other models may be attempted (e.g. Backus, Krief, SCA), but from the reasons described in Section 2.8.4 they seem less applicable here. In this section the analysis focuses on the vertical moduli C_{33} and C_{55} at brine-saturated conditions. Figure 65 shows C_{33} and C_{55} versus the kerogen-factored porosity ($\phi_{kf} = \phi + 0.5 \cdot f_o$). Because the moduli are plotted against ϕ_{kf}, "HS kerogen" and "HS+BAM" curves of minimum and maximum organic contents are calculated to delineate the range of model predictions. In addition, the exponential fits obtained in Figure 54 and Figure 55 are shown in Figure 65. The "HS+BAM" model uses the measured values of C_{33} and C_{55} to create a best-fit model with an average normalized stiffness

factor ($w_{C_{ii}}$). It is no surprise that the "HS+BAM" gives the best estimations because it uses the average normalized stiffness factors that were derived from the results (Table 11). The "HS kerogen" model overestimates the moduli of the post-pyrolysis samples because of the porosity enhancement. As seen before, single exponential regression can describe the experimental data quite well, independently of the maturity level. However, the exponential trends cannot distinguish between the contribution of porosity and organic material separately. Therefore, the discussion of this chapter mainly focuses on the "HS kerogen" and "HS+BAM" models. Important to note that hydrocarbon saturation should naturally occur during thermal maturation, and thus lower the modulus of the pore-fluid (K_f) and the stiffness constants of the rock. The lowermost value K_f can attain is where the rock is entirely saturated with gas (as in dry samples). This is further addressed in section 3.7.

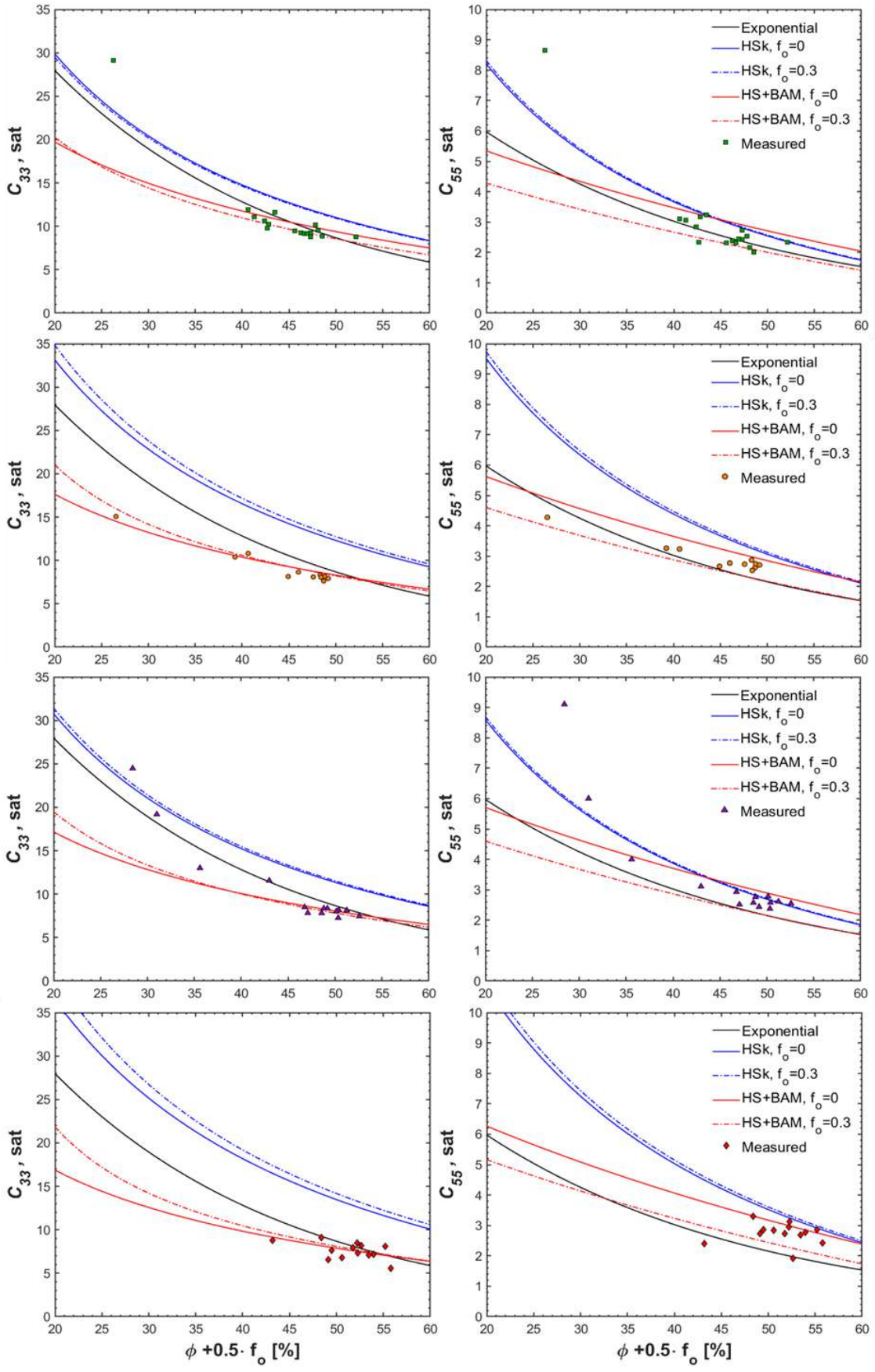
C_{33}, sat
C_{55}, sat
Exponential
HSk, f_o=0
HSk, f_o=0.3
HS+BAM, f_o=0
HS+BAM, f_o=0.3
Measured
ϕ +0.5· f_o [%]

Figure 65 (in the previous page): Models of moduli regression versus kerogen-factored porosity, at all maturity levels: modelled vertical P- wave (C_{33}, left column) and S-wave (C_{55}, right column) moduli are plotted versus the kerogen-factored porosity at brine-saturated conditions. From top row to bottom: Ex41 (early-mature, a and b), Ex43 (mature 1, c and d), Ex47 (mature 2, e and f) and Ex42 (over-mature, g and h). The modelled curves include: 1) "HS kerogen" predictions of zero and 30 % organic content (solid and dotted blue curves); 2) "HS+BAM" predictions of zero and 30 % organic content (solid and dotted red curves); and 3) estimations using the exponential regression from Figure 54 and Figure 55 (solid black curve).

Table 11: Average BAM normalized stiffness factors at each maturity level.

Lab ID	Vertical		Horizontal	
BAM normalized stiffness factor	$w_{C_{33}}$	$w_{C_{55}}$	$w_{C_{11}}$	$w_{C_{66}}$
Immature	0.195	0.22	0.29	0.3
Ex41	0.145	0.247	0.23	0.32
Ex43	0.11	0.26	0.265	0.33
Ex47	0.102	0.264	0.337	0.4
Ex42	0.088	0.265	0.173	0.29

Figure 65 shows that as the pyrolysis-induced maturity progresses, the "HS kerogen" predictions plot higher than the measured data. This means that the post-pyrolysis samples are extremely compliant due to extensive loss of solid volume and porosity enhancement in the absence of confining pressure. This is best pronounced in the over-mature stage (Figure 65g, h). Over-mature rock porosity is believed to be significantly lower in naturally-matured rocks primarily due to contemporaneous compaction, which would increase the normalized stiffness factors. To overcome the bias induced by unconfined pyrolysis, a kerogen-supported rock model is postulated to model an organic-rich chalk at different natural maturity levels. This assumption allows porosity to change due to compaction, as long as the rock fabric remains kerogen-supported. The "HS+BAM" and "HS kerogen" models are further examined in section 3.7.

3.6 SEM

BSEM images at two maturity stages (Ex41 and Ex42) are presented in Figure 66. Qualitative elemental analysis is enabled by energy dispersive spectroscopy (EDS). The porosity includes three main types: intra-calcite porosity, soft micro-nano porosity inside the kerogen, and inter-particle porosity. More detailed descriptions of the immature rock microstructure, including

anisotropy and poroelastic parameters, are given in Section 2.7. The samples were selected from the early-mature and over-mature stages to identify the microstructural processes at the onset of bitumen generation (Ex41) and termination of hydrocarbon expulsion (Ex42).

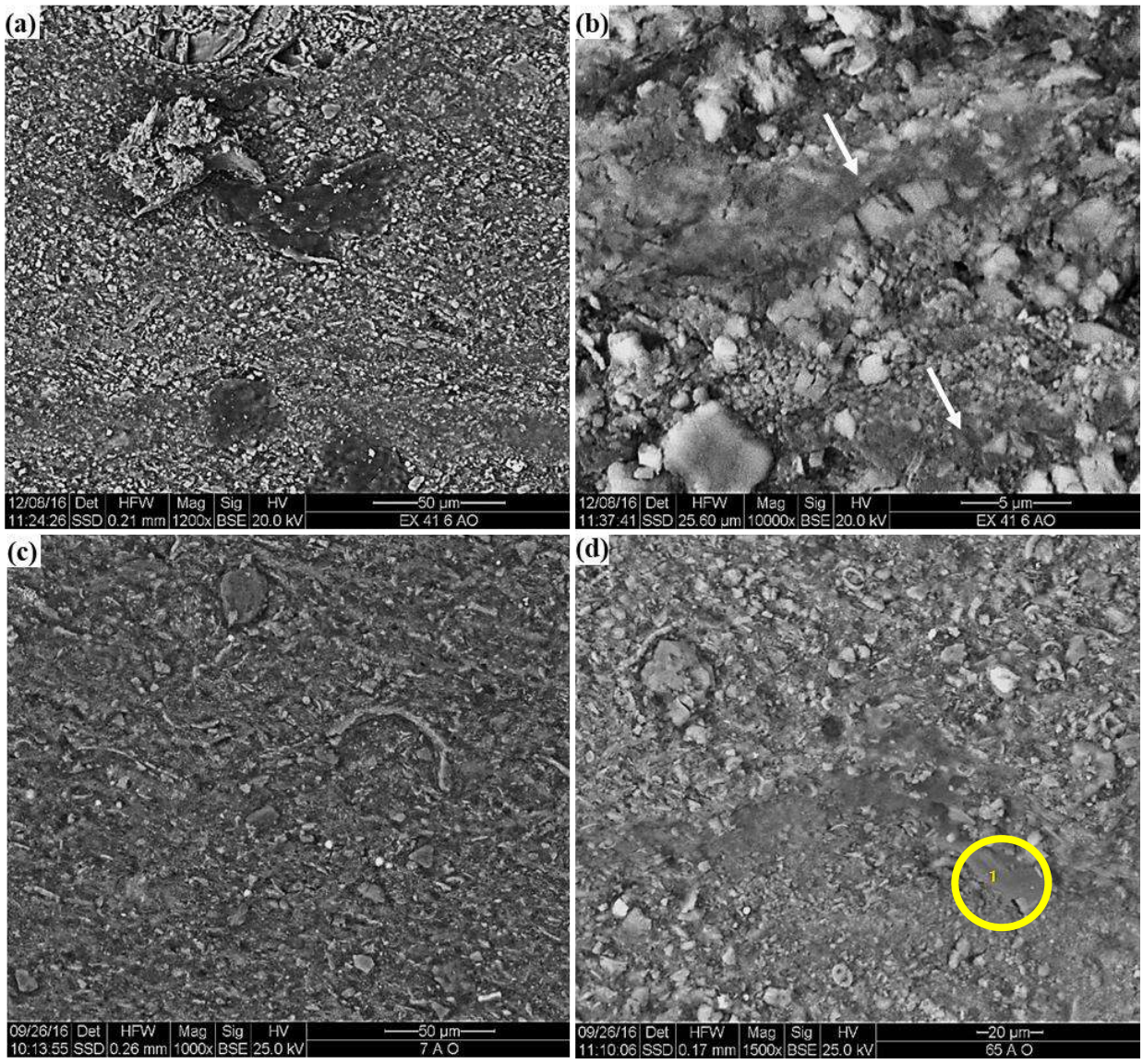

Figure 66: BSEM collection of the post-pyrolysis Ghareb-Mishash chalk in its early-mature state (a, b), and over-mature state (c, d). Properties of the scanned samples: a) and b) Early-mature rock, $\phi = 36\%$, $f_{bit} = 4\%$, $f_k = 10\%$, $w_{C33} = 0.15$, $w_{C55} = 0.28$, white arrows point to bitumen flow texture (b) ; c) Over-mature rock, $\phi = 47\%$, $f_{bit} = 1.5\%$, $f_k = 3\%$, $w_{C33} = 0.08$, $w_{C55} = 0.28$; d) Over-mature rock, $\phi = 47\%$, $f_{bit} = 1.2\%$, $f_k = 2.5\%$, $w_{C33} = 0.1$, $w_{C55} = 0.27$, pure organic-matter is detected (marked by circle).

In the early-mature state the rock preserves the density contrast between the kerogen and the minerals. At this stage the bitumen content (f_{bit}) is relatively high. This is uniquely attributed to sulfur-rich source rocks (Baskin and Peters 1992), where sulfur-sulfur and carbon-sulfur bonds are cracked early in the maturation process to produce bitumen. Bituminous zones can be identified by extremely dark areas (Figure 66a), that seem to spread radially in the surrounding matrix from kerogen-rich areas. They may also be identified by flow texture (Figure 66b), that records the bitumen invasion into pre-existing pores during maturation. These occurrences of bitumen exhibit bedding-parallel elongation presumably due to the permeability anisotropy of the rock. These two observations propose a source for w_{C33} decrease following pyrolysis-induced maturation. On the other hand, w_{C55} increases possibly because of kerogen stiffening.

The most prominent changes occur at the over-mature stage. The density contrast becomes much less distinctive due to kerogen densification (Figure 66c, d). The organic material has the same proportions as in the early-mature state with approximately 30% bitumen and 70% kerogen, only that the kerogen at this maturity stage exhausted the entire potential of hydrocarbon expulsion. This results in a drastic volume decrease of the organic phase (high conversion ratio in Table 8). Severe porosity enhancement is taking place within the kerogen, so that the scanned rock samples are made of nearly 50% voids, although it is not easily seen in the images. This is attributed to newly generated micro to nano-scale porosity in the kerogen. The residual amounts of bitumen and the enhanced porosity in the kerogen cause the organic-rich zones to appear somewhat darker than the minerals. A pure organic matter grain (or aggregate) in Figure 66d, detected using EDS spotting, exhibits bright shades almost as much as the surrounding calcite grains. This spotted zone may be either residual kerogen or petroleum coke, both of which represent the sharp density increase of the organic material. The notions brought here are important for examining the unusually high kerogen densities encountered at the over-mature state. The post-pyrolysis rock matrix is very compliant at this stage, indicated by $w_{C_{33}} \leq 0.1$ (Table 11), due to high porosity of the pyrolyzed core samples. The opposite trend of shear stiffening, evident by w_{C55}~0.27, is caused by significant increase of kerogen density and stiffness.

3.7 Rock physics templates

Rock physics templates (RPT) are typically cross-plots of parameters obtained from field measurements (well-logs and seismic surveys). The most common layout of RPT plots the Vp/Vs

ratio versus acoustic impedance 'AI' ($= \rho_b \cdot Vp$). RPT's are useful because data from well-logs and seismic surveys are laid out in a way that reveals changes in rock properties, such as porosity, fluid saturation, mineralogy, and organic content (Figure 67). Typically, most of the data are collected in the bedding-normal direction (zero-offset), whereas the rock beds are frequently horizontal. In order to examine the interrelationships between rock properties, RPT's are created here for the Ghareb-Mishash chalk.

Table 12: Response of physical properties and parameters on the axes of rock physics templates (in bold), to increase in porosity, organic content, maturity and decrease in water saturation. Note: AI=$\boldsymbol{\rho_b}$·Vp, MFI=$\boldsymbol{\rho_s}$·Vs.

Parameter / Increase in	Vp	Vs	ρ_b	ρ_s	**Vp/Vs**	***AI***	***MFI***
Porosity	↓↓	↓	↓	-	**↑**	**↓**	**~↓**
Organic content	↓	↓	↓	↓↓	**?**	**↓**	**↓↓**
Maturity	~↓	~↑	↑	↑	**↑**	**~↓**	**↑**
Gas saturation (decreasing water saturation)	↓	~-	↓	-	**↓**	**↓**	**-**

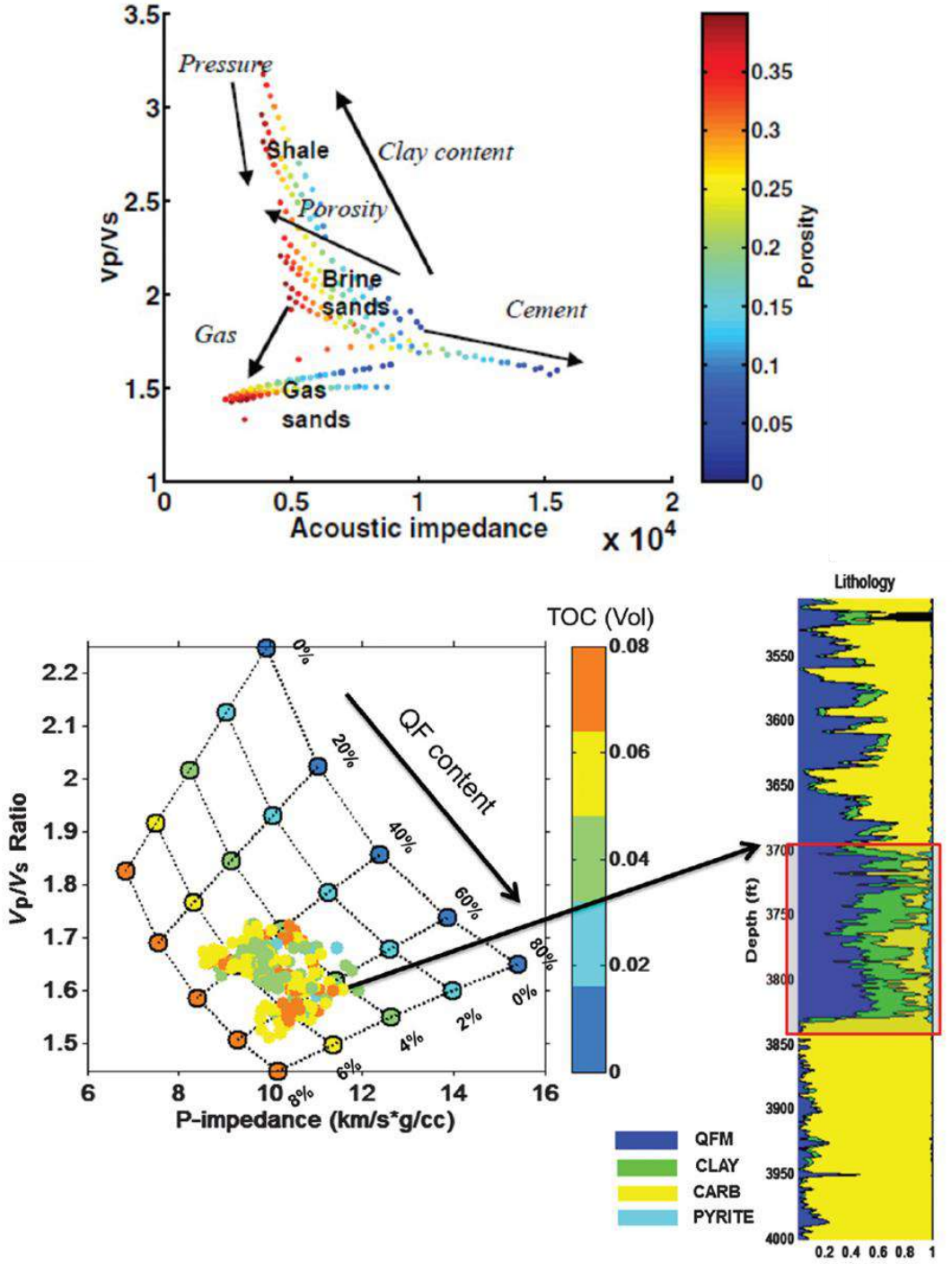

Figure 67: Examples for rock physics templates and their interpretation: On top (Ødegaard and Avseth 2003), rock physics interpretation of porosity, mineralogy, fluid content, cementation, pressure and clay content. Bottom (Zhao et al 2016): rock-physics interpretation of log data based on RPT of over-mature Barnett shale in the Fort Worth Basin (QF: quartz-feldspar).

RPT presentation of a complex rock such as the Ghareb-Mishash chalk is challenging, because the seismic signature is significantly affected by several variables, e.g. porosity, organic content, maturity, fluid saturation and mineralogy. Additionally, two different rock physics models are presented in the RPT plots, so it is desired to simplify the RPT's as much as possible. For this reason, it is decided to focus on the changes induced by porosity, organic content and maturity, while fluid composition and mineralogy are assumed to be constant (these assumptions will be discussed later in this section). The RPT's utilize the average moduli of minerals and organic matter (Table 1), and the petrophysical model of each maturity level (based on Figure 46). The RPT's in Figure 68 are presented separately at each maturity level. Each RPT includes curves that vary by organic matter content (f_o), so that the free parameter that changes continuously along the curves is porosity. The models being used are: 1) the experimentally fitted "HS+BAM" model, which assumes an average normalized stiffness factor 'w' at each maturity level, based on the post-pyrolysis measurements (see Section 2.2.2 for definition); and 2) the "HS kerogen" model, which assumes that the rock remains kerogen-supported during maturation (see Section 2.2.3 for definition). Both models estimate the P-wave modulus, M, and S-wave modulus, μ (Equations (23)-(27) and (32)), so that the Vp/Vs ratio is calculated by $\sqrt{M/\mu}$. The moduli are converted to Vp and Vs using the bulk density ($\sqrt{M/\rho_b}$ and $\sqrt{\mu/\rho_b}$, respectively). The bulk density is calculated by:

$$\rho_b = \phi\rho_w + f_o\rho_o + (1-\phi-f_o)\rho_m \ . \tag{80}$$

The acoustic impedance, AI, is therefore calculated by $\sqrt{\rho_b M}$. Because of the high porosity of the Ghareb-Mishash chalk, the effect of organic matter is masked in the conventional RPT's. In order to mimic organic matter associated effects, a matrix-focused impedance is used (MFI). The MFI is defined here by the product of solids density and S-wave velocity (ρ_sVs). The solids density is calculated by:

$$\rho_s = \frac{f_o}{1-\phi}\rho_o + \frac{1-\phi-f_o}{1-\phi}\rho_m \ . \tag{81}$$

The MFI is used here to create a rock physics template with a matrix-focused layout (MFL, i.e. Vp/Vs versus ρ_sVs). A conceptual guide table is presented in order to show the influence of each parameter on RPT plotting (Table 12).

The RPTs of the five maturity stages are presented in Figure 68, using both conventional layout (left column – a, c, e, g, i) and MFL (right column – b, d, f, h, j). The "HS+BAM" was fitted to the measured data, so it seems more representative. On the other hand, the "HS kerogen" is entirely theoretical and is not bound to the laboratory measurements. Nevertheless, it is questionable how representative are the pyrolyzed samples of naturally-matured rocks. It is seen that the "HS+BAM" curves span over a large Vp/Vs range, due to the highly porous state of the pyrolyzed samples. The "HS+BAM" curves exhibit a 'U', i.e. there is a minimum Vp/Vs which increases towards both higher and lower impedances. On the contrary, the "HS Kerogen" model predicts continuous decrease in Vp/Vs with increasing impedance, hence the 'L' shape of the curves. To the knowledge of the author, no 'U' shape curves were ever encountered in rock physics templates, hence seem unrealistic, while 'L'-shaped curves are routinely observed (e.g. Lucier, Hofmann and Bryndzia 2011; Avseth and Carcione 2015; Zhao *et al.* 2016). Therefore, "HS kerogen" is thought to be representative of native-state organic-rich chalk.

At all maturity stages, the organic content differences are clearly indicated by the "HS+BAM" model, while they are indistinct in the "HS kerogen" curves. The color-coded measured values in Figure 68 exhibit an organic-enrichment trajectory towards low Vp/Vs and acoustic impedance (bottom left of the RPT's), which is found typical to organic-rich shales (Lucier *et al.* 2011; Zhao *et al.* 2016). The organic-enrichment trajectory of the "HS kerogen" curves appears consistent with this trend, but the opposite direction is seen in the "HS+BAM" curves (organic-enrichment directs upwards). It is inferred that the "HS+BAM" model is not representative of naturally matured organic-rich rock. There are two possible reasons for that: 1) Marion's BAM model is designed for fluid substitution at a certain state, and different porosities are associated with different values 'w' (the BAM normalized stiffness factor); 2) the unconfined conditions in the pyrolysis resulted in extremely loose grain packing which is not believed to occur in nature. In conclusion, the "HS kerogen" model is chosen for modeling of native-state organic-rich chalk, while "HS+BAM" is useful for fluid substitution solely.

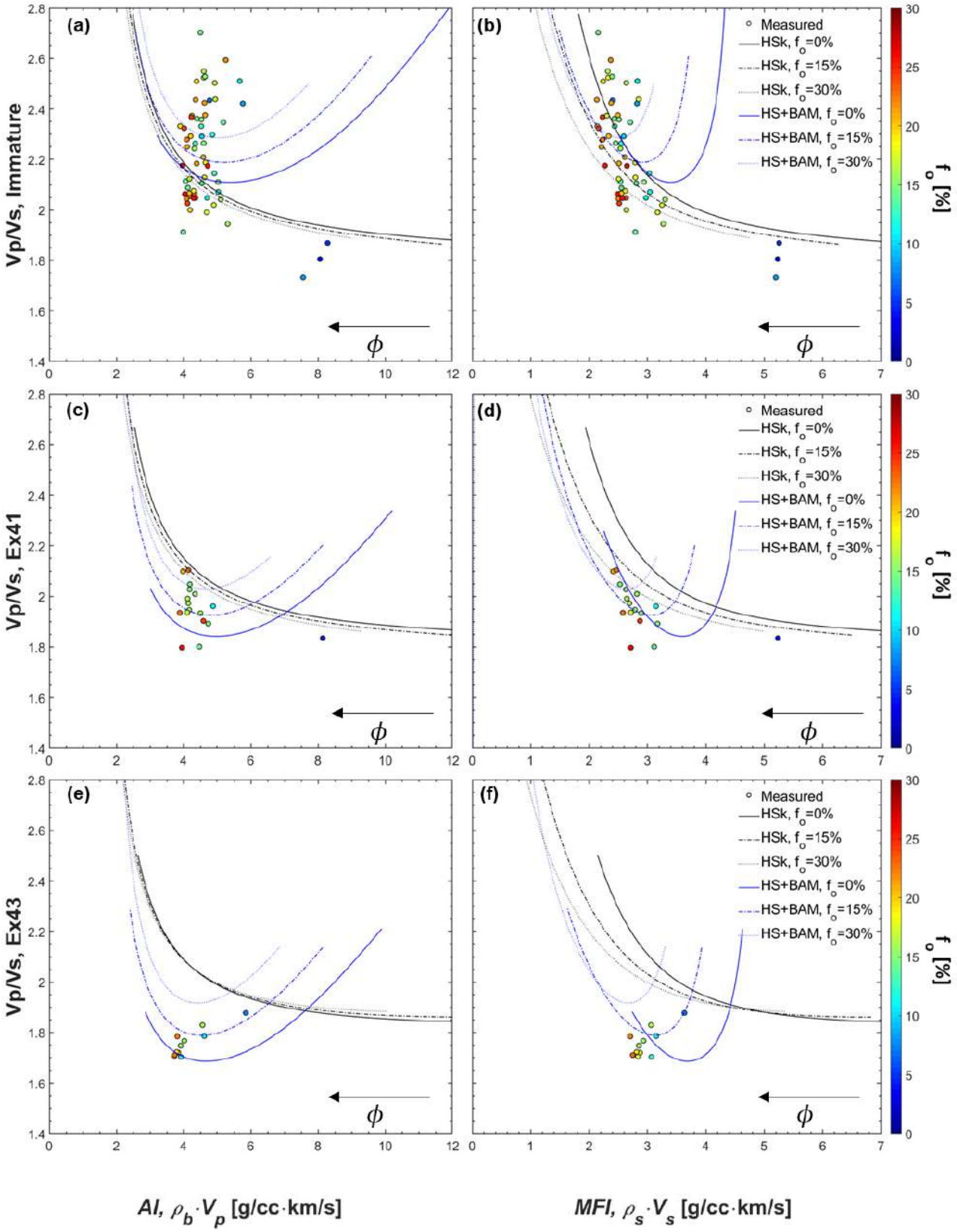
(a)
(b)
(c)
(d)
(e)
(f)
Vp/Vs, Immature
Vp/Vs, Ex41
Vp/Vs, Ex43
Measured
HSk, f_o=0%
HSk, f_o=15%
HSk, f_o=30%
HS+BAM, f_o=0%
HS+BAM, f_o=15%
HS+BAM, f_o=30%
f_o [%]
ϕ
AI, ρ_b·V_p [g/cc·km/s]
MFI, ρ_s·V_s [g/cc·km/s]

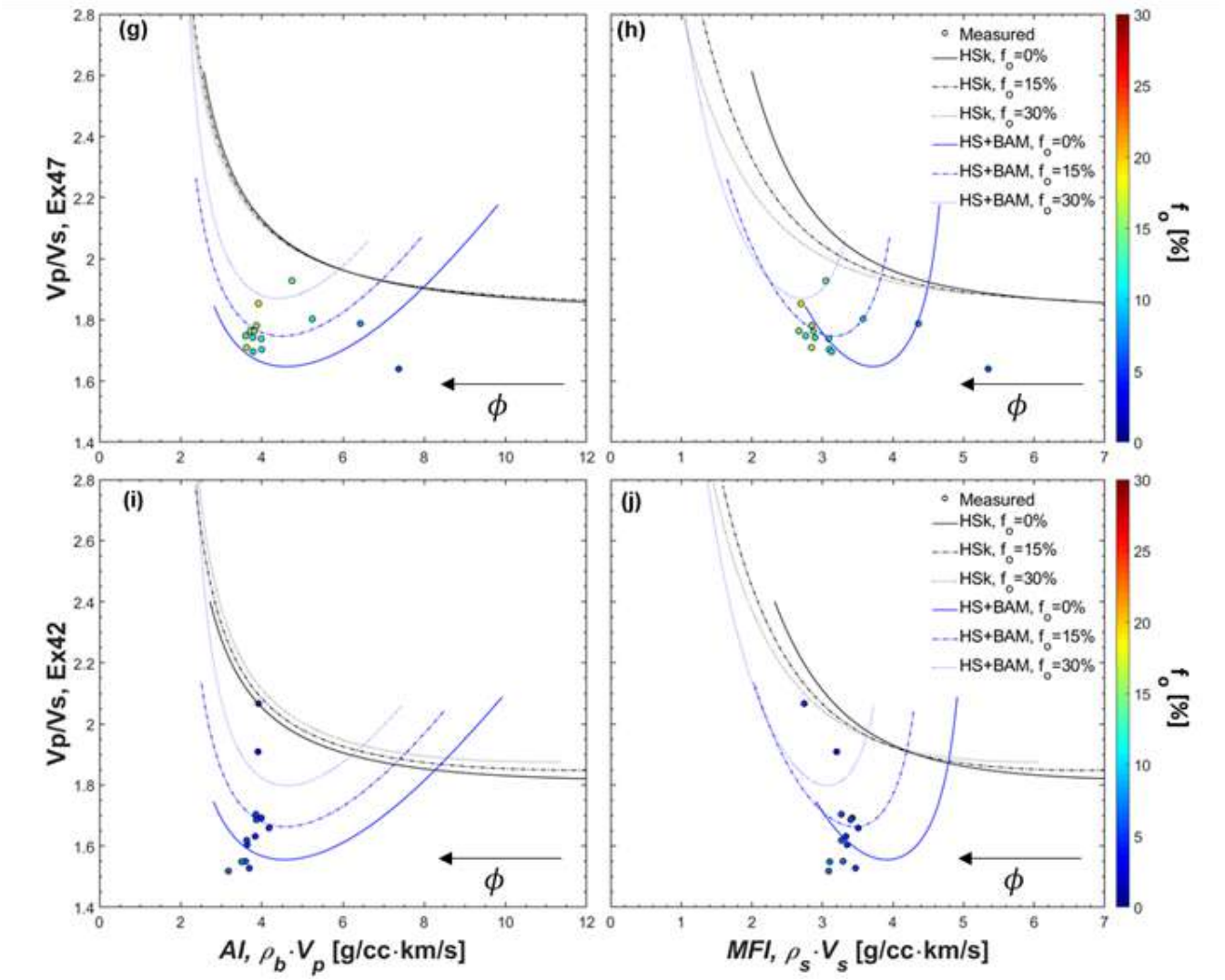

Figure 68: Rock physics templates of the Ghareb-Mishash chalk data, at different maturity levels (top to bottom): immature (a-b), early-mature (c-d), mature 1 (e-f), mature 2 (g-h), and over-mature (i-j). The left column shows the conventional RPT layout, plotting the Vp/Vs ratio versus acoustic impedance. The right column shows the matric focused layout, plotting Vp/Vs versus the matrix-focused impedance ($\rho_s Vs$), where the effect of porosity is damped. The data points were measured on immature and post-pyrolysis plugs in the bedding-normal direction, and color-coded to organic content. General direction of porosity increase is marked by the arrows, pointing from right to left in each plot. Rock physics models are the "HS kerogen" (HSk) and "HS+BAM", calculated at zero, average and maximum organic contents (0%, 15% and 30%), considering brine-saturated conditions.

Figure 69 is shows the effect of maturation on the Ghareb-Mishash chalk. In this case, high organic content is considered in the plots (f_o=30%). The "HS+BAM" curves show a decrease of Vp/Vs with increasing maturation, just as the trends of the bedding normalized stiffness factors (Table 11). This general trend has been seen before in organic-rich shale modeling (Bredesen *et al.* 2015;

Zhao *et al.* 2016), but the curves are shifted to higher values of acoustic impedance, as well as the point of maximum curvature. This is because organic-rich shales are naturally much less porous than the Ghareb-Mishash chalk. The "HS kerogen" curves show only minor changes between the maturity levels because changes in elastic moduli of the organic matter are small compared to the effect of porosity and organic content. It may seem that maturity cannot be indicated using this method. However, it should be kept in mind that the models assume brine-saturated conditions, while thermal maturation causes hydrocarbon saturation that may reduce the fluid incompressibility (K_f).

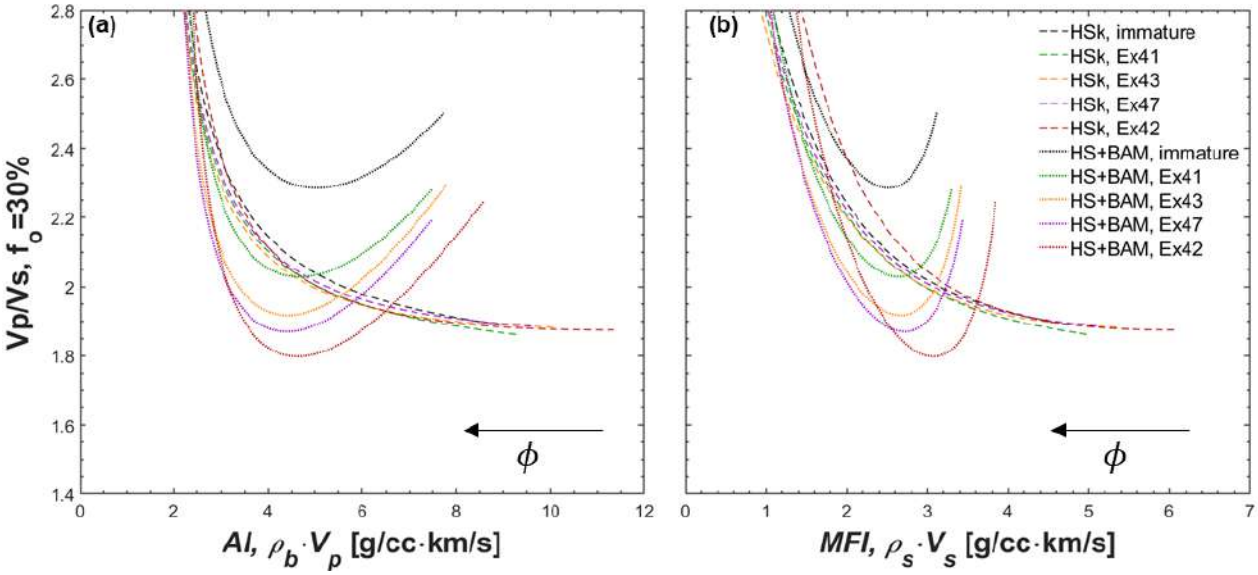

Figure 69: Rock physics templates at constant organic content, calculated using the "HS kerogen" (dashed curves) and "HS+BAM" models (dotted curves), assuming brine-saturated conditions. Templates are constructed using high organic content of 30%, to highlight the influence of maturity on matrix properties. General direction of porosity increase is marked by the arrows, pointing from right to left in each plot. "HSk" curves show very little maturity effects on the matrix density and stiffness. "HS+BAM" curves do show clear differentiation between the maturity levels, but they exhibit unreasonable predictions at high densities and velocities.

To test models' applicability in another basin, native-state Ghareb-Mishash chalk from the Southern Golan Heights basin is examined in Figure 70, using measurements by Gordin *et al.* (in prep.). The Ghareb-Mishash chalk in this basin is more mature (approximately early-mature), less porous and buried deeper. Gordin *et al.* performed measurements using dry core plugs, thus RPT's of dry organic-rich chalk are presented in Figure 70. An average organic content of 15% and early-

maturation (as in Ex41) are assumed. The "HS kerogen" model is clearly seen applicable for modeling the Ghareb-Mishash chalk, while the "HS+BAM" is not to be used for purposes other than fluid substitution. Therefore, the "HS Kerogen" curves of a brine-saturated rock are less indicative of thermal maturation, and more diagnostic of porosity and organic content in a high porosity organic-rich chalk.

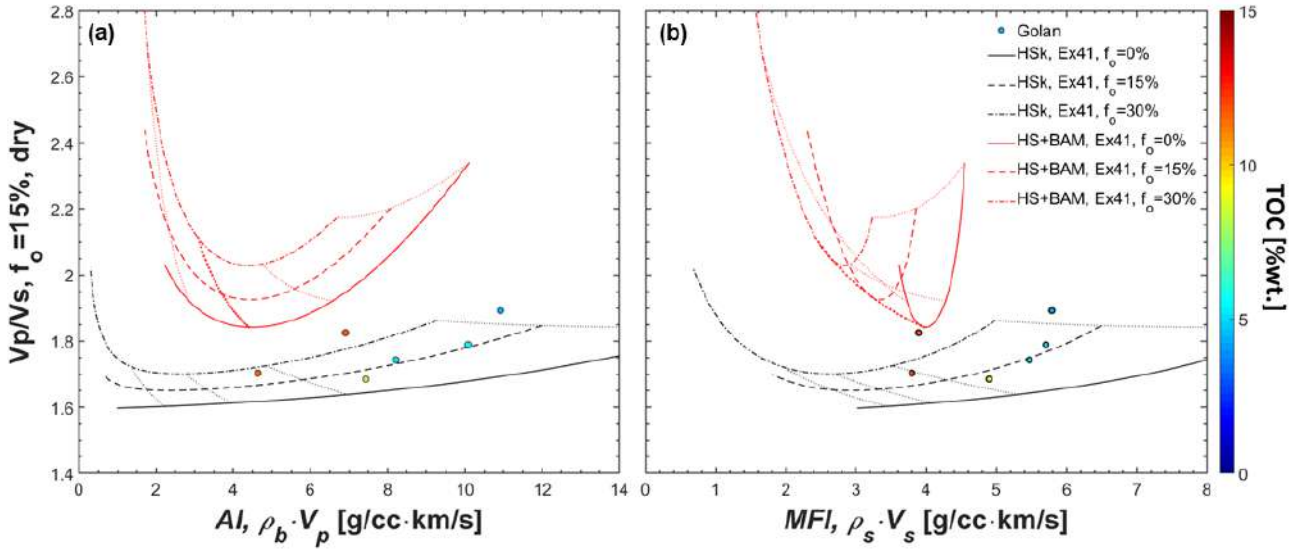

Figure 70: Rock physics templates of naturally-matured and artificially-matured Ghareb-Mishash chalk : early-mature rock is modelled at dry conditions and average organic content of ~15% to examine applicability of the rock physics models. The data points are native state, early-mature Ghareb-Mishash samples from the Golan Heights as measured by Gordin *et al.* (in prep.). The color-bar shows TOC instead of volumetric organic content due to uncertainty regarding the density of the organic material. Unlike Figure 68 and Figure 69, where iso-porosity lines are overloading the plots, here the iso-porosity lines are shown.

By now, only changes within the matrix were considered in the analysis while fluid saturations were not investigated. To present the effect of variable fluid saturation, RPT of the Ghareb-Mishash chalk is created by considering different fluid incompressibility values (K_f), which depend on the fluid composition. Note that the translation of K_f to fluid saturation is not straightforward, as there are different mixing laws which depend on the distribution of the fluids in the pores and dispersion. This will be elaborated in Section 4.2.3. The RPT's in Figure 71 mark the strong effect of fluid saturation on the acoustic signature of the Ghareb-Mishash chalk. The arrows in Figure 71 represent the general trajectory of increasing hydrocarbon saturation which can be either oil or gas in the pores. Using the conventional RPT, a change in saturation would

move a point in both vertical and horizontal directions, while in the MFL the horizontal location is relatively constant. This way, by projecting field data over the MFL template it is easier to determine K_f, and then convert to fluid saturation. It is therefore suggested that rock physics analysis should be carried by observing RPT in both conventional layout and MFL.

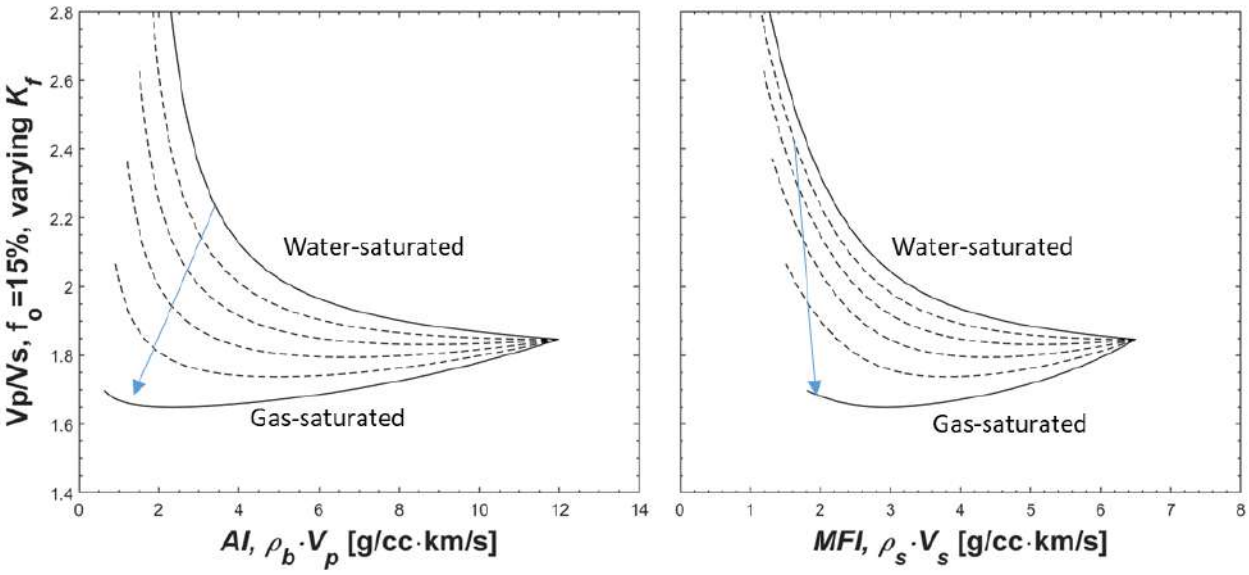

Figure 71: Rock physics templates that model early-mature Ghareb-Mishash chalk, demonstrate the effect of fluid hydrocarbon saturation. The modelled curves vary by fluid compressibility (K_f), from 2.5 GPa (top) to 0.001 GPa (bottom) incremented by 0.5 GPa. K_f can be converted to fluid saturation using proper fluid mixing laws and consideration of dispersion effects (explained in the Chapter 4). The arrows represent the general trajectory of increasing hydrocarbon saturation which can be either oil or gas in the pores

3.8 Discussion

3.8.1 Applicability of the post pyrolysis results

Looking at the whole analysis of pyrolyzed rock samples, there are few issues that require further examination. First, it is questionable how much do the pyrolysis experiments simulate natural thermal maturation process and the consequent changes in rock properties. The pyrolysis experiments were performed at unconfined, anhydrous (water-free) conditions. Porosity enhancement should naturally be followed by compaction, whereas the porosity developed during the pyrolysis evolved under unconfined conditions. Hence, naturally-matured samples are expected to be less porous. An attempt for simulating field conditions in the AVS350 system measurements was made but the samples failed at high confining pressures (20 – 30 MPa),

probably due to pore collapse. Therefore, the induced deformation in this case is thought to be unrepresentative of natural compaction, in which the strain rates are lower by several orders of magnitude. Strain in organic-rich rocks is time-dependent (Yang and Zoback 2016) and there was no ability to increase the pressure at a sufficiently low strain rate. Previous pyrolysis experiments of the Ghareb-Mishash chalk from the Shefela basin (Bisnovat 2013) examined the effect of 150 psi (1 MPa) backpressure on the pyrolysis process. Compared to unconfined pyrolysis, the petrophysical results were found similar, only that TOC loss in the pressurized experiment was slightly lower. Discrepancies may also originate from other sources such as exaggerated microcracking in unconfined pyrolysis (Allan *et al.* 2014). It is believed that conducting pyrolysis experiments under confined conditions (e.g. Gayer 2015) would yield a better replication of natural maturation. Geochemical alterations at the absence of water (as in anhydrous pyrolysis) may cause additional deviations from natural maturation conditions. Hydrous pyrolysis experiments on Irati oil shale (Gayer 2015) indicate higher conversion rates of kerogen to hydrocarbons than in anhydrous pyrolysis. However, in organic-rich carbonates this difference is minor (Koopmans *et al.* 1998). The deviations mentioned here should be accounted for when extrapolating rock properties from artificially to naturally matured states.

The lack of confinement during the pyrolysis affected the acoustic velocities and porosity the most. The natural maturity process is associated with increasing burial and lithostatic stress; thus porosity should decrease if no significant overpressure is built-up. The high porosity lowers the P-wave modulus significantly, hence, in a naturally-matured organic-rich chalk the Vp/Vs ratios and acoustic impedances should be higher than encountered here. In this study, it is attempted to overcome this effect by using the kerogen-supported matrix model, which may require further refinements relating to kerogen/oil conversion rates, fluids expulsion and migration from the rock, microcracking, and other factors. In addition, the presumption that the matrix remains kerogen-supported may be questioned, as the shrinkage of the organic phase upon maturation may alter its mechanical dominance. For example, Zhao *et al.* (2016) suggested that an over-mature kerogen in an organic-rich shale is effectively-distributed in the matrix in immature and mature stages but reduces to inclusions at over-maturity. In this case, the organic contents at Ex42 are 5-10%, still high with respect to other source rocks. However, if it reduces to inclusions then the matrix is expected to become more minerals-supported. Also, it should be kept in mind that upon natural

maturation due to increased burial depth, other geological factors come into play (e.g. cementation, stylolites, recrystallization, minerals alteration).

The applicability of the permeability measurements should also be questioned. They indicate decrease in mean pore radius in the post-pyrolysis samples. This may be attributed to bitumen choking of pre-existing pores or development of nano-porosity in kerogen during maturation (Bernard *et al.* 2012; Loucks *et al.* 2012). Permeability has been reported to reach minimum values at mature level ($\%R_{o,eq.}$=0.88) where bitumen saturation is high (Ghanizadeh *et al.* 2014). Here, it seems that the minimum permeability is at early-mature level ($\%R_{o,eq.}$~0.64), but this variation may be associated with the difference in bitumen generation in sulfur-rich kerogen, such as the Ghareb-Mishash chalk. Nevertheless, the applicability of gas permeability measurements to tight organic-rich rocks should be considered. Klinkenberg's gas slippage effect is important in tight rocks (Tanikawa and Shimamoto 2009) but the pressure dependence is non-linear (Moghadam and Chalaturnyk 2014). Klinkeberg-corrected permeability may exhibit large scatter due to kinetic effects of the gas molecules in nano-capillaries (Fathi, Tinni and Akkutlu 2012). Further deviations may be caused where matrix stiffness is considerably low and poroelasticity-based pressure corrections are required (Wang et al. 2014). The permeability analysis shown here is simplified to obtain some sense regarding permeability evolution during maturation, and the mentioned sources for errors are beyond the scope of this study. Further research in this direction should include adjustments of laboratory experimentation in the permeability measurements, measurements of bitumen-extracted samples, and development of theoretical approaches to better analyze an organic-rich chalk.

3.8.2 Kerogen density

Kerogen density is known to increase with maturity, due to the expulsion of hydrocarbons and depletion in hydrogen, which result in increased carbon concentration. In nature, the residual solid organic phase may reach anthracite rank and even pure graphite (Labani and Rezaee 2015). The vitrinite reflectance, $\%R_o$, is the most prevalent proxy for thermal maturation and some relationships have been proposed to relate $\%R_o$ with kerogen density. A study based on the Marcellus shale, indicated that within the $\%R_o$ range of 1.5-2.68%, the kerogen density increases from 1.5 to 1.89 g/cc, and they are related by the following trend (Ward 2010; Labani and Rezaee 2015):

$$\rho_k = 0.342R_o + 0.972\ . \tag{82}$$

This relationship was back-calculated from well-logs that indicate organic richness (γ-ray log) and bulk density. Vernik, in his studies, indicated another relationship that follows a power-law trend (Vernik 2016):

$$\rho_k = 1.293R_o^{0.2}\ . \tag{83}$$

Vernik's relationship leads to lower kerogen densities at the high-maturity range than those predicted by Equation (82). The petrophysical results obtained here indicate high organic material density (~2.2 g/cc) at the over-mature state. This leads to strikingly high kerogen density (~2.7 g/cc), by excluding the bitumen from the organic matter. Values of over-mature kerogen density reported in the literature were never found to be this high (Vernik and Nur 1992; Okiongbo, Aplin and Larter 2005; Alfred and Vernik 2012). On the other hand, it is possible that bitumen saturation inside over-mature kerogens has been overlooked in past studies. The high kerogen density is obtained here from simple mass-volume balance relationships between solids density and TOC (e.g. Figure 18, Figure 46). The increase in shear wave velocity and the lowering of the contrast in backscatter SEM images at the over-mature stage align with kerogen stiffening and densification. Solids density increase may be attributed to pyrite precipitation, but only to a restricted extent. It is also possible that the sulfur that remains in the organic material contributes to the density increase of an over-mature Type IIs kerogen. Yet, the over-mature kerogen density values are significantly higher than previously assumed.

Figure 72 shows the organic material density and kerogen density versus maturity level. The data points include the native-state immature and the four maturity levels simulated by pyrolysis. Results of immature Aderet samples from Bisnovat (2013) are also included. The error bars account for uncertainty in the approximations of $C_{pr}, \rho_m, \rho_{bit}$, and the error on the a_2 regression coefficient (refer to Section 2.2.1 for description of the model). The errors on density of the organic phase and the kerogen are small within the range of immature-mature levels, but at the over-mature level the errors are quite large. This is because the normalized error on a_2 at this stage (~35%) is much larger than in the other maturity levels (~3-4%). For this reason, in Figure 72 only the negative range of the error of the over-mature kerogen is presented, as the positive range is highly unlikely. Therefore, two empirical relationships of kerogen density versus vitrinite reflectance are

calculated, including and excluding the over-mature kerogen density. The curve that includes the over-mature datapoint exhibits steep increase towards unreasonable densities for organic material (> 2.5 g/cc). The curve that ignores the over-mature kerogen density still falls within the lowermost range of the over-mature datapoint, thus believed to be representative at all maturity levels. Also, the values predicted by it make much more sense. For comparison, the relationships proposed by Labani and Rezaee (2015) and Vernik (2016) are shown. Although these relationships are widely used for estimations of kerogen density, it should be kept in mind that they were developed using organic-matter density (including bitumen, see Section 2.2.1). Either way, both the organic matter densities and kerogen densities encountered here are higher, from reasons described in the previous paragraph. Conclusively, Figure 72 suggests that the kerogen density here can be described by:

$$\rho_k = 1.31e^{0.217 \cdot \%R_o} \quad . \tag{84}$$

This relationship is representative of maturation of a Type IIs kerogen in an organic-rich chalk.

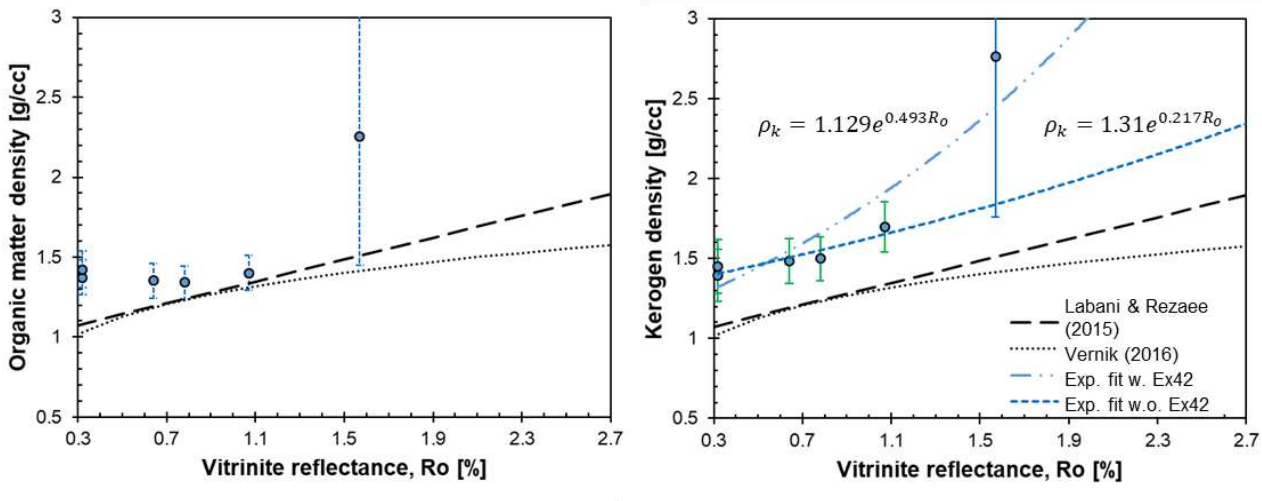

Figure 72: The density of the organic material (a) and kerogen (b) increases with maturity level, represented by vitrinite reflectance. Note that $\%R_o$ values of the data points of the pyrolyzed samples (i.e. early- mature to over-mature) are equivalent vitrinite reflectance values $\%R_{o,eq.}$ (Table 7). The error bars represent the possible errors by inaccurate assumptions in the density calculations, as explained in Section 2.2.1. The ρ_k versus $\%R_o$ trends are calculated twice: including and excluding the abnormal over-mature kerogen density. The curves below the observed values are calculated based on relationships proposed by Labani and Rezaee (2015) and by Vernik (2016).

3.9 Conclusions

The effect of unconfined pyrolysis-induced maturation on rock physics of a high porosity organic-rich chalk is examined here using petrophysical and acoustic measurements. Post-pyrolysis rock properties at early-mature, mature 1, mature 2 and over-mature levels are compared with the native-state (immature) rock properties. Data analysis is made using careful differentiation between bitumen and kerogen and selection of their elastic moduli, in order to model properly the elastic properties of the Ghareb-Mishash chalk at different maturity levels. Two models, based on Hashin-Shtrikman variational approach, are used to analyze the measured data and extrapolate to natural conditions. The post-pyrolysis data collected here lead to the following conclusions:

1. Upon maturation, the matrix density and porosity increase at a rate that depends on initial organic richness. The matrix density at the over-mature stage reaches 2.7 g/cc, indicating the reduction in organic material volume and the increased organic material density, due to full exhaustion of volatile hydrocarbons from the solid kerogen. The porosity is significantly enhanced, and at the absence of confinement in the pyrolysis the matrix obtains an extremely soft pore geometry. The porosity enhancement leads to significant increase in permeability.
2. Petrophysical evolution of the rock should be analyzed while accounting for the bitumen content. The bitumen causes the measurements to underestimate the matrix porosity, density and permeability. It also causes a decrease in the mean pore size due to invasion into and choking of existing pores. Proper consideration of bitumen content enables correction of the porosity and solids density measurements.
3. Using the data of porosity, solids density, TOC, and bitumen extraction experiments, the maturation-associated increase in kerogen density is described. It increases from ~1.4 g/cc at the immature stage, through 1.5-1.7g/cc at mid-maturity levels, and up to ~2.7 g/cc at the over-mature stage. The over-mature kerogen density seems too high and perhaps the large errors in its estimation are the cause for that. Yet the analysis shows that over-mature kerogen density is at least 1.7 g/cc. High kerogen densities are also implied from backscatter SEM images and increased S-wave velocity. Kerogen densities at all maturity levels are higher than reported in the literature, possibly because they mistakenly disregard bitumen content, or because of high sulfur content in the Ghareb-Mishash kerogen.

4. The acoustic velocities show diverging trends for bedding-normal P-wave and S-wave velocities upon pyrolysis: Vp decreases due to porosity enhancement, while Vs increases due to densification and stiffening of the post-pyrolysis solid matrix. Representative BAM normalized stiffness factors depict a similar behavior: upon maturation w_{C33} decreases from 0.2 to 0.09, and w_{C55} increases from 0.22 to 0.26. The initial organic richness and the maturity level dictate the magnitude of change in the velocities.
5. The bedding-normal and bedding-parallel P-wave and S-wave moduli, at both saturated and dry conditions, show a good correlation with the kerogen-factored porosity using kerogen influence factor of κ=0.5. Exponential fits are proposed to estimate the moduli in each case.
6. Unexpectedly, acoustic anisotropy shows no dependence on organic content, but it is increased with porosity. This suggests that porosity induces mechanical anisotropy, as observed for permeability and tensile strength anisotropy in Chapter 2. In dry conditions, the relationship between the anisotropy parameters Ω and ε is the same as in other organic-rich rocks.
7. Rock physics modeling is done using two models: "HS+BAM" which is calibrated to the results of the post-pyrolysis plugs, and "HS kerogen" which simulates a kerogen-supported matrix. The "HS kerogen" model overestimates the moduli of the post-pyrolysis plugs because of the extreme softness of the post-pyrolysis material. However, naturally-matured organic-rich chalk from the Golan Heights is well predicted using the "HS kerogen" model. Analyses using rock physics templates confirm that the "HS kerogen" model is realistic, while the "HS+BAM" model is found suitable for fluid substitution only.
8. Rock physics templates are created using both conventional and matrix-focused layouts (MFL), i.e. plot Vp/Vs ratio versus ρ_bVp and ρ_sVs, respectively. Both layouts are strongly influenced by porosity. The MFL shows better the changes in organic content, mainly in the "HS kerogen" curves. The 'U' shape of the "HS+BAM" curves and the trajectory of organic enrichment are found unrepresentative of native-state rocks. Because brine-saturated rock is modelled, maturity level is hardly indicated in the templates. However, in naturally-matured organic-rich rocks fluid saturations may change significantly, which decrease the fluid incompressibility.

While pyrolysis aims at simulating thermal maturation, a true replication of natural maturation is prevented by the absence of ambient field conditions such as lithostatic pressure, pore pressure, slow heating rate, variation in fluid type and saturations, and time-dependent response of the mineralogical matrix. Specifically, the lack of confining pressure, which should simulate compaction, seems the most crucial.

4 Field Application

4.1 Chapter introduction

This chapter on field measurements is entirely focused on the Shefela basin. Two sections in the Shefela basin were studied: Zoharim and Aderet (locations in Figure 6). Analytical approaches were developed based on the laboratory and field measurements of the Zoharim section. Therefore, this section is first focused on the Zoharim section. Then, the models are applied to the Aderet dataset in order to examine the applicability of models in a broader perspective. Unfortunately, the Aderet well-logs do not include density and porosity logs, but only P-wave velocity, γ-ray, and resistivity logs. The way this difference between the datasets was dealt with is described in Section 4.3. The basics of the logging tools being used in this analysis are presented briefly in this introduction. Another dataset used here was obtained using continuous coring, where TOC measurements are spaced by 1-meter intervals in the depth section. Although these measurements were obtained at the laboratory, they are referred to as field measurements because they provide the most dense and continuous TOC dataset.

4.1.1 Logging tools

Density log: The density tool measures formation density using the scattering of gamma-rays between a source and a detector (Dewan 1983). Gamma-rays emitted continuously by the source, typically 0.66 Mev energy from Cs^{137}, are channeled into the formation. The gamma-rays undergo multiple collisions with orbital electrons that cause them to lose energy and scatter in all directions, a mechanism called "Compton scattering". Compton scattering depends only on the electron density of the rock (number of electrons per cc), which is closely related to bulk density, ρ_b. The bulk density is also used to determine porosity. The density log-derived porosity is known as "density porosity", denoted by ϕ_D, and computed using Equation (59) ($\phi = \frac{\rho_s - \rho_b}{\rho_s - \rho_f}$). The density of the solid matrix and the fluid (ρ_s and ρ_f) are determined based on the lithology and fluid type (respectively), and the bulk density is measured using the density tool.

Neutron log: The neutron tool measures the hydrogen density in the rock using emission of fast neutrons which spread in all directions. The neutrons are slowing and colliding with nuclei within the rock, so they are absorbed or captured by the present nuclei. Being most similar in mass to neutrons, hydrogen atoms are very effective in slowing neutrons. Hydrogen may be present in

various phases such as water, oil, gas and clays. The amount of the hydrogen within the rock is indicative of the porosity, lithology and fluid type. The neutron log appears in the porosity track, and where the rock is fully saturated by water and has no clay, organic matter or gas, the neutron log porosity equals the porosity of the rock. Hence, the parameter that represents the neutron log is the neutron porosity, ϕ_N. Usually the neutron porosity is displayed together with the density porosity, ϕ_D, in order to detect and quantify features in the rock (e.g. lithologies, porosity, gas).

Gamma-ray log: Gamma-ray logs measure the natural gamma rays emitted by the rock surrounding the tool. The radioactivity arises from the isotopes K^{40}, U^{238} and Th^{232}. These radioactive elements are more abundant in shale than in clean sands or carbonates, thus high values are usually associated with the shale content in the rock. Gamma-rays response is measured in American Petroleum Institute Units (APIU), generally ranging from 0 APIU to 200 APIU (twice the values of typical shale ~ 100 APIU). Most clay-free rock types give low readings of 0-30 APIU (Dewan 1983). The basic gamma-ray devices use a detector lowered into the borehole, measuring the count rates within a pre-defined time interval (1-2 seconds). Organic-rich shales are associated with high APIU, not only because of the shale response but also because of uranium within the organic-matter. Therefore, the gamma-ray tool is indicative of both lithology and organic content.

Resistivity tools: Electrical resistivity tools measure the resistivity of the rock in several distances from the wellbore, in order to detect hydrocarbons saturation and mobility. Hydrocarbons increase the bulk resistivity of the rock, while brine lowers the resistivity (depending on the NaCl concentration). The resistivity is useful for water saturation calculation using Archie's laws (Archie 1942):

$$R_t = R_o S_w^{-n} = R_w \phi^{-m} S_w^{-n} \ , \tag{85}$$

where the three different resistivities, denoted by R, describe the formation water resistivity (w), the resistivity of water-saturated rock (o) and the resistivity of a rock containing oil and some amount of water saturation (t). The R_o value is usually picked at a zone where water saturation is 100%. The exponent 'm' is called the cementation index, and usually equals ~2. The exponent 'n' is called the saturation index which is also about 2. Once the water saturation is derived, hydrocarbon saturation can be estimated.

Sonic tool: A sonic logging tool measures travel time of sonic waves in the rock. Unlike the pad-type tools (e.g. density, neutron) it is centralized in the bore and not pushed against the wellbore wall. Transmitters and receivers are positioned at the lower and upper ends of the tool. Pulses are generated by an electrical source that generates a pressure pulse at about 3-30 kHz frequency. There are several types of waves that travel in the borehole in this type of measurements, although here the attention is dedicated to the arrival times of P-waves in the rock. The energy is emitted from the source, transmitted through the mud in the borehole, reaches the rock so that a head wave is propagated along the borehole wall at the speed of P-wave velocity of the rock. The travel times of the waves are divided by the spacing between the transmitters and receivers and corrected for travel in the mud (in the travels from the transmitter and to the receiver), as well as changes in the bore diameter. The resultant quantity is the slowness of the rock, which is the inverse of the velocity, and typically presented in $\mu sec/ft$. Note that the in the Zoharim and Aderet wells, only P-wave data were available.

4.2 Zoharim well

4.2.1 Petrophysical properties estimation

As presented in Section 2.3, a combination between well-logs and continuous coring data enables application of RPM's to the entire depth section. The dataset available from the Zoharim well includes log measurements of bulk density, P-wave velocity, neutron porosity and natural gamma-ray emission. There is no direct TOC measurement at the field scale, but continuous coring data, spaced by 1 meter throughout the depth section, enables estimation of rock porosity, organic content, and thus elastic moduli and acoustic velocities. The methodology and results of these estimations are described below.

First, to pair TOC data with log measurements which are spaced by 0.15 m (0.5 ft), the different datasets (of different sizes) need to reduce to the size of the smaller dataset (i.e. continuous coring data). To do that, depths in the continuous coring data are the target depths (Z), and the values from log measurements were averaged from five measurements at five depths adjacent to Z. The paired dataset is therefore spaced by 1 m and can be defined as the continuous coring-well log (CCWL) data. The most useful combination is the continuous coring-density log (CCDL) combination. The porosity calculation is performed based on Equation (59), assuming minerals density of ρ_m=2.74 g/cc, fluid density ρ_f=1 g/cc, and the solids density is calculated using

Equation (17), with $a_2 = 0.0132$. The volume fractions of the organic matter and the mineralogical phase are then straightforwardly derived (Equation (16)). The volume proportions within the logging interval (330-550 m depth in the Zoharim well) are presented in Figure 73. The estimated volume fractions will be used in the next section for estimation of the elastic moduli and acoustic velocities of the rock.

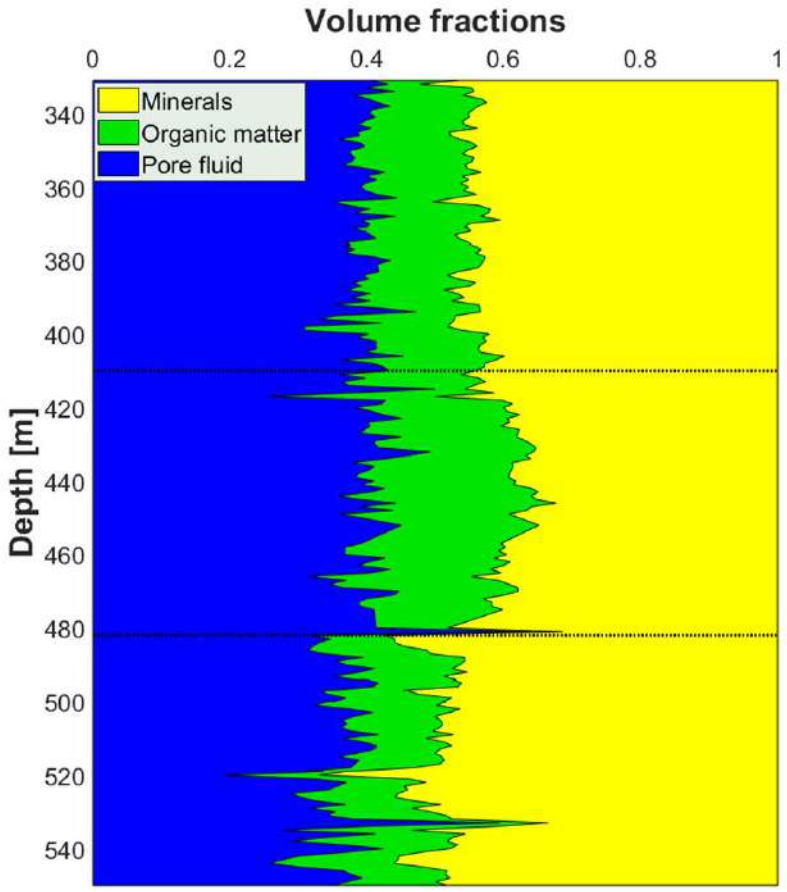

Figure 73: Volume fractions of minerals, porosity and organic matter are profiled versus depth in the Zoharim section. The volume fractions were calculated using the CC-DL combination.

Examination of TOC influence on the neutron-porosity (ϕ_N) reading can be performed using the CCDL porosity (i.e. ϕ_D). The ϕ_N is derived from the hydrogen neutron logging tool, that is sensitive to the hydrogen density in the rock. The ϕ_N underpredicts the porosity at lower hydrogen densities (e.g. hydrocarbon gas substitutes water) and overpredicts where the mineralogy includes hydrogen (e.g. OH groups in clays). The ϕ_N and the CCDL porosity are compared with the core porosity measured in the laboratory (Figure 74). As expected, CCDL estimations are in good

agreement with the core porosity, while the neutron porosity overestimates the porosity. The Ghareb-Mishash chalk is lean in clays, but the high organic content (which includes hydrogen) causes overprediction of the neutron porosity. To demonstrate this effect, the magnitude of overprediction is calculated by ϕ_N-ϕ_D, and plotted against TOC in Figure 75. Note that ϕ_D is derived using the CCDL combination and assumed to be the true porosity. It is clearly seen that TOC controls the overestimation of ϕ_N. The scatter of the data may be due to several mechanisms, such as hydrogen-containing minerals (e.g. clays), gas-induced decrease of ϕ_N, variation in hydrogen concentration in the organic material, and variability of the CCDL input parameters (e.g. mineralogy, organic matter density, C_{pr}).

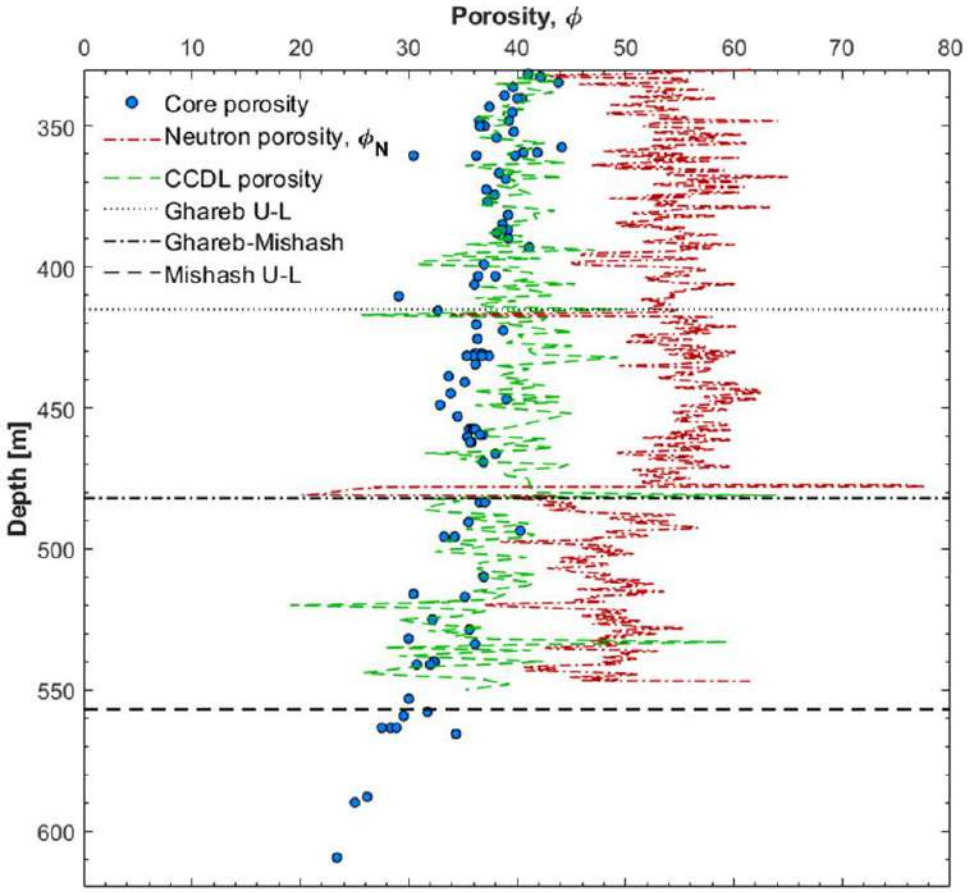

Figure 74: Depth profile of three different porosity measurements: 1) core porosity, measured in the laboratory; 2) neutron porosity (ϕ_N), that measures hydrogen content in the formation; and 3) density porosity (ϕ_D) computed using the CCDL combination. CCDL porosity and core porosity reveal a good match.

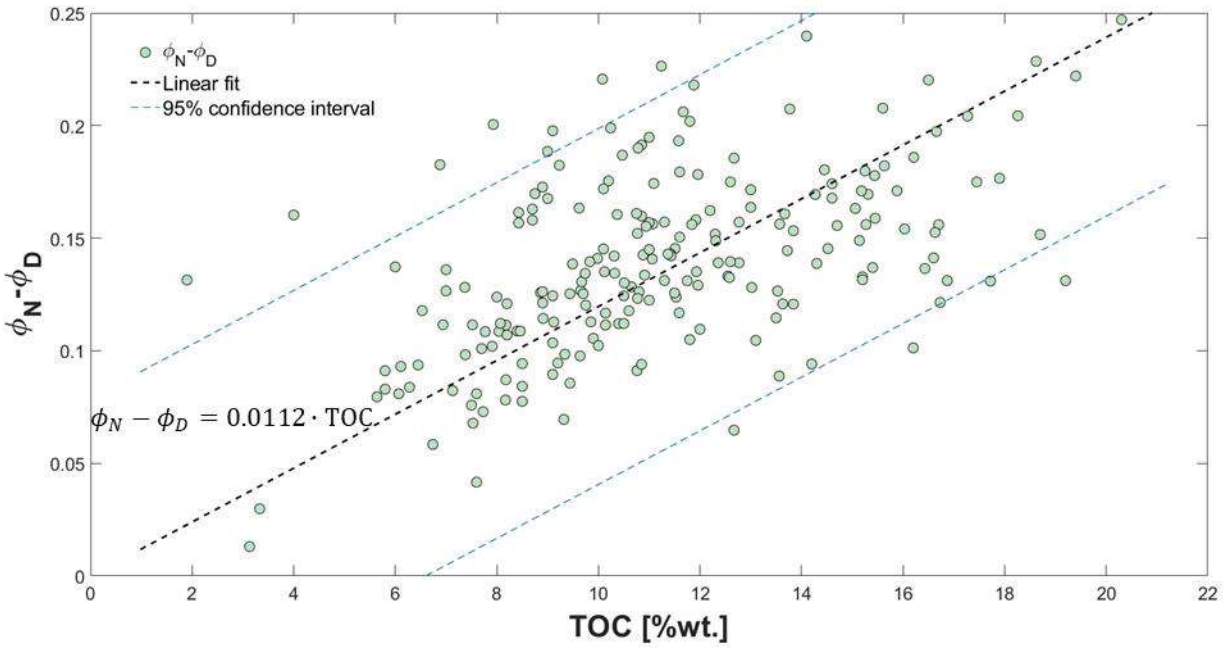

Figure 75: The excess hydrogen in the formation, represented by the difference between neutron porosity and density porosity ($\phi_N - \phi_D$), is associated with the organic material. Note that the linear curves cross the axes origin, i.e. there is almost no other sources for hydrogen in the rock.

In the absence of TOC data, it is much harder to perform the analysis presented above. To allow for TOC estimation from a basic logging suite such as in this case, it is possible to generate an empirical correlation between TOC and the measured parameters influenced by it. These parameters are the gamma-ray log, neutron log and density log. TOC is known to influence the gamma-ray log response due to the uranium associated with organic matter (Tiab and Donaldson 2016). The neutron log, which measures hydrogen density in the rock, reads also the hydrogen associated with the TOC. The bulk density is influenced by the matrix density and therefore by the TOC. All of these logging tools are influenced by other factors, but a multiple variable regression can be used to estimate TOC. By performing a multi-variable linear regression analysis, based on a least squares method, the following relationship is obtained:

$$TOC_{est.} = 28.193 + 0.0331 \cdot GR + 9.784 \cdot \phi_N - 14.257 \cdot \rho_b \qquad (86)$$

where $TOC_{est.}$ estimated TOC, and GR is the measured gamma-ray. Figure 76 shows TOC predictions using this relationship. It also shows an empirical fit of TOC versus GR only, as performed routinely in source rocks evaluation. The multiple variable linear regression in Equation (86) leads to better estimations of the TOC.

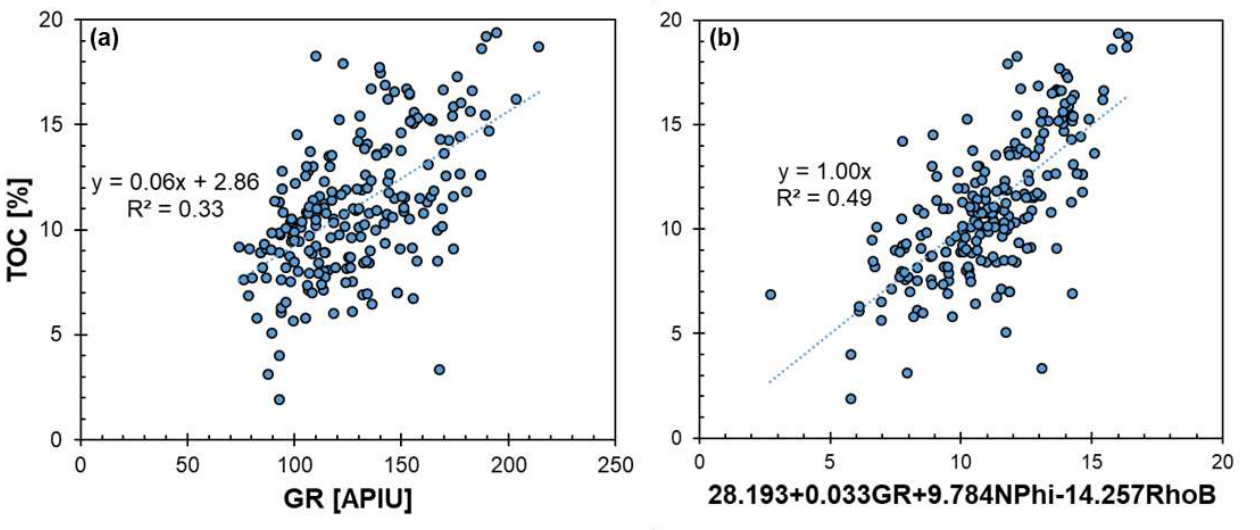

Figure 76: Empirical estimations of TOC using well-logs: a) TOC is estimated using the γ-ray log only; b) TOC is estimated using a combination of the γ-ray log with neutron porosity (NPhi) and bulk density (RhoB) logs. The accuracy of TOC approximation is improved using the multivariable regression. TOC values were obtained by LECO measurements, carried on samples collected during continuous coring.

4.2.2 Estimation of elastic moduli

In the previous section, the generation of a depth profile of various petrophysical properties was presented, with values spacing of 1 m. This enables the estimation of bedding-normal velocities and elastic moduli using the "HS kerogen" model. The modeling workflow is as follows: 1) theoretical elastic moduli are assigned to the pore-fluid (brine), organic-matter (kerogen) and mineral (Table 1); 2) the "HS kerogen" Equations (32) are calculated at each depth, to obtain the vertical oedometer and shear moduli; 3) Equation (80) is employed to calculate the bulk density at each depth and the vertical P-wave velocity ($V_p = \sqrt{M_v/\rho_b}$) and S-wave velocity ($V_s = \sqrt{\mu_v/\rho_b}$) are estimated; and 4) the estimated P-wave velocities are compared with the measured values from the sonic log. Unfortunately, no shear wave velocity data were available from the logs and that limited the extent of implications that can be drawn from the logs. Depth profiles of the vertical oedometer modulus, shear modulus, P-wave velocity and S-wave velocity are presented in Figure 77 and Figure 78. The "HS kerogen" model is found to overestimate the moduli using the elastic moduli of the organic matter from the analysis of core measurements (Table 1). However, if the elastic moduli reported for immature organic matter are used (Zhao *et al.* 2016) the predictions are accurate. Thus, the organic material moduli used in the "HS kerogen" predictions are K_k=3.5 GPa, μ_k=1.75 GPa. This variation in moduli compared to the values in Table 1 is most likely to originate

differences between laboratory and field measurements, expressed by different frequencies (500 kHz in the laboratory, 20 kHz in the logs), and by the state of the rock in laboratory and *in-situ* conditions (core sample versus rock mass). Figure 77 and Figure 78 include two curves, the "HS kerogen" ("HSk") predictions and the log measurements. The area between the curves shows in blue where the "HSk" predictions are higher, and shows in red where it is the other way. At depths greater than 410 m (lower part of the Ghareb and upper part of the Mishash), good agreement between the two curves is seen. In the upper part of the Ghareb formation, the "HSk" curve overpredicts the P-wave velocities and moduli, as the prediction were made assuming full water saturation. This hints a gas zone at the upper part of the Ghareb-Mishash sequence. This gas zone will be evaluated in the next section.

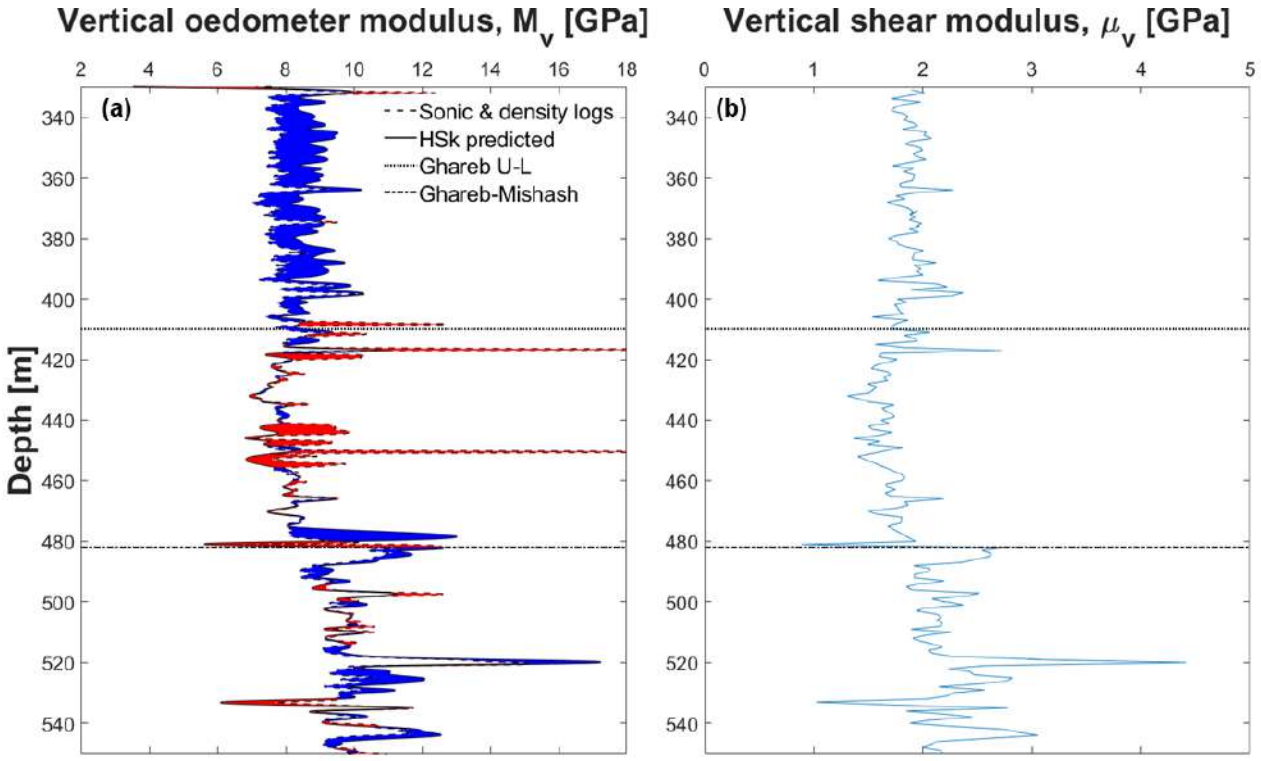

Figure 77: Depth profiles of the vertical dynamic moduli in the Zoharim section: a) The P-wave (oedometer) moduli were obtained from the sonic and density logs. The area between the curves shows in blue where the "HSk" predictions are higher, and shows in red where it is the other way. The "HS kerogen" model predictions are accurate, except in the gas zone at the upper part of the Ghareb. b) The S-wave moduli are predicted using the "HS kerogen" model (S-wave velocities were not measured in the logs).

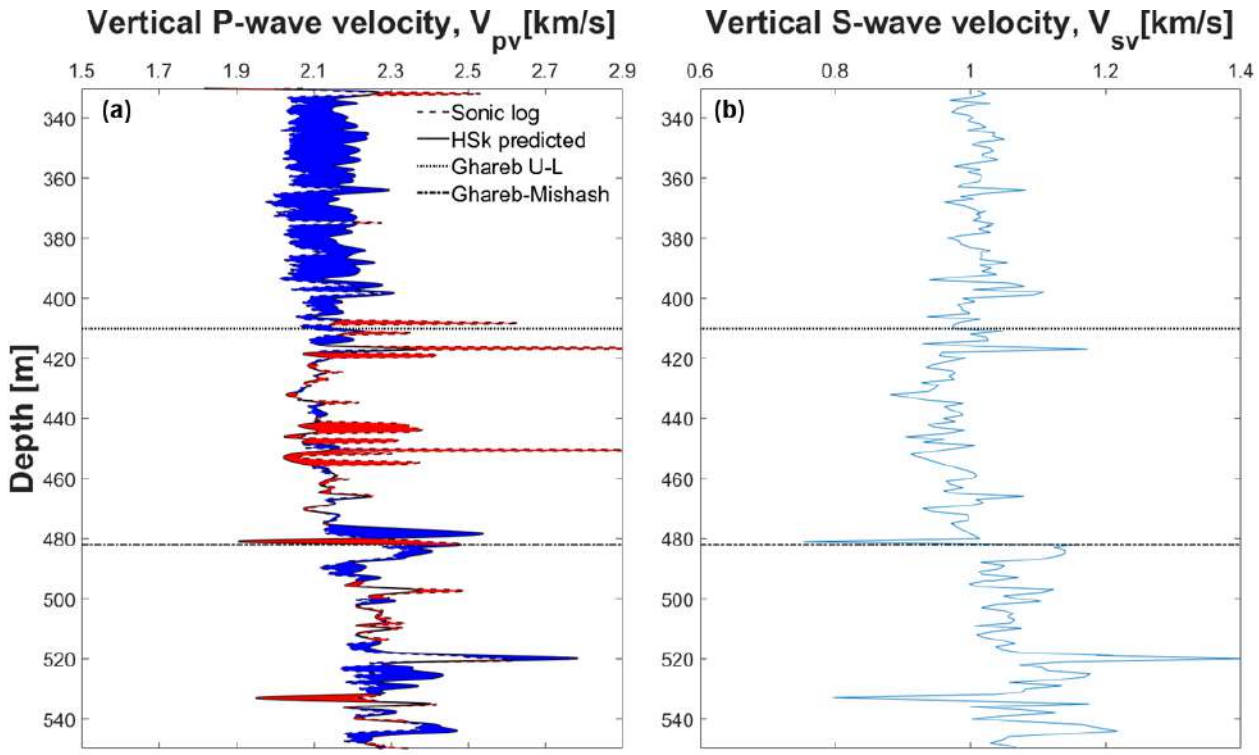

Figure 78: Depth profiles of the bedding-normal sonic velocities in the Zoharim section: a) The P-wave velocities were obtained from the sonic log. The area between the curves shows in blue where the "HSk" predictions are higher, and shows in red where it is the other way. The "HS kerogen" model predictions are accurate, except in the gas zone at the upper part of the Ghareb. b) The S-wave velocities are predicted using the "HS kerogen" model (S-wave velocities were not measured in the logs).

One of the most important properties for seismic exploration is the acoustic impedance (AI= $\boldsymbol{\rho_b}$·Vp). The density and sonic logs provide the measured value of AI on a log scale (0.15 m spacing). The combination of the "HS kerogen" model with the petrophysical model provided the estimated values on the CCDL scale (1 m spacing). The AI is strongly related to the porosity and organic content. Using the "HS kerogen" model, the porosity (or the organic content) can be estimated from measurements of AI and organic content (or porosity). This way, the relationship between organic content and AI can be used to estimate porosity (Figure 79), and the relationship between porosity and AI can be used to estimate organic content (Figure 80). In these comparisons, the gas zone in the Zoharim section is distinguished from the rest of the data as it may exhibit lower values of density and P-wave velocity in the logs. However, no distinction between the gas zone and brine-saturated zone is observed in Figure 79 and Figure 80. This inference applies for the gas saturations encountered in the Zoharim well, and could vary if gas saturations were higher.

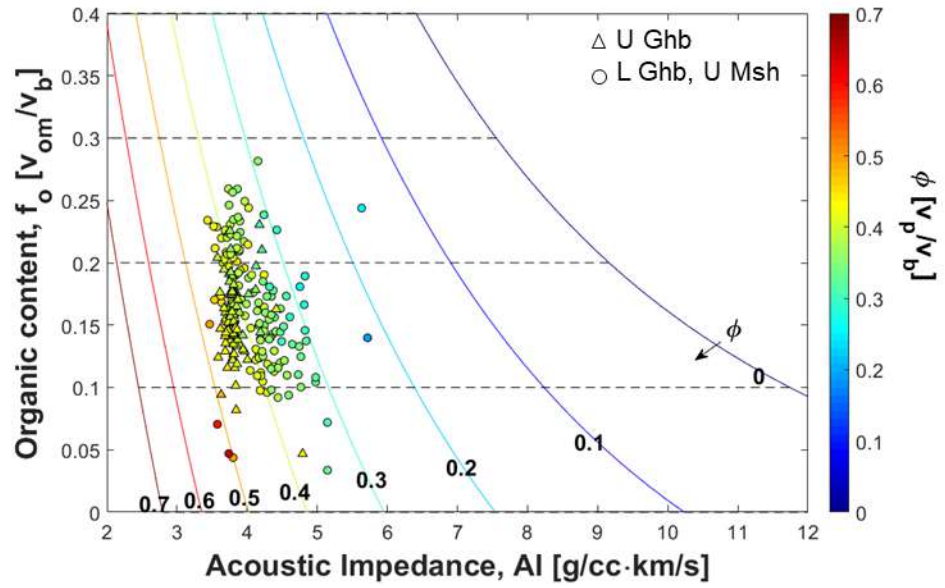

Figure 79: Organic content and acoustic impedance in the Zoharim section: The grid shows iso-porosity and iso-organic content curves calculated using the "HS kerogen" model, considering a brine-saturated rock. Data points are color-coded to porosity, and match their location in the modelled grid. Symbols: circles are from the brine-saturated zone at the lower Ghareb and upper Mishash zones, and triangles are from the gas-zone in the upper Ghareb.

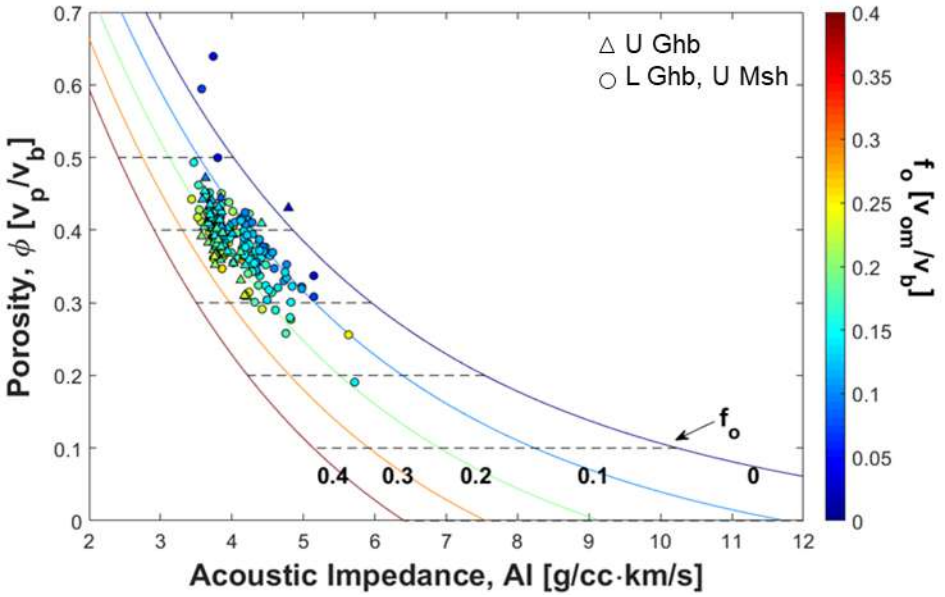

Figure 80: Porosity and acoustic impedance in the Zoharim section: The grid shows iso-porosity and iso-organic content curves calculated using the "HS kerogen" model, considering a brine-saturated rock. Data points are color-coded to organic content, and match their location in the modelled grid. Symbols: circles are from the brine-saturated zone at the lower Ghareb and upper Mishash zones, and triangles are from the gas-zone in the upper Ghareb.

4.2.3 Gas in Zoharim

The gas in the upper part of the Ghareb Formation is assumed to be a mixture of ~2/3 methane and ~1/3 carbon dioxide. Note that no gas composition measurements we available for this study, but gas sampling conducted by IEI prompts the reason behind this assumption (internal information provided by IEI Ltd.). Considering the approximate pore pressure of 2.9 - 3.6 MPa in the reservoir depths of 330 – 410 m, and temperature of ~ 25 -27 °C (Burg and Gersman, 2016), the bulk modulus of the gas is ~ 0.001 GPa. In order to calculate the gas saturation within the upper part of the Ghareb Formation it is important to choose the most appropriate fluid mixing law, considering a brine-gas mixture. These mixture laws depend strongly on the probing central frequency; for instance, at low frequency (below 1kHz) harmonic average is applicable:

$$K_f = \sum_{i=1}^{n} \left[\frac{S_i}{K_i}\right]^{-1}, \tag{87}$$

where S_i is fluid saturation and K_i is the bulk modulus of each fluid. Sonic logging frequency is typically 10-20 kHz, and K_f is higher than predicted using the harmonic average. A heuristic model by Brie (Brie *et al.* 1995) is commonly used (Lee 2004; Carcione *et al.* 2011; Carcione and Avseth 2015; Papageorgiou, Amalokwu and Chapman 2016):

$$K_f = \left(K_w - K_g\right)S_w^e + K_g \ , \tag{88}$$

where subscripts ‘w’ and ‘g’ denote water and gas, and ‘e’ is Brie’s exponent, ranging from 1 (~arithmetic average) and 40 (~harmonic average). The ‘e’ exponent depends on many variables, such as probing frequency and reference frequency, as well as the degree of consolidation. Reported values are usually within the range of e=2-5 (e.g. Lee et al. 2004). The main pitfall in this model is that the determination of the reference frequency is based on White’s model (White 1975), which is complicated and involves assumptions and approximations which may be incorrect. However, in a recent work by Wollner and Dvorkin (2018) it was shown that the fluid’s modulus can be approximated using 75% of arithmetic average plus 25% of harmonic average, i.e.:

$$K_f = 0.75 \cdot \sum_{i=1}^{n} S_i K_i + 0.25 \cdot \sum_{i=1}^{n} \left[\frac{S_i}{K_i}\right]^{-1} . \tag{89}$$

This approximation has been proven accurate for four different types of grain-packs. This model is employed here. In addition, Brie's model is applied using 'e' values of 2, 3, 4 and 5. To obtain the target value of K_f, the "HS kerogen" model is modified in such way that the measured values are used to invert K_f:

$$K_f = \frac{\phi}{\frac{1}{K_{log} + \frac{4}{3}\mu_k} - \frac{1-\phi-f_o}{K_m + \frac{4}{3}\mu_k} - \frac{f_o}{K_k + \frac{4}{3}\mu_k}} - \frac{4}{3}\mu_k \ , \tag{90}$$

where $K_{log} = M_v - \frac{4}{3}\mu_{HSk}$, as M_v is derived from the logs and μ_{HSk} is estimated (Figure 77). Using Brie's model, the water saturation is:

$$S_w = \left(\frac{K_f - K_g}{K_w - K_g}\right)^{\frac{1}{e}} . \tag{91}$$

Using Wollner and Dvorkin approximation, the water saturation is solved iteratively:

$$K_f = 0.75\big(S_w K_w + (1-S_w)K_g\big) + 0.25\left(\frac{1}{\frac{S_w}{K_w} + \frac{1-S_w}{K_g}}\right) . \tag{92}$$

Depth profiles of the water and gas saturations within the Ghareb Formation are given in Figure 81. In the upper part of the Ghareb, the approximated saturations using Wollner and Dvorkin average are most similar to the e=3 scenario, where gas saturation is ~0.12. At the lower part of the Ghareb, the gas saturations reduce to zero. It is therefore concluded that gas is accumulated within the upper part of the Ghareb Formation.

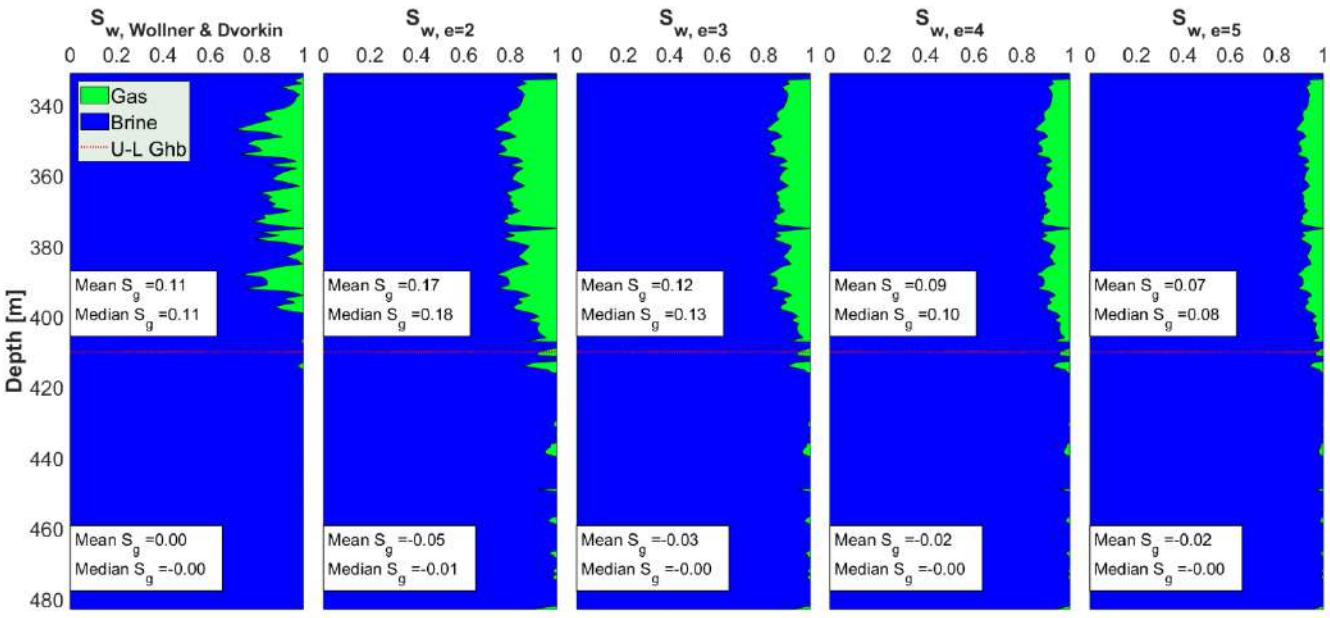

Figure 81: Gas saturations in the upper and lower parts of the Ghareb Formation in the Zoharim well: predictions are made using the "HS kerogen" model and different models for the dependence of fluid incompressibility (K_f) on water saturation (S_w). The figure shows six scenarios (left to right): the approximation by Wollner and Dvorkin (2018) and by Brie (1995) model with five different values of the 'e' parameter, within a reasonable range (1-5). Mean and median gas saturations within the upper and lower parts of the Ghareb are reported in each scenario. Note that the gas saturation diminishes at the transition from the upper part of the Ghareb Fm. to the lower part.

In order to improve the certainty of the analysis, it is preferable to compare the obtained gas saturations with another methodology, e.g. Archie's law:

$$S_w = \left(\frac{R_t}{R_w}\phi^m\right)^{\frac{1}{-n}}. \tag{93}$$

Archie's equation in a brine-saturated rock reduces to:

$$R_t = R_w\phi^{-m}. \tag{94}$$

Thus, by plotting the R_t (deep resistivity) versus the porosity, an empirical power-law should be used to represent the data. Burg and Gersman (2016) generated a depth profile of R_w assuming m=2 and full water saturation (disregarding the gas in the upper part of the Zoharim section). These assumptions are not made here as R_w is obtained from the parts below the gas zone and 'm' is obtained from the power-law regression. To do that, two pairs of data sets are used: 1) deep

resistivity log with core porosity (415-590 m depth); and 2) deep resistivity log with CCDL porosity (415-550 m depth). To satisfy $S_w = 1$, only depths below 415 m are taken for this analysis. Figure 82 shows that the cementation exponent is m=1.68 and the water resistivity is ~0.8 Ωm. To quantify gas saturation, the saturation exponent ('n') is a missing variable, typically ranging from 1.8 to 2.2. No results were obtained to allow for derivation of 'n', hence gas saturations were estimated within this range of 'n' values. The analyses show very littles changes at different 'n' values, so the results are presented assuming n=2. The resultant mean and median gas saturations are 0.12 and 0.11, respectively. Conclusively, the results from the different models suggest that the gas saturation within the upper part of the Ghareb Formation averages at ~0.12.

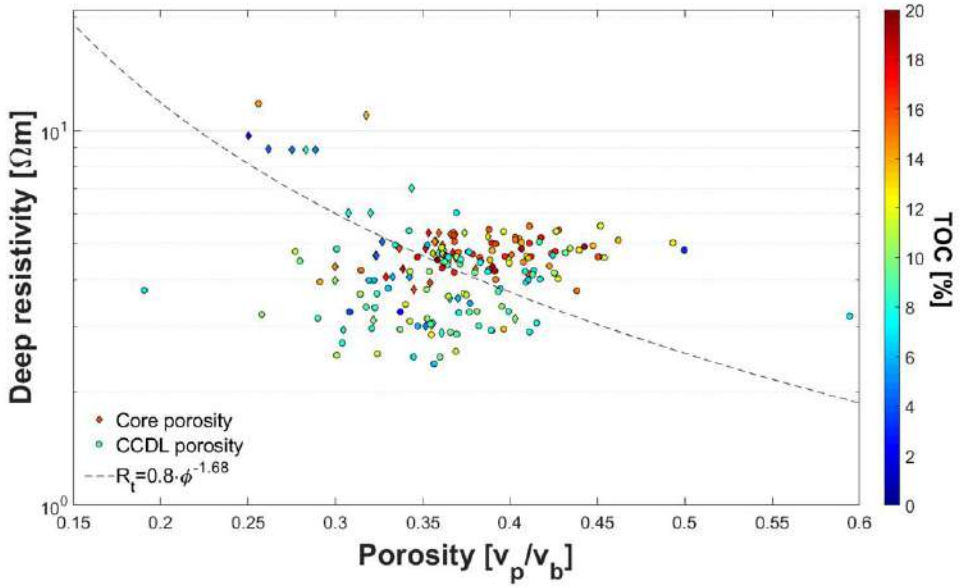

Figure 82: Resistivity versus Porosity: resistivity was measured by the deep laterolog tool; porosity was measured in the laboratory (diamonds) and approximated using the CCDL combination (circles). Data points are color-coded to TOC. The dashed curve is a power-law trendline from which the cementation exponent and formation water resistivity, m=1.68 and R_w=0.8 $\Omega \cdot m$ are derived.

The origin of the gas is uncertain, as it occurs only in the upper part of the Ghareb Formation. Three possible mechanisms are proposed: 1) the gas was generated in place due to the higher degree of maturation in the upper section; 2) the gas was generated somewhere else, migrated and trapped by the overlying Taqiye formation (Marl); and 3) the gas is of biogenic origin. Mechanism (2) seems unlikely because: i) the Ghareb-Mishash sequence is situated in a syncline; ii) the low permeability of the rock is unfavorable to migration into it; and iii) the observed gas saturations

are below the critical gas saturation at which gas starts to flow in a water-wet rock (typically 20-30%). Therefore, the gas is assumed to have been generated in place within the upper part of the Ghareb formation. Currently, the lack of gas composition data does not allow to determine whether the gas is thermogenic or biogenic (mechanism (1) or (3)). As maturation is typically assumed to increase with depth, mechanism (1) is less reasonable. However, it may still be supported by T_{max} data provided by IEI Ltd., that indicate higher maturity levels in the upper section. This reverse maturity-depth profile may result from variability in the kerogen composition. On the other hand, mechanism (3) which describes a biogenic source is the easiest to assume at this point, as it is not bounded to thermal conditions. It is stated here that more data are required to resolve this enigma.

4.2.4 Estimation of static moduli in the Zoharim section

The dynamic elastic moduli are useful not only for prospecting, but also for engineering purposes. Static moduli are the ones being used for prediction of compaction, stress perturbations, stability, and surface subsidence induced by pore-pressure changes in a reservoir. For this purpose, drained conditions are assumed because these processes are considered to be slow. To make such calculations, dry rock moduli are needed, and not undrained moduli (i.e. saturated). The static-dynamic relationships established at the course of this study enable this kind of estimation. First, the dynamic moduli in dry conditions are estimated using the "HS kerogen" model. Then, the static-dynamic conversion relationships for vertical oedometer modulus and vertical Young's modulus are applied (Equations (73) and (74)). Finally, depth profile of the estimated static moduli is created (Figure 83). The vertical oedometer modulus represents the one-dimensional elastic contraction of the rock (i.e. uniaxial strain at the vertical direction). Using the "HS kerogen" model the dynamic M_v of dry rock is computed, so that the static M_v is obtained using Equation (73). The ratio of M_v over the vertical Young's modulus E_v was found to be $M_v/E_v \cong 1.11$ in dynamic conditions. This way, the dynamic E_v is estimated and using Equation (74) a depth profile of the vertical Young's modulus is generated.

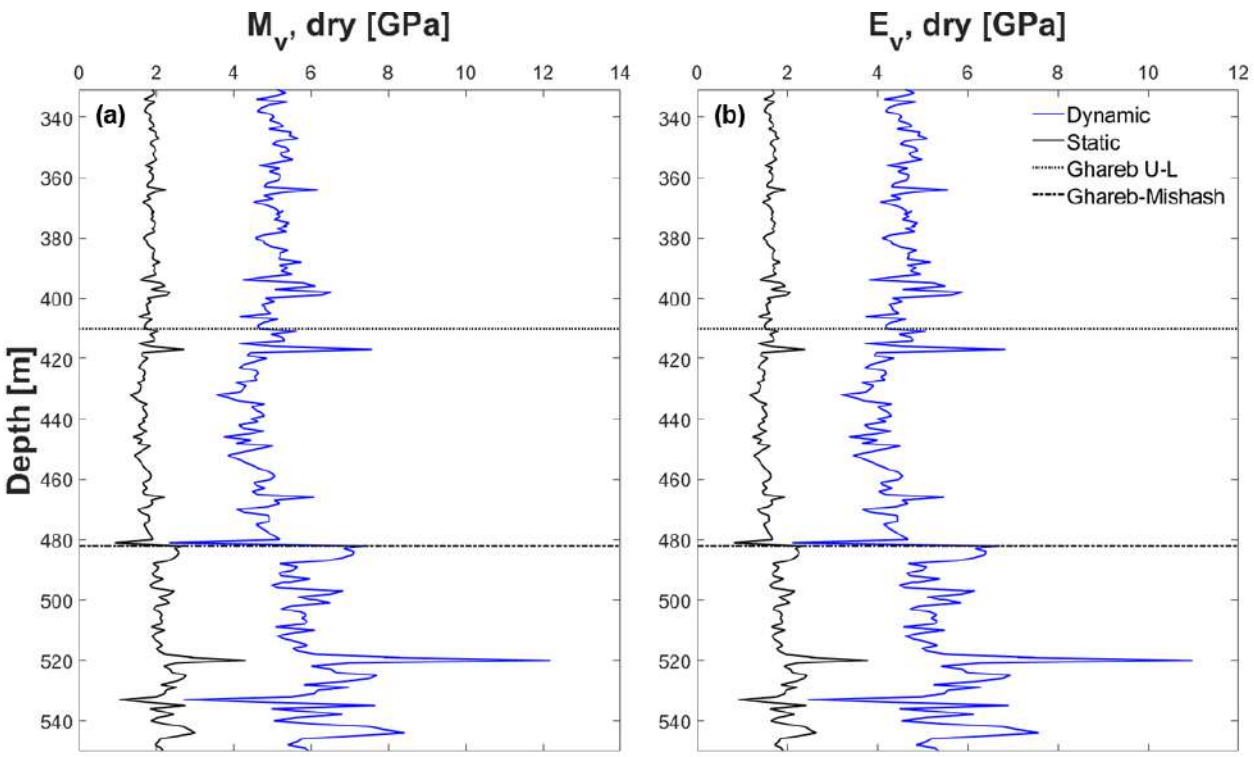

Figure 83: Depth profiles of static and dynamic moduli in the Zoharim section: vertical oedometer modulus (a) and vertical Young's modulus (b) are estimated considering drained conditions (i.e. dry conditions). The dynamic moduli are "HS kerogen" predictions and static moduli are calculated from Equations (73) and (74). For explanation as to why dry moduli are calculated instead of saturated, the reader is directed to the text right above this figure.

4.2.5 Porosity and compaction curve

Compaction curves are commonly employed for prediction of porosity at depths in undrilled locations. The predicted porosities assist in approximating other rock properties, such as bulk density and sonic velocities. Compaction curves are created for different lithologies using porosity measurements in depth. Generally, porosity decreases due to the increase in effective stress σ_v, which is calculated by the total vertical stress generated by weight of the rock column S_v, minus the pore pressure P_p, factored by Biot's coefficient β (Equation (31)). In this study, porosity data is available from several sources: measurements using core samples from Zoharim and Aderet wells, CCDL calculated porosities measured in the field, and results by Gordin *et al.* (in prep.). Compaction trends are assumed to follow an exponential regression (Vernik 2016):

$$\phi = \phi_0 e^{-\sigma_v / C_m} , \tag{95}$$

where ϕ_0 is the porosity of the rock at initial sedimentation, and C_m is the inelastic compaction modulus, which typically ranges from 24 to 31 MPa. It is reasonable to approximate ϕ_0 to 0.75, as ooze porosities are usually found within the porosity range of 70-80% (Fabricius 2003). The vertical effective stress is calculated by the gradients of vertical total stress and pore pressure in each depth section. The resultant C_m is about 6.1 MPa, much lower than reported in Vernik (2016). In some studies, the trend in Equation (95) is given in terms of depth (z) instead of effective stress:

$$\phi = \phi_0 e^{-Cz} . \tag{96}$$

Organic-rich mud-rocks have been reported to exhibit C of $1.3 - 2.6 \cdot 10^{-4} m^{-1}$ (C. Li *et al.* 2017).In this study, C is approximately $1.7 \cdot 10^{-3} m^{-1}$. In both cases, it appears that the compaction rates are quite high, i.e. porosity rapidly decreases with depth. This may point to the compliant nature of the Ghareb-Mishash chalk. However, it should be remembered that at greater depths porosity also reduces due to cementation, recrystallization and pressure dissolution. These phenomena are rare or absent in the shallow Shefela basin but encountered in the Southern Golan Heights basin. Either way, compaction of the Ghareb-Mishash chalk in specific, and organic-rich chalks in general, should be studied further by compiling data from more locations and dedicating more attentions to microstructural evolution upon burial. The results presented here should assist in advancing future research in this direction.

4.3 Aderet well

4.3.1 Petrophysical properties estimation

As mentioned before, the logging suite in Aderet did not include any porosity or density tool, thus data compilation was more complicated and speculated with respect to the Zoharim dataset. As in the Zoharim well, the Aderet well includes three datasets: well-logs, continuous coring, and laboratory measurements. Continuous coring data provided a dense depth profile of TOC (measurements are spaced by 1 m). Laboratory measurements yielded an extensive and accurate core porosity and solids density dataset, available from hundreds of Coreval30 measurements at performed by Bisnovat (2013) and the current study. The core porosities are spaced inconsistently due to variability of core recovery; some intervals include multiple measurements while others could not have been measured. In order to apply the models on the sampled depth section, estimates of porosity and organic content must be made. In the next paragraphs, data interpolation and

compilation are described. In this case, the depth section of interest is 265-530 m, including the upper part of the Ghareb Fm. (which contains gas, 265-390m), the lower part of the Ghareb Fm. (organic-rich, 390-460m), and the upper part of the Mishash Fm. (460-530m).

The TOC depth profile was created exactly as in the Zoharim section, although pairing of the TOC values with porosity and density data was unavailable. To overcome this, the laboratory measurements of porosity and solids density were paired with their corresponding TOC value (TOC was also measured for each core plug measured in the Coreval30 system). This relationship indicated the density of the organic phase is 1.37 g/cc. Carbon percentage in the thermally immature organic matter was evaluated to 65%wt. (data by IEI Ltd.). This relationship also provides the estimated solids density (ρ_s). Assuming bitumen concentration is similar to that in the Zoharim section (6% of the organic matter volume), the kerogen density is 1.39 g/cc. Subsequently, the organic content is estimated using Equation (16). In order to do that, the measured core porosities were interpolated linearly to match the scale of the continuous coring dataset (recall that $\rho_{dry} = \rho_s(1-\phi)$). Although this interpolation may seem speculative, it should be indicated that the number of core porosity measurements is quite high within this depth range (n=241) and hence this dataset is sufficiently dense. Then, the interpolated porosity was paired with the TOC and solids density from the continuous coring dataset. After the compilation of laboratory and continuous coring datasets, the values from the well-logs were scaled down to the continuous dataset as done with the Zoharim data: average of 5 nearest values at the target depth (in the continuous coring dataset). At this point, the petrophysical evaluation of the Aderet interval is established, and the "HS kerogen" model can be applied (Figure 84, Figure 85).

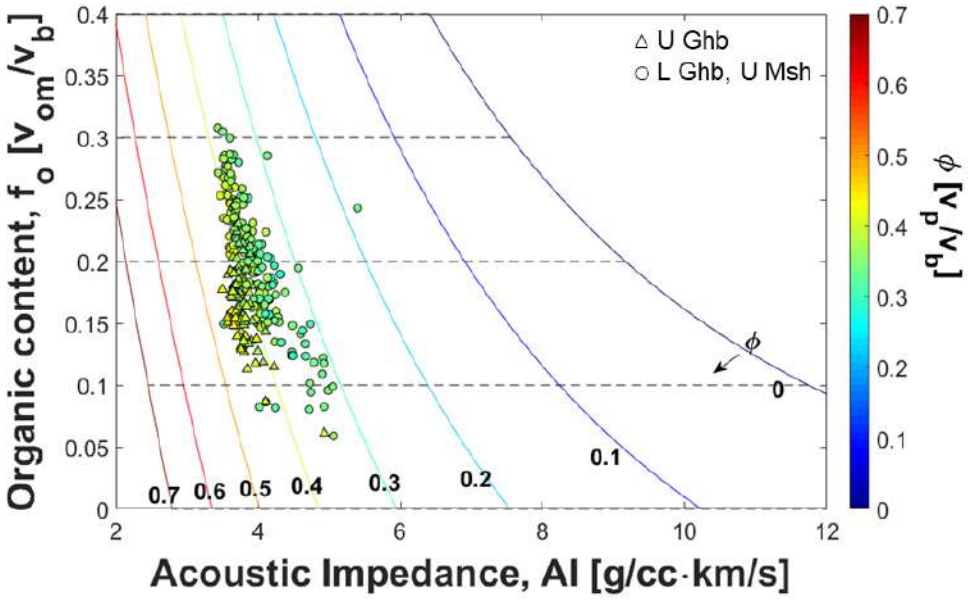

Figure 84: Organic content and acoustic impedance in the Aderet section: The grid shows iso-porosity and iso-organic content curves calculated using the "HS kerogen" model, considering a brine-saturated rock. Data points are color-coded to porosity, and match their location in the modelled grid. Symbols: circles are from the brine-saturated zone, and triangles are from the gas-zone in the upper Ghareb.

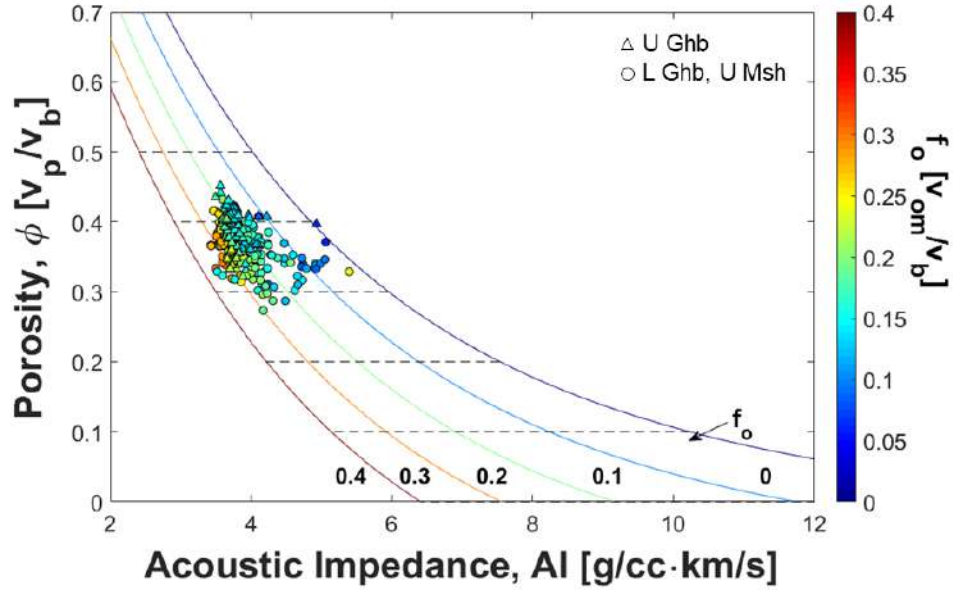

Figure 85: Porosity and acoustic impedance in the Aderet section: The grid shows iso-porosity and iso-organic content curves calculated using the "HS kerogen" model, considering a brine-saturated rock. Data points are color-coded to organic content, and match their location in the modelled grid. Symbols: circles are from the brine-saturated zone, and triangles are from the gas-zone in the upper Ghareb.

4.3.2 Elastic moduli, velocities and gas detection

As in the Zoharim well, the volume fractions are used to estimate the elastic moduli and acoustic velocities of the rock. The results appear similar, despite the difference in depths between the two wells. The Elastic moduli and acoustic velocities are presented versus depth in Figure 86 and Figure 87. Once again, reliable depth profiles of these properties are obtained using the "HS kerogen" model. The upper part of Ghareb Formation in the Aderet well also contains gas, thus the same set of calculations is performed. Based on this analysis, the mean gas saturation in the Aderet section is similar but slightly higher than in the Zoharim well ($S_g \cong 0.15$). Unfortunately, the data could not have been compared with deep resistivity logs as they show unreliable results (constant resistivity over the entire range of porosities).

The observation of similar gas saturations at the top of the Ghareb in both the Zoharim and Aderet wells located 7 kilometers apart suggest the gas may be ubiquitous over the entire Shefela basin.

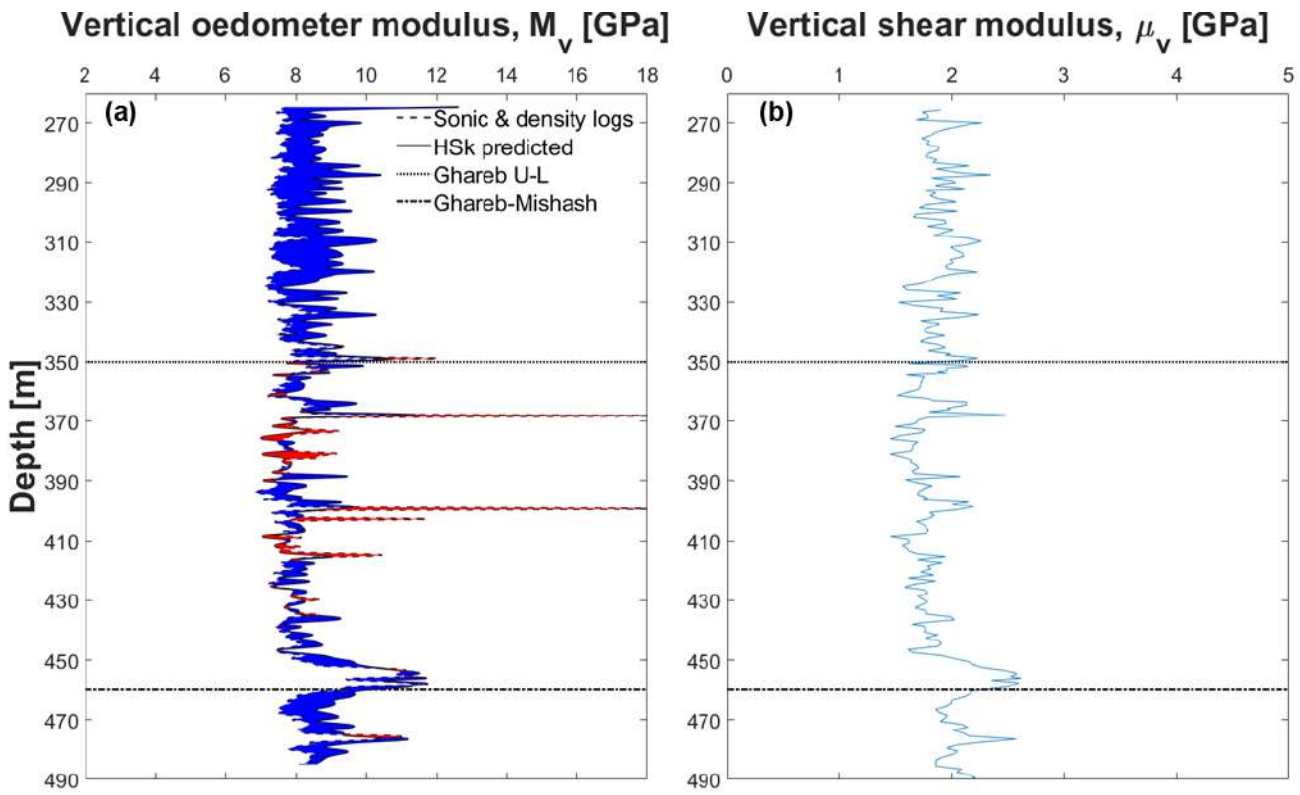

Figure 86: Depth profiles of the vertical dynamic moduli in the Aderet section: a) The P-wave moduli were obtained from the sonic and density logs. The area between the curves shows in blue where the "HSk" predictions are higher, and shows in red where it is the other way. The "HS kerogen" model predictions are accurate, except in the gas zone at the upper part of the Ghareb. b) The S-wave moduli are predicted using the "HS kerogen" model (S-wave velocities were not measured in the logs).

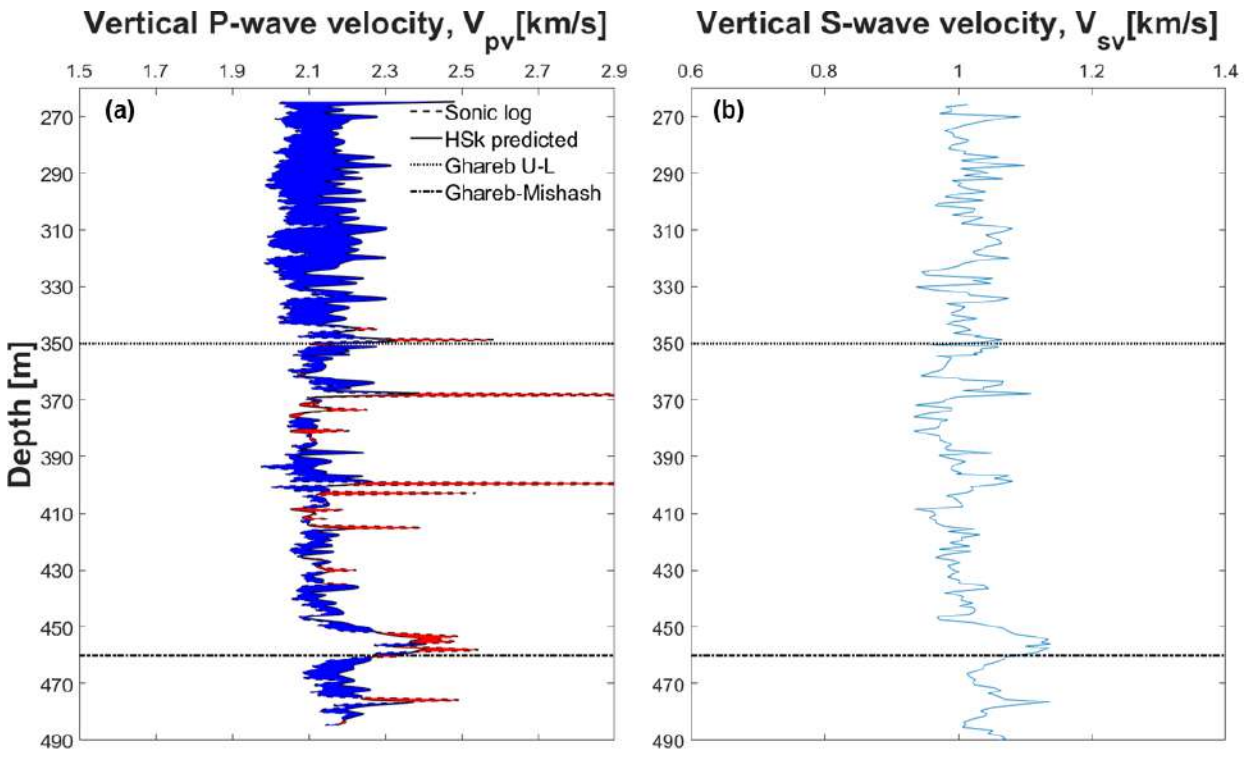

Figure 87: Depth profiles of the bedding-normal sonic velocities in the Aderet section: a) The P-wave velocities were obtained from the sonic log. The area between the curves shows in blue where the "HSk" predictions are higher, and shows in red where it is the other way. The "HS kerogen" model predictions are accurate, except in the gas zone at the upper part of the Ghareb. b) The S-wave velocities are predicted using the "HS kerogen" model (S-wave velocities were not measured in the logs).

4.4 Discussion

This part of the dissertation extended the rock physics analysis of the Ghareb-Mishash chalk from the laboratory to the field scale, using well-logs from the Zoharim and Aderet wells in the Shefela basin. The transition from laboratory to field scale seems successful. Yet, there are few issues to raise in this upscaling procedure.

The logging suite utilized in the Shefela basin was rather limited. In advanced logging suites the porosity is measured using different kinds of logging tools (e.g. nuclear magnetic resonance, litho-density). Sonic velocities usually include azimuthal S-waves measurements for identification of fractures and anisotropy, while here no S-wave velocity data were available. Permeability estimation is routinely performed using Stoneley waves in the sonic logs and NMR. Spectral gamma-ray are preferred over the basic gamma-ray tool to allow for identification of the source of

radioactivity (uranium is often associated with organic matter, potassium and thorium with clays). Variability in mineralogy is detectable using elemental spectroscopy tools (e.g. pulsed neutron spectroscopy, elemental capture spectroscopy). Resistivity measurements are usually done using various arrays of electrodes, to measure resistivity at different distances from the wellbore wall. The logging tools mentioned here are only part of the information that could have been obtained using more advanced logging suites. Therefore, the analysis shown in this Chapter is based on a limited dataset. This does not limit the reliability of the analysis, but only the amount and resolution of information that can be derived from it.

Field measurements also include seismic surveys, which were not part of this study. If seismic sections had been available, several attributes could have been estimated, mostly relating to the acoustic properties. For example, the areal extent of the gas at the top of Ghareb Formation could have been detected and evaluated using amplitude versus offset (AVO) inversion. Another example is where wells have already been drilled and evaluation of rock properties has already been performed (as done in this chapter), then the seismic profile might reveal location of maximum gas saturations and organic contents. More information is available by cross-plotting seismic attributes such as acoustic impedance, Vp/Vs, shear impedance (ρ_bVs), and Lame's parameters λ and μ, intercept and gradient from AVO analysis, and others. Such analysis requires a comprehensive research program, dedicated to seismic interpretation solely. A study of this kind should include the rock physics models such as those proposed in this thesis.

4.5 Conclusions

In this chapter the case study of the Ghareb-Mishash chalk was extended from the laboratory to the field. The field measurements used here are well-logs, that provide the porosity, density, P-wave velocity and organic-contents. Combined with continuous coring data, rock physics analysis of the data was enabled, so that acoustic velocities, elastic moduli and acoustic impedances are predicted reliably. The petrophysical evaluation of the rock using the CCDL combination is found successful. The main findings from this chapter are:

1. The petrophysical model proposed in this thesis is applicable generally for source rocks evaluation, especially where the porosity is high.
2. Most of the excess neutron porosity is associated with organic content. This supports the observation that the Ghareb-Mishash chalk is very lean in clay content.

3. In the absence of TOC measurements, it is preferable to estimate the TOC using a multivariable linear regression that includes the density, neutron and gamma-ray logs, instead of using the gamma-ray alone.
4. The bedding-normal acoustic velocities are accurately predicted using the "HS kerogen" model, proposed in Chapter 2.
5. A gas saturation is identified at the top of the Ghareb Formation. The gas is sealed by the impermeable overlying Taqiye Formation. Gas saturation within the upper part of the Ghareb Formation (80-90 m thick) are about 10-15%. This estimation was established from rock physics analysis combining Brie's method with Wollner and Dvorkin's approximation, and cross-examined using Archie's law for the influence of water saturation on the resistivity of the rock.

5 Concluding remarks

Organic-rich rocks are routinely evaluated using methodologies suitable for low porosity, laminated clay-rich shales. This study confronts a case of high porosity organic-rich chalk, with a typical chalk texture. This forces modifications in the analytical approaches. Rock physics is studied comprehensively, by accounting for the petrophysical, mechanical, geochemical, sedimentological and geophysical attributes. This study is first of a kind, and therefore combines approaches proper for organic-rich shales and non-organic chalks. This study characterizes the Ghareb-Mishash chalk in an extremely systematic and thorough fashion, where the effects of porosity, organic content and maturity on various physical properties are investigated. The analysis required reconsideration of common practice methods, which may have been insufficient. By this carefulness, innovative approaches were developed, such as the "hydrostatic strain ratio", "HDC-TIES" method, "HS kerogen" model, and improved petrophysical evaluation of source rocks. Rock physics of organic-rich chalks in general, and the Ghareb-Mishash chalk in particular, should be studied further with greater consideration to micro-structural properties, anisotropy, stress dependency, mineralogical variability, kerogen-bitumen-oil-gas conversion chain and the resultant porosity and saturation, as well as other processes and features. Noting that, the findings of this research provide a deep understanding of the rock, even more than initially expected.

The elastic moduli of the Ghareb-Mishash chalk, at all maturity levels, exhibit dependence on the kerogen-factored porosity, calculated by $\phi + 0.5 \cdot f_o$. The porosity is the primary factor that influences the elastic stiffness, anisotropy, strength, permeability, and acoustic velocities. The second most important parameter is the organic content, which affects the elastic stiffness, but has little or no impact on elastic anisotropy or strength. The anisotropy of this chalk is considered weak-to-moderate, with Ω of 0.4-1, and Thomsen's ε of 0-0.3 in brine-saturated conditions; in dry conditions the anisotropy is much larger, with Ω as low as 0.3 and ε of 0.5. The organic matter has a key role in the acoustic response of the rock, as the bedding-normal velocities are accurately predicted using the "HS kerogen" model, i.e. the kerogen forms a connected network within organic contents of 5-25 %. Numerous observations suggest that the Ghareb-Mishash chalk is quite soft, with low BAM normalized stiffness factor (w~0.2), and the static-dynamic relationship typical of a soft rock.

The BAM model is found suitable for fluid substitution and parameterization of rock stiffness, but less so for geophysical prospecting. Remote evaluation of the rock properties should be done using the "HS kerogen" model. This is supported by laboratory measurements, rock physics templates and well-logs, as it tracks changes in porosity and organic content reliably. Gas saturations in the upper part of the Ghareb Formation are estimated using the "HS kerogen" model combined with Brie's fluid incompressibility model using e~3.

The maturation effects on the rock properties can be partly described using results of unconfined anhydrous pyrolysis. The changes in the organic matter seem reasonable, where kerogen stiffening and densification occur. Bitumen contents calculated using the modified petrophysical model, allow the analysis to be done more precisely by differentiating kerogen and bitumen from the organic content. However, the maturity-associated changes are minor with respect to porosity and organic content as they only change the density and intrinsic kerogen moduli and are not enough to be exhibited in the acoustic response of a high porosity brine-saturated rock. However, if hydrocarbon saturation is accounted for then the maturation can be identified; but this requires estimation of kerogen-bitumen-oil-gas conversion at each maturity level, as well as pore-pressure build up. This will require further examination.

The conclusion of this research is that Ghareb-Mishash chalk belongs to the family of organic-rich shales and non-organic chalks. It displays features of both groups, but when combined it obtains an identity of its own. No common rock physics model is applicable without adjustments. The physical properties of it are strongly influenced by its geological history, including burial depth, sedimentological composition, organic matter accumulation and preservation, tectonic environment, and diagenesis. In the shallow buried Shefela basin, the porosity is very high due to limited compaction and cementation, and the organic matter is immature. In other basins in Israel, the same rock unit may display cementation, pressure dissolution, compaction, and increased maturity. In other cases, the acoustic velocities could depart from the "HS kerogen" model, as the calcite concentration increases. Yet, the general models and procedures employed here may be implemented in many other cases, including organic-rich shales.

References

Ahmadov, R., Vanorio, T., & Mavko, G. (2009). Confocal laser scanning and atomic-force microscopy in estimation of elastic properties of the organic-rich Bazhenov Formation. *The Leading Edge, 28*(1), 18-23. DOI: 10.1190/1.3064141

Alam, M. M., Borre, M. K., Fabricius, I. L., Hedegaard, K., Røgen, B., Hossain, Z., & Krogsbøll, A. S. (2010). Biot's coefficient as an indicator of strength and porosity reduction: Calcareous sediments from Kerguelen Plateau. *Journal of Petroleum Science and Engineering, 70*(3), 282-297. DOI: 10.1016/j.petrol.2009.11.021

Alfred, D., & Vernik, L. (2012). A new petrophysical model for organic shales. Paper presented at the *SPWLA 53rd Annual Logging Symposium,*

Allan, A. M., Vanorio, T., & Dahl, J. E. (2014). Pyrolysis-induced P-wave velocity anisotropy in organic-rich shales. *Geophysics, 79*(2), D41-D53. DOI: 10.1190/geo2013-0254.1

Al-Tahini, A., Sondergeld, C., & Rai, C. (2004). The effect of cementation on static and dynamic properties in jauf and unayzah formations at saudi arabia. Paper presented at the *SPE Annual Technical Conference and Exhibition,* DOI: 10.2118/90448-MS

American Petroleum Institute (API). (1998). *Recommended practices for core analysis.* (No. 40, 2nd Edition). Washington, DC: American Petroleum Institute, Exploration and Production Department.

Archie, G. E. (1942). The electrical resistivity log as an aid in determining some reservoir characteristics. *Transactions of the AIME, 146*(01), 54-62.

Avseth, P., & Carcione, J. M. (2015). Rock-physics analysis of clay-rich source rocks on the Norwegian Shelf. *The Leading Edge, 34*(11), 1340-1348. DOI: 10.1190/tle34111340.1

Baskin, D. K., & Peters, K. E. (1992). Early generation characteristics of a sulfur-rich Monterey kerogen. *AAPG Bulletin, 76*(1), 1-13.

Bernard, S., Horsfield, B., Schulz, H., Wirth, R., Schreiber, A., & Sherwood, N. (2012). Geochemical evolution of organic-rich shales with increasing maturity: A STXM and TEM study of the Posidonia Shale

(Lower Toarcian, northern Germany). *Marine and Petroleum Geology, 31*(1), 70-89. DOI: 10.1016/j.marpetgeo.2011.05.010

Biot, M. A. (1941). General theory of three-dimensional consolidation. *Journal of Applied Physics, 12*(2), 155-164.

Bisnovat, K. (2013). *Mechanical and Petrophysical Behavior of Oil Shale from the Judea Plains, Israel.* M.Sc. thesis, Ben-Gurion University of the Negev, Israel.

Bisnovat, K., Hatzor, Y. H., Vinegar, H. J., Nguyen, S. V., Palchik, V., & Feinstein, S. (2015). Mechanical and petrophysical behavior of organic-rich chalk from the Judea Plains, Israel. *Marine and Petroleum Geology, 64*, 152-164. DOI: 10.1016/j.marpetgeo.2015.02.044

Bredesen, K., Jensen, E. H., Johansen, T. A., & Avseth, P. (2015). Seismic reservoir and source-rock analysis using inverse rock-physics modeling: A Norwegian Sea demonstration. *The Leading Edge*, DOI: 10.1190/tle34111350.1

Bridges, M. (2016). *Mechanical Properties of the Niobrara.* M.Sc. thesis, Colorado School of Mines, Golden, Colorado. http://hdl.handle.net/11124/170636.

Brie, A., Pampuri, F., Marsala, A., & Meazza, O. (1995). Shear sonic interpretation in gas-bearing sands. Paper presented at the *SPE Annual Technical Conference and Exhibition*,

Brotons, V., Tomás, R., Ivorra, S., Grediaga, A., Martínez-Martínez, J., Benavente, D., & Gómez-Heras, M. (2016). Improved correlation between the static and dynamic elastic modulus of different types of rocks. *Materials and Structures, 49*(8), 3021-3037. DOI: 10.1617/s11527-015-0702-7

Burg, A., & Gersman, R. (2016). Hydrogeology and geochemistry of low-permeability oil-shales–Case study from HaShfela sub-basin, Israel. *Journal of Hydrology, 540*, 1105-1121. DOI: 10.1016/j.jhydrol.2016.07.026

Burnham, A. K. (2018). Thermomechanical properties of the Garden Gulch Member of the Green River Formation. *Fuel, 219*, 477-491. DOI: 10.1016/j.fuel.2018.01.122

Carcione, J. M. (2000). A model for seismic velocity and attenuation in petroleum source rocks. *Geophysics, 65*(4), 1080-1092. DOI: 10.1190/1.1444801

Carcione, J. M. (2014). *Wave fields in real media: Wave propagation in anisotropic, anelastic, porous and electromagnetic media* (3rd ed.), Elsevier.

Carcione, J. M., & Avseth, P. (2015). Rock-physics templates for clay-rich source rocks. *Geophysics, 80*(5), D481-D500. DOI: 10.1190/geo2014-0510.1

Carcione, J. M., Helle, H. B., & Avseth, P. (2011). Source-rock seismic-velocity models: Gassmann versus Backus. *Geophysics, 76*(5), N37-N45. DOI: 10.1190/geo2010-0258.1

Cavallini, F. (1999). The best isotropic approximation of an anisotropic Hooke's law. *Bollettino Di Geofisica Teorica Ed Applicata, 40*(1), 1-18.

Cheng, C., & Johnston, D. H. (1981). Dynamic and static moduli. *Geophysical Research Letters, 8*(1), 39-42.

Darcy, H. (1856). *Les fontaines publiques de la ville de dijon: Exposition et aplication... de distribution d'eau...*, Victor Dalmont.

del Monte, A. A., Antonielli, E., De Tomasi, V., Luchetti, G., Paparozzi, E., & Gambacorta, G. (2018). Methods for source rock identification on seismic data: An example from the Tanezzuft Formation (Tunisia). *Marine and Petroleum Geology, 91*, 108-124. DOI: 10.1016/j.marpetgeo.2017.12.015

Detournay, E., & Cheng, A. H. (1993). Fundamentals of Poroelasticity.

Dewan, J. T. (1983). *Essentials of modern open-hole log interpretation*, PennWell Books.

Dewhurst, D. N., Siggins, A. F., Sarout, J., Raven, M. D., & Nordgård-Bolås, H. M. (2011). Geomechanical and ultrasonic characterization of a Norwegian Sea shale. *Geophysics, 76*(3), WA101-WA111. DOI: 10.1190/1.3569599

Eliyahu, M., Emmanuel, S., Day-Stirrat, R. J., & Macaulay, C. I. (2015). Mechanical properties of organic matter in shales mapped at the nanometer scale. *Marine and Petroleum Geology, 59*, 294-304. DOI: 10.1016/j.marpetgeo.2014.09.007

Emmanuel, S., Eliyahu, M., Day-Stirrat, R. J., Hofmann, R., & Macaulay, C. I. (2016). Impact of thermal maturation on nano-scale elastic properties of organic matter in shales. *Marine and Petroleum Geology, 70*, 175-184. DOI: 10.1016/j.marpetgeo.2015.12.001

Eseme, E., Urai, J., Krooss, B., & Littke, R. (2007). Review of mechanical properties of oil shales: implications for exploitation and basin modeling. *Oil Shale, 24*(2), 159-174.

Eshet, Y., Almogi-Labin, A., & Bein, A. (1994). Dinoflagellate cysts, paleoproductivity and upwelling systems: a Late Cretaceous example from Israel. *Marine Micropaleontology, 23*(3), 231-240.

Fabricius, I. L. (2003). How burial diagenesis of chalk sediments controls sonic velocity and porosity. *AAPG Bulletin, 87*(11), 1755-1778. DOI: 10.1306/06230301113

Fabricius, I. L., Høier, C., Japsen, P., & Korsbech, U. (2007). Modeling elastic properties of impure chalk from South Arne Field, North Sea. *Geophysical Prospecting, 55*(4), 487-506. DOI: 10.1111/j.1365-2478.2007.00613.x

Fabricius, I. L. (2014). Burial stress and elastic strain of carbonate rocks. *Geophysical Prospecting, 62*(6), 1327-1336. DOI: 10.1111/1365-2478.12184

Fairhurst C. (1964). The validity of the "Brazilian" test for brittle materials. *Int J Rock Mech Min Sci Geomech* Abstr 1(4):535–546. DOI:10.1016/0148-9062(64)90060-9

Fathi, E., Tinni, A., & Akkutlu, I. Y. (2012). Correction to Klinkenberg slip theory for gas flow in nano-capillaries. *International Journal of Coal Geology, 103*, 51-59. DOI: 10.1016/j.coal.2012.06.008

Fjær, E., Holt, R. M., Raaen, A., Risnes, R., & Horsrud, P. (2008). *Petroleum related rock mechanics*, Elsevier.

Fjær, E., Stroisz, A. M., & Holt, R. M. (2013). Elastic dispersion derived from a combination of static and dynamic measurements. *Rock Mechanics and Rock Engineering, 46*(3), 611-618.

Flexer, A. (1968). Stratigraphy and facies development of Mount Scopus Group (Senonian-Paleocene) in Israel and adjacent countries. *Israel Journal of Earth Sciences, 17*(3), 85-113.

Gardosh, M., A, & Tennenbaum, E. (2014). The petroleum systems of israel. In L. Marlow, C. Kendall & L. Yose (Eds.), *Petroleum systems of the tethyan region:AAPG memoir 106* (pp. 179-216)

Gassmann, F. (1951). Elasticity of porous media. *Vierteljahrsschrder Naturforschenden Gesselschaft, 96*, 1-23. DOI: 10.1190/1.9781560801931.ch3p

Gayer, J. L. (2015). *Artificial maturation of oil shale: the Irati Formation from the Paraná Basin, Brazil.* M.Sc. thesis, Colorado School of Mines, Golden, Colorado.

Gersman, R., Bartov, Y., & Rozenthal, A. (2012). *Summary report of zoharim survey well hydro-geological findings.* (No. IEI/3/2012). Jerusalem: IEI Ltd.

Ghanizadeh, A., Amann-Hildenbrand, A., Gasparik, M., Gensterblum, Y., Krooss, B. M., & Littke, R. (2014). Experimental study of fluid transport processes in the matrix system of the European organic-rich shales: II. Posidonia Shale (Lower Toarcian, northern Germany). *International Journal of Coal Geology, 123*, 20-33. DOI: 10.1016/j.coal.2013.06.009

Golder Associates. (2011). *Zoharim in-situ stress measurement- hydraulic jacking.* (No. 113-81968). Tel Aviv: Golder Associates.

Gommesen, L., & Fabricius, I. L. (2001). Dynamic and static elastic moduli of North Sea and deep sea chalk. *Physics and Chemistry of the Earth, Part A: Solid Earth and Geodesy, 26*(1), 63-68. DOI: 10.1016/S1464-1895(01)00024-2

Goodarzi, M., Rouainia, M., & Aplin, A. (2016). Numerical evaluation of mean-field homogenisation methods for predicting shale elastic response. *Computational Geosciences, 20*(5), 1109-1122. DOI: 10.1007/s10596-016-9579-y

Goodarzi, M., Rouainia, M., Aplin, A., Cubillas, P., & de Block, M. (2017). Predicting the elastic response of organic-rich shale using nanoscale measurements and homogenisation methods. *Geophysical Prospecting, 65*(6), 1597-1614. DOI: 10.1111/1365-2478.12475

Gordin, Y., Hatzor, Y. H., & Vinegar, H. J. (in prep.). *Anisotropy evolution during early maturation of organic-rich carbonate.*

Gvirtzman, G., Moshkovitz, S., & Reiss, Z. (1985). Senonian to Early Eocene Mount Scopus Group in the HaShefela region, Central Israel: stratigraphy and basin evolution. *Israel Journal of Earth-Sciences, 34*(4), 172-192.

Gvirtzman, G., Almogi-Labin, A., Moshkovitz, S., Lewy, Z., Honigstein, A., & Reiss, Z. (1989). Upper Cretaceous high-resolution multiple stratigraphy, northern margin of the Arabian platform, central Israel. *Cretaceous Research, 10*(2), 107-135. DOI: 10.1016/0195-6671(89)90001-3

Han, D., Liu, J., & Batzle, M. (2006). Acoustic property of heavy oil-measured data. Paper presented at the *SEG Technical Program Expanded Abstracts 2006,* New Orleans. 1903-1907. DOI: 10.1190/1.2369898

Hashin, Z., & Shtrikman, S. (1963). A variational approach to the theory of the elastic behaviour of multiphase materials. *Journal of the Mechanics and Physics of Solids, 11*(2), 127-140. DOI: 10.1016/0022-5096(63)90060-7

Higgins, S. M., Goodwin, S. A., Bratton, T. R., & Tracy, G. W. (2008). Anisotropic stress models improve completion design in the Baxter shale. Paper presented at the *SPE Annual Technical Conference and Exhibition,* Denver, Colorado. DOI: 10.2118/115736-MS

Hofmann, R. (2006). *Frequency dependent elastic and anelastic properties of clastic rocks.* Ph.D. thesis, Colorado School of Mines, Golden, Colorado.

Hondros, G. (1959). The evaluation of Poisson's ratio and the modulus of materials of a low tensile resistance by the Brazilian (indirect tensile) test with particular reference to concrete. *Australian Journal of Applied Science, 10*(3), 243-268.

Hood, A., Gutjahr, C., & Heacock, R. (1975). Organic metamorphism and the generation of petroleum. *AAPG Bulletin, 59*(6), 986-996. DOI: 10.1306/83D91F06-16C7-11D7-8645000102C1865D

International Society for Rock Mechanics. (2007). *The complete ISRM suggested methods for rock characterization, testing and monitoring: 1974-2006*, International Soc. for Rock Mechanics, Commission on Testing Methods.

Japsen, P., Bruun, A., Fabricius, I. L., Rasmussen, R., Vejbæk, O. V., Pedersen, J. M., . . . Høier, C. (2004). Influence of porosity and pore fluid on acoustic properties of chalk: AVO response from oil, South Arne Field, North Sea. *Petroleum Geoscience, 10*(4), 319-330. DOI: 10.1144/1354-079303-586

Jizba, D., Mavko, G., & Nur, A. (1990). Static and dynamic moduli of tight gas sandstones. *SEG technical program expanded abstracts 1990* (pp. 827-829) Society of Exploration Geophysicists. DOI: 10.1190/1.1890352

Jones, S. C. (1972). A rapid accurate unsteady-state Klinkenberg permeameter. *Society of Petroleum Engineers Journal, 12*(05), 383-397. DOI: 10.2118/3535-PA

Katz, B., & Arango, I. (2018). Organic porosity: a geochemist's view of the current state of understanding. *Organic Geochemistry, 123*, 1-16. DOI: 10.1016/j.orggeochem.2018.05.015

King, M. S. (1964). *Wave velocities and dynamic elastic moduli of sedimentary rocks.* Ph.D. thesis, University of California, Berkeley,

King, M. S. (1969). Static and dynamic elastic moduli of rocks under pressure. Paper presented at the *The 11th US Symposium on Rock Mechanics (USRMS),*

Klinkenberg, L. (1941). The permeability of porous media to liquids and gases. Paper presented at the *Drilling and Production Practice,* New York, NY, USA. 200-213.

Koopmans, M., Carson, F., Damsté, J. S., & Lewan, M. (1998). Biomarker generation from Type II-S kerogens in claystone and limestone during hydrous and anhydrous pyrolysis. *Organic Geochemistry, 29*(5), 1395-1402. DOI: 10.1016/S0146-6380(98)00187-9

Korsnes, R., Wersland, E., Austad, T., & Madland, M. (2008). Anisotropy in chalk studied by rock mechanics. *Journal of Petroleum Science and Engineering, 62*(1), 28-35. DOI: 10.1016/j.petrol.2008.06.004

Krenkel, E. (1924). Der Syrische Bogen. *Centralbl.Mineral, 9*, 274-281.

Kuster, G. T., & Toksöz, M. N. (1974). Velocity and attenuation of seismic waves in two-phase media: Part I. Theoretical formulations. *Geophysics, 39*(5), 587-606. DOI: 10.1190/1.1440450

Kutuzov, I. (2017). *Study of the early stage immature oil produced from the israeli oil shale.* Unpublished M.Sc. thesis. Ben-Gurion University of the Negev, Be'er Sheva, Israel.

Labani, M., & Rezaee, R. (2015). Petrophysical Evaluation of Gas Shale Reservoirs. *Fundamentals of Gas Shale Reservoirs,* , 117-137.

Ledbetter, H.1993. Dynamic vs. static young's moduli: A case study. *Materials Science and Engineering: A***165**(1), L9-L10. DOI: 10.1016/0921-5093(93)90634-Q

Lee, M. W. (2004). Elastic velocities of partially gas-saturated unconsolidated sediments. *Marine and Petroleum Geology, 21*(6), 641-650. DOI: 10.1016/j.marpetgeo.2003.12.004

Li, Y., Guo, Z., Liu, C., Li, X., & Wang, G. (2015). A rock physics model for the characterization of organic-rich shale from elastic properties. *Petroleum Science, 12*(2), 264-272. DOI: 10.1007/s12182-015-0029-6

Li, C., Zhang, L., Luo, X., Zhang, L., Hu, C., Qi, Y., . . . Yu, Y.2017. Calibration of the mudrock compaction curve by eliminating the effect of organic matter in organic-rich shales: Application to the southern ordos basin, china. *Marine and Petroleum Geology* **86**, 620-635. DOI: 10.1016/j.marpetgeo.2017.06.027

Lo, T., Coyner, K. B., & Toksöz, M. N. (1986). Experimental determination of elastic anisotropy of Berea sandstone, Chicopee shale, and Chelmsford granite. *Geophysics, 51*(1), 164-171. DOI: 10.1190/1.1442029

Lockridge, J., & Pollastro, R. (1988). Shallow upper cretaceous niobrara gas fields in the eastern denver basin. In S. Goolsby, & M. Longman (Eds.), *Occurrence and petrophysical properties of carbonate reservoirs in the rocky mountain region* (pp. 63-74). Denver: Rocky Mountain Association of Geologists.

Löhr, S. C., Baruch, E. T., Hall, P. A., and Kennedy, M. J.2015. Is organic pore development in gas shales influenced by the primary porosity and structure of thermally immature organic matter? *Organic Geochemistry***87**, 119-132. DOI: 10.1016/j.orggeochem.2015.07.010

Loucks, R. G., Reed, R. M., Ruppel, S. C., & Hammes, U. (2012). Spectrum of pore types and networks in mudrocks and a descriptive classification for matrix-related mudrock pores. *AAPG Bulletin, 96*(6), 1071-1098. DOI: 10.1306/08171111061

Lucier, A. M., Hofmann, R., & Bryndzia, L. T. (2011). Evaluation of variable gas saturation on acoustic log data from the Haynesville Shale gas play, NW Louisiana, USA. *The Leading Edge, 30*(3), 300-311. DOI: 10.1190/1.3567261

Maldonado, A., Batzle, M., & Sonnenberg, S. (2011). Mechanical properties of the Niobrara formation. *AAPG Rocky Mountain Section Meeting,* Cheyenne, Wyoming, USA.

Marion, D. P. (1990). *Acoustical, mechanical, and transport properties of sediments and granular materials.* Ph.D. thesis, Stanford University, CA, US.

Mashinsky, E. I. (2003). Differences between static and dynamic elastic moduli of rocks: physical causes. *Russian Geology and Geophysics, 44*(9), 953-959.

Mavko, G., Mukerji, T., & Dvorkin, J. (2009). *The rock physics handbook: Tools for seismic analysis of porous media*, Cambridge University Press.

Meilijson, A., Ashckenazi-Polivoda, S., Illner, P., Alsenz, H., Speijer, R. P., Almogi-Labin, A., . . . Abramovich, S. (2015). Evidence for specific adaptations of fossil benthic foraminifera to anoxic–dysoxic environments. *Paleobiology, 42*(1), 77-97. DOI: 10.1017/pab.2015.3

Meilijson, A., Ashckenazi-Polivoda, S., Ron-Yankovich, L., Illner, P., Alsenz, H., Speijer, R. P., . . . Püttmann, W. (2014). Chronostratigraphy of the Upper Cretaceous high productivity sequence of the southern Tethys, Israel. *Cretaceous Research, 50*, 187-213. DOI: 10.1016/j.cretres.2014.04.006

Meléndez-Martínez, J., & Schmitt, D. R. (2016). A comparative study of the anisotropic dynamic and static elastic moduli of unconventional reservoir shales: Implication for geomechanical investigations. *Geophysics, 81*(3), D245-D261. DOI: 10.1190/geo2015-0427.1

Minster, T. (2009). *Oil shale deposits in israel.* (No. GSI/18/2009). Jerusalem, Israel: GSI.

Modica, C. J., & Lapierre, S. G. (2012). Estimation of kerogen porosity in source rocks as a function of thermal transformation: Example from the Mowry Shale in the Powder River Basin of Wyoming. *AAPG Bulletin, 96*(1), 87-108. DOI: 10.1306/04111110201

Moghadam, A. A., & Chalaturnyk, R. (2014). Expansion of the Klinkenberg's slippage equation to low permeability porous media. *International Journal of Coal Geology, 123*, 2-9.

Najibi, A. R., Ghafoori, M., Lashkaripour, G. R., & Asef, M. R. (2015). Empirical relations between strength and static and dynamic elastic properties of Asmari and Sarvak limestones, two main oil reservoirs in Iran. *Journal of Petroleum Science and Engineering, 126*, 78-82. DOI: 10.1016/j.petrol.2014.12.010

Ødegaard, E. & Avseth, P., (2003). Interpretation of Elastic Inversion Results Using Rock Physics Templates: *EAGE, Expanded Abstracts, E17.*

Okiongbo, K. S., Aplin, A. C., & Larter, S. R. (2005). Changes in type II kerogen density as a function of maturity: Evidence from the Kimmeridge Clay Formation. *Energy & Fuels, 19*(6), 2495-2499. DOI: 10.1021/ef050194+

Olsen, C. (2007). *Elastic and electric properties of North Sea Chalk.* Ph.D. thesis, Technical University of Denmark, Department of Environmental Engineering, Kongens Lyngby, Denmark.

Olsen, C., Christensen, H. F., & Fabricius, I. L. (2008). Static and dynamic Young's moduli of chalk from the North Sea. *Geophysics, 73*(2), E41-E50. DOI: 10.1190/1.2821819

Olsen, C., Hedegaard, K., Fabricius, I. L., & Prasad, M. (2008). Prediction of Biot's coefficient from rock-physical modeling of North Sea chalk. *Geophysics, 73*(2), E89-E96. DOI: 10.1190/1.2838158

Ong, O. N., Schmitt, D. R., Kofman, R. S., & Haug, K. (2016). Static and dynamic pressure sensitivity anisotropy of a calcareous shale. *Geophysical Prospecting, 64*(4), 875-897. DOI: 10.1111/1365-2478.12403

Orr, W. L. (1986). Kerogen/asphaltene/sulfur relationships in sulfur-rich Monterey oils. *Organic Geochemistry, 10*(1-3), 499-516. DOI: 10.1016/0146-6380(86)90049-5

Ortega, J. A., Ulm, F., & Abousleiman, Y. (2007). The effect of the nanogranular nature of shale on their poroelastic behavior. *Acta Geotechnica, 2*(3), 155-182. DOI: 10.1007/s11440-007-0038-8

Palchik, V. (2013). Is there link between the type of the volumetric strain curve and elastic constants, porosity, stress and strain characteristics? *Rock Mechanics and Rock Engineering, 46*(2), 315-326. DOI: 10.1007/s00603-012-0263-9

Papageorgiou, G., Amalokwu, K., & Chapman, M. (2016). Theoretical derivation of a Brie-like fluid mixing law. *Geophysical Prospecting, 64*(4), 1048-1053. DOI: 10.1111/1365-2478.12380

Pollastro, R., & Scholle, P. (1986). Diagenetic relationships in a hydrocarbon-productive chalk-The Cretaceous Niobrara Formation. *Studies in Diagenesis: US Geological Survey Bulletin, 1578*, 219-236.

Prasad, M., Mba, K. C., Sadler, T., & Batzle, M. L. (2011). Maturity and impedance analysis of organic-rich shales. *SPE Reservoir Evaluation & Engineering, 14*(05), 533-543. DOI: 10.2118/123531-PA

Qin, X., Han, D., & Yan, F. (2016). Rock-physics modeling of shale during smectite-to-illite transition. Paper presented at the *SEG International Exposition and 86th Annual Meeting, 2016,* Dallas, TX, US. 3416-3421. DOI: 10.1190/segam2016-13967508.1

Røgen, B., Fabricius, I. L., Japsen, P., Høier, C., Mavko, G., & Pedersen, J. M. (2005). Ultrasonic velocities of North Sea chalk samples: influence of porosity, fluid content and texture. *Geophysical Prospecting, 53*(4), 481-496. DOI: 10.1111/j.1365-2478.2005.00485.x

Rosenberg, Y. O., Meshoulam, A., Said-Ahmad, W., Shawar, L., Dror, G., Reznik, I. J., . . . Amrani, A. (2017). Study of thermal maturation processes of sulfur-rich source rock using compound specific sulfur isotope analysis. *Organic Geochemistry, 112*, 59-74. DOI: 10.1016/j.orggeochem.2017.06.005

Ryan, R. C., Fowler, T. D., Beer, G. L., & Nair, V. (2010). Shell's in situ conversion process− from laboratory to field pilots. *Oil shale: A solution to the liquid fuel dilemma* (pp. 161-183) ACS Publications.

Sarout, J., Molez, L., Guéguen, Y., & Hoteit, N. (2007). Shale dynamic properties and anisotropy under triaxial loading: Experimental and theoretical investigations. *Physics and Chemistry of the Earth, Parts A/B/C, 32*(8), 896-906. DOI: 10.1016/j.pce.2006.01.007

Sayers, C. M. (2013a). The effect of anisotropy on the Young's moduli and Poisson's ratios of shales. *Geophysical Prospecting, 61*(2), 416-426. DOI: 10.1190/1.3513382

Sayers, C. M. (2013b). The effect of kerogen on the elastic anisotropy of organic-rich shales. *Geophysics, 78*(2), D65-D74. DOI: 10.1190/geo2012-0309.1

Sayers, C. M., & Dasgupta, S. (2014). Elastic anisotropy of the Middle Bakken formation. *Geophysics, 80*(1), D23-D29. DOI: 10.1190/geo2014-0219.1

Sayers, C. M., Fisher, K., & Walsh, J. J. (2015). Rock physics of the eagle ford shale. Paper presented at the *Unconventional Resources Techology Conference (URTeC),* San Antonio, Texas, USA. 2236-2248. DOI: 10.15530/urtec-2015-2151459

Shirav, M., & Ginzburg, D. (1984). *Geochemistry of israel oil shales.* (No. GSI/24/84). Jeusalem: Geological Survey of Israel.

Simmons, G., & Brace, W. (1965). Comparison of static and dynamic measurements of compressibility of rocks. *Journal of Geophysical Research, 70*(22), 5649-5656. DOI: 10.1029/JZ070i022p05649

Sone, H., & Zoback, M. D. (2013a). Mechanical properties of shale-gas reservoir rocks—Part 1: Static and dynamic elastic properties and anisotropy. *Geophysics, 78*(5), D381-D392. DOI: 10.1190/geo2013-0050.1

Sone, H., & Zoback, M. D. (2013b). Mechanical properties of shale-gas reservoir rocks—Part 2: Ductile creep, brittle strength, and their relation to the elastic modulusMechanical properties of gas shale—Part 2. *Geophysics, 78*(5), D393-D402. DOI: 10.1190/geo2013-0051.1

Spiro, B. (1980). *Geochemistry and mineralogy of bituminous rocks in israel.* Unpublished Ph.D. thesis. The Hebrew University of Jerusalem., Israel.

Suarez-Rivera, R., & Fjær, E. (2013). Evaluating the poroelastic effect on anisotropic, organic-rich, mudstone systems. *Rock Mechanics and Rock Engineering, 46*(3), 569-580. DOI: 10.1007/s00603-013-0374-y

Sweeney, J. J., & Burnham, A. K. (1990). Evaluation of a simple model of vitrinite reflectance based on chemical kinetics (1). *AAPG Bulletin, 74*(10), 1559-1570. DOI: 10.1306/0C9B251F-1710-11D7-8645000102C1865D

Talesnick, M., Hatzor, Y., & Tsesarsky, M. (2001). The elastic deformability and strength of a high porosity, anisotropic chalk. *International Journal of Rock Mechanics and Mining Sciences, 38*(4), 543-555. DOI: 10.1016/S1365-1609(01)00024-7

Tanikawa, W., & Shimamoto, T. (2009). Comparison of Klinkenberg-corrected gas permeability and water permeability in sedimentary rocks. *International Journal of Rock Mechanics and Mining Sciences, 46*(2), 229-238. DOI: 10.1016/j.ijrmms.2008.03.004

Thomsen, L. (1986). Weak elastic anisotropy. *Geophysics, 51*(10), 1954-1966. DOI: 10.1190/1.1442051

Thomsen, L. (2017). Fluid dependence of rock compressibility, post Biot-Gassmann. *SEG technical program expanded abstracts 2017* (pp. 3690-3694) Society of Exploration Geophysicists.

Tiab, D., and Donaldson, E. C.2016. Chapter 12 - shale-gas reservoirs., 719-774. DOI: 10.1016/B978-0-12-803188-9.00012-7

Tissot, B. P., & Welte, D. H. (1984). *Petroleum formation and occurrence*: New York. Springer-Verlag. 699p.

Togashi, Y., Kikumoto, M., & Tani, K. (2017). An Experimental Method to Determine the Elastic Properties of Transversely Isotropic Rocks by a Single Triaxial Test. *Rock Mechanics and Rock Engineering, 50*(1), 1-15. DOI: 10.1007/s00603-016-1095-9

Tutuncu, A., & Sharma, M. (1992). Relating static and ultrasonic laboratory measurements to acoustic log measurements in tight gas sands. Paper presented at the *SPE Annual Technical Conference and Exhibition,* DOI: 10.2118/24689-MS

Vanorio, T., Mukerji, T., & Mavko, G. (2008). Emerging methodologies to characterize the rock physics properties of organic-rich shales. *The Leading Edge, 27*(6), 780-787. DOI: 10.1190/1.2944163

Vernik, L. (1994). Hydrocarbon-generation-induced microcracking of source rocks. *Geophysics, 59*(4), 555-563. DOI: 10.1190/1.1443616

Vernik, L. (2016). *Seismic petrophysics in quantitative interpretation*, Society of Exploration Geophysicists. DOI: 10.1190/1.9781560803256

Vernik, L., & Landis, C. (1996). Elastic anisotropy of source rocks: Implications for hydrocarbon generation and primary migration. *AAPG Bulletin, 80*(4), 531-544.

Vernik, L., & Liu, X. (1997). Velocity anisotropy in shales: A petrophysical study. *Geophysics, 62*(2), 521-532. DOI: 10.1190/1.1444162

Vernik, L., & Milovac, J. (2011). Rock physics of organic shales. *The Leading Edge, 30*(3), 318-323. DOI: 10.1190/1.3567263

Vernik, L., & Nur, A. (1992). Ultrasonic velocity and anisotropy of hydrocarbon source rocks. *Geophysics, 57*(5), 727-735. DOI: 10.1190/1.1443286

Villamor Lora, R., Ghazanfari, E., & Asanza Izquierdo, E. (2016). Geomechanical Characterization of Marcellus Shale. *Rock Mechanics and Rock Engineering, 49*, 3403-3424. DOI: 10.1007/s00603-016-0955-7

Wang, G., Ren, T., Wang, K., & Zhou, A. (2014). Improved apparent permeability models of gas flow in coal with Klinkenberg effect. *Fuel, 128*, 53-61. DOI: 10.1016/j.fuel.2014.02.066

Wang, G., Wang, T., Simoneit, B. R., Zhang, L., & Zhang, X. (2010). Sulfur rich petroleum derived from lacustrine carbonate source rocks in Bohai Bay Basin, East China. *Organic Geochemistry, 41*(4), 340-354. DOI: 10.1016/j.orggeochem.2009.12.010

Wang, Z., & Nur, A. (Eds.). (2000). *Seismic and acoustic velocities in reservoir rocks, vol. 3, recent developments* (Geophysics Reprint Series Number 19 ed.). Tulsa, OK:, Society of Exploration Geophysicists.

Wang, Z., Wang, H., & Cates, M. E. (2001). Effective elastic properties of solid clays. *Geophysics, 66*(2), 428-440. DOI: 10.1190/1.1444934

Ward, J. (2010). Kerogen density in the Marcellus shale. Paper presented at the *SPE Unconventional Gas Conference,* DOI: 10.2118/131767-MS

Wetzel, M., Kempka, T., & Kühn, M. (2017). Predicting macroscopic elastic rock properties requires detailed information on microstructure. *Energy Procedia, 125*, 561-570. DOI: 10.1016/j.egypro.2017.08.195

White, J. (1975). Computed seismic speeds and attenuation in rocks with partial gas saturation. *Geophysics, 40*(2), 224-232.

Wollner, U., & Dvorkin, J. (2018). Effective bulk modulus of the pore fluid at patchy saturation. *Geophysical Prospecting, 66*(7), 1372-1383. DOI: 10.1111/1365-2478.12632

Yan, F., Han, D., & Yao, Q. (2016). Physical constraints on c13 and δ for transversely isotropic hydrocarbon source rocks. *Geophysical Prospecting, 64*(6), 1524-1536. DOI: 10.1111/1365-2478.12265

Yan, F., & Han, D. (2013). Measurement of elastic properties of kerogen. Paper presented at the *2013 SEG Annual Meeting,* Houston, Texas. DOI: 10.1190/segam2013-1319.1

Yan, F., Han, D., Sil, S., & Chen, X. (2016). Analysis of seismic anisotropy parameters for sedimentary strata. *Geophysics, 81*(5), D495-D502. DOI: 10.1190/geo2016-0062.1

Yang, Y., & Zoback, M. (2016). Viscoplastic deformation of the Bakken and adjacent formations and its relation to hydraulic fracture growth. *Rock Mechanics and Rock Engineering, 49*(2), 689. DOI: 10.1007/s00603-015-0866-z

Yang, Y., & Mavko, G. (2018). Hydrous pyrolysis-based rock-physics modeling for organic-rich shales at various levels of thermal maturity. *SEG technical program expanded abstracts 2018* (pp. 3744-3748) Society of Exploration Geophysicists. DOI: 10.1190/segam2018-2998023.1

Zargari, S., Prasad, M., Mba, K. C., & Mattson, E. D. (2013). Organic maturity, elastic properties, and textural characteristics of self resourcing reservoirs. *Geophysics, 78*(4), D223-D235. DOI: 10.1190/geo2012-0431.1

Zargari, S., Wilkinson, T. M., Packard, C. E., & Prasad, M. (2016). Effect of thermal maturity on elastic properties of kerogen. *Geophysics, 81*(2), M1-M6. DOI: 10.1190/geo2015-0194.1

Zhao, L., Qin, X., Han, D., Geng, J., Yang, Z., & Cao, H. (2016). Rock-physics modeling for the elastic properties of organic shale at different maturity stages. *Geophysics, 81*(5), D527-D541. DOI: 10.1190/geo2015-0713.1

Zhao, L., Qin, X., Zhang, J., Liu, X., Han, D., Geng, J., & Xiong, Y. (2017). An Effective Reservoir Parameter for Seismic Characterization of Organic Shale Reservoir. *Surveys in Geophysics, ,* 1-33. DOI: 10.1007/s10712-017-9456-9

Zisman, W. A. (1933). Comparison of the Statically and Seismologically Determined Elastic Constants of Rocks. *Proceedings of the National Academy of Sciences of the United States of America, 19*(7), 680-686.

Zoback, M. D. (2010). *Reservoir geomechanics*, Cambridge University Press.

יחסים בין תכונות פיסיקליות ודרגת המטורציה בקרטון עשיר בחומר אורגני בשני אגנים בישראל: מדידות מעבדה ושדה

מחקר לשם מילוי חלקי של הדרישות לקבלת תואר "דוקטור לפילוסופיה"

מאת

עמרי שטרית

הוגש לסינאט אוניברסיטת בן גוריון בנגב

י"ז באדר ב', תשע"ט **24.03.2019**

באר שבע

יחסים בין תכונות פיסיקליות ודרגת המטורציה בקרטון עשיר בחומר אורגני בשני אגנים בישראל: מדידות מעבדה ושדה

מחקר לשם מילוי חלקי של הדרישות לקבלת תואר "דוקטור לפילוסופיה"

מאת

עמרי שטרית

הוגש לסינאט אוניברסיטת בן גוריון בנגב

אושר ע"י המנחים:

פרופ' יוסף ח. חצור _____

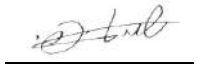

פרופ' שמעון פיינשטיין _____

פרופ' הרולד ויניגר _____

אישור דיקן בית הספר ללימודי מחקר מתקדמים ע"ש קרייטמן _____

י"ז באדר ב', תשע"ט **24.03.2019**

באר שבע

<u>העבודה נעשתה בהדרכת</u>

פרופ׳ יוסף ח. חצור

פרופ׳ שמעון פיינשטיין

פרופ׳ הרולד ויניגר

מהמחלקה למדעי הגיאולוגיה והסביבה
הפקולט למדעי הטבע
אוניברסיטת בן-גוריון בנגב

הצהרת תלמיד המחקר עם הגשת עבודת הדוקטור לשיפוט

אני, עמרי שטרית, החתום מטה מצהיר/ה בזאת:

חיברתי את חיבורי בעצמי, להוציא עזרת ההדרכה שקיבלתי מאת מנחה/ים.

החומר המדעי הנכלל בעבודה זו הינו פרי מחקרי מתקופת היותי תלמיד/ת מחקר.

תאריך 24.3.2019 שם התלמיד/ה עמרי שטרית

חתימה 

<u>תקציר</u>

תזה זו מציגה מחקר מעמיק של התכונות הפיסיקליות של קרטון עשיר בחומר אורגני, מתצורות ע׳רב-מישאש שבאגן השפלה בישראל. המחקר מבוסס על מגוון מדידות מעבדה ועל תיאוריות מתחום פיזיקת הסלע (rock physics), לשם הבנת ההשפעה של משתנים כגון פורוזיות, תכולת חומר אורגני, בגרות תרמלית ורווית נוזלים בחללים. זה נעשה ע״י התאמת מודלי פיזיקת הסלע (RPM) למיקרו-סטרוקטורה הייחודית של הסלע. לצורך כך, מדידות מעבדה נעשות על דוגמאות מגלעינים מהקידוחים זוהרים ואדרת שבאגן השפלה. תכונות הסלע אשר בהן מתמקד המחקר הן פורוזיות, צפיפות, מהירויות גלים, מקדמים אלסטיים, פרמיאביליות, חוזק בלחיצה וחוזק במתיחה. ההשפעה של בגרות תרמלית (מטורציה) על תכונות הסלע נבחנת באמצעות ניסויי פירוליזה שבוצעו על המדגמים, על מנת לדמות דרגות מטורציה שונות. לאחר מכן, ממצאי המחקר המעבדתי מושווים עם מדידות בשדה מלוגים של הקידוחים הנ״ל. עבודה זו מספקת כלים לניתוח כמותי של קרטון ע׳רב-מישאש לצרכי אקספלורציה גיאופיסית ותכנונים הנדסיים בסלע.

לרוב, סלעים עשירים בחומר אורגני הם פצלים עשירי-חרסיות, אשר ניכרים בפורוזיות נמוכה, תכולות חומר אורגני משתנות, ובעלי מבנה לאמינרי. בניגוד לפצלים עשירים בחומר אורגני, הקרטון של ע׳רב-מישאש הוא בעל פורוזיות גבוהה, והוא בעל טקסטורות mudstone-wackestone. החומר האורגני מפוזר במטריקס של הסלע ולא מסודר בלמינות כפי שקורה בפצלים. לכן, גישות RPM המיושמות במחקר זה בעלות מאפיינים של RPM של פצלים עשירים בחומר אורגני ושל קרטונים. קרטון ע׳רב-מישאש שבאגן השפלה מצוי כיום בעומקים רדודים (מאות מטרים) ומעולם לא חווה קבורה משמעותית. כתוצאה מכך דרגות המטורציה, הקומפקציה והצמנטציה של הסלע אינן גבוהות. ישנן שלוש פאזות דומיננטיות בסלע: 1) מינרלים, בעיקר קלציט (60-80% נפחיים); 2) פורוזיות, 25-45%; ו-3) חומר אורגני, 5-25%, ברובו קרוגן Type IIs. סידור המוצקים בסלע מביא למבנה אנאיזוטרופי מסגנון vertical transverse isotropy (VTI): בהנחה שכיוון השיכוב הוא אופקי, המישור האופקי הוא איזוטרופי, ובכיוון האנכי מתקבלות תכונות שונות מאשר באופקי. האנאיזוטרופיה באה לידי ביטוי בתכונות פיסיקליות שונות של הסלע, כמו מהירויות גלים, מקדמים אלסטיים, חוזק, פרמיאביליות. שימוש ב RPM נעשה תוך התחשבות בפרופורציות הנפחיות של המרכיבים בסלע, סידורם במטריקס והשפעתם על מכניקת הסלע.

בעבודה זו מוצגים ארבעה פיתוחים תיאורטיים ושיטתיים לצורך ניתוח תכונות של סלעים עשירים בחומר אורגני וסלעים אנאיזוטרופיים:

- **<u>יחס העיבורים בלחיצה הידרוסטטית, Ω:</u>** במצב של לחץ שווה מכל הכיוונים (לחיצה הידרוסטטית), סלעים VTI טיפוסיים יתקצרו בניצב לשיכוב יותר מאשר במקביל לשיכוב. היחס בין העיבורים האנכי והאופקי מוגדר כאן לראשונה ע״י הפרמטר Ω, אשר מכמת את האנאיזוטרופיה בסלע. לכן, Ω בסלעים VTI טיפוסיים קטן מ 1 וגדול מ 0. בזכות ההגדרה הפשוטה שלו, זהו פרמטר אשר מעניק אינטואיציה פיסיקלית באשר לאנאיזוטרופיה בתכונות האלסטיות של הסלע. הגדרת הפרמטר Ω נעשית על בסיס חוק הוק לקשרי מאמץ-עיבור אלסטיים, הנקבעים ע״י מטריצת הקשיחות האלסטית של החומר. הפרמטר Ω מחושב באמצעות ארבעה מתוך חמשת הפרמטרים המרכיבים את המטריצה, ובכך נותן ייצוג טוב של האנאיזוטרופיה בחומר. לפיכך, Ω הוא פרמטר אינפורמטיבי במיוחד, אשר מביא לידי ביטוי תכונות בניצב, במקביל ובזווית לכיוון השיכוב. ע״י יצירת גרף של Ω מול הפרמטר ε של ת׳ומסן לאנאיזוטרופיה בגלי P (Thomsen 1986), מתקבל קשר חזק בין השניים. הפרמטר Ω מתגלה כיותר רגיש פי 2 בערך בדרגות אנאיזוטרופיה הנמוכות. בעוד רוב הפרמטרים לאנאיזוטרופיה

אלסטית מתאימים לתנאים דינמיים של מעבר גלים בסלע, Ω הוא היחיד שמתאים לתנאים של לחיצה סטטית. לכן, הגדרת Ω מסייעת משמעותית בחקר אנאיזוטרופיה בסלעים.

- **<u>שיטת *HDC-TIES*:</u>** סלעים *VTI* לרוב נבדקים בבדיקות לחיצה באמצעות ציוד מיוחד וייעודי לדרגת האנאיזוטרופיה, או באמצעות קדיחת מספר דוגמאות בכיוונים שונים. השיטה המוצעת פותחה לצורך ניתוח תוצאות בדיקת לחיצה טריאקסיאליות שמבוצעת על דוגמת סלע *VTI* בודדת, שנקדחה בניצב לשכבות. הפרמטרים האלסטיים של הסלע מחושבים באמצעות שילוב של התצפיות משלבי הלחיצה ההידרוסטטית והדביאטורית: <u>H</u>ydrostatic-<u>D</u>eviatoric <u>C</u>ombination for <u>T</u>ransversely <u>I</u>sotropic <u>E</u>lastic <u>S</u>tiffnesses (HDC-TIES). שיטת HDC-TIES לוקחת בחשבון את מערך הבדיקות הכי נפוץ- מדידות מאמצים ועיבורים בכיוון הצירי והרדיאלי של דוגמאות גליליות. בשיטת HDC-TIES, המקדמים האלסטיים מחושבים ע״י שילוב המקדמים שמעריכים באופן שיגרתי מלחיצה דביאטורית (מקדמים יאנג E_v ומקדם פואסון ν_v בכיון האנכי), ומלחיצה הידרוסטטית (מודול הנפח K, והפרמטר שמוצע כאן Ω). ע״י שילוב הפרמטרים הללו בתוך קשרי המאמץ-עיבור, ניתן לחשב את הקבועים ממטריצת הקשיחות של החומר: C_{11}, C_{12}, C_{66}, וגם ניתן להגדיר גבולות עבור המקדמים $C_{13}, C_{33}, C_{11}+C_{12}$. בכך, ע״י מדידה בודדת מתקבלת אינפורמציה רבה על סלע אנאיזוטרופי. שיטת HDC-TIES תורמת במספר דרכים: 1) במקרה שאין מספיק חומר, ניתן לקבל אינפורמציה רבה ממדידה בודדת; 2) בהיעדר ציוד ייעודי למדידת חומרים אנאיזוטרופיים; 3) הטרוגניות בין דוגמאות אינה מהווה בעיה; 4) היא מספקת הערכה ישירה של הפרמטר C_{13}, אשר הוא בעל חשיבות מיוחדת עבור מחקרים גיאופיסיים; 5) ניתן ליישם את השיטה על רקורד קיים של בדיקות ובכך לתקן את התוצאות.
- **<u>מודל "HS kerogen":</u>** גבולות חשין-שטריקמן (HS, Hashin and Shtrikman 1963, Mavko et al. 2009) הם מודל נפוץ להערכת המקדמים האלסטיים ומהירויות הגלים של חומר גרגריים. המודל מניח את הסידורים הרך והקשיח ביותר שניתן לעשות בסלע עבור פרופורציה ספציפית בין המרכיבים השונים. בסלעים נקבוביים, הגבול התחתון מתאר חומר תמוך-נוזל (תרחיף) ואילו הגבול העליון מתאר רציפות מכאנית של הפאזה הקשיחה. העיקרון של מודל זה מיושם כאן לצורך תיאור סלע תמוך-קרוגן, חומר אורגני מוצק אשר קשיח יותר מהנוזל הממלא את החללים ורך יותר מהמינרלים בסלע. המודל מוגדר כאן כ "HS kerogen". המודל מתאר תערובת מינרלים-קרוגן-חללים, כאשר הקרוגן מסודר במטריקס באופן אפקטיבי כך שהוא שולט בתגובה המכאנית של הסלע. נמצא כי מהירויות הגלים של קרטון ע׳רב-מישאש שנמדדות בניצב לשכבות מתוארות באופן מדוייק ע״י המודל.
- **<u>תיקון למודל פטרופיסיקלי של סלעים עשירים בחומר אורגני:</u>** הערכת המאסות והנפחים של הפאזות השונות במחקרי פיזיקת הסלע על סלעי עשירים בחומר אורגני נמצאה כלא מדוייקת. מדידות תכולת חומר אורגני יוחסו באופן ישיר לתכולת הקרוגן, תוך התעלמות מפאזת הביטומן. בנוסף, ההתחשבות בפורוזיות שבסלעים נמצאה כשגויה ומבלבלת, מה שהביא לשגיאות משמעותיות בסלעים בעלי פורוזיות גבוה, כמו למשל קרטון ע׳רב -מישאש. בעבודה זו מוצע תיקון למודל: 1) תוצאות מדידות אחוז משקלי של פחמן אורגני במטריקס (TOC) מומרות לנפח חומר אורגני ולא לנפח קרוגן, ומוצעת שיטה לחישוב נפחי קרוגן וביטומן על בסיס מדידות מיצוי ביטומן מהסלע; 2) הכללת הפורוזיות במודל תוך הבדלה ברורה בין נפח המוצקים בסלע והנפח הכולל שלו.

השיטות החדשות המוצעות בעבודה זו מהוות חלק חשוב מאנליזת פיזיקת הסלע של קרטון ע׳רב-מישאש. החלק הניסויי של המחקר כולל שלושה חלקים עיקריים: 1) איפיון נרחב ומעמיק של תכונות הסלע במצבו הטבעי, כשהוא לא בוגר תרמלית, על בסיס מדידות מעבדה באמצעות דוגמאות גלעין מאגן השפלה; 2) חקירת השינוי בתכונות הפיסיקליות כתוצאה ממטורציה מלאכותית (פירוליזה); 3) ניתוח לוגים מקידוחים זוהרים ואדרת.

הדיגום הנרחב ממקידוח זוהרים (כ -280 מ׳ של גלעינים) איפשר לבצע סכימת מדידות מקיפה ביותר על הסלע במצבו הטבעי, כשהוא אינו בוגר תרמלית. המדידות שבוצעו הן פורוזיות, צפיפות, פרמיאביליות, מהירויות גלים (מקדמים אלסטיים דינמיים), בדיקות לחיצה תלת צירית לקבלת החוזק והמקדמים האלסטיים הסטטיים, ובדיקות ברזיליאניות לקבלת חוזק הסלע במתיחה. ההשפעה של תכולת חומר אורגני

על כל אחת מהתכונות הללו נחקרה באמצעות נתוני TOC. נמצאה כי אין כל השפעה של החומר האורגני על הפורוזיות בסלע, משמע החומר האורגני הוא מהווה מרכיב של המטריקס (הימצאות קרוגן באה על חשבון גרגר מינרלי). הפרוזיות והחומר האורגני הם שני משתנים בלתי תלויים, אשר שולטים בתכונות הפיסיקליות השונות של הסלע. צפיפות המטריקס קשורה באופן חזק ל TOC, והמודל הפטרופיסיקלי מסייע בחישוב הצפיפות הממוצעת של המינרלים והחומר האורגני בחתך (2.74 ג׳ לסמ״ק ו 1.43 ג׳ לסמ״ק, בהתאמה). צפיפות החומר האורגני נחשבת לגבוהה יחסית, זאת כתוצאה מתכולת גופרית גבוהה בקרוגן (מסווג כ Type IIs) וכתוצאה מריכוז ביטומן זניח.

המקדמים הדינמיים האנכיים, המתקבלים ע״י מדידות מהירויות גלי P ו S בניצב לשכבות, מתוארים היטב באמצעות מודל ״HS kerogen״. סריקות במיקרוסקופ סורק אלקטרונים (SEM) מאשרות שהמטריקס דק-הגרגר מורכב מתערובת של קרוגן וחלקיקי קלציט קטנים. כאשר משליכים את המקדמים הדינמיים ביחס לגבולות חשין-שטריקמן, ניתן להשתמש בפרמטר w (משיטת BAM של מאריון, Marion 1990) המתאר את המרחק המנורמל בין הגבולות, כשערכו הוא 1 בגבול העליון ו 0 בתחתון. נמצא כי הסלע הוא בעל סידור ״רך״ של המרכיבים, עם ערך w ממוצע של 0.2. באמצעות מודל זה ניתן גם להעריך את השתנות המקדמים כתלות ברווית הנוזל/ גז בחללים. המקדמים האלסטיים, גם הדינמיים וגם הסטטיים, קטנים ככל שפורוזיות ותכולת קרוגן גדלות. ההשפעה של הפורוזיות על המקדמים היא בערך כפולה מההשפעה של הקרוגן. המקדמים הדינמיים גדולים משמעותית מהמקדמים הסטטים כשמשווים ביניהם במצב יבש. היחס ביניהם קטן מ~4 עד ~2, עם עליית תכולת הקרוגן. בניגוד למקדמים האלסטיים, חוזק הסלע בלחיצה ובמתיחה תלוי בעיקר בפורוזיות, ולא ניתן להבחין בהשפעה של החומר האורגני על החוזק.

האנאיזוטרופיה בסלע ניכרת במקדמים הסטטיים והדינמיים (וכך גם מהירויות הגלים), בפרמיאביליות ובחוזק המתיחה של הסלע. זה נובע מאוריינטציית המרכיבים המיושרים עם כיוון השיכוב (בעיקר שברי מאובנים), וכך גם הקישוריות בין החללים משופרת בכיוון זה. באופן מפתיע, האנאיזוטרופיה אינה תלויה בתכולת החומר האורגני, אלא בעיקר בפורוזיות. ולמרות זאת, הקשרים בין הפרמטרים לאנאיזוטרופיה אלסטית (Ω, והפרמטרים של ת׳ומסן) דומים לאלו שרואים בסלעים אחרים אשר עשירים בחומר אורגני.

על מנת לחקור את ההשפעה של מטורציה תרמלית על תכונות הסלע, החומר מגלעיני קידוח זוהרים נלקחו לניסויי פירוליזה המדמים באופן מלאכותי מטורציה. ארבע דרגות מטורציה שונות התקבלו מניסויי הפירולויזה: בגרות מוקדמת, בוגר 1, בוגר 2, ובגרות יתר. במהלך הפירוליזה, הפורוזיות גדלה על חשבון החומר האורגני, עקב היעדר לחץ מקיף בניסויים. תכולת ביטומן בסלע גדלה עם המטורציה עד לדרגת בוגר 2, ומשם דועכת עד לכדי מיצוי פוטנציאל היצירה של נפט וגז מהחומר האורגני (בגרות יתר). באמצעות המודל הפטרופיסיקלי, פורוזיות וצפיפות מוצקים מתוקנים לפי ריכוזי הביטומן תוך התחשבות בו כנוזל ממלא חללים. עם המטורציה, צפיפות הקרוגן גדלה מ 1.4 ג׳ לסמ״ק במצב לא בוגר ל 1.5 במצב של בגרות התחלתית ובוגר 1, לאחר מכן עולה ל 1.7 ג׳ לסמ״ק בבוגר 2, ולבסוף עולה עד מעבר 1.8 ג׳ לסמ״ק בשלב בגרות יתר. הרצף הזה ניכר גם במדידות מהירויות הגלים, כאשר מהירות גלי S עולה עקב עלייה בקשיחות הקרוגן השאריתי (תופעה אשר עלולה להיות ייחודית לקרוגן Type IIs בפירוליזה). לעומת זאת, מהירויות גלי P קטנות עם דרגת המטורציה עקב העלייה המשמעותית בפורוזיות. המודולים של גלי P וגלי S (צפיפות* מהירות בריבוע) בניצב ובמקביל לשכבות, מראים דעיכה אקספוננציאלית עם העלייה בערך הסכום של

פורוזיות ותכולת קרוגן, באופן בלתי תלוי בדרגת המטורציה. האנאיזוטרופיה גדלה עם העלייה בפורוזיות, וללא כל תלות בתכולת החומר האורגני.

מידול פיזיקת הסלע בדרגות המטורציה השונות נעשה באמצעות שני מודלים: 1) מודל "HS+BAM", המתכייל לתוצאות המעבדה; ו- 2) מודל "HS kerogen", המתאר סלע גרגרי תמוך קרוגן. ניתוח של מודלים אלו נעשה באמצעות גליונות פיזיקת הסלע (RPT) משני סוגים: היחס מהירויות גלי P ו S (Vp/Vs) אל מול העכבה האקוסטית (מכפלת הצפיפות במהירות גלי P), והיחד Vp/Vs אל מול מכפלת צפיפות המוצקים במהירות גלי S. ניתוח התוצאות מצביע על כך שמודל "BAM+HS" מניב צורה ומגמות לא ריאליות, ולכן מודל זה מתאים אך ורק לחישוב fluid substitution. למרות שמודל "HS kerogen" אינו מייצג את החומר שעבר פירוליזה, הוא נמצא משמעותית יותר ריאלי ומדוייק עבור סלעים אשר עברו מטורציה טבעית. ה RPT מבציעים על כך שהפורוזיות מהווה את התפקיד המשמעותי ביותר, ולאחר מכן תכולת החומר האורגני. מכיוון שהונח כי הסלע נמצא ברווית-מים מלאה, לא נצפים שינויים משמעותיים בתכונות הסלע עם המטורציה. עם זאת, מטורציה בדרך כלל מלווה בשינויים בהרכב הנוזלים והגזים בחללים, דברים אשר מביאים ליריד ביחס Vp/Vs.

התצפיות מהמחקר המעבדתי עוברות השוואה למדידות מלוגים של קידוחים בזוהרים ואדרת. על מנת לייצר פרופיל רציף של החומר האורגני בבאר, נעשה שימוש במדידות TOC מדוגמאות גלעון רציף (continuous coring) אשר נדגמו ברווחים של 1 מ'. השילוב בין מדידות TOC ולוג הצפיפות (CCDL) מאפשר חישוב פורוזיות ותכולת קרוגן לאורך כל החתך בבאר. בהתבסס עליהם, מודל "HS kerogen" מחושב עבור החתך בבארות. המודל הנ"ל נמצא כאמין ביותר עבור מהירויות הגלים בקידוחים זוהרים ואדרת. באזור החלק העליון של תצורת ע'רב מתגלה אזור של הצטברות גז, ע"י כך שערכי "HS kerogen" גבוהים יותר מאלו שנמדדו בלוגים באינטרוול זה. באמצעות שילוב המודל "HS kerogen" ותיאוריות שונות לקישור דחיסות הנוזל לרווית גז, נמצא כי דרגות רוויית הגז הן כ 10-15%. בנוסף, מוצעים קשרים לשם הערכת TOC באמצעות לוגים gamma-ray, הניוטרון והצפיפות. נמצא קשר בין המימן העודף בסלע (ההפרש בין לוג הניוטרונים ולוג הצפיפות) ובין ה TOC. הפרוצדורות שמוצגות בעבודה זו ניתנות ליישום להערכת סלעים פורוזיביים עשירים בחומר אורגני בפרט, וסלעים עשירים בחומר אורגני בכלל, וזאת בהסתמך על מערך לוגים בסיסי ביותר.

<u>מילות מפתח:</u>
פיזיקת הסלע, פטרופיסיקה, מכניקת הסלע, סלעים עשירים בחומר אורגני, קרטון ע'רב מישאש, סלע מקור, פורוזיות, קרוגן, מקדמים אלסטיים סטטים ודינמיים, מהירויות גלי P ו S, אנאיזוטרופיה, איזוטרופיה משוכבת, רווית נוזלים וגזים, פירוליזה, בגרות תרמלית